Biomechanical Experimental Simulation of Pelvic Fracture

by

Calvin Cherng-Bing Jee

A thesis submitted in partial fulfillment of the requirements for the degree of

Master of Science

Department of Mechanical Engineering

University of Alberta

Abstract

With a growing elderly population, osteoporotic pelvic fractures have been an increasingly common worldwide problem. Due to the complexity of the human pelvis, difficulties exist in the diagnosis of subtle fractures and complications may arise from standard treatments. Guidelines for approaching pelvic fracture have been established, but the uniqueness and complexity of the pelvis leaves much to professional discretion. This thesis showed how a biomechanical study provides more objective insights in dealing with the pelvic fractures.

A three-dimensional digital image correlation (3D-DIC) was used for its ability to extract mechanical measurements across a sizeable area of the contoured pelvic surface. From a preliminary study, a procedure was established to effectively conduct an optimized experiment with this technique and to quantify the uncertainty of its measurements. An existing experimental setup was redesigned and reconfigured for testing and measuring with an integrated DIC system. From initial experimentation and validation, it was shown that crack behavior can be accurately characterized using the ability of the test setup to measure crack edge openings as small as 0.03 mm with less than 10% uncertainty.

When testing on an intact pelvis, the measurements were very repeatable, observed to be about 10% for strain measurements. After testing a fractured pelvis and comparing the results to the intact pelvis, it could be seen how a crack causes shifts in the tension and compression profiles experienced by a normal pelvis. It was also shown that the test setup could observe crack behavior on a microscopic scale while observing a significant area of the pelvis. Crack edge opening measurements with less than 10% uncertainty were then used to characterize the stability of the fractured specimen. The designed setup was proven to be an effective tool for analyzing the mechanics and stability of a fractured pelvis.

Acknowledgements

First and foremost, I would like to give thanks to my advisor, Dr. Kajsa Duke, for providing me this opportunity and guiding me through it from start to end. Thank you for supporting me financially and academically, allowing me to access learning opportunities across the country and worldwide. You always showed me respect and were never dismissive of my opinions. Your ever-present encouragement, patience, and trust in my work brought me past the difficult moments of this academic endeavor. And your constant effort towards my personal growth, within and beyond the program, has always been invaluable to me. Working with you led to instructional opportunities, advisory roles of expertise, and networking opportunities which the academic pursuit itself could not have. Still, you continue investing into my future growth as an engineer beyond this master's by providing me with contacts and opportunities in the biomedical industry. Thank you for giving me this profound opportunity and for the future opportunities to come.

I would also like to present my gratitude towards Dr. David Nobes, who became a mentor, a guide, and a source of inspiration during my research. During my time here, I could not have achieved the volume of technical learning that I did without your assistance. The equipment, resources, and collaborative personnel which you provided me with was instrumental in my progress. I also appreciated you going to extra lengths to ensure my best chances for success at paper submissions for journals and conferences. But above that, I most truly valued your personal time and effort that you volunteered to aid me and the patience you showed towards me during the initial stages of my learning. Thank you for your great contributions to my learning experience.

My interactions with colleagues strongly shaped and nurtured the positivity of this journey. The biomechanics group, comprised by the combined labs of Dr. Kajsa Duke, Dr. Samer Adeeb, and Dr. Lindsey Westover, provided the opportunity to share my work and receive feedback and allowed me to reciprocate, participate, and learn from my peers. I would also like to thank my many friends from Dr. David Nobes' Fluid Dynamics and Sterling Engine Research Groups and Dr Jason Carey's Composite and Biomedical Materials Research Group for their kindness and support. Also, I would like to thank Dr. Martin Ferguson-Pell and the Rehabilitation Robotics Group for welcoming and including

Table of Contents

List of Tables

List of Figures

xviii

List of Abbreviations

ANOVA	Analysis of variance
ASME	American Society of Mechanical Engineers
ASTM	American Society for Testing and Materials
CT	Computed tomography
DIC	Digital image correlation
DOE	Design of Experiments
FE	Finite element
FFP	Fragility fractures of the pelvis
FOV	Field of view
IQR	Interquartile range
ISO	International Organization for Standardization
LED	Light emitting diode
MABTA	Multi-axis biomechanical testing apparatus
MRI	Magnetic resonance imaging
PDF	Probability density function
PSU	Power supply unit
ROI	Region of interest
SENT	Single edge notched tension
SI	Sacroiliac
SIF	Stress intensity factor

Chapter 1: Introduction

1.1   Motivation

With an increasing population and generally longer lifespans, there has been a continual growth in the elderly population of the world. Although no marked increases in the overall population are predicted, the percentage of the population aged 50 years or older is estimated to increase by 56% in men and 41% in women over the next 25 years in the European Union [1]. Furthermore, anticipated increases in life expectancy result in heightened estimates for the elderly aged 85 years or older: 129% increase in men and 73% increase in women [1]. As humans age, we become increasingly susceptible to a condition known as osteoporosis. Due to an aging population, the frequency of osteoporotic cases is rising.

Osteoporosis is a diagnosis that applies to individuals with a bone mineral density or bone mineral content more than 2.5 standard deviations below that of the average young adult [2], [3]. One is diagnosed with severe osteoporosis when they meet the criteria for osteoporosis, but additionally have one or more bone fractures that are primarily caused by the increase in bone fragility [2], [3]. Among the elderly population, 6% of men and 21% women are diagnosed with osteoporosis [1] and are consequentially more prone to osteoporotic fracture. This significant percentage, in combination with the growing elderly population, forecasts a 28% increase in cases of osteoporotic fracture over a span of 15 years in the EU; in actual numbers, this is a growth from 3.5 million to 4.5 million annual cases [1].

Some cases of osteoporosis are suspected to be substance abuse or disease related and possibly preventable [4]. However, most cases of osteoporosis are due to general aging or the anatomic effects of menopause [4], making preventative measures much less viable. From this, it is likely that the number of cases for osteoporosis and osteoporotic bone fracture will increase. It has also been found that the majority of osteoporotic bone fractures occur at the pelvis [5]. With regards to the elderly population, consequences of pelvic fracture are highly severe. Post-treatment, only 16% of patients were able to carry on without the assistance of walking aids, and only 18% were capable of independent living (compared to pre-injury statistics of 42% and 38% respectively) [6]. Early in-hospital

mortality rates have been estimated between 4% and 14% [6]–[9]. The mortality rate 1-year after treatment of the injury has been approximated between 13% [7] and 28% [9], [10]. The 5-year mortality rate has been estimated between 54% [7] and 64% [10] . And finally, the 10-year mortality rate was estimated to be 94% and was observed to be significantly statistically higher than that of an age-matched population [10].

Due to the increasing elderly population, the number of instances of osteoporotic bone fracture is predicted to rise. Typically, preventative measures are preferable to reactive ones. But many cases of osteoporotic bone fracture are inevitable as they are consequential to age and natural changes and deterioration of the human anatomy. Pelvic fracture is the most common and severe case of osteoporotic bone fracture, with many reported cases of loss of function or life post-treatment. The broad scope of this area of research is to assess possible approaches for addressing this continually growing societal issue. This thesis aims to do so through biomechanical experimentation and analysis.

1.2   Pelvic fracture terminology

1.2.1 Anatomy of the pelvis

To understand the complexity of this issue, it is important to build upwards from a strong, foundational knowledge base. This means starting with contextualizing the pelvis in the human body. As shown in, Figure 1 (a), the pelvic bone is a musculoskeletal interface between the lower body and the upper body. It is susceptible to large physiological loads as it is subject to compressive forces associated with many normal activities from standing to walking to running. In contrast to the leg, in which the loading is typically along the length of the femur, the pelvis has a more complex loading conditions due to its function and geometry. As Figure 1 (b) shows, the pelvis is mechanically analogous to a ring structure [11]. There are two mirrored pelvic bones, also known has hemipelvises, which interface with one another at the pubic symphysis and individually affix to the spine via the sacrum. Pelvic fractures need not be symmetrical; they can occur at either or both hemipelvises and at differing locations.

2
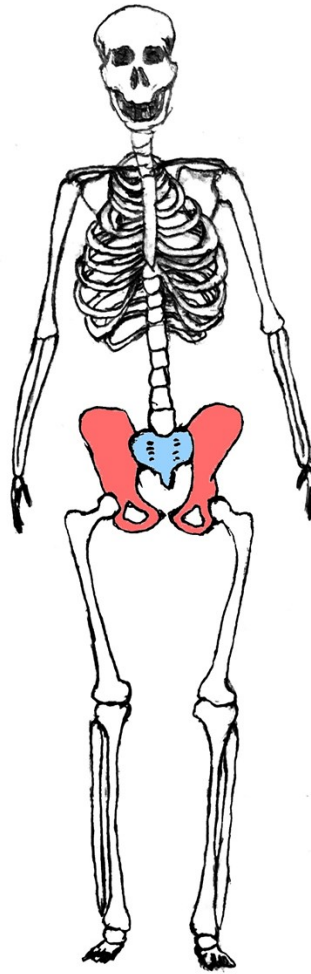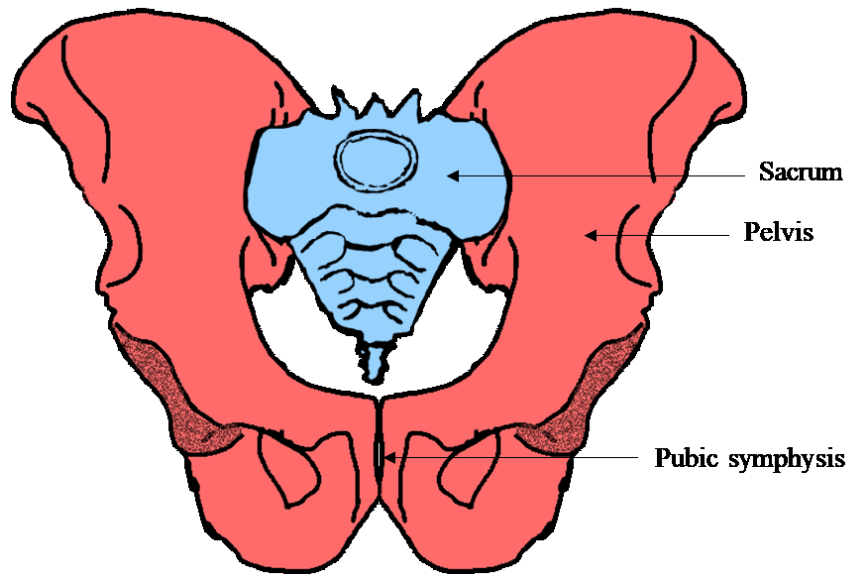
Figure 1. Anatomy of pelvis, showing **(a)** the pelvis (red) located in the human skeleton, and **(b)** a labelled diagram of the pelvic girdle as a ring support structure.

The hemipelvis is a complex part with common and extensive terminology that defines anatomical landmarks. Figure 2 introduces some of the terminology that is significant in this study. Shown in the lateral view of Figure 2, the acetabulum, commonly known as the hip socket, is the area of the pelvis into which the femur is inserted. This means it is also the region of the pelvis at which loads from the lower body are transferred through. A hemipelvis can be divided into three major parts about the acetabulum. Each part corresponds to a relative location on the hemipelvis and can be described using the typical terms for anatomical physical relations – superior indicates a location towards the top of the body, inferior is towards the bottom, anterior is towards the front, and posterior is towards the back. The ilium is the superior portion of the hemipelvis and adjoins to the sacrum at the sacroiliac (SI) joint. The pubis is the anterior-inferior portion of the pelvis and provides interface and support between the left and right hemipelvises at the pubic symphysis shown in the medial view of Figure 2. Finally, the ischium is the posterior-inferior part of the pelvis and completes the support structure of the hemipelvis.
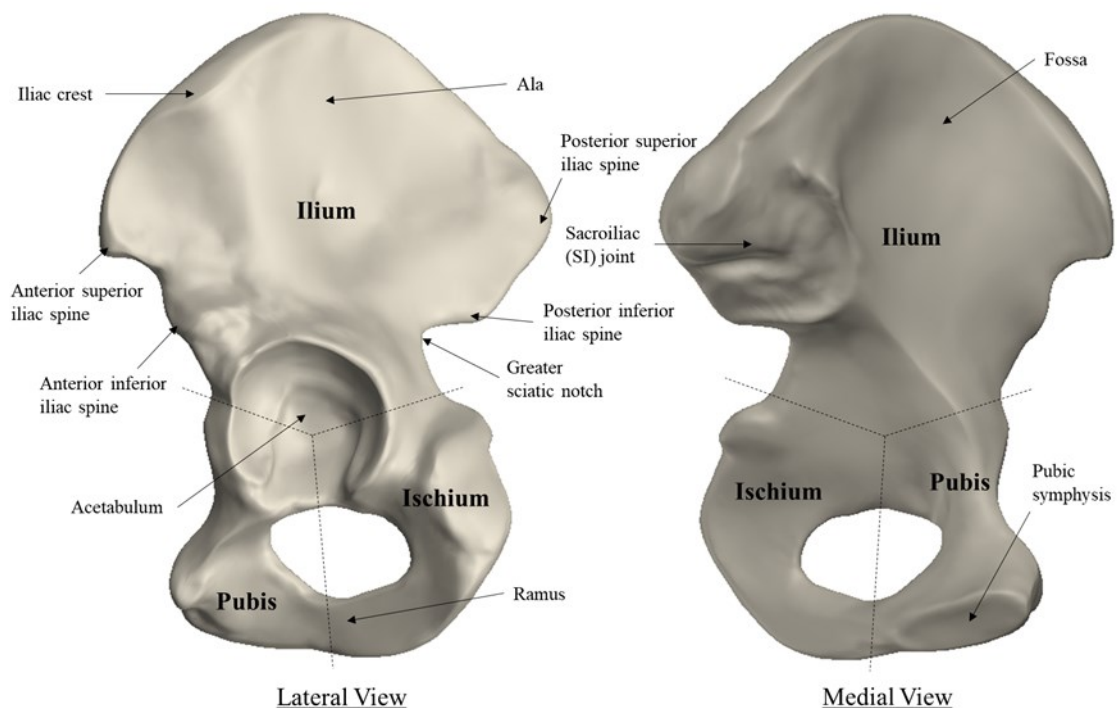
Figure 2. Diagram of a left hemipelvis, showing lateral and medial views.

A general anatomical coordinate system has been established in literature [12], [13], as shown in Figure 3. It defines the planes as quasi-sagittal, quasi-coronal, and quasi-transverse. The origin is located at the midpoint between the anterior inferior iliac spines of the hemipelvises. The x-direction is positive anteriorly, the y-direction is positive superiorly, and the z-direction is positive from left to right. The quasi-transverse plane runs through the anterior superior iliac spines and the midpoint between the posterior superior iliac spines. The quasi-coronal plane extends through the anterior superior iliac spines orthogonal to the quasi-transverse plane. And finally, the quasi sagittal plane is orthogonal to the two other planes and through the origin.
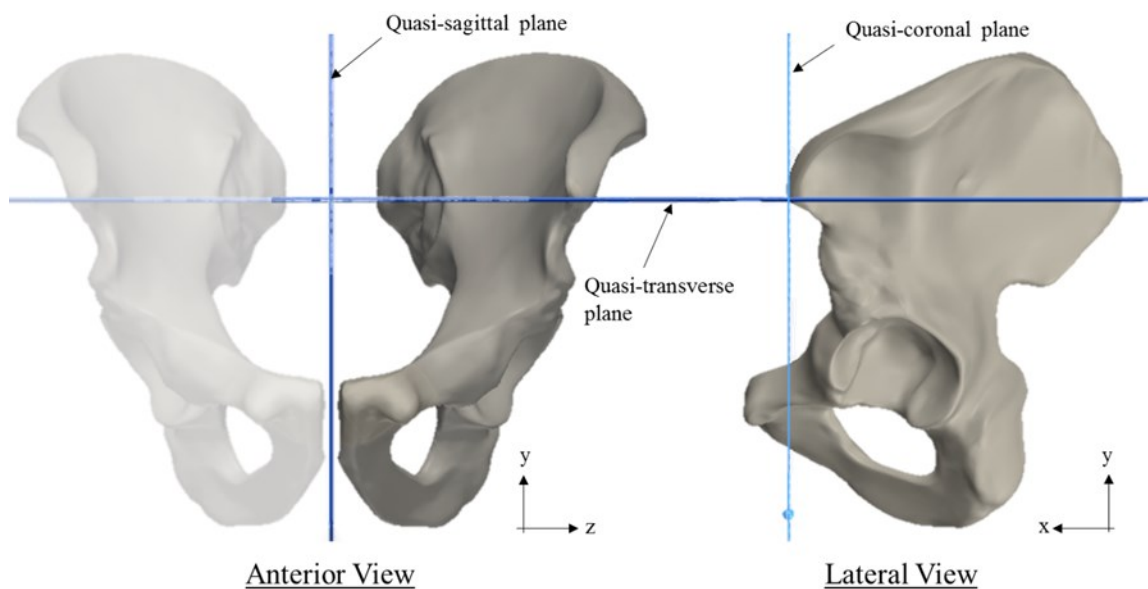
Figure 3. General coordinate system of pelvis, using anatomical landmarks to locate reference geometries.

1.2.2 High energy fractures

A large number of cases of pelvic fracture are due to high energy trauma. This can include major motor accidents or falls from great heights [14]. In these injuries, there are various extents of disruptions to the pelvic ring which can involve either bone, ligaments, or a combination of the two [11], [15]. As the geometry of the pelvis is quite complex, there are many ways for high energy fracture to occur. For this reason, the appropriate treatment for each trauma case may be unclear. To alleviate this ambiguity, classification models have been created and widely adopted. One is known as the Tile model [11], which adapted and modified the Pennal model [16] by using stability as the defining characteristic

fracture. It is a comprehensive classification system that identifies pelvic fractures by severity and type, then recommends rule-of-thumb treatment methods. This system is briefly laid out in Table 4.

Table 1. Tile classification system for pelvic ring disruptions [11].

Type	Specifications
Type A: Stable pelvic ring *Treatment:* typically non-operative	A1: Avulsion of the innominate bone A2: Stable iliac wing fracture or stable minimally displaced ring fractures A3: Transverse fractures of the sacrum and coccyx
Type B: Partially stable *Treatment:* case-dependent, can be operative or non-operative	B1: Open-book injury B2: The lateral compression injury B3: Bilateral B injuries
Type C: Complete unstable *Treatment:* requires fixation (operative)	C1: Unilateral C2: Bilateral, one side B, one side C C3: Bilateral C lesions

Another classification system was created by Young and Burgess [15], shown on Table 2. This model categorizes fractures based on the direction of the disruptive force and has proven to be an effective classification system for identifying and treating fractures [15]. For each classification and sub-classification, there are recommended treatments.

Table 2. Young and Burgess classification system for pelvic ring disruptions [15].

Type	Specifications
Lateral compression (anterior transverse fracture – pubic rami)	LC-I: Sacral compression on side of impact LC-II: Crescent (iliac wing) fracture LC-III: Contralateral open-book (APC) injury
Anteroposterior compression (symphyseal diastasis or anterior vertical fracture)	APC-I: Slight widening of pubic symphysis and/or SI joint; stretched but intact anterior and posterior ligaments APC-II: Widened SI joint; disrupted anterior ligaments; intact posterior ligaments APC-III: Complete hemipelvis separation, no vertical displacement; complete SI joint disruption; complete anterior and posterior ligament disruption
Vertical shear (symphyseal diastasis or anterior vertical fracture)	Vertical displacement anteriorly and posteriorly, usually through SI joint, occasionally through iliac wing and/or sacrum
Combined mechanical	Combination of other injury patterns: LC/VS or LC/APC

1.2.3 Low energy fractures

Bone fractures due to low energy trauma are commonly known as "stress" fractures. There are two general subclasses of stress fractures: fatigue and insufficiency fractures [5]. Fatigue fractures occur in healthy bones and are a result of repetitive stress. Most cases of fatigue fractures are observed in athletics, due to the extraordinarily high loading placed on the bones [17]. Insufficiency fractures describe those that occur under normal or sub-threshold repetitive stress conditions due to the decreased ability of the bone to withstand such loads. "Fragility fractures" is a more recent term used describe insufficiency fractures caused by reduced bone mineral content or density (*i.e.*, osteoporotic fractures) [18]. Fragility fractures are the fracture type of primary interest in this thesis.

Unlike fractures caused by high energy trauma, stress fractures often occur from much more seemingly benign events, ranging from a fall from standing to long-term stress from walking to even simply coughing [19]. Furthermore, the mechanics of the fracture are different between high and low energy trauma. High energy trauma often involves ligamentous rupture in addition to bone fracture, but low energy trauma is typically a disruption of the bone structure only. It is often the case with stress fractures that the strength of the bone is lower than the surrounding ligaments [18]. The intact ligaments consequentially form anatomical borders for the fracture fragments [18].

Due to these mechanical differences, the classification systems used for high energy trauma may not apply to low energy fractures. A classification system for fragility fractures in the pelvis (FFP) was proposed by Rommens et al. based on location and stability of the injury [18]. In summary, as listed in Table 3, it is recommended that low instability cases (FFP Type I) can be treated non-operatively; moderate instability cases (FFP Type II) can be treated percutaneously; high instability cases (FFP Type III) can be treated with open reduction and internal fixation; and highest instability cases (FFP Type IV) require iliolumbar fixation [18]. This system is relatively new, and no protocol for the treatment of FFPs is widely accepted to the extent of the Tile and Young and Burgess models.

Table 3. Rommens classification system for fragility fractures of the pelvis [18].

Type	Specifications
FFP Type I: Anterior disruption only *Low instability; non-operative*	FFP Type Ia: unilateral disruption FFP Type Ib: bilateral disruption
FFP Type II: Non-displaced sacral disruption *Moderate instability; closed reduction*	FFP Type IIa: unilateral sacral fracture FFP Type IIb: sacral crush zone, anterior disruption FFP Type IIc: unilateral sacral fracture, anterior disruption
FFP Type III: Complete anterior disruption + *dorsal disruption *High instability; open reduction*	FFP Type IIIa: + complete unilateral iliac disruption FFP Type IIIb: + iliosacral disruption FFP Type IIIc: + unilateral sacral disruption
FFP Type IV: Complete dissociation between spine and pelvic ring *Highest instability; iliolumbar fixation*	FFP Type IVa: bilateral iliac disruption FFP Type IVb: bilateral sacral disruption FFP Type IVc: combination of dorsal instabilities

1.3 Fragility fractures of the pelvis

1.3.1 Causes

As the definition of FFPs specifies fracture due to reduced bone quality or mineralization, most cases of FFPs are osteoporosis related [5], [20]. More specifically, occurrences are most common in elderly women with osteoporosis [21]. As previously mentioned, postmenopausal women are the demographic most susceptible due to the combined effects of menopause and age. Regarding the elderly and those with osteoporosis, the majority of FFPs are instigated by a standing height fall [6], [22]. However, even daily activities, such as transferring from bed to chair or even bearing the weight of one's body alone, can incite fracture [18].

Less common causes of FFPs have been documented but, similarly to osteoporosis, they predispose individuals to FFPs via bone degradation. For example, radiotherapy or cases of tumor have been reported to cause local bone alterations that lead to FFPs [23]. Pregnancy and lactation also have been linked to FFPs due to alteration in bone structure and mass as well as postural changes, weight gain, and even pelvic ring instability induced by relaxation of pelvic ligaments [24]. FFPs can also be influenced by a previous hip surgery on an individual [25], [26]. Following hip surgery, biomechanical loads are

reoriented. The surgery may enable pain-free motion, causing individuals to perform more physically demanding activities that the muscles are capable of, but the previously unstressed pubis is not [27]. Analogously, fragility fractures of the sacrum have been observed to be encouraged by spinal surgical instrumentation [28], [29].

1.3.2 Diagnosis

FFPs most often present themselves in cases reporting back or groin pain, especially in the elderly population [18], [20], [30]. However, it is believed that the number of cases of FFPs is underreported [20]. This is partly because the vulnerable population may also show effects of dementia and may not remember any instances of trauma that could cause a fragility fracture [20]. But moreover, it could be that the culprits are low energy trauma events which are seemingly insignificant and thus forgotten by the patient. Another potential explanation is the general unawareness of physicians that the presentation of such symptoms indicates a possible FFP [31]. Misdiagnosis may also occur if the symptoms present themselves after a hip surgery. In some cases, the issue has been misdiagnosed as a loosening of surgical instrumentation or an infection at the fracture site [32].

There is a general approach in addressing the chronic back pain symptoms that may indicate pelvic fracture [20]. Radiography is usually the first step. However, it has a low detection rate for FFPs because, as most cases are osteoporotic fractures, the compromised bone structure results in decreased visual contrast on the x-ray results, making the fragility fracture difficult to see [33]. If pain management and assisted mobilization therapy are unsuccessful following a negative x-ray result, a computed tomography (CT) scan is performed. CT scans have been documented to have a decent detection rate, significantly better than radiography [5]. It, however, has shown difficulties in detecting occult fractures and may not detect an FFP. Scintigraphy is used less commonly in the current day but was previously shown to be much better than radiography and comparably effective to CT scans [5]. It falls short in its lack of ability to differentiate fracture and metastasis [20]. As magnetic resonance imaging (MRI) became more widely available and proved to be more effective [20], scintigraphy became less desirable. The MRI technique has the highest detection rate for FFPs. A major advantage is that this method can detect bone bruises, which have been reported as indicators of microfracture [34]. Despite the ability to detect

FFPs with decent success rate, due to the nature of the diagnostic procedure, the diagnosis of FFPs may not be immediate.

1.3.3 Treatments

Once a FFP has been diagnosed, there are several known treatment options. Typically, the most conservative applicable to the fracture case is preferred. Non-displaced fractures are firstly approached non-operatively by initial bedrest and pain medication, then progressing to mobilization and weight bearing physiotherapy [35]. In some cases, patients may suffer prolonged pain, indicating that more invasive procedures may be required, such as those used for displaced fractures. However, it is desirable to avoid surgical reduction whenever possible. The mechanical constraining effect of implants alter the loading profile of the supporting bone, lessening the loads that it would typically bear [36]. This is a concept known as stress shielding, which has been evidenced to have an osteoarthritic impact as it can cause implant loosening and bone resorption [36]–[39]. Therefore, surgical options should be pursed only when necessary.

Various surgical options of different invasiveness levels are available for displaced fractures or non-displaced fractures where non-operative treatment failed [20]. Variations of percutaneous screw techniques have been used, in which surgical reduction is performed by placing a screw in the fracture location through a small incision of the patient's skin. As the body is not dangerously exposed in this procedure, it is a closed reduction technique. For fractures that are more unstable or located at locations unreachable by the percutaneous screw techniques, open reduction and internal fixation may be required. This may involve a combination of screws and plate fixtures, depending on what the surgeon deems appropriate for the specific case [40].

Other less common or peripheral treatment methods exist, such as sacroplasty. Sacroplasty involves injection of polymethyl methacrylate cement into the sacral ala to reinforce the fracture. It is a minimally invasive technique. Some studies have observed reduction of fracture motion using this technique [41], [42]. However, other studies have suggested that this technique does not result in improvements of strength or stiffness from its reduction [43]. Furthermore, in some cases, cement leakage was detected [44] which

can potentially necessitate additional surgery [45]. The overall benefit of sacroplasty is currently debatable, but interest is growing.

Pharmacological treatment is another potential treatment for FFPs. For bone repair, conducting regular injections of parathyroid hormone has proven beneficial for the healing process [46]. When the hormonal treatment was applied to an osteoporotic pelvis, faster fracture healing, pain reduction, and better functional outcome were observed after 3 months [47]. Though studies have indicated its potential application for fragility fracture recovery, it is not yet widely accepted and not yet supported by regional guidelines.

1.3.4 Complications

There are potential complications that may arise following treatment of FFPs. Generally, the patient begins with bedrest and total weight-bearing restriction. Immobilization of a patient can cause a variety of problems, however. Excessive bedrest can lead to muscle weakening and atrophy, contractures (fixed deformities of joints due to immobilization), and even a further increased presence of osteoporosis [48]. Immobilization can also promote respiratory complications (such as decreased ventilation and pneumonia), decreased metabolic function, gastrointestinal effects (such as anorexia and constipation), and reduction in motor and cognitive function [49]. Regarding the cardiovascular system, immobilization can diminish cardiac function and venous thromboembolism [48]. Venous thromboembolism is a case where, a blood clot that forms in the leg due to inactivity has the potential to break off and flow to the lungs and cause a blockage there known as a pulmonary embolism; such an event may be fatal. Pressure sores are another common complication of immobilization. They most often lead to infection, but can extend to drainage (protein and water loss that may cause anemia) and muscle and nerve damage [49]. Aside from physical complications, immobilization and bedrest place a significant economic burden on the healthcare system [50]. For all these reasons, it is desirable to begin mobilization as early as possible.

However, premature mobilization can be detrimental as well. Forced mobilization has the potential to increase the risk of fracture progression or displacement [18]. As fragility fractures result in some level of instability, a poorly implemented weight-bearing mobilization program can lead to increased instability [51], [52]. Therefore, minimal

bedrest may be required for some patients. There have been many cases that demonstrated greater improvement with total weight-bearing restriction for 6-week period [5]. However, other studies have recommended anywhere between 1 to 7 weeks [5], [53]. There is no standard procedure for determining an appropriate non-operative treatment or post-operative recovery plan for FFPs, and there are many potential consequences for either under-prescribing or overprescribing bedrest. One goal of this thesis is to investigate possible approaches for determining a consistent and optimal treatment and recovery plan for FFPs.

1.4 Biomechanical studies

1.4.1 Methods

In pelvic biomechanics, investigations were predominantly experimental at the beginning. They can date back as early as the 1970s [54]. The early experimentation on the pelvis utilized strain gages to extract surface measurements at points desired by the experimenter [55]–[57]. However, as strain gages are point-based measurement devices, the quality of the results was dictated by the placement of the strain gages in the early experiments. Studies of photoelastic models exist [58], [59], though they are much less common. Although they are able to produce full field data, they are limited by the excessive and complex contouring of the pelvic surface [60].

As numerical simulations became more accessible due to technological advances, finite element (FE) modelling became increasingly present in pelvic biomechanical studies. The appeal is that they produced full field data and allowed for quick and inexpensive simulations and reconfigurations in contrast to clinical and experimental studies [60]. As experiments can be costly, some studies have validated their FE models by comparison with literature [61]. But more typically, a proposed FE model is validated experimentally in the same study [62]–[65]. This is done by placing strain gages at regions of high stress as predicted by the FE model and comparing the measurements to the model. Strain measurement studies are typically concerned with the correlation of the loading profile between a normal pelvis and a treated fractured pelvis to assess the extent of stress shielding that the instrumentation may be inducing [66], [67].

Some experiments are interested in other mechanical measurements that strain gages cannot measure. The effect of acetabular fracture has been measured by comparing the acetabular contact pressure of an intact pelvis to a fractured one using pressure sensitive film [68], [69]. For experiments that seek to determine pelvic fracture displacements, measurement methods have ranged from simple measurements with goniometers [70] to more complex systems using electromagnetic motion sensors [71]. Studies have measured fracture displacement using mercury strain gages [40], [72], linear variable differential transformers [73], motion tracking techniques [74], [75], and ultrasound devices [76], [77]. Some investigations quantify the quality of fracture reduction simply by the crack width [40], [72], [78], [79], prioritizing it above concerns of alterations to load bearing.

More recently, the use of digital image correlation (DIC) has established popularity in biomechanical studies of the pelvis [60], [66], [78], [79]. In short, DIC is a technique that uses digital cameras to measure surface displacements of a test specimen which are then used to calculate surface strains [80]. DIC is particularly beneficial in experiments involving pelvic fracture because full field data is attained, allowing for a more complete comparison to an FE analysis. It is also able to do this while simultaneously measuring crack displacement. Previously described measurement techniques can only do one or the other, making DIC highly desirable. DIC is the principal measurement technique explored in this thesis and will be later described in detail.

1.4.2 Specimens

Classically, biomechanical studies have used cadaveric specimens as test subjects [54], [55]. However, they are fairly costly, availability is scant, and they are not easy to implement [81]. Such aspects as transportation, storage, containment, biosafety, and disposal create difficulties. Also, as human bodies are unidentical to one another, it is difficult to ascertain consistent or statistically significant results with cadaveric specimen [40], [82]. Furthermore, these specimens are typically donated by the elderly; the bone quality of this population has high variance, as they may have various levels of osteoporotic influence adding difficulty in interpreting experimental results [83].

In response to the obstacles presented by cadaveric testing, recent studies have trended towards the use of composite bone models [60], [66], [84]. In studies of long bone

composite models, low variability and high agreement to cadaveric testing was observed [85]. Another study was performed by Girardi et al. [86], focusing on the agreement between hemipelvis composite models and cadaveric subjects. Even though the stiffness of the composite hemipelvis was found to be greater than that of a cadaveric specimen, the composite model was still determined to be a reasonable and repeatable subject for biomechanical research [86]. Therefore, the studies conducted in this thesis were decidedly performed on composite models.

For both cadaveric and composite models, there are studies that attempt to simulate an intact pelvis under normal loading conditions [60], [62], [86] as well as studies that investigate the effects of fracture and fixation on a pelvis [66], [69], [72], [78]. Regarding fractured specimens, there is little commonality among existing studies as there are a wide variety of fractures. Results from a study of acetabular wall fracture [69] are not comparable with those of an iliac wing [40] as the mechanical alterations are completely different. Some studies also favor the use of a fully intact pelvic girdle while others simplify the simulation by examining only a single hemipelvis.

1.4.3 Mechanics

The primary traditional method of setting up a pelvic test is the "double-leg stance", which is a simulation of a normal standing position [55]. This requires a full pelvic girdle specimen, meaning that the hemipelvises are joined with one another as well as the sacrum. Some studies remove a portion of the femur and fix both ends by potting, which is essentially cementing it into place [76], [87]–[89]. Other studies remove the femur completely and add a prosthetic mock femur for more control of the loading orientation [55], [90]. With the pelvic girdle essentially supported at both acetabula, a load is enforced downwards at the sacrum to simulate the weight of the body. Typically, a cadaveric specimen is used for double-leg stance simulations, as it is difficult to create an accurate model representation of such a complex part. The benefit of this test setup is that the pelvic girdle is intact and the ligament structure is retained, allowing for a fairly representative simulation of pelvic loading [87]. However, there are more obstacles in the setup and difficulties in acquiring the specimen [91].

The "single-leg stance" simulation is another popular approach that circumvents the difficulties of the double-leg stance setup. This typically involves only one hemipelvis fixed such that it appropriately represents the mechanics of the pelvic ring structure [40]. Hemipelvis models are often used in these tests [60], [66], [73], [75], [92] as they are less expensive and more representative of the pelvic structure than a full pelvic girdle. Nonetheless, cadaveric hemipelvis specimens are used as well, often in studies comparing fracture fixation methods [40], [67], [72], [78], [79], [93]. Single leg stance has been defined between 12° [60] to 15° [69] adduction to simulate maximum force in the gait cycle, shortly after heel strike. However, some hemipelvis testing oriented the force perpendicular to the acetabulum for maximum load and fracture displacement [67], [94]. To approximate the full pelvic ring structure, the hemipelvis is typically fixed at the SI joint (usually by cement potting) and with a sliding constraint at the pubic symphysis [60], [86]. Due to the implementation of these constraints, the loading scenario is less representative than double-leg stance. However, when properly constrained, and not over-constrained, the single-leg hemipelvis test can be a reasonable representation [95]. Therefore, due to its accessibility, relatively low expense, and repeatability, a composite hemipelvis was selected as the specimen for the experiments conducted in this research.

Although the double-leg and single-leg stances exist as models for an experimental setup, there are still many differences between the way they have been conducted in literature. There are guidelines and strong templates in literature, but there is no hard standard for conducting biomechanical studies on the pelvis. Loading limits have been prescribed as 500 N to prevent failure and allow for specimen reusability [87], 1500 N to simulate body weight conditions [60], [66], or up to 3000 N for maximum displacement [78], [79]. Imaging studies typically conduct step loading [60], [66], [94] because data sets are inherently large and too many samples can be computationally costly. Some studies implement cyclic loading to investigate fatigue mechanics [67], [75]. There are also studies that conduct a low-rate linear ramp loading profile [78], [79], likely for simplicity. Experiments that operate with displacement-based loading condition have ranged from 0.2 mm/s (step-based loading) [94] to 0.2 mm/min (continuous loading) [78], [79]. An explanation for this wide discrepancy is that step-based loading rates are generally higher than continuous as they simulate quasi-static conditions by holding a step until equilibrium

is reached, whereas the slow rate of continuous loading experiments is to maintain quasi-static conditions for the entire experiment. There are other experiments that operate with force-based loading. In general, cyclic loading experiments have greater loading rates than maximum loading ones. Cyclic loading rates can range from 40 N/s [75] to 50 N/s [67], whereas forced-base ramping has been performed at 14 N/s [60]. Due to the significant variability between studies, it is difficult to compare results with literature, which is likely why most investigations conduct both numerical and experimental simulations to validate the results of the testing.

1.4.4 Purpose

Although there are many differences in how researchers conduct biomechanical studies of the pelvis, there are common purposes for pursuing these studies. Experiments are often conducted to validate an FE model, as the latter can be quicker, easier, and less expensive to repeat or modify simulations on the pelvis. For example, Leung et al. used FE modeling to vary properties of the pelvis to show a relation between areas susceptible to high mechanical load and common regions of osteoporotic fracture [87]. Anderson et al. developed and validated an approach to generating subject-specific FE modelling based on volumetric CT scans [62]. Shim et al. used FE analysis to geometrically optimize plate and screw fixation for greatest stability [75].

Another common reason for biomechanical pelvic studies is to compare existing fracture fixation techniques and determining which methods are most appropriate for different fracture types. Simonian et al. has compared fixation techniques for different fracture types, including an iliac wing fracture [40] and a T-type acetabular fracture [72]; both studies observed no statistical difference between the resultant stability common fixation methods. On the contrary, a more recent study by Kourkoulis et al. showed that a combination of conventional and locking plates improved reduction of a T-type fracture [79]. Zhang et al. performed a study on fixing a posterior wall fracture with interfragmentary screws along, with conventional plates, and with locking plates, observing that no method was statistically better than another and all were sufficient at stabilizing the fracture [76].

Instead of comparing different reduction techniques, some studies compare the biomechanics of a fractured pelvis that has been fixed by typical methods to its original intact function. A study by Olson et al. showed that the biomechanics of a pelvis with a posterior wall fracture were different than an intact pelvis, and that reduction of this fracture did not completely restore original mechanical function; from this the researchers concluded that weight-bearing should be restricted for a short period after surgery to prevent fracture progression [69]. Mehin et al. showed that locking plates induced less mechanical alteration than conventional plates, as they need not conform so strictly to pelvic contours [67]. Dickinson et al. demonstrated that the material of an acetabular cup implant can affect the loading mechanics on a pelvis, and that some materials such as carbon-fiber-reinforced polyetheretherketone have a greater capacity to retain the original mechanical loading profile [66].

Additionally, some researchers explore new approaches and techniques instead of evaluating current ones. Cimerman et al. showed benefits of computer simulation and 3D-visualization of a fractured pelvis in the preoperative stage [96]. In a study by Zeng et al., a patient-specific pelvic model was 3D-printed such that fixation plates could be pre-bent to better adhere to the surface of the actual individual pelvis; greater fracture reduction was observed [92]. Chen et al. did a similar preoperative approach, but 3D-printed guiding templates for the plate to adhere to rather than the entire model; improved reduction was also found in this study [93].

In addition to studying functional outcome, researchers have also investigated novel experimentation techniques to assess the suitability of their application to pelvic biomechanical studies. Rudert et al. developed and validated a device to measure dynamic contact stresses of the hip joint, as the standard of pressure sensitive films can only measure static pressures [97]. DIC is also a technique that is still growing in pelvic experiments, and early studies such as that by Ghosh et al. [60] showed the validity and benefits of the technique. Overall, there is much complexity and nuance regarding pelvic biomechanics. Much still remains unknown and studies in this field of research are, in some form another, expanding our knowledge on this matter.

1.5   Objectives

Broadly speaking, this thesis aimed to further the knowledge in the field of pelvic biomechanics. The focus was on FFPs, and how to understand and improve treatment of such fractures. Pursuing this involved developing an experimental system to simulate the biomechanics of a pelvis. As the benefits of a DIC measurement system were desired, a large portion of the research involved learning the fundamentals of DIC and developing and validating a system suitable for pelvic experimentation. After firmly establishing an understanding of the system, loading experiments were performed on intact and fractured pelvises to assess possible approaches and improvements regarding FFPs. Thus, the process can be outlined as so:

1. Investigation of DIC
   - Establishing a fundamental understanding, setup, and procedure for DIC
   - Optimizing the measurement quality of the system
   - Determining a method for quantifying the DIC measurement uncertainty
2. Development and validation of the experimental setup
   - Restoring the hardware and software of an existing testing apparatus
   - Setting up the test rig with an integrated DIC system
   - Material tensile testing – simple experiment to validate strain measurements with theoretical and numerical analysis
   - Crack testing – more complex experiment to validate simple fracture measurements and determine appropriate quantification of fracture motion
3. Intact pelvis simulation study
   - Examine repeatability of setup for pelvic loading simulation
   - Evaluate accuracy of experimental and numerical simulations
   - Establish baseline of mechanical comparison for fractured pelvis
4. Biomechanical analysis of pelvic fracture
   - Assess setup for load simulation and measurement of fractured pelvis
   - Analyze effect of fracture via mechanical comparison with intact pelvis
   - Use mechanical measurements to characterize pelvic fracture stability

Chapter 2: Digital image correlation study

2.1 Introduction

2.1.1 Background

DIC is a measurement technique that uses camera images to measure surface deformations on a subject. It has been used in mechanical experiments since the early 1980s and today is widespread. Studies from Peters et al. [98] and Chu et al. [99] are some of the pioneering uses of DIC in experimental mechanics. Investigations on validating and optimizing the method were conducted by Bruck et al. [100] and Sutton et al. [101] in the mid to late 1980s. At this stage, DIC systems used one camera to measure planar displacements [101]. In the 1990s, the use of stereo DIC systems (two cameras) to measure 3D-deformations gained popularity [102], [103]. To this day, DIC has presence in more complex applications and a broader range of fields of study, such as biomechanics [104]–[106], composite materials [107], fracture mechanics [108], [109] geotechnical engineering [110], material classification [111], [112], microscopy [113], [114], and structural mechanics [115], [116].

2.1.2 Principles of digital image correlation

In a DIC experiment, a camera (or multiple cameras) is used to capture images of a test specimen surface at different stages of loading. Using the movement of contrasting shapes between images in a data set, displacements can be measured and used to calculate strain fields on the specimen's surface. A 2D-DIC experiment uses a single camera to measure planar deformations, whereas a 3D-DIC experiment uses two cameras in a stereo configuration to capture out-of-plane measurements as well. The technique is popular for its ability to obtain full field measurements, as well as the benefit of contact-free measurements.

The typical procedure of a DIC experiment involves: 1) preparing the specimen, 2) calibrating the system, 3) collecting the image data, and 4) processing the images to determine the measured deformations [80]. Images in a DIC experiment require tracking of contrasting features to determine movement between images. As many specimen surfaces can be smooth or featureless, preparation involves painting the specimen black

with a random array of white speckles to introduce traceable features. This can also reduce the reflectivity of a surface, as glare can distort measurements from image data.

The calibration of a DIC system involves collecting images of a calibration plate. The calibration plate has high contrast dots of known size and spacing. The calibration images are used to convert image data into physical measurements using the known dimensions of the calibration plate. In 2D systems, multiple images of a flat calibration plate at various distances and angles are required [117]. A 3D system only requires a single image of a 3D calibration plate (with varying surface heights of known dimensions) [118]. In a 3D system, two types of calibration parameters exist: intrinsic and extrinsic. Intrinsic parameters describe the qualities of the camera (focal length, resolution, *etc.*) whereas extrinsic parameters describe the parameters in the experiment space (angle, translation, *etc.*).

Collecting experiment data involves first capturing an image of the specimen at zero-loading. This image is known as the reference image. During the experiment, images are taken of the specimen at various stages of loading. These are known as the deformed images. In a 3D-DIC system, each camera captures a simultaneous image pair. Instead of collecting a single reference image and deformed images, a reference image pair and deformed image pairs would be collected. Once the loading specifications of the experiment have been satisfied and the image data set is adequate, the data collection step is complete.

The data set is then processed to convert the images to physical measurements. In general, every deformed image is compared to the reference image. This is done by dividing both the deformed and reference images into equally-sized, equally-spaced subsets (like a grid). Each subset of the reference image is transformed until it matches a subset in the deformation image. The resultant transformation of one subset is the average displacement of the area within the subset. The displacement is obtained this way for every subset in an image and collectively they yield a vector displacement field. This process is performed on all deformed images in a data set to obtain the measured displacement fields for all sampled stages in the experiment. If the experiment involves mechanical loading, the displacement fields can be used to calculate the strain fields in each sampled stage in the experiment.

2.1.3 Defining uncertainty

The American Society of Mechanical Engineers (ASME) expresses the measurement uncertainty of a parameter in two parts: bias error and precision error [119]. This is presented in ASME PTC 19.1 [120]. The bias error is the difference between the true average measurement and the true value. It is difficult to define and is often estimated by expert discretion [119]. The precision error is the difference between a single measurement and the true average. It is defined statistically using the standard deviation of a measurement,

$$S = \sqrt{\frac{\sum_{i=1}^{n}(x_i - \bar{x})^2}{n - 1}} \tag{1}$$

where:

S is the standard deviation,

x_i is the value of a measurement,

$\bar{x}$ is the true average, and

n is number of measurements.

Combining the two yields the measurement uncertainty. For a 99 percent confidence level estimation [119], the uncertainty is expressed as

$$U = B + 2S \tag{2}$$

where:

U is the total measurement uncertainty and

B is the bias error.

There are many thorough guidelines and best practices for how to properly conduct and minimize uncertainty in a DIC experiment [80], [121], [122]. However, DIC measurement systems involve many components, each of which affects the measurement uncertainty to varying extents. Table 4 lists some of the potential errors in the system, showing that there are sources of uncertainty associated with every step of the DIC process. In the specimen preparation step, Lecompte et al. [123], Pan et al. [124], and many others have shown that speckle pattern quality affects measurement uncertainty. A study by Reu [125] had investigated the effect of calibration quality on overall uncertainty. Haddadi et

21

al. [126] showed that various sources of uncertainty in the experiment, including illumination and environmental effects, had different impact on the uncertainty. The correlation function has been investigated by many researchers, including Bornert et al. [127] and Pan et al. [128], showing that using different shape functions influences the measurement uncertainty differently.

Due to the complexity of a DIC experiment, there are many metrics in defining the uncertainty of the system for various applications and parameters [122]. However, the author is not aware of any current universal standard for quantifying the uncertainty of a DIC system.

Table 4. Some potential sources of uncertainty in a DIC system.

Step	Sources of uncertainty
Specimen preparation	Paint adhesion Speckle pattern quality Surface alteration
Calibration	Calibration image quality Calibration model Calibration plate dimensions Camera positioning
Data collection	Aliasing Data synchronicity Environment Illumination Lens distortion
Image processing	Image filtering Subpixel interpolation Subset sizing

2.1.4 Speckle pattern quality

This study aims to contribute to the research community efforts in establishing a standard of quantifying uncertainty in a DIC system by examining the effect of speckle pattern quality on the measurement uncertainty. Lecompte et al. [123] demonstrated that speckle size and subset size have a combined effect on the measurement error. Average speckle size was used to characterize the speckle pattern quality of the entire image. Yaofeng and Pang [129] derived a parameter called subset entropy which represented the average of absolute intensity deviations within a subset. Reu [130] determined that speckles must be

at least 3 pixels in diameter to produce proper measurements, and that an optimum size is between 3-5 pixels [122]. In contrast to average speckle size, subset entropy assesses measurement uncertainty in a localized area. Pan et al. derived parameters known as the sum of square of subset intensity gradients to assess the quality of a speckle pattern and calculate an optimal subset size for a speckle pattern. The examination of intensity gradient was taken further by Pan et al. [124] by expanding the scope from the subset to the entire speckle pattern, globally characterizing the speckle pattern quality with a parameter called the mean intensity gradient. Crammond et al. [131] performed morphological analysis on speckle patterns to examine the effect of its physical properties, showing that evenly distributed speckles within a pattern are more accurate than those with great size disparity. It also showed that larger sized speckles have greater variation of shape, which may result in lower measurement errors in comparison to smaller speckles.

In this study, the speckle pattern was characterized with three parameters: 1) the speckle density, 2) the speckle diameter, and 3) the speckle diameter variation. Reu has suggested a good rule of thumb is for speckles to be at least 3 pixels in diameter to avoid aliasing [132], agreeing with an earlier study by Zhou and Goodson which determined a reasonable speckle size to be at least 3 to 5 [133]. Also, Reu reported that 2 to 3 pixels for each correlation subset is a reasonable speckle density [130]. A study by Crammond et al. [131] showed a general trend that greater speckle size variation results in greater uncertainty. Park et al. [134] used statistical distributions of intensity levels to quantify a speckle pattern quality, which has links to size variation but is still a measure of an entirely different parameter. To the author's knowledge, there is currently no metric to quantify variation of the physical size of the speckles. This investigation contributes to the research field by quantifying the relationships between measurement uncertainty of a speckle pattern and its density, diameter, and diameter variation. The novelty of this study is to examine both individual and interactive effects of these three speckle pattern parameters in how they impact measurement uncertainty.

2.1.5 Design of experiments

Design of experiments (DOE) is a concept that emphasizes structuring and conducting an experiment to ensure the results are interpretable and statistically robust [135]. As per usual, an experiment is comprised of the manipulation of input variables, the observation of their effects on response variables, and the identification of control variables. But a proper implementation of DOE uses the best methods and experiment models to obtain reliable and meaningful results for the specific experiment at hand [135]. It has had proven success in many applications. Melenka et al. [136] used DOE to study 3D print part quality and determine which parameters had the greatest effect on the material properties. Benardos and Vosniakos [137] used DOE to ascertain which aspects of a computer numerical control milling machine most strongly affected the surface finish and develop an algorithm to predict surface roughness. In machine vision application, Elango and Karunamoorthy [138] examined multiple parameters of lighting conditions to ascertain which had the most significant effect on the optical measurement of surface roughness.

The novelty of this study is the implementation of DOE to observe the individual and interactive effects of the speckle density, the speckle diameter, and the speckle diameter variation on the measurement uncertainty. As there is no current metric for speckle diameter variation, this investigation also explores the feasibility of quantifying the speckle diameter variation using the interquartile range (IQR), which is the middle 50% of a data set, as a percentage of the mean diameter. Furthermore, the study aims to use the observations from the experiment to predict the quality of an experimentally realistic speckle pattern, as it is difficult to control these parameters using most accessible methods of creating a speckle pattern [131]. The results from this investigation can offer a deeper understanding of which characteristics of a speckle pattern contribute to the quality of results of a DIC experiment.

2.2   Methods and materials

As a brief overview, the components used to conduct the experiment are listed in Table 5. They are explained in detail in the following section.

Table 5. Components used in experiment.

Component	Model
Optical Components	
Cameras (×2):	GX-3300, Allied Vision
Lenses (×2):	f#2.8, Arax (80-mm with lens tilt)
Calibration plate:	Type 22, LaVision GmbH
Illumination:	CN-600SA, Nanguang Photo & Video Systems Co.
Mechanical Components	
Rail mounts:	ThorLabs imperial rails
Mechanical stage:	Generic micrometer-mounted stage
Airbrush:	PCMT70536, Porter Cable
Software	
Pattern generation:	PIVLab (MATLAB open-source)
Image acquisition:	*StereoCam
Uncertainty quantification:	*DIC_Uncertainty
Morphological analysis:	*DIC_SpeckleMorphology
Image correlation:	DaVis 8.4, LaVision, GmbH
Statistical analysis:	Minitab 18, Minitab Inc.

*Indicates MATLAB software developed by author (more detail in appendices).

2.2.1 Experimental design and setup

The goal of this experiment was to investigate how characteristics of a speckle pattern – namely 1) density, 2) diameter, and 3) diameter variation – affected the uncertainty in a DIC measurement, which is the responding variable of the experiment. Thus, a DOE experiment model known as a 2^3 full factorial [135] was implemented to allow for the individual and interactive effects of all three pattern characteristics on measurement uncertainty to be assessed. Each of the parameters were assigned two levels, a low and high, and eight different speckle patterns were created based on all possible combinations of parameter levels. The values of the input levels in the experiment are given, in Section 2.2.2 below, where it is also explained how the values were derived. The components of the experiment and the procedure of collecting and processing the data were held constant in the experiment.

The physical setup of the experiment is shown in Figure 4. Two identical commercial machine vision cameras (GX-3300, Allied Vision) were used in a stereo configuration to measure 3D displacements. The camera resolution was 3296×2472 pixels and images were captured at an 8-bit depth. The bit depth was deemed acceptable as studies have shown that increases in bit depth have minimal improvement in correlation quality [139]. The cameras were used with 80-mm fixed length commercial SLR lenses (f#2.8, Arax). They were mounted on a rigid bar set up and oriented at a $\pm\,40°$ stereo angle offset. Figure 4 also shows the use of a 6° Scheimpflug angle to reorient the focal planes of the angled cameras to be in line with the specimen for image focus across the imaged surface. The process for determining the geometry of the Scheimpflug imaging setup is detailed in Appendix A).
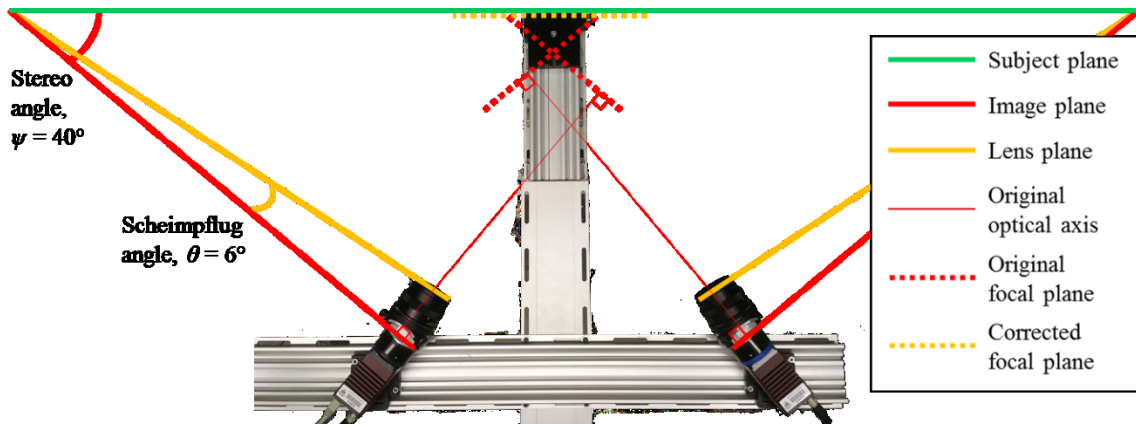
Figure 4. Image of DIC setup, showing orientation and Scheimpflug correction.

A 3D calibration plate (Type 22, LaVision GmbH) was used to convert the measurements from image space to physical space. A diffuse light emitting diode (LED) white light source (CN-600SA, Nanguang Photo & Video Systems Co.) was used to illuminate the specimen while minimizing glare. A traversing stage was set up on a rigidly fixed optical rail at an approximate orthogonal distance of 600 mm from the cameras to satisfy the Scheimpflug condition. Test specimens were mounted on this stage, and movement was micrometer-controlled and limited to out-of-plane motion.

2.2.2 Specimen preparation

Tests were performed on speckle patterns that were synthetically generated, printed onto paper, and affixed to a flat, rigid surface. This method of pattern creation allowed for greater control over the three inputs of the experiment: density, diameter, and diameter variation in a speckle pattern. Using an open source software [140], a set of eight different speckle pattern images were generated each of which was a unique combination of the three inputs at either a high or a low level, as required by the 2^3 full factorial model. For example, one specimen is created with a high speckle density, large speckles, and minimal variation in speckle diameter while another may have low speckle density, small speckles, and significant variation in speckle diameter. A comparison of sub-regions of each speckle pattern is shown in Figure 5.
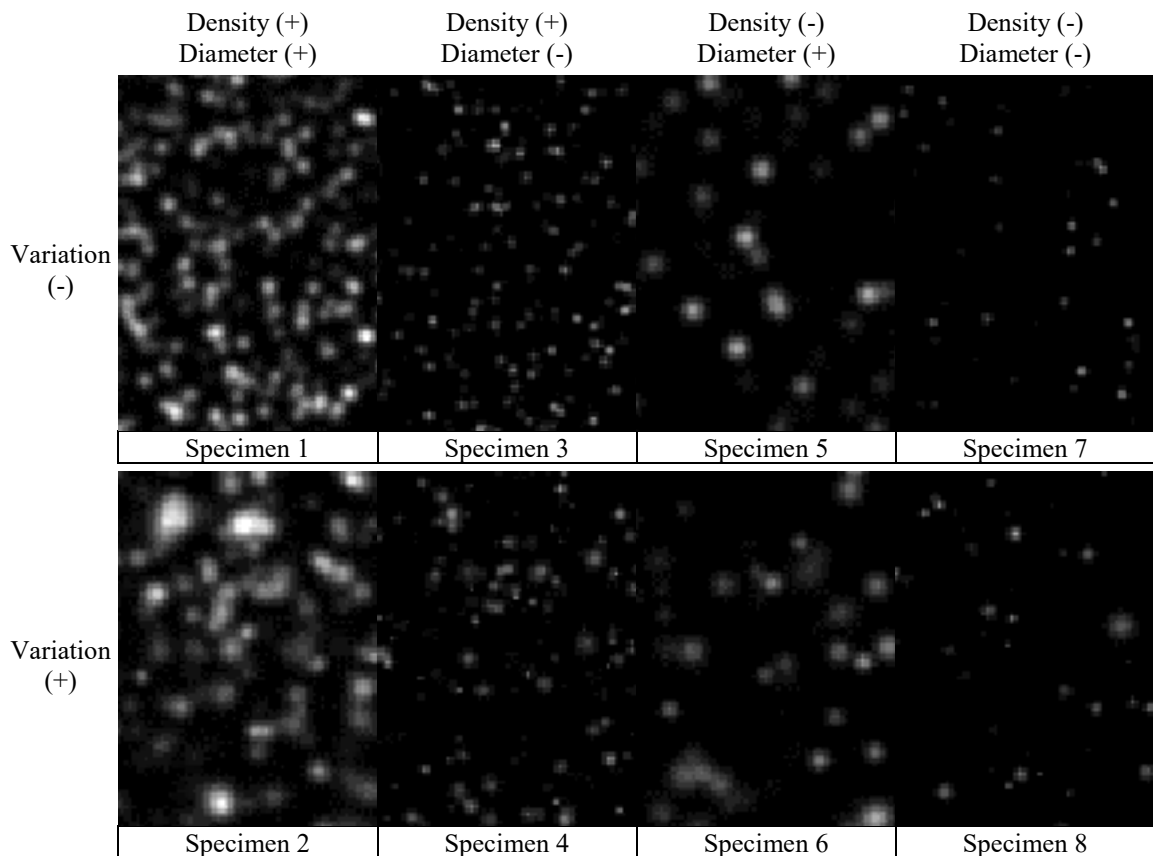
Figure 5. Comparison of all image files of printed speckle specimens, where (-) and (+) indicate when a parameter is set at the low or high level respectively.

Each was printed with an inkjet printer (Stylus Pro 9900, Epson) at 1440 dots per inch (dpi) on matte paper for glare reduction. They were printed as black dots on white paper with the captured image inverted to simulate white speckles on a black background. This was to reduce ink bleed from the printing process. The samples were then adhered to a flat acrylic surface. This allowed for uniform rigid body displacements of the printed samples. An example of a printed specimen for a small region is shown in Figure 6. The figure compares the original print file and clear pixilation of the speckles in Figure 6 (a) with the same region imaged with the optical system in Figure 6 (b). While the same groups of speckle images can be discerned, there is blurring of the speckles due to the re-sampling of a pixelated image. Figure 6 also shows that the pixel sizing of the captured image was not on a 1:1 scale with the original file. This is due to magnification of the sample from the geometry of the optical system. A perfect match is not possible with a stereo DIC system because the two cameras have an angled perspective of the subject. So, the values used to generate the pattern could not be used as the values of the input parameters in the experiment.

(a)   **(b)**
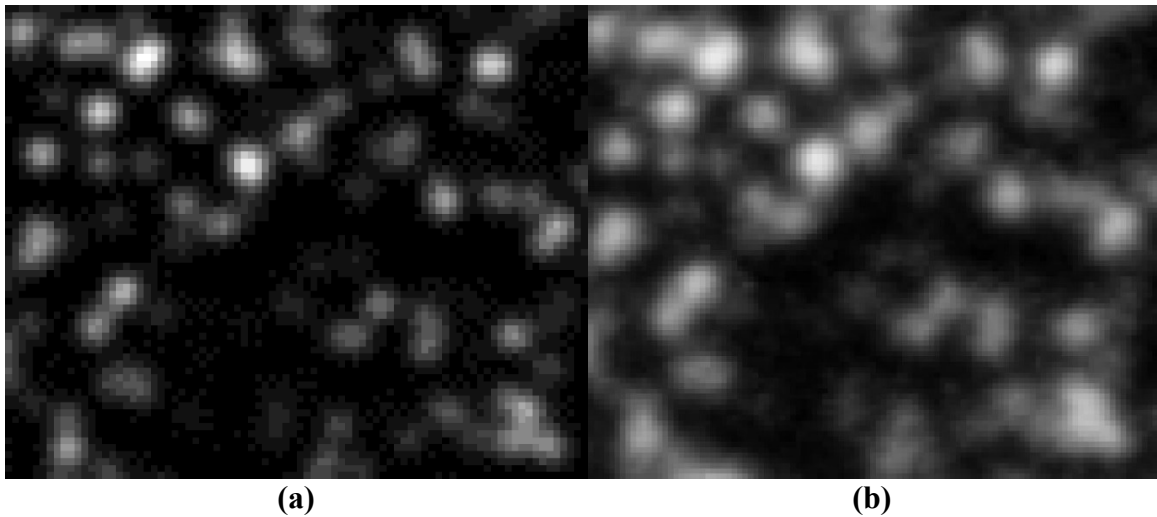
Figure 6. Comparison of **(a)** the original pattern image file and **(b)** the captured image of the printed specimen.

To quantify the input parameters of the pattern, in-house software was developed (see Appendix B) to morphologically analyze the speckles. An example of the process is shown in Figure 7. The original image to be characterized is shown in Figure 7 (a). First, the image was normalized and its contrast was enhanced on a global scale, as shown in Figure 7 (b). Next, Figure 7 (c) shows local edge sharpening applied in combination with a local Laplacian filter to improve the separation of distinct speckles in close proximity to one another. Finally, thresholding was applied to filter out noise and then image was binarized, allowing the speckle search algorithm to unambiguously determine the size of every speckle in each image as shown in Figure 7 (d). The number of speckles found and the speckle size distribution were respectively indicative of the speckle density and speckle diameter variation. Figure 8 compares specimen 1 and specimen 2, two patterns only differentiated by speckle diameter variation. It shows that the IQR can be used as an indicator for diameter variation. The variation was measured and quantified using Equation (3),

$$v = \frac{IQR}{d} \tag{3}$$

where:

v is the variation (as a percentage),
IQR is the range encompassed by the middle 50% of the data (in pixels), and
d is the average diameter (in pixels).

By performing the morphological analysis on all eight test specimens and averaging the values within each parameter level, the actual values for all input parameters were ascertained and listed on Table 6. For context, the smallest average speckle size of 3.72 pixels was approximately 0.15 mm in physical size.
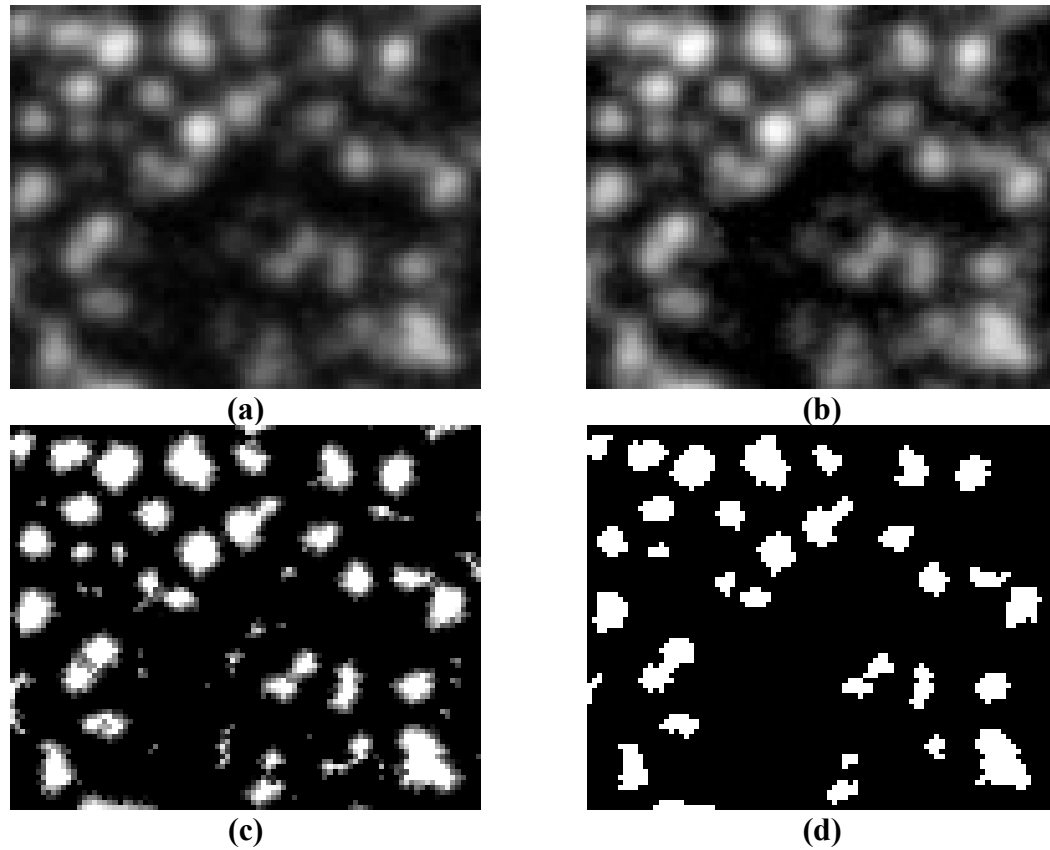
Figure 7. Morphological speckle characterization, showing **(a)** the original image, **(b)** global enhancement, **(c)** local enhancement, and **(d)** final thresholding.
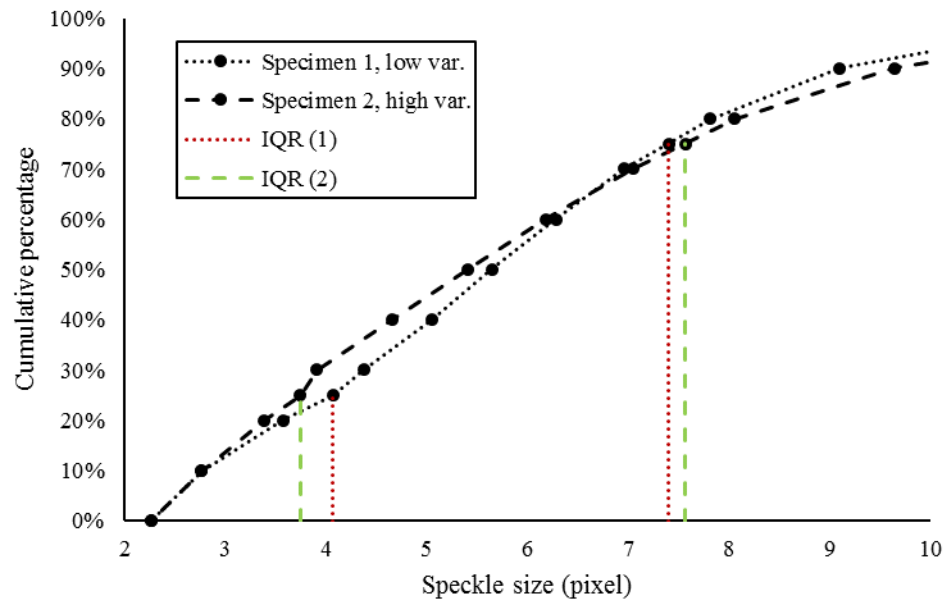
Figure 8. Cumulative percentage of speckles over increasing speckle size, comparing size distribution and diameter variation of specimen 1 (low level variation) and specimen 2 (high level variation).

Table 6. Quantifying input parameters of experiment using morphological analysis.

Specimen #	Density (speckles per subset)	Diameter (in pixels)	Variation (IQR as % of mean)
1	4.93	5.87	56.8
2	4.68	5.85	65.4
3	5.89	3.72	53.5
4	5.26	4.34	63.7
5	2.48	5.20	59.8
6	2.55	5.47	63.6
7	2.85	4.03	56.6
8	2.44	4.05	65.4
Full factorial level	Density (speckles per subset)	Diameter (in pixels)	Variation (IQR as % of mean)
Low (-)	2.58	4.04	56.7
High (+)	5.19	5.60	64.5

2.2.3 Calibration

A 3D calibration plate (Type 22, LaVision GmbH) was inserted at approximately the same location of the sample surface during the experiment. Images of the calibration plate were captured and commercial DIC software (DaVis 8.4, LaVision, GmbH) was used to calibrate the system based on a 2nd-order pinhole model. This allowed for the data to be converted from image measurements to physical measurements. The same calibration image pair was used for all eight specimens in the experiment to extract the physical measurements. The software's 2nd-order pinhole model was used instead of the 1st-order as it more effectively accounts for radial distortion at the image edges.

The typically reported calibration parameters for this setup are listed in Table 7. The image centers of both cameras were expected to be the same in a well-calibrated system, and the focal length should have match that of the actual lenses. However, because a Scheimpflug adapter was used, the effective focal length of the imaging system was longer than the lens used. This means that the calibration parameters were fitted differently, explaining why the values differed from the normally expected result.

Table 7. Calibration results of stereo DIC system for printed patterns with 2nd-order pinhole model.

Intrinsic	Camera 1	Camera 2
Image center (pixels)	(3356.7, 1446.1)	(309.9, 1452.2)
Focal length (mm)	91.8	90.3
Focal length (pixels)	2331.9	2293.9
Scale (pixels/mm)	25.41	25.41
1st-order term, k_1	-0.1196	-0.0412
2nd-order term, k_2	0.0200	0.0191
Extrinsic	**Camera 1**	**Camera 2**
Stereo angles (°)	(0.4, -39.7, 0.3)	(1.5, 38.1, 0.2)
Translation (mm)	(-57.7, 2.3, 668.8)	(63.8, -7.3, 637.0)

2.2.4 Data collection

The first speckle specimen was set up on the micrometer-controlled traversing stage and displaced in 1-mm steps up to a maximum of 5 mm in the out-of-plane direction. In-house software was developed to control the two cameras to capture simultaneous images at each displacement step (see Appendix C for more details). This procedure was repeated for the remaining seven specimens. The experiments were conducted in random order and in the shortest possible timeframe (no breaks in between), as these are common practices of DOE used to establish more robust experimental conditions [135]. Reu has reported that running tests under the same calibration is acceptable within the same day [141].

2.2.5 Data processing

The experiment data was analyzed using the same DIC software that was used to calibrate the system (DaVis 8.4, LaVision, GmbH). First, data set of image pairs was compiled for each specimen. As shown in Figure 9, a sliding minimum filter was applied to the data set to homogenize the illumination across the image and improve the overall contrast. Then, image correlation was performed to attain the surface displacements. For all images in the experiment, the correlation was performed using a subset size of 31 pixels and a step size of 15 pixels. The subset size was set constant to have a controlled comparison of the speckle densities of each specimen in the terms of number of speckles per subset. A step size of approximately half the subset size was chosen to minimize the amount of repeated data generated from the correlation; a smaller step size has more subset overlap, thus reuses

more data in the overall measurement. Affine transformation is the method used by the software, which is a linear model that accounts for the rotation, translation, and warping of each subset.

(a)   **(b)**
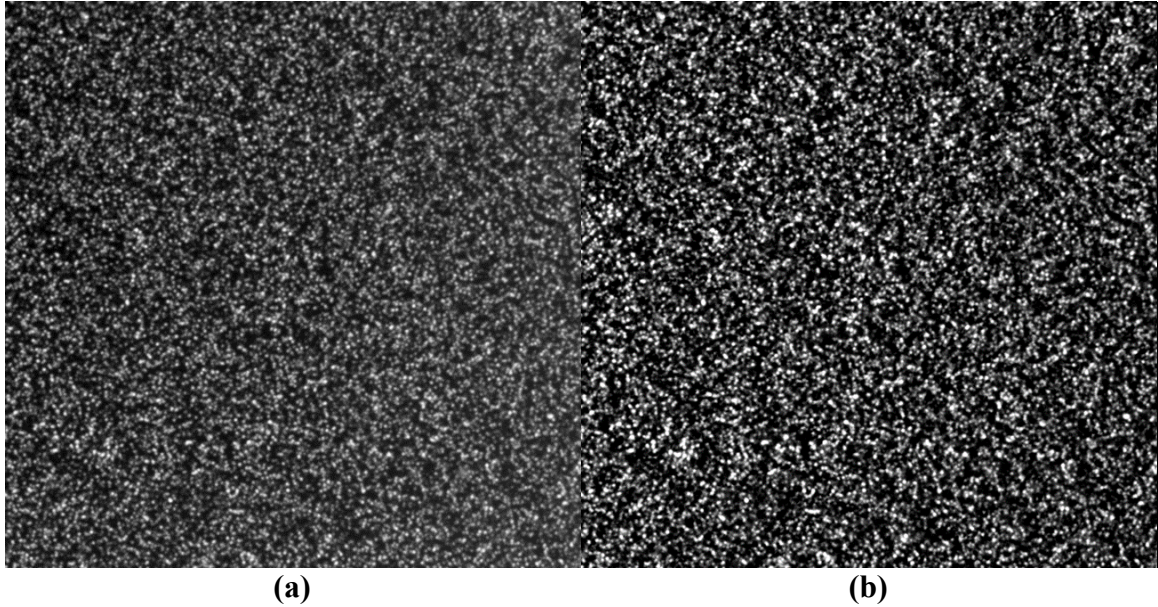
Figure 9. Comparison of **(a)** an original captured image and **(b)** a pre-processed captured image.

The results are the measured physical x-, y-, and z-displacement vectors across the entire specimen surface for each image pair. Even though physical displacement in the experiment was restricted unidirectionally in the z-direction, very miniscule x- and y-displacements were still measured in the correlation. This is because it is extremely difficult to perfectly align the experiment coordinate system with the camera calibration coordinates. Therefore, the measurements were reoriented to the out-of-plane direction of the experiment coordinate system by calculating the norm of the three orthogonal displacement vectors. As an example, Figure 10 (b) illustrates a measured displacement field from Figure 10 (a), the deformed image captured in the experiment.
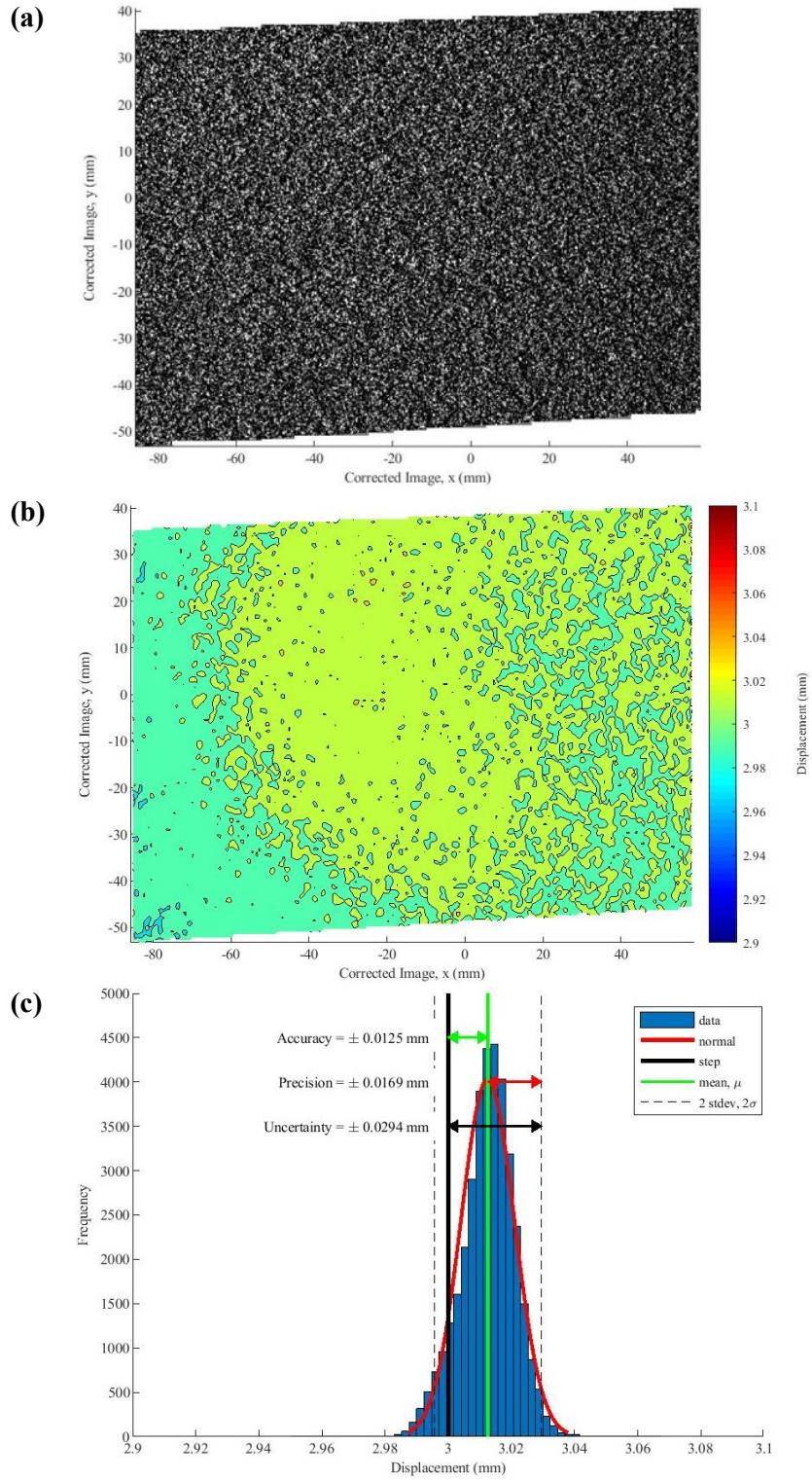
Figure 10. Quantification of uncertainty, showing **(a)** the captured image of the specimen surface, **(b)** the measured displacement field, and **(c)** the resultant PDF.

2.2.6 Uncertainty quantification

In the physical experiment, the displacement across the entire specimen surface was uniform, as rigid body motion is applied. However, the measurements contained miniscule discrepancies due to random error. Using in-house software (see Appendix D), a probability density function (PDF) of all vectors in each displacement field was used to quantify the uncertainty of the measurement of each step. An example of this result is shown in Figure 10 (c). In conjunction with the previous definition of uncertainty (refer to Section 2.1.3), the difference between the mean measurement and the prescribed step was defined as the bias error, the two standard deviation spread was defined as the precision error, and the total uncertainty in the measurement is the sum of the two. Using this approach, the uncertainty for each measurement step of each of the eight specimens in the experiment was quantified consistently.

Analysis of variance (ANOVA) was conducted on the 2^3 full factorial experiment model using commercial software (Minitab 18, Minitab Inc.). This yielded six *p*-values which represented how each of the following affected measurement uncertainty: the three experiment inputs (speckle density, diameter, and diameter variation) and the three possible input interaction pairs (density-diameter, density-diameter variation, and diameter-diameter variation). A 95% statistical confidence was used, meaning that an observed effect with a *p*-value greater than 0.05 does not significantly affect the uncertainty.

2.3   Results and discussion

2.3.1 Significant effects

The *p*-values for the observed effects of the inputs and input interactions were attained from the ANOVA on the 2^3 full factorial experiment data and listed on Table 8. The speckle diameter variation and the density-diameter interaction were observed to have the most significant effects on the overall uncertainty (*p*-value < 0.001).

Table 8. Observed effects *p*-values and coefficients in regression model.

Effect	*p*-value	Regression coefficient
*Constant	–	$C_0 = -0.3568$
Density	0.084	$C_1 = 0.0186$
Diameter	0.811	$C_2 = 0.0607$
Diameter variation	**< 0.001**	$C_3 = 0.4728$
Interaction (density/diameter)	**< 0.001**	$C_4 = -0.0053$
Interaction (density/variation)	0.524	$C_5 = 0.0135$
Interaction (diameter/variation)	0.082	$C_6 = -0.0671$

*Regression model constant only, not an observed effect.

From the ANOVA, a regression model was fitted to predict the uncertainty for values of each parameter within the bounds of the experiment. Table 8 lists the constant of the fit model and the regression coefficients for each effect, all of which are used in Equation (4),

$$u = C_0 + C_1\rho + C_2 d + C_3 v + C_4 \rho d + C_5 \rho v + C_6 dv \qquad (4)$$

where:

u is the measurement uncertainty,
C_x are the regression coefficients,
ρ is the speckle density (speckles per subset),
d is the average diameter (in pixels), and
v is the variation (IQR as % of average diameter).

This model uses the statistical analysis of the data collected in the experiment to predict the uncertainty for a speckle pattern with a given density, diameter, and diameter variation. Figure 11 shows a comparison of the uncertainty of the eight specimens in this experiment as predicted by the regression model, using the measured parameter values given in Table 6. It shows that in this experiment, the speckle pattern with the lowest uncertainty was specimen 7 with an uncertainty of 0.429 pixels.
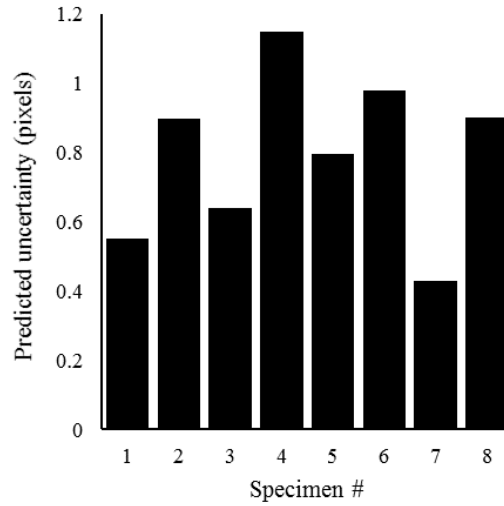
Figure 11. Normalized comparison of predicted uncertainties of all speckle patterns from regression analysis.

Uniformly sized speckles resulted in a lower uncertainty as the means plot of the effect of speckle diameter variation in Figure 12 shows. This is expected, as larger speckles tend to dominate the correlation and the smaller speckles essentially fade to noise in the background. As the difference between large and small speckles increases, the stronger this effect becomes. To clarify, the variation refers to the relative size, not the shape. In a study by Crammond et al. [131], it was determined that speckles that are random in distribution and shape actually result in better measurements.
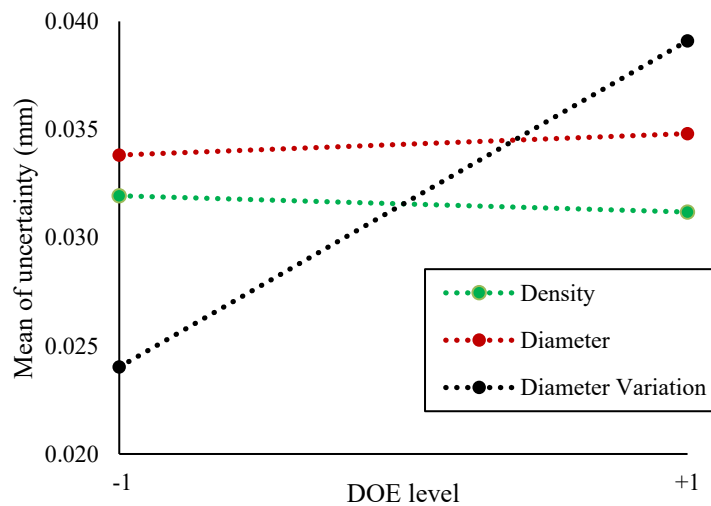
Figure 12. Means plot comparing individual effects on measurement uncertainty, showing diameter variation to be significant.

The contour plot of the density-diameter interaction effect in Figure 13 shows that the patterns with lower uncertainty had either large speckles at a high density or small speckles at a low density. In this experiment, a speckle pattern in the description of the former would have an average speckle diameter of 5.60 pixels and a density of 4.67 speckles per subset, whereas the latter would have an average speckle diameter of 2.58 pixels and a density of 3.92 speckles per subset (refer to Table 6 for 2^3 full factorial levels). As previously mentioned, studies have suggested an optimal speckle diameter to be between 3 and 5 pixels [133], and that a reasonable speckle density is 2 to 3 pixels for each correlation subset [130]. Specimen 7 in this experiment yielded the least measurement uncertainty with a density of 2.85 speckles per subset and an average diameter of 4.03 pixels, agreeing with the findings in literature for optimal pattern quality.
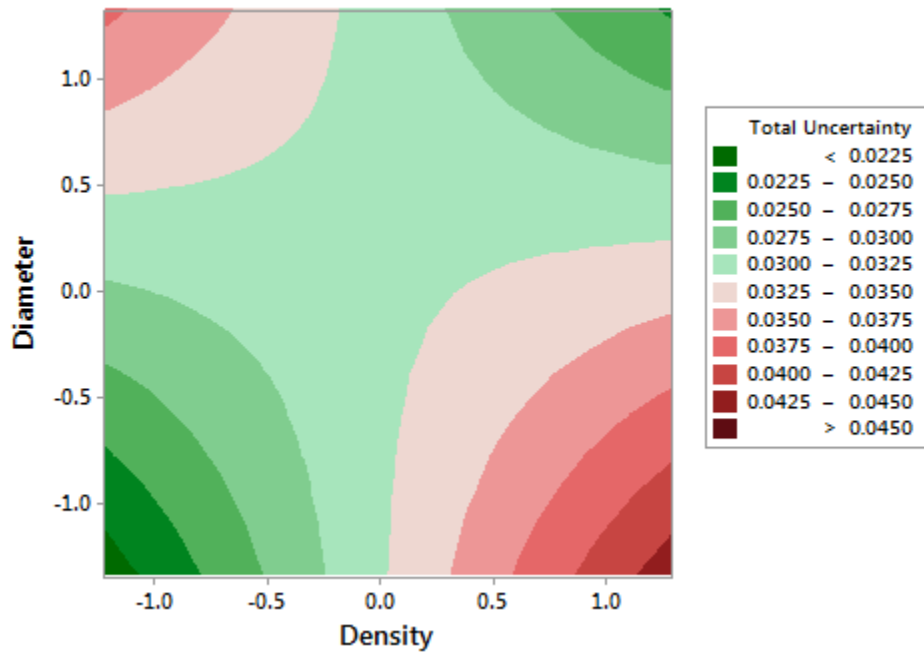
Figure 13. Contour plot of the interactive effect of density and diameter on uncertainty.

2.3.2 Other effects

Image contrast is known to be another reliable indicator of speckle quality [1]. However, the focus of this study was the physical characteristics of the speckles in the pattern. Pattern contrast was out of scope of this analysis because it can be also affected by other aspects of the system, such as exposure, gain, and lighting. However, it may still have had an unobserved effect in this experiment. In the creation of the original speckle pattern files, large speckles at high density (*e.g.*, specimen 1 in Figure 5) had a tendency to overlap one another. The increased speckle intensity from this phenomenon resulted in greater contrast between the speckles and the background. Compared to the high density, large-speckled pattern, small speckles at high density (*e.g.*, specimen 3 in Figure 5) had little spatial overlap. As a result, more grey noise, thus an effectively lower contrast, could be seen in the high density, small-speckled pattern. This means that in creating the specimens of the experiment, the image contrast may not have been strictly controlled across patterns and may have had an unobserved effect on the results.

In this experiment, calibration was performed once for the entire data set. The calibration images were captured prior to the data collection, then all eight specimen displacement tests were done one after another in quick succession. An alternative approach would have been to calibrate prior to each displacement test. In doing so, however, the experiment would have been conducted over a longer period of time, allowing for more environmental disturbances – such as ambient temperature or externally-induced motion – to affect the results. Also, in the alternative method, the calibration parameters would no longer be a constant in the experiment. Using the same calibration and conducting all eight specimens in a shorter timeframe was decidedly more experimentally robust in a DOE sense [135]. In the field of DIC, it is generally seen as acceptable for one calibration to be used for a series of experiments conducted within the day [141]. They were also tested in random order to mitigate bias regarding the time of testing, and the effect of run order in the analysis was observed to be insignificant.

When swapping specimens between tests, it is likely that minor shifts had occurred. With the same calibration applied across all tests, the alignment of the specimen in the system may have varied. This means that direction of displacements may not have been non-parallel to the out-of-plane direction to an amount that differs between the test

specimens. This was why the displacement vectors of each specimen were individually realigned by calculating the norm of the vectors in the three orthogonal directions of the calibration coordinates. Overall, the effect of specimen misalignment was insignificant, as the maximum in-plane displacement was measured to be about 1% of the z-direction displacement.

2.3.3 DOE evaluation

For the 2^3 full factorial experiment, the validity relies on the high and low levels to be the same across each parameter. When generating the simulated speckle patterns, all inputs for density, average diameter, and diameter variation were set to one of two values. However, the actual input parameter values of the experiment are those measured from the captured image files, not the original speckle pattern file. As seen on Table 6, those values were unique for each parameter across all specimens. This is because the software used to generate the patterns did not account for overlapping speckles, creating discrepancies in the pattern output. For example, when comparing specimens 1 and 2 to 4 and 5, the only difference between the respective pairs should have been density. However, the diameter of the former pair was greater than that of the latter. This was because at higher densities, speckle overlap was more frequent, resulting in apparently larger speckles. When comparing patterns 3 and 4, because pattern 4 is at a high variation level, there are more large speckles and more resultant overlap. This is why pattern 3 exhibits a higher density but a lower diameter.

Another cause of discrepancy is the loss of particles in the pattern generation. For example, specimens 7 and 8 should have had the same density and diameter, with only diameter variation differentiating the two. But some of the speckles towards the smaller end of the diameter variation were lost as they became too small to be tracked, resulting in a lower density than intended. But in this comparison, because more of the diameter variations above the mean were tracked, the resultant average diameter was greater at high variation than at low Nonetheless, for each input there was significant spread between the range of low and high values and no overlap between them: the input levels were 2.58 ± 0.27 and 5.19 ± 0.70 speckles per subset for speckle density, 4.04 ± 0.32 and 5.60 ± 0.40 px for average diameter, and values of IQR as a percentage of mean of 56.7 ± 3.2 and 64.5

± 1.0 % for diameter variation. This means that the results can still be valid but must be assessed with caution.

The results of the experiment from the DOE model used are only valid within the bounds of the low and high levels of each input. In this experiment, the individual effects of density and average diameter were found to be insignificant. However, the bounds for speckle density, [2.58, 5.19] speckles per subset, are close to the optimal speckle density range of 2 to 3 pixels per subset. This suggests that although insignificant in this experiment, the individual effect of speckle density may be significant in an experiment with more spread between the low and high levels. The same applies to the individual effect of average diameter, where its bounds in this experiment, [4.04, 5.60] pixels, are close to the optimal speckle diameter range of 3 to 5 pixels. In an experiment with increased bounds, a significance may be observed regarding the individual effect of average diameter on the measurement uncertainty.

2.4   Validation

2.4.1 Experimentally realistic patterns

Another set of tests were performed on two speckle patterns representative of typical experimental samples. They were used to validate the speckle print study and to showcase the application in a more typical experiment environment [142]. In preparing these specimens, flat acrylic sheets were first coated with flat black paint to minimize glare. Then, with a typical airbrush (PCMT70536, Porter Cable), white speckles were sprayed onto the specimen surfaces. The airbrush settings were modified to create two distinctly varied speckle patterns. Subregion examples of the two different speckle patterns are compared in Figure 14. Morphological analysis was conducted on each airbrush pattern to quantify their characteristic differences. Again, variation was defined as the average diameter divided by the IQR; Figure 15 graphically shows that the pattern in Figure 14 (b) has greater variation than that in Figure 14 (a). The measured physical characteristics of each pattern and the resultant uncertainties are reported on Table 9.
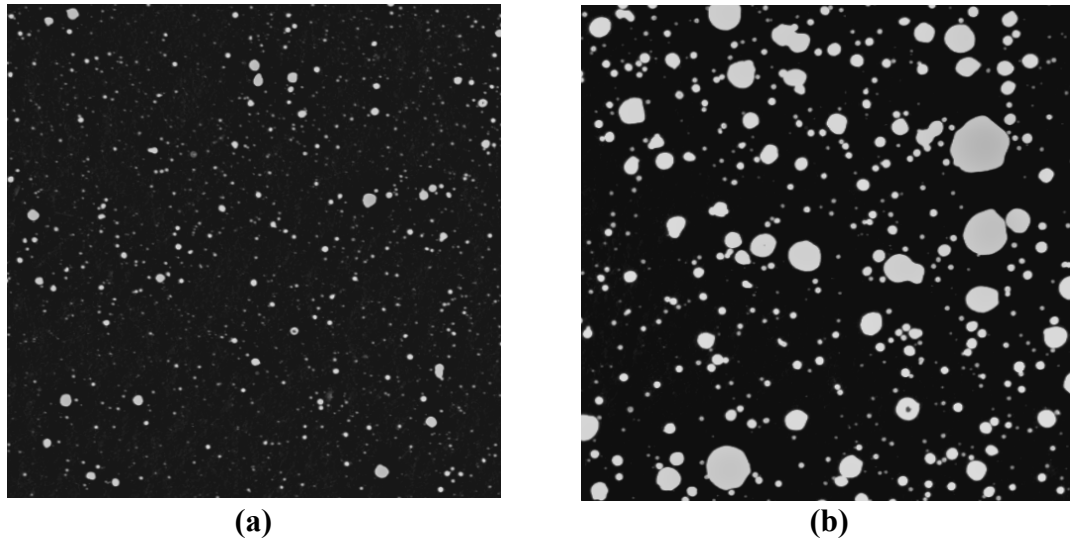
Figure 14. Comparison of airbrushed speckle specimens, showing **(a)** a small, uniform speckle pattern, and **(b)** a larger speckle pattern with variation.
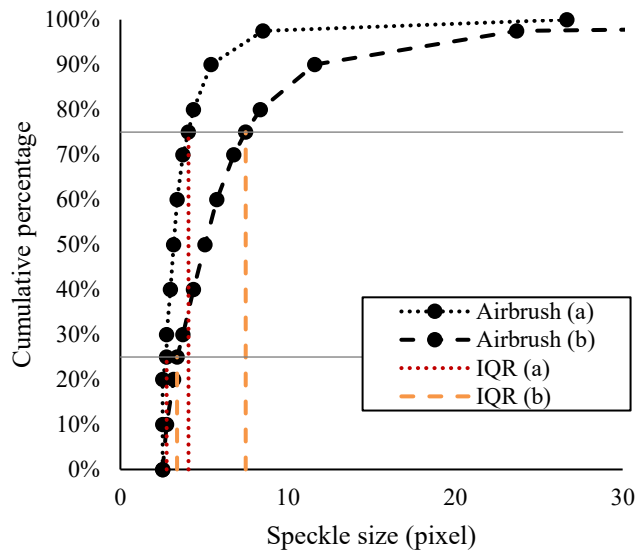
Figure 15. Cumulative percentage of speckles over increasing speckle size, comparing size distribution of airbrush speckle patterns.

Table 9. Morphological and uncertainty comparisons of airbrush speckle patterns.

Characteristics	Airbrush (a)	Airbrush (b)
Density (speckles per subset)	2.36	1.84
Diameter (pixels)	3.69	6.73
Variation (IQR as % of mean)	35.2	60.9
Measurement uncertainty (pixels)	0.303	0.368

After the specimen preparation, the experiment with the airbrush patterns was conducted in the same way as with the printed speckle patterns. The system was calibrated with the same calibration plate and fit model, with the parameters reported in Table 10. After calibration, both specimens were displaced in 1-mm steps to a maximum of 5 mm in the out-of-plane direction, capturing images at every step. The images were combined and pre-processed with a sliding minimum filter to homogenize the illumination across the specimen surface and increase image contrast. They were then correlated with an affine transformation function using a subset size of 31 pixels and a step size of 15 pixels. The measured displacement fields were plotted on a PDF which was then analyzed to determine the bias error and the precision error; the total uncertainty was quantified as the sum of the two. ANOVA was not conducted as there were only two specimens allowing for a direct comparison to one another.

Table 10. Calibration results of stereo DIC system for airbrushed patterns with 2nd-order pinhole model.

Intrinsic	Camera 1	Camera 2
Image center (pixels)	(3389.4, 1450.4)	(270.0, 1542.8)
Focal length (mm)	92.6	90.6
Focal length (pixels)	2451.66	2395.6
Scale (pixels/mm)	26.47	26.47
1st-order term, k_1	-0.1345	-0.0909
2nd-order term, k_2	0.0190	0.0207
Extrinsic	Camera 1	Camera 2
Stereo angles (°)	(0.4, -39.4, 0.3)	(1.4, 38.0, 0.2)
Translation (mm)	(-76.5, 4.3, 635.4)	(40.9, -4.2, 631.9)

2.4.2 Results and discussion

The measurement uncertainty for the airbrush patterns were determined to be 0.303 and 0.368 pixels for the patterns shown in Figure 14 (a) and Figure 14 (b) respectively. For the Figure 14 (a) pattern, the density was 2.36 speckles per subset and the average diameter was 3.69 pixels, both of which fall within the recommended ranges of 2-3 speckles per subset for density and 3-5 pixels for diameter. The Figure 14 (b) pattern had a density of 1.84 speckles per subset and an average diameter of 6.73 pixels, both of which are beyond the recommended ranges. Regarding the diameter variation, the pattern in Figure 14 (a) had an IQR to mean ratio of 35.2% compared to the 60.9% measured in the Figure 14 (b)

pattern. In the contexts of literature and the printed pattern experiment, the features of the pattern in Figure 14 (a) were more optimally defined than that in Figure 14 (b). The result was a lower measurement uncertainty in the former compared to the latter, showing agreement with the previous experiment and with existing studies. It also validates the use of the IQR to mean ratio as a way of quantifying the evenness of a speckle pattern.

2.5   Conclusion

This study investigated a novel, intuitive metric for assessing the quality of a DIC speckle pattern: the IQR variation. Using DOE concepts, measures were taken in the design and execution of the experiment to ensure statistical robustness in the results. A 2^3 full factorial experiment model was implemented to assess the effects of a pattern's speckle density, average speckle diameter, and speckle diameter variation on the measurement uncertainty of a DIC system. Eight speckle specimens of different combinations of known densities, average diameters, and diameter variations were generated as image files and printed. They were then individually displaced in prescribed steps of rigid body displacement in the out-of-plane direction. For each step, the entire specimen surfaces were measured, processed, and analyzed to quantify the uncertainty of the displacement step measurement.

The test specimens with high variation in speckle diameter produced the most uncertainty. The interaction between density and diameter was also significant, showing that both parameters should be considered together, rather than individually, in assessing the quality of a speckle pattern based on these characteristics. The results were validated by comparing airbrush speckle specimens of varying density, average diameter, and diameter variation under the same test conditions. The pattern with less diameter variation and a more optimal density and sizing, in the context of literature and the experiment, was observed to have a lower measurement uncertainty than the other with less optimal characteristics. The results show that DOE can be an effective tool in conducting DIC research experiments and that the IQR variation is an intuitive and easily determined parameter that can be used in assessing the quality of a DIC speckle pattern.

For this system, an optimal speckle pattern had a density of 2.85 speckles per subset with an average diameter of 4.03 pixels and minimum variation in the speckle diameter. These parameters were aimed to be replicated in the subsequent tests of this study.

Chapter 3: Experimental design

3.1 Introduction

3.1.1 Background

At the University of Alberta, a machine known as the multi-axis biomechanical testing apparatus (MABTA) was designed and used to experimentally validate a finite element model of a knee [143]. It has since been adapted to experimentally simulate the loading of a pelvis [144]. This thesis expands on the pelvic research described in the latter through the development of a system that can simulate the mechanical loading of a fractured pelvis and extract high quality measurements throughout the experiment. The initial state of the MABTA had issues involving a lack of safeguards, inconsistent sampling frequency, and inability to synchronize with camera measurements. Before proceeding with experimentation, these issues needed to be addressed.

The biomechanics of pelvic loading are very complicated and difficult to mimic in an experimental setting. This is due to the highly contoured geometry of a pelvis, as well as its complex boundary conditions. Additionally, every pelvis is unique in size and shape, causing further difficulties in attaining consistent and comparable results across experiments. There is no strong standard for comparison or conduct of a pelvic loading experiment. Most existing studies self-validate by conducting both numerical and experimental simulations and comparing the two. Existing pelvic biomechanical studies also examine different cases ranging from intact composite models [60] to cadaveric models of various fractures [78], [79]. Due to the individuality of the current studies and the complexity of the problem, it can be difficult to determine the validity and accuracy of the results of a pelvic experimental simulation.

To address these concerns, a series of experiments, starting simple and increasing in complexity, were conducted to confirm that with any experiment using the MABTA, there is accuracy and confidence in the results. The simplistic experiments involved dogbone testing to evaluate the in-plane strain measurement of the system, and single edge notched tension (SENT) test to evaluate the quality of measurements on cracked specimens.

3.2 Equipment

The main components of the testing experimental setup belong to either the MABTA or the imaging system. The following section focuses on the design improvements and implementations. For more detailed information and instructions on usage, refer to Appendix E for the MABTA and Appendix C for the camera system. The optical and mechanical components comprising the imaging system of the following sets of experiments are the same as those used in Chapter 2: and are listed in Table 5.

3.2.1 MABTA

The MABTA is shown in Figure 16 below. The frame of the MABTA contains a fixed base, to which one end of the test specimen is held, and a loading base which is displaced vertically to induce either compressive or tensile loading. A wide assortment of test specimen shapes and sizes can be accommodated by designing jigs to interface with the specimen and the MABTA frame. The loading base is mounted to a load cell (MC6-6-2000, AMTI), which measures the orthogonal forces and moments at the loading base as a change in resistance using strain gages up to a reported maximum of 9000 N. A signal amplifier (MSA-6 MiniAmp, AMTI) connects with the load cell and converts data measured by the load cell from the change in resistance to digital data. The starting position of the loading base can be set to any height within the range of motion of the MABTA to accommodate varying specimen sizes. The position of the loading base is controlled by a motor (EC3BK32-5005B-150-MF3-FT1E-PB, IDC), which linearly positions the stage that the loading base is upon up to a maximum load of 7200 N. A digital servo amplifier (Servostar S30661, Kollmorgen) communicates with the motor's position sensors to output the position of the loading base. The measurement components of the MABTA connect to a computer equipped with the MABTA control software which has been programmed on commercial software (LabWindows/CVI, National Instruments) and redeveloped by the author. An image of the MABTA control user interface is shown in Figure 17 below.
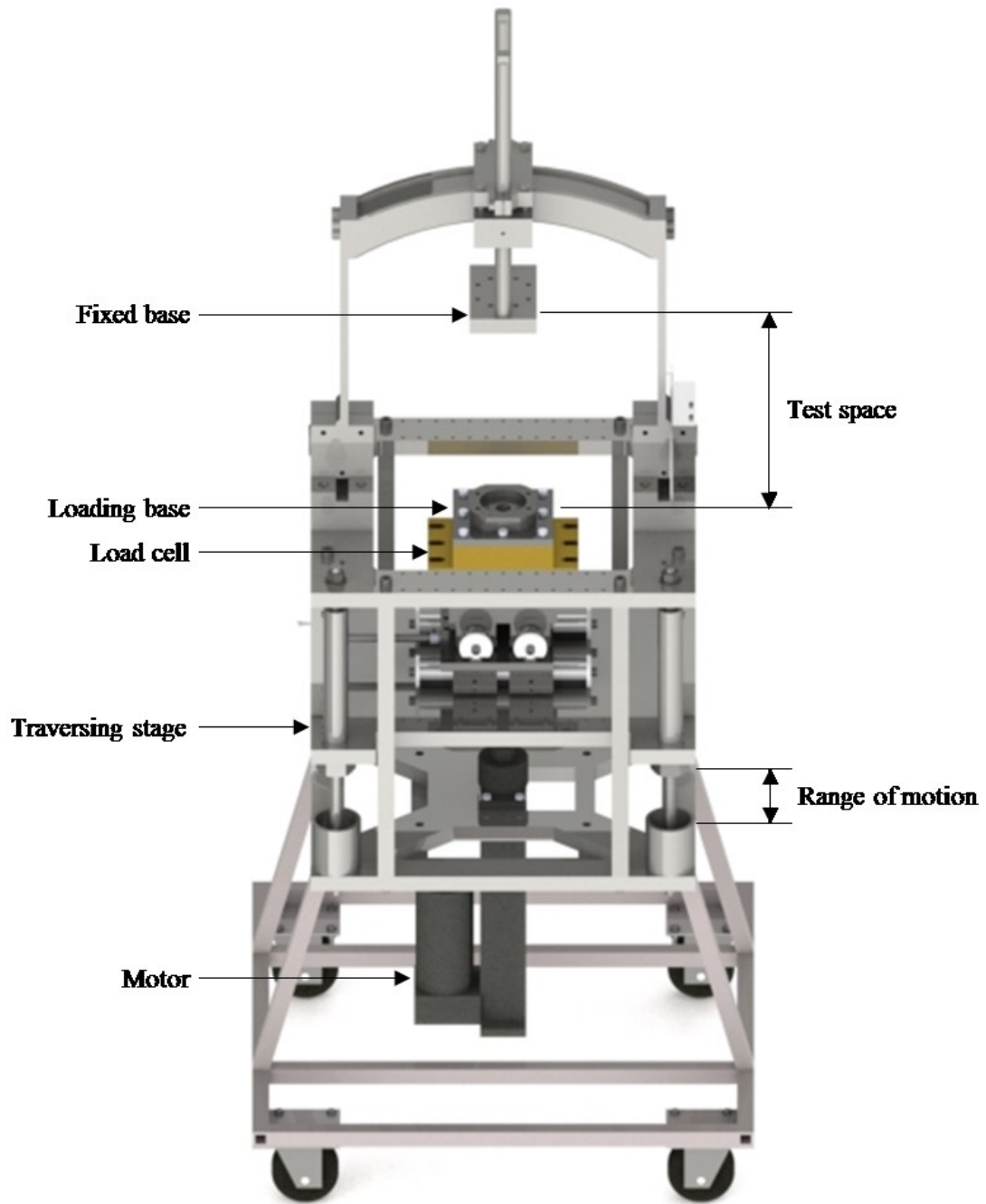
Figure 16. Multi-axis biomechanical testing apparatus (MABTA) diagram.
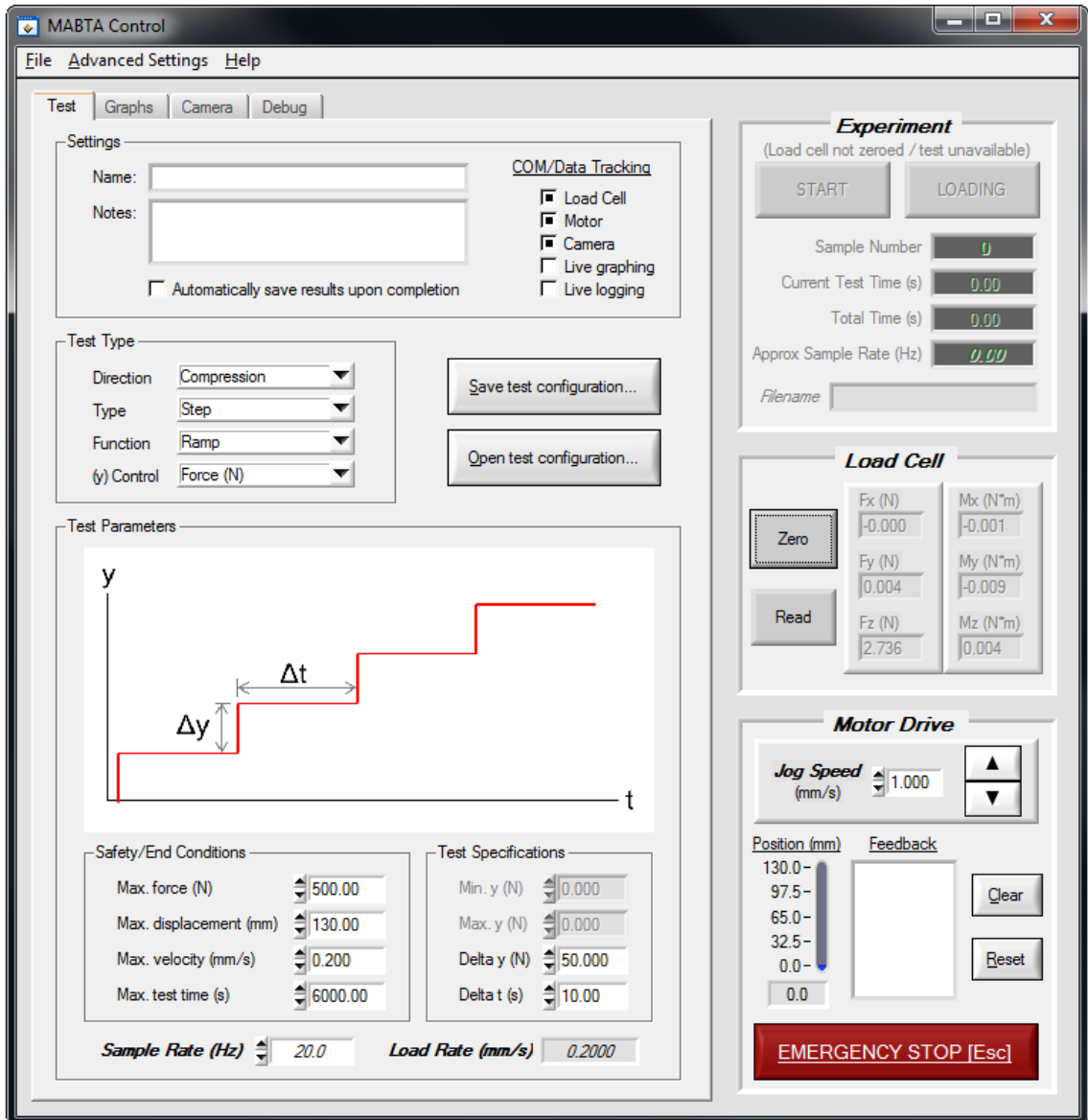
Figure 17. Redesigned MABTA control software.

The MABTA control software is used to run experiments and measure the loading and displacement throughout the experiment. The general procedure for conducting a test is provided in Appendix E; the focus of this section is on the design implementations of the current version of the program. The previous version of the software performed only displacement-based continuous loading. In this version of the software, two more test types have been integrated: force-based step loading and displacement-based step loading. During step-loading tests, the MABTA stops motor motion and hold the load when the specified displacement or force interval is reached. The motor holds the load at this step for the prescribed step time, after which loading continues to the next step. Also, the user can manually trigger the next step preemptively during the experiment.

Safety and end conditions of experimentation were improved in this version of the software. In older versions of the program, the user would be able to set the motor velocity in the experiment and the maximum force before ending the experiment. This version includes a displacement limit, a velocity limit, and a time limit for more safety and test options. If any are exceeded during the experiment, the program ends the experiment, unloading the specimen at the same rate in the opposite direction until a zero-load state has been reached. The same unloading procedure is conducted when manually stopping the experiment as well. The load limits of the load cell and motor (9000 N and 7200 N respectively) have also been integrated into the code, as they previously were not. This allows the software to prevent the user from overloading the components of the MABTA. In other urgent situations, the user can manually activate the emergency stop function to halt the motor immediately.

The graphing functionality of the MABTA control software was improved upon in this updated version, shown in Figure 18. In previous versions, it was only possible to view the position and loads with respect to time. This version is more maneuverable, allowing for more y-axis variables, such as sample rate and velocity, as well as more x-axis variables, such as position and camera image number. Furthermore, the software holds the data collected for all tests conducted in the session, allowing for graphical comparisons between different tests. This allows the user to visually assess the repeatability of successive tests.
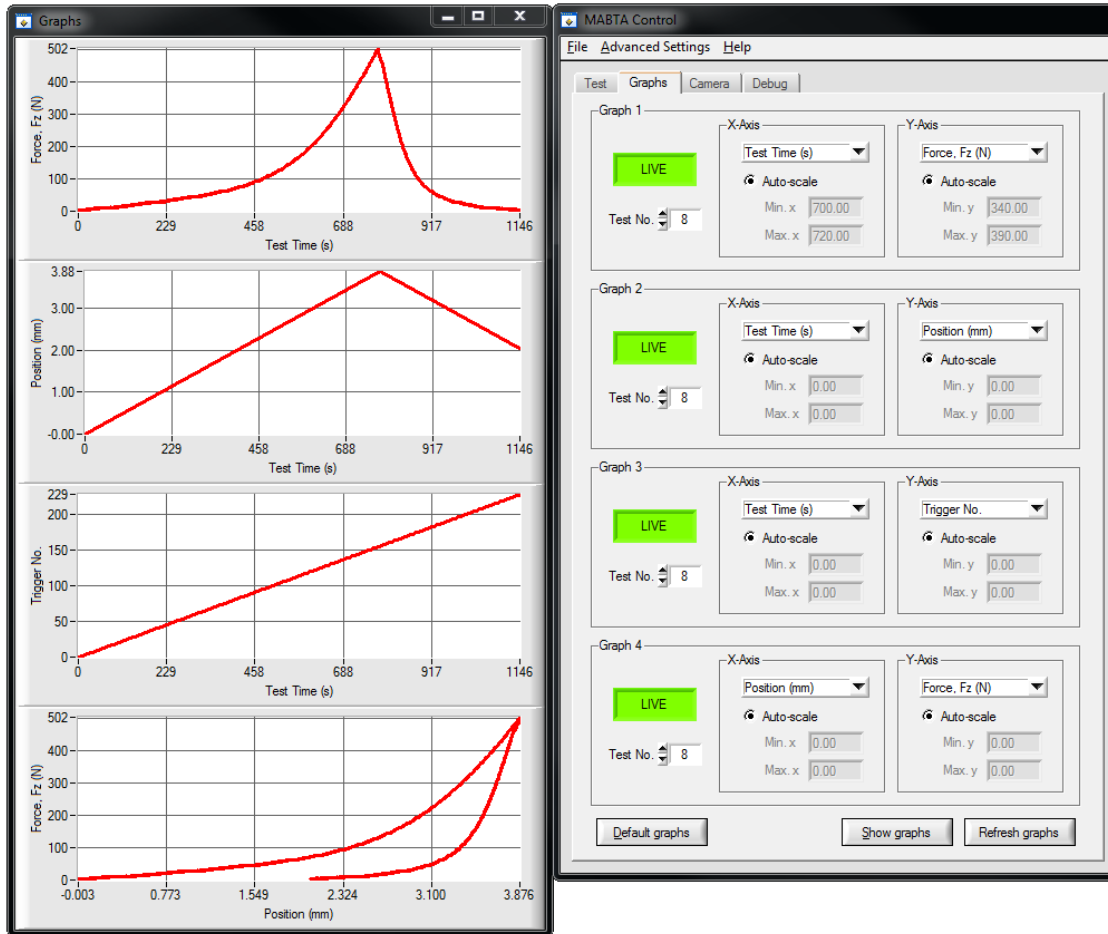
Figure 18. Graphical interface update for MABTA control software.

The prevention of the motor exceeding its range of motion was another one of the safety features implemented by the author. Whenever the MABTA is turned on, the motor position resets. This means the program assumes the motor is at position zero, which may cause the motor to unknowingly force the traversing frame to attempt to move past its range of motion, butting up against the frame and potentially over-torqueing the motor. To address this, the program now prompts the user to physically read a position from the MABTA frame and enter into the program, as shown in Figure 19 below. This value is then defined as the starting position of the motor, allowing the program to identify the physical position of the motor. Hard limits were then implemented to prevent the motor from exceeding its range of motion and damaging itself based on the user-entered starting position.
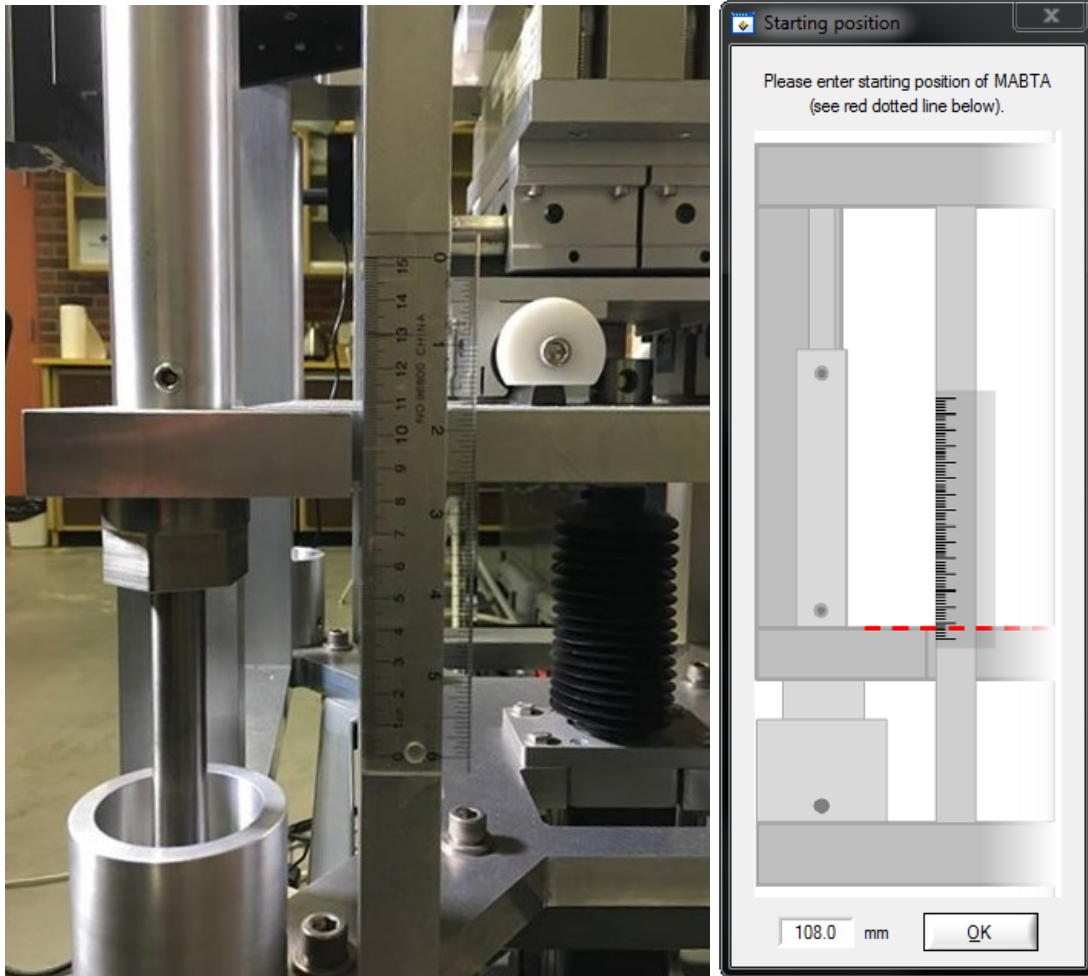
Figure 19. MABTA control software safety implementation for motor range of motion.

The MABTA control code was modified to improve its sampling. Previously, the program would attain measurements at a sample rate of approximately 1.5 to 2.5 Hz. It would do so variably, collecting measurements as quickly as the program would allow it. By reprogramming the MABTA control software, a constant sample rate can now be set up to 30 Hz, depending on how many functions the program is running (graphing, logging, *etc*.). In terms of safety, this feature allows for the software to more quickly determine when physical or user-defined experimental limits have been reached and stop the motor or unload the specimen accordingly.

Previously, because the sample rate was variable, there were problems with combining data sets. Because handling camera images is very demanding on computer resources, captured camera images are handled by a computer different from the one

controlling the MABTA. This means that image data was captured separately from the load and position data, requiring the combination of the data sets after the experiment. The variable sample rate made direct data stitching of the two sets impossible, requiring the MABTA data to be quantized through interpolation so that it can fit the acquired image data. This means that some of the data analyzed is not real but rather estimated from the collected data set. With the constant sampling improvement, data sets acquired by the different sources can be combined to the lowest multiple, allowing all used data to be of real measurements.

As mentioned before, the DIC image data was acquired independently from the MABTA load and position data. This meant that the data had to be manually matched after the experiment, which is difficult and potentially erroneous as the selected starting image may not be in line with the loading measurements. To address this, camera control and synchronization was programmed into the MABTA control software, as shown in Figure 20. It allows for the same software controlling the MABTA to also communicate with the cameras. At the same time the load cell and motor measurements are read, the MABTA control software sends a signal to the cameras, commanding them to capture an image. This improvement allowed for all data desired in this experiment to be collected synchronously, eliminating the labor and error associated with manually matching data sets. In terms of safety, the more frequent the loads and position are monitored, the quicker the software can command the MABTA to cease a dangerous or unwanted operation. However, image collection is likely to be at a lower frequency, as the images are large in file size thus difficult to collect at a high frequency. To address this, the camera trigger settings can be set independent of the load and position measurements to allow for the MABTA to measure and monitor the loads at a higher frequency than the collection of images. Doing so still allows for synchronized data collection, as the cameras are still triggered at intervals of load and position measurements. The triggering can be specified to occur at a constant rate for all experiments. For a step loading experiment, it can be set to trigger throughout each step at the specified rate, or once at the end of each step. The procedures and requirements for establishing communication lines between the MABTA control software and the cameras are described in detail in the following section.
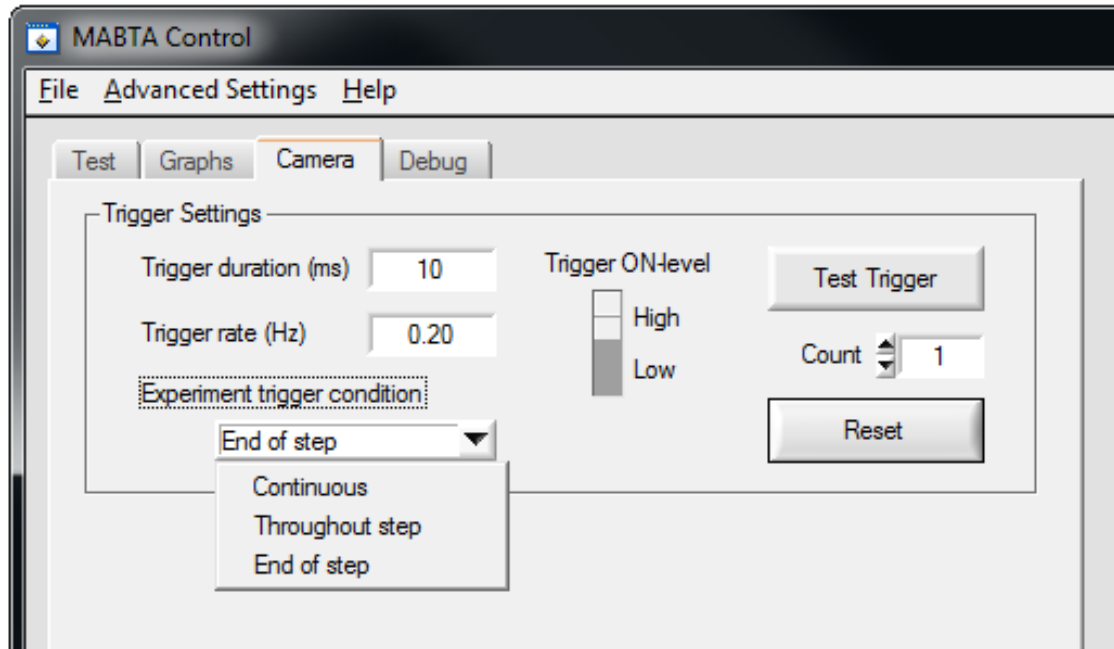
Figure 20. Integration of external camera communication into MABTA control software.

3.2.2 DIC system

To measure the strain on the test specimens in the experiments, the DIC technique is used (refer to Section 2.1.2 if further explanation is required). The same optical and mechanical components were used in this experiment as that in Chapter 2: of this thesis listed in Table 5. As shown in Figure 21, the DIC components are assembled and fixed directly onto the MABTA frame for rigidity between the optical and mechanical components. Commercially available optomechanical rails and connections (from Thorlabs) were used for the mounting and positioning of the cameras. The rigid bar set up allowed for adjustments to be made in the x-, y-, and z-direction while ensuring the height (y-component) and the stand-off distance (z- component) of both cameras were the same. The distance between cameras (x- component) was positioned to be equidistant from the center of the region of interest (ROI).
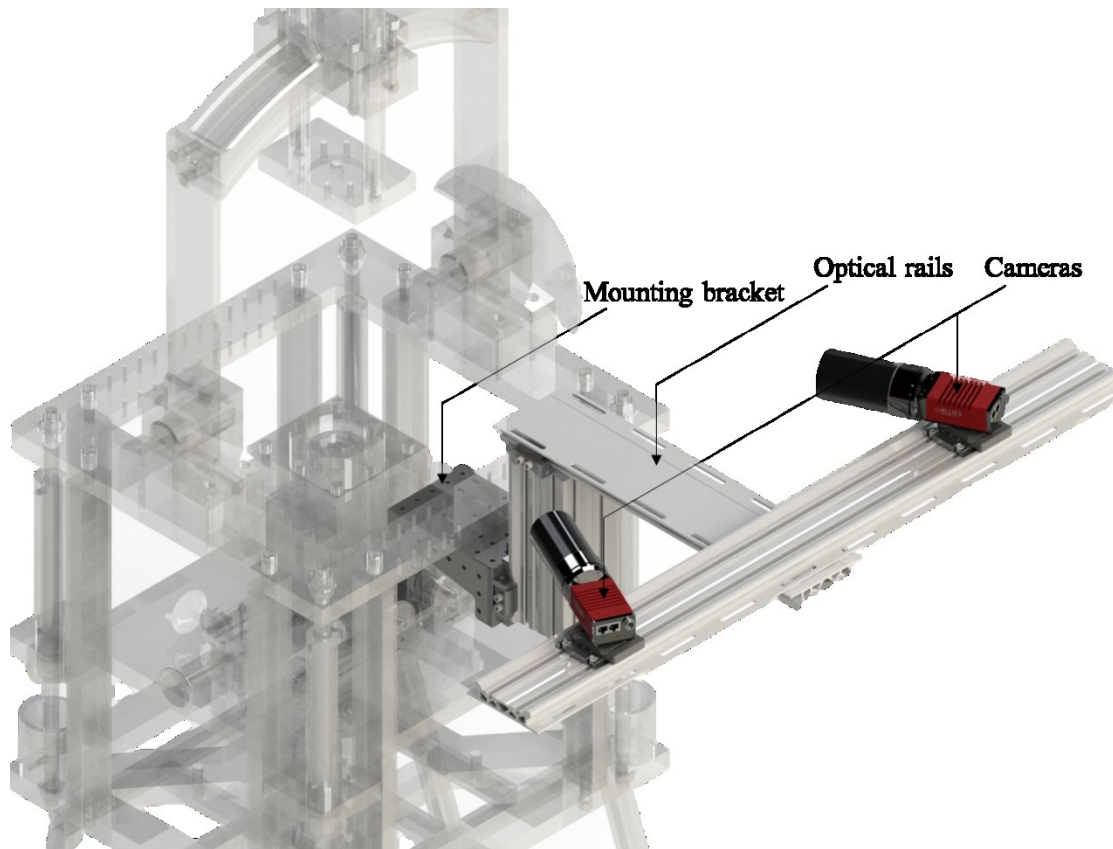
Figure 21. Mounting of optics and optomechanics onto MABTA (displayed with translucency).

The signal diagram in Figure 22 shows to set up the experiment components to allow the MABTA computer communication with the cameras and synchronization with the image data. To supply the cameras with power, a 115 VAC power supply unit (PSU) (EG425P-VE, Enermax) was connected to a pair of camera boxes which then carry the power to the cameras. It provides the external power as well as the trigger signal power. The MABTA computer sends a timed 5 V signal to a custom-designed trigger circuit board, which then relays the 12 V trigger power from the PSU to the cameras, causing them to capture an image. During experiments, images captured by the stereo camera system are saved to a second computer equipped with a GigE card (PRO/1000 PT, Intel®).
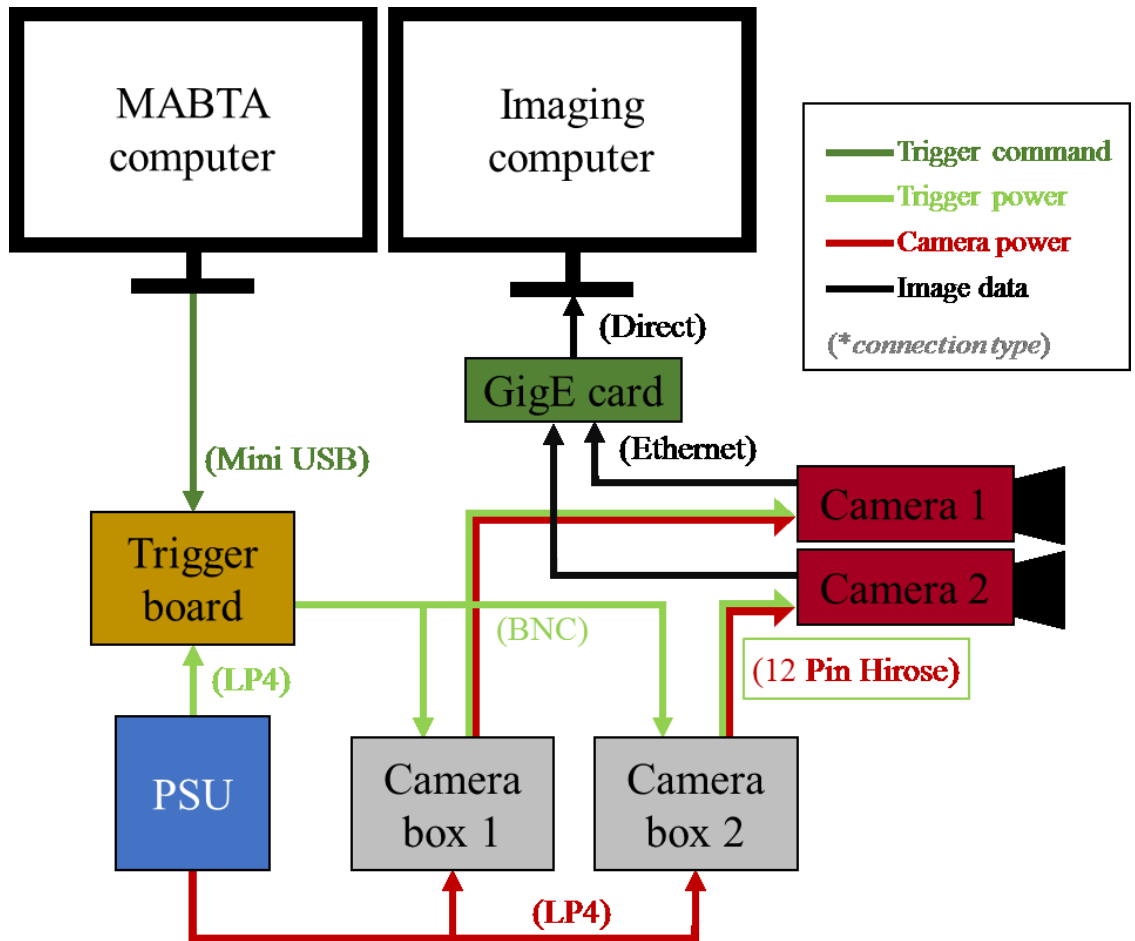
Figure 22. Signal diagram for image acquisition with camera hardware triggering via MABTA control.

The schematic in Figure 23 shows the trigger circuit board that was designed and created to receive a trigger command and route the trigger power to the cameras. This is achieved by using a commercial solid state relay (SSR-40DD, Sodial®). By default, the output circuit (from trigger power to camera) is held in an off state by a pair of NPN transistors in the relay. The circuit is closed when an input signal sent by the MABTA control program to a commercial breakout board (FTDI Basic-5V, SparkFun), which then forwards the signal through the control circuit. A pair of LEDs convert the electric current of the control signal into light energy. This light energy is received at the base of the phototransistor of the load circuit, converting it back to electric current. When this occurs, the transistor is set to an on state, allowing electric current to flow from the PSU to the cameras to trigger the acquisition of an image. The MABTA control software then stops sending the control signal causing the LEDs to stop emitting light energy, which in turn

causes the transistors to revert to the off state and cut off the trigger current supply to the cameras. The floating current is reset to zero with a pulldown resistor, readying the next trigger signal. The physical object is shown in Figure 24.
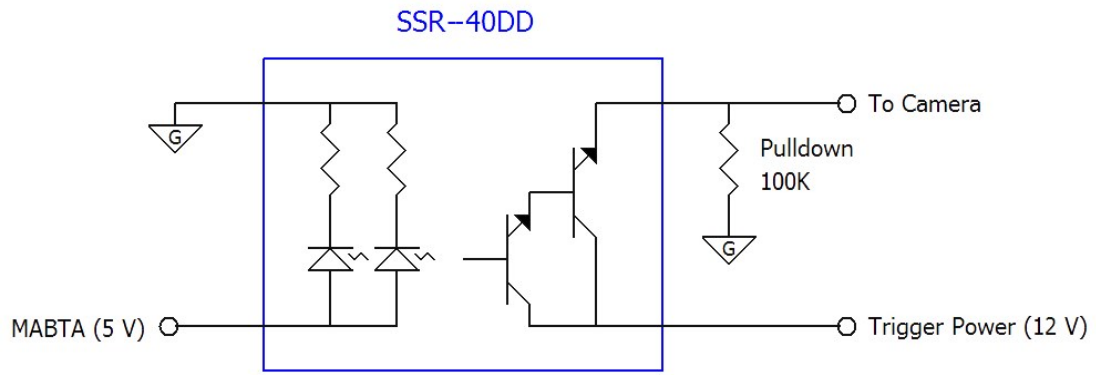
Figure 23. Circuit diagram showing MABTA control software electronically triggering cameras.
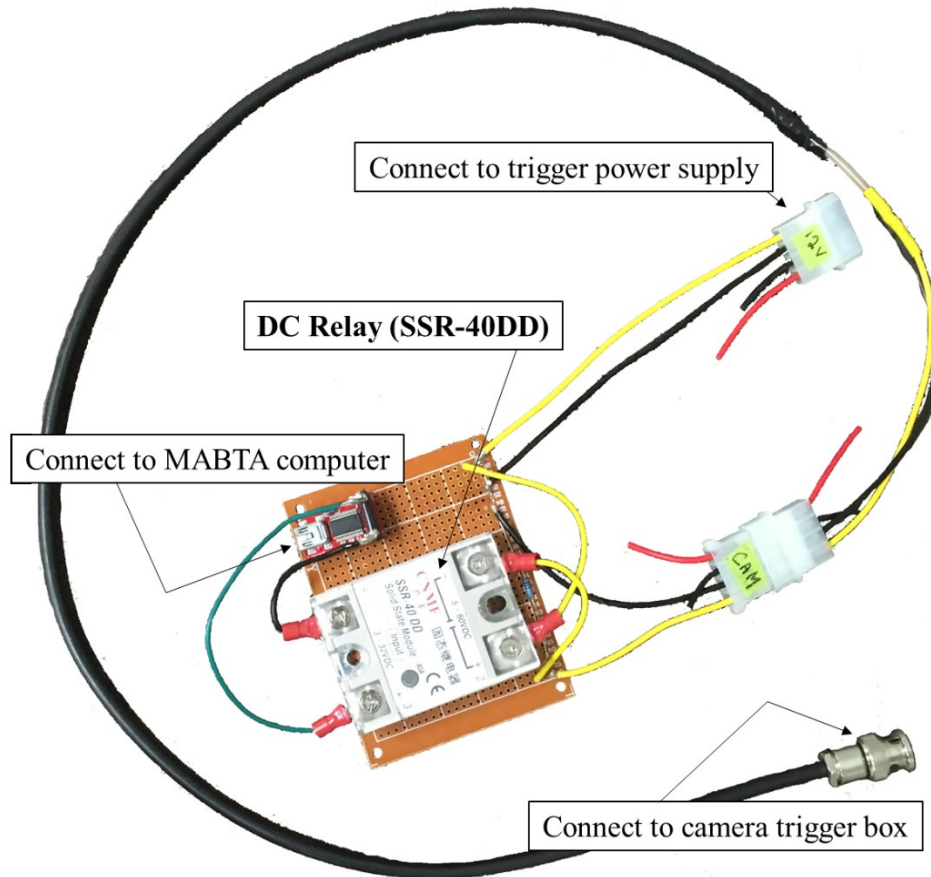
Figure 24. Physical diagram of designed trigger circuit board.

There are numerous benefits to hardware triggering. In previous experiments, the cameras were triggered by a signal sent from the computer controlling the cameras. The computer must allocate resources to send the software trigger, putting more strain on the machine. The software trigger itself takes time to send, limiting the maximum achievable frame rate of the image acquisition. Additionally, each camera requires an individual trigger, resulting a delay between images in an image pair demonstrated in Figure 25 (a). With software triggering, only static or quasi-static experiments can be properly measured. As shown in Figure 25 (b), the hardware triggering method implemented in this research achieves camera synchronization with each other as well as with the external data collection system (MABTA software). It also functions on an analog voltage signal, which does not take computational resources or time. This means that the signal is sent immediately, resulting in more synchronization. It also means that the next signal is readied in a shorter time frame, allowing for a higher frame rate to be achieved. The implementation involves more complexity, software, and setup, but the system and software was designed to be intuitive and simple in achieving the benefits of hardware triggering.

(a)

(b)
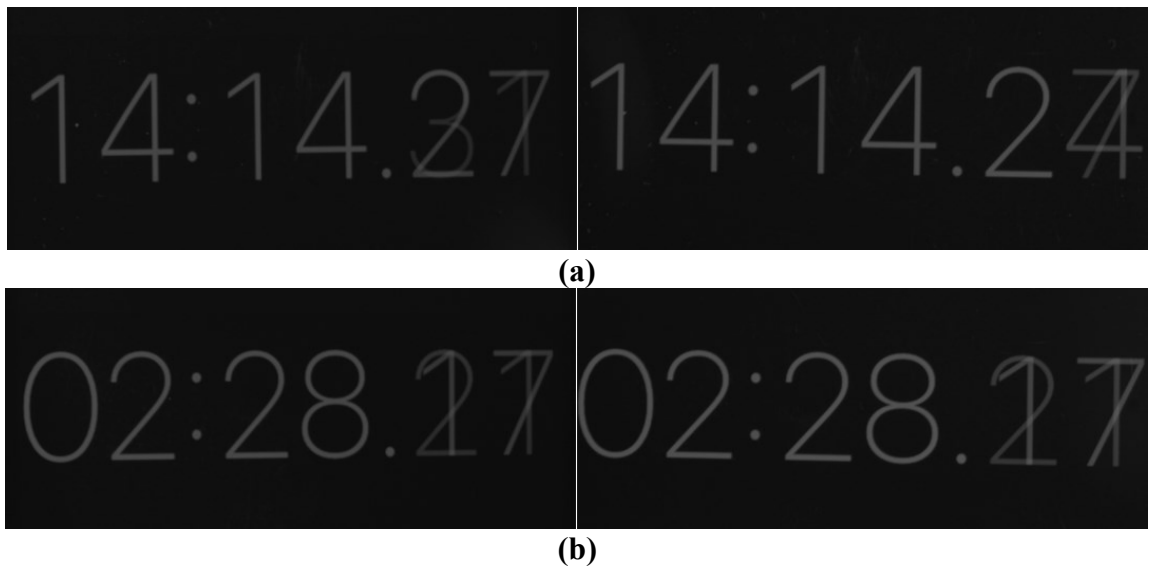
Figure 25. Comparison of camera synchronization between triggering methods, showing the left and right images of a pair using **(a)** the old method of software triggering and **(b)** the improved method of hardware triggering.

Camera control software used in previous experiments [144] was not compatible with the cameras used in this experiment. Therefore, the MATLAB program shown in Figure 26 was created for camera compatibility and functionality of the triggering method previously described. Other additional improvements include stereo camera previewing to facilitate test setup, histogram snapshot capability to quantify intensity levels during setup, more data handling options for different applications, and simple and intuitive integration of different cameras by future users. For more detail on the software, refer to Appendix C.
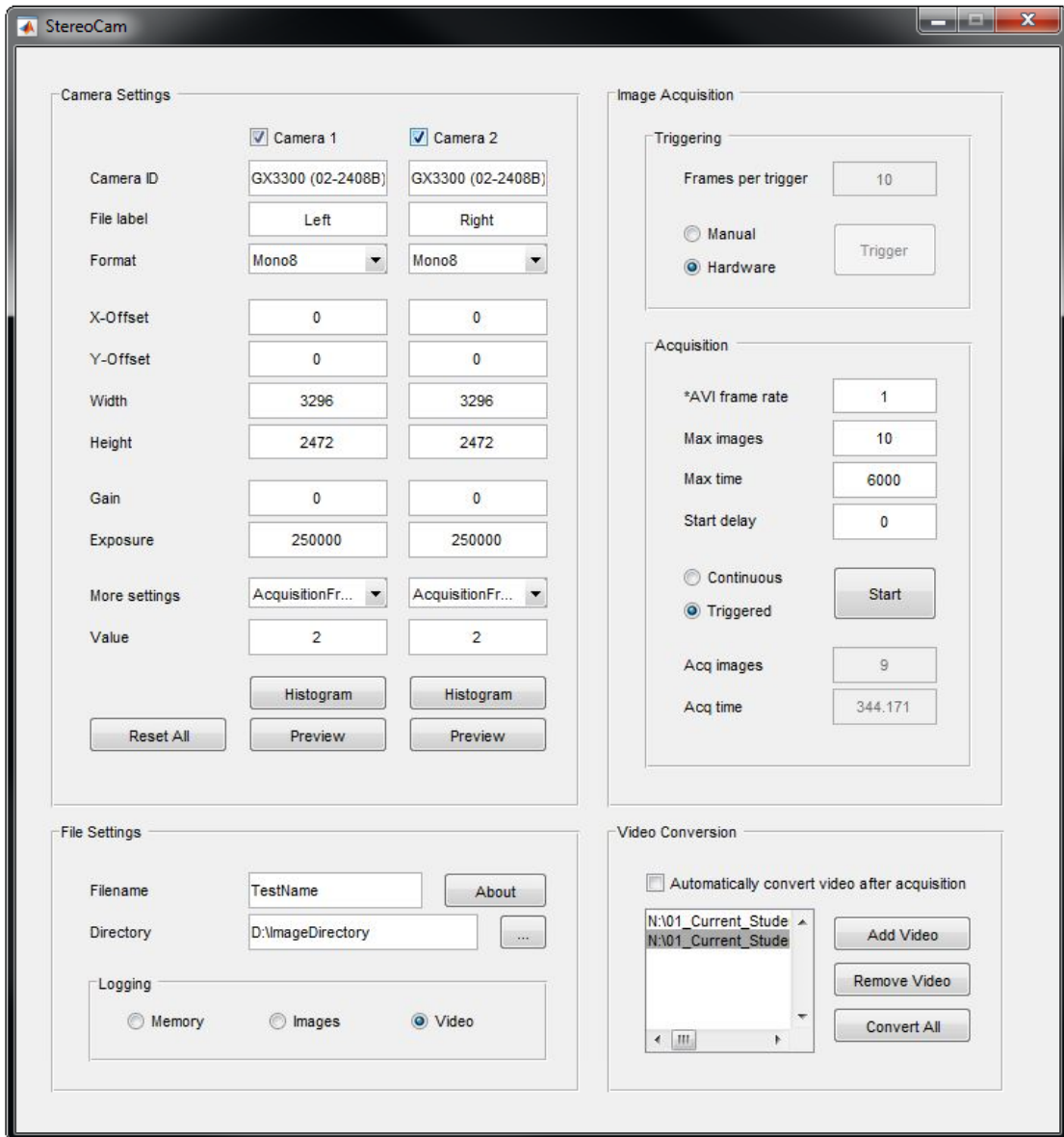
Figure 26. MATLAB program created for stereo camera control.

3.2.3 Error estimation

The potential sources of error associated with the components of the system were analyzed to determine potential areas of high error. The load cell measurement error was assessed in a previous study [144] and found the error to be fairly constant as a percentage of the load measured. In this study, the error in force measurement was taken to be the most conservative measurement from that study, which was ± 1.24% of the measured force. The sensitivity of the load cell was about 1.5 N, which was estimated to be the minimum uncertainty of the force measurement.

The displacement measurement uncertainty of the imaging system was determined using the out-of-plane rigid body displacement technique described in Section 2.2.6. This method yields a conservative uncertainty estimate for the entire imaging system. For tests prior to the updated hardware triggering technique, there would also be uncertainty due to image asynchronization. Any lack of synchronization would not be accounted for in the out-of-plane displacement method as those images collected there are static. The synchronization uncertainty was estimated as the maximum amount of potential displacement of a point between the images in a stereo pair as shown in Equation (5),

$$U_{sync} = displacement\ rate \times stereo\ image\ delay \tag{5}$$

where the estimated delay in time is 0.1 s for a software triggered image acquisition. It should be noted that the displacement rate of a point may not be equal to the loading rate of the system. The estimation of this value may differ between experiments. The total displacement measurement uncertainty of the imaging system is the out-of-plane uncertainty plus the synchronization uncertainty.

3.3   Dogbone tensile testing

The first tests conducted using the MABTA and camera setup were dogbone tensile tests. There were three methods of analysis compared in this study: 1) the theoretical calculation, 2) the numerical simulation (SolidWorks Simulation 2017, Dassault Systèmes), and 3) the experimental results. The simplicity of the dogbone tensile tests allows for a ground-level understanding of the sources of discrepancy in the numerical simulation and the experimental results by comparing them with the theoretical calculation. This

understanding can be layered upon as incrementally complex problems are analyzed. The main parameters of comparison in this investigation were the elastic modulus, E, the yield strain, ε_y, and the yield stress, σ_y of the specimen. The expected values of these parameters were provided by the polypropylene manufacturer's material specification documents (see Appendix F).

3.3.1 Experimental setup

The general setup is shown in Figure 27. The dogbone material used was polypropylene (PP-DWST, Simona®). For these tests, a more ductile material was selected as it could be easily observed using DIC. The experiments were conducted in accordance with the American Society for Testing and Materials (ASTM) standard for determining the tensile properties of plastics [145]. The dogbone geometry was designed to comply with the standard and the previously designed grips that were used for this experiment (see Appendix F for engineering drawings). They were cut from a polypropylene sheet by the waterjet cutter at the mechanical engineering department of the University of Alberta. Afterwards, the testing areas of the specimens were manually finished to a P240 surface roughness to meet compliance with the standard. The specimen must be measured before testing, as the original cross-sectional area is required. The width and thickness of the specimen were measured five times across the gage length then multiplied and averaged to calculate the area as in Equation (6),

$$A = \frac{1}{5} \sum_{i=1}^{5} w_i t_i \tag{6}$$

where:
    w is the measured width, and
    t is the measured thickness.
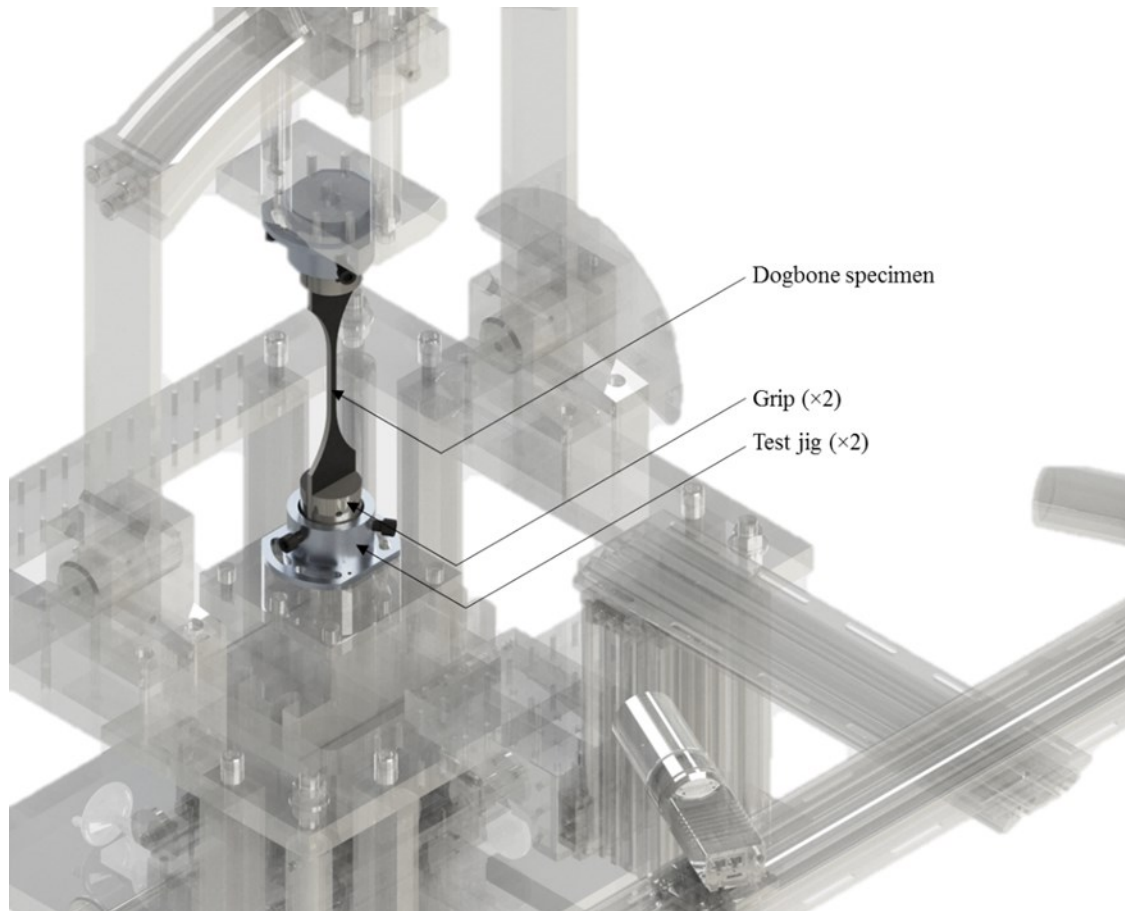
Figure 27. Setup of dogbone tensile test, with MABTA and optics displayed with translucency.

Next, the DIC system was set up similarly to the previous experiment in Chapter 2:. Here, the cameras were at an approximate standoff distance of 530 mm and a stereo angle of about $\pm 25°$ centered about the dogbone specimen. To accommodate this geometry, the Scheimpflug angle was set to 4°. The specimen was prepared for a DIC test by painting the viewing surface black with white speckles. It was temporarily set up in the field of view (FOV) of the experiment to focus the cameras. Then, it was removed and replaced by the calibration plate and the cameras were calibrated. The specimens were then set up on a micrometer-controlled stage and moved in 0.1-mm steps in the out-of-plane direction up to a final cumulative step of 1 mm to quantify the DIC system uncertainty.

Morphological analysis was performed on the four dogbone speckle patterns shown in Figure 28 and the results, shown in Table 11, were used to characterize the speckle pattern quality and determine the optimal subset settings for image processing. The subset size was set to 23 pixels and the displacement steps were processed for all dogbones. The

uncertainty was then quantified as per the method used in Section 2.2.6. As expected, the speckle pattern with the least variation, dogbone 1, yielded the least pixel uncertainty. The greatest uncertainty was found with dogbone 3, as its diameter was much too small for the recommended 3-5 pixel size and much too dense for the recommended 2-3 speckles per subset. Dogbones 1, 2, and 4 were all within the recommended ranges and thus resulted in reasonably low measurement uncertainties.

| Dogbone 1 | Dogbone 2 | Dogbone 3 | Dogbone 4 |
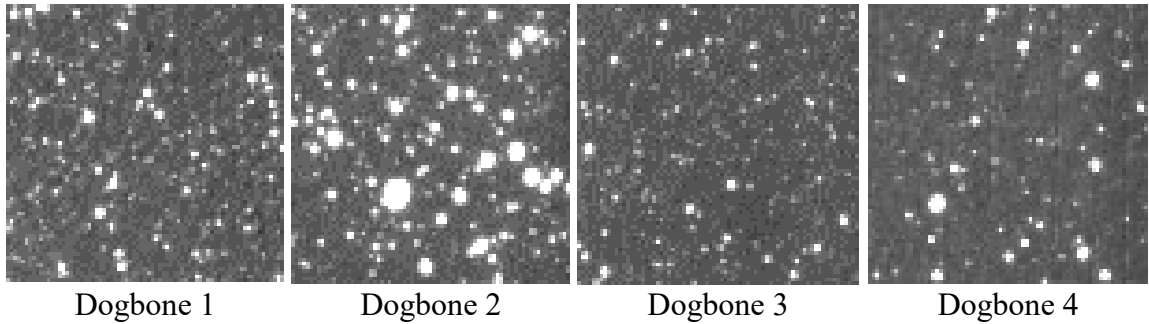
Figure 28. Comparison of dogbone speckle patterns used in morphological analysis for uncertainty quantification.

Table 11. Morphological and uncertainty analysis of dogbone speckle patterns.

Characteristics	Dogbone 1	Dogbone 2	Dogbone 3	Dogbone 4
Subset size	23	23	23	23
Density (speckles per subset)	3.67	3.70	6.23	3.42
Diameter (pixels)	2.96	3.47	2.16	2.77
Variation (IQR as % of mean)	38.2	42.8	43.0	44.6
Uncertainty (mm)	0.0074	0.0123	0.0375	0.0081
Scale (pixel/mm)	17.21	17.29	17.29	25.08
Uncertainty (pixels)	**0.127**	**0.213**	**0.649**	**0.202**

The image processing settings used for the displacement measurements were the same used for the loading measurements. These settings are also similar to those used in the experiment in Chapter 2: of this thesis which can be consulted for more detailed information (see Section 2.2.5). For brevity, the settings for this set of experiments are simply listed in Table 12 below. The out-of-plane displacements were processed with 23-pixel subsets, which were determined to be a viable subset size from the morphological analysis. It provided a good balance between resolution and measurement error. The

maximum uncertainty measured from the out-of-plane displacements was used to quantify the uncertainty of the experiment measurements. The measurement uncertainty is listed in Table 11 for each specimen.

Table 12. Summary of image processing settings for dogbone tensile testing.

Detail	Specification
Software	DaVis 8.4
Image filtering	Subtract sliding minimum
Subset size (pixels)	23
Step size (pixels)	11
Shape function	Affine transformation

After setting up the cameras, the specimen was gripped in the MABTA test space as shown in Figure 27. The jigs are bolted to the frame and the grips are locked into position by set screws, holding the specimen and allowing for loading. The speed of testing was 0.1 mm/s, which resulted in yielding in the standard specified range of 0.5 to 5 minutes [145] for all experiments. The forces and moments applied to the dogbone specimens were measured by the load cell and the surface strains were measured by the cameras. From the measured area, forces, and strain, a stress-strain curve was generated and used to quantify material parameters. Then, the yield stress was calculated as shown in Equation (7),

$$\sigma_y = \frac{F_{max}}{A} \tag{7}$$

where:

σ_y is the yield stress,
F_{max} is the maximum measured force, and
A is the gage area.

The yield strain was the measured strain at the same point as the yield stress. And the elastic modulus was the slope of the stress vs. strain curve between 0.05% and 0.25% strain. This method was specified by the International Organization for Standardization (ISO) standard for properties of Type-C plastics [146], which follow the general shape shown in Figure 29. The experiment results were then compared with the theoretical and numerical results. Note that dogbones 1 to 3 were tested prior to the implementation of the synchronized imaging system.
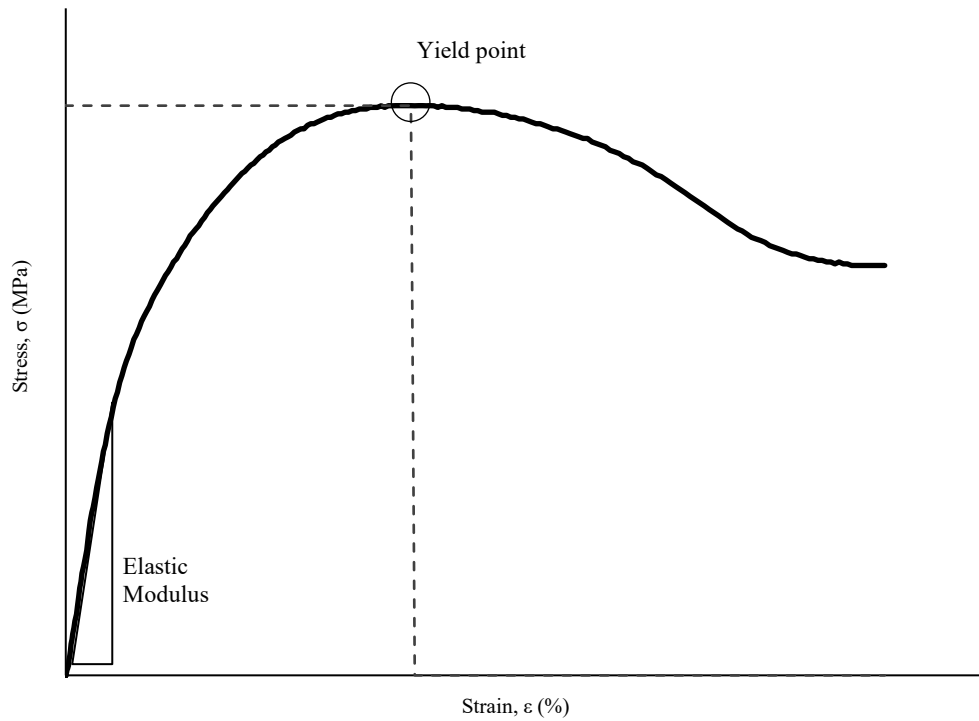
Figure 29. A typical stress-strain curve for type-C plastics, as classified by ISO-527.

3.3.2 Numerical simulation

The setup for the numerical simulation is shown in Figure 30. It was performed using a non-linear model, as the polypropylene is ductile. The solver settings used are listed in Table 13. The upper set of holes were set as fixed hinges and the lower set of holes were loaded downwards at a rate of 0.1 mm/s, which is the speed of loading in the experiment. A mesh was generated using a meshing algorithm built into the simulation program, with the mesh parameters listed in Table 14. Mesh refinement was conducted to verify mesh independence as shown in Figure 31.
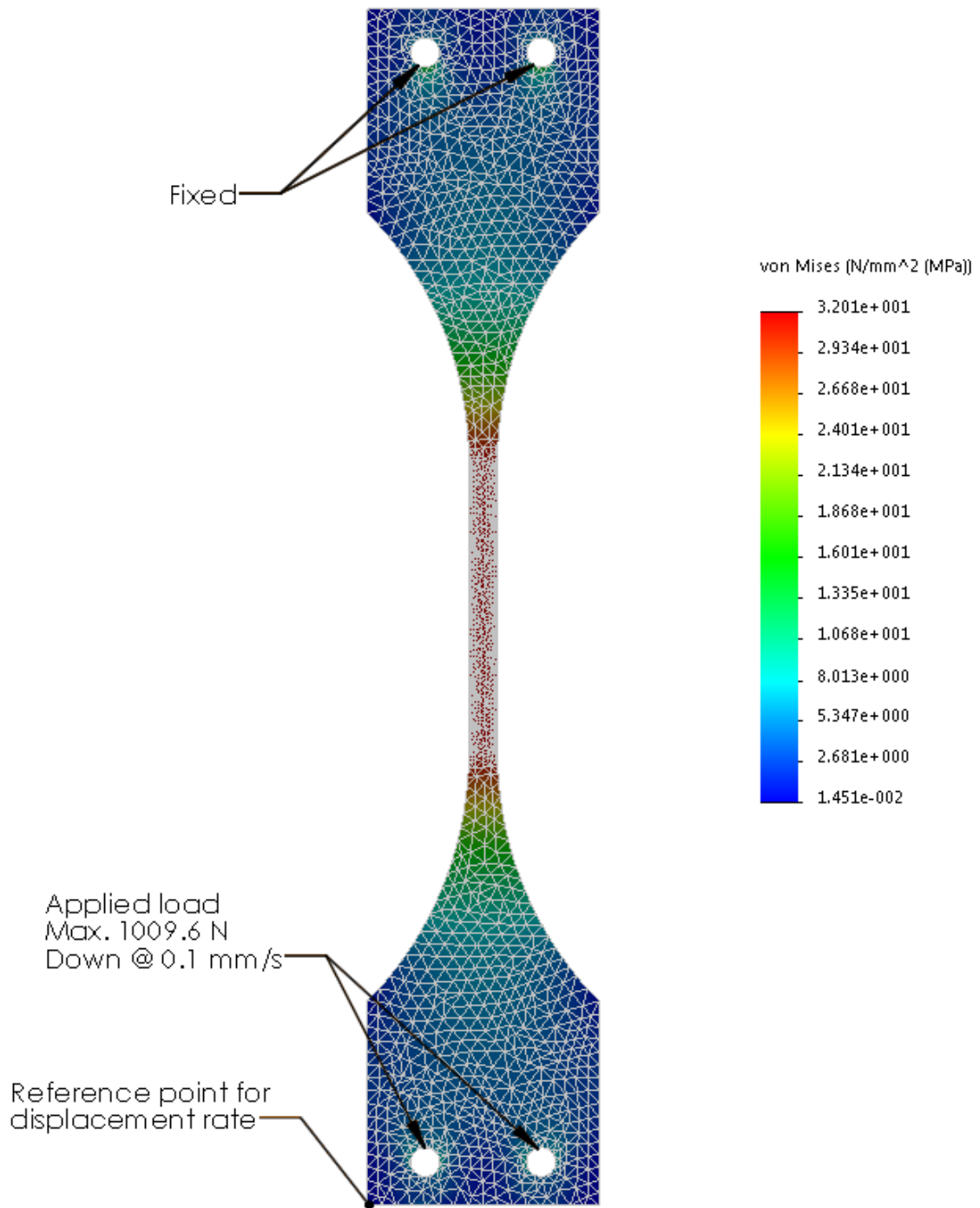
Figure 30. Numerical simulation setup for dogbone test, showing final mesh, stress distribution, and boundary and loading conditions.

Table 13. Summary of solver settings for dogbone numerical simulations.

Attribute	Value
Specimen	Dogbone
Mechanics	Nonlinear static
Boundary conditions	Upper bolt holes: fixed hinge
Loading conditions	Lower bolt holes: displacement-based, 0.1 mm/s downwards
Software	Solidworks Simulation 2017
Solver	Direct sparse solver (Implicit)
Algorithms	Newton-Raphson
Convergence criteria	0.1%

Table 14. Dogbone numerical simulation mesh settings and results per iteration.

Mesh	Iteration 1	Iteration 2	Iteration 3	Iteration 4
Mesher	Curvature-based	Curvature-based	Curvature-based	Curvature-based
Jacobian points	4	4	4	4
Mesh control	-	-	Bolt holes, gage area	Bolt holes, gage area
Max. element size (mm)	4.5	3.2	3.0	3.0
Min. element size (mm)	1.5	1.067	1.0	1.0
Number of nodes	9334	18828	37507	76667
Number of elements	5071	10731	22120	47367
Max. aspect ratio	3.5721	3.9188	4.0513	4.1723
Aspect ratio < 3 (%)	99.2	99.5	99.5	99.5
Aspect ratio < 10 (%)	0	0	0	0
Max Stress (MPa)	32.062	32.037	32.011	32.010
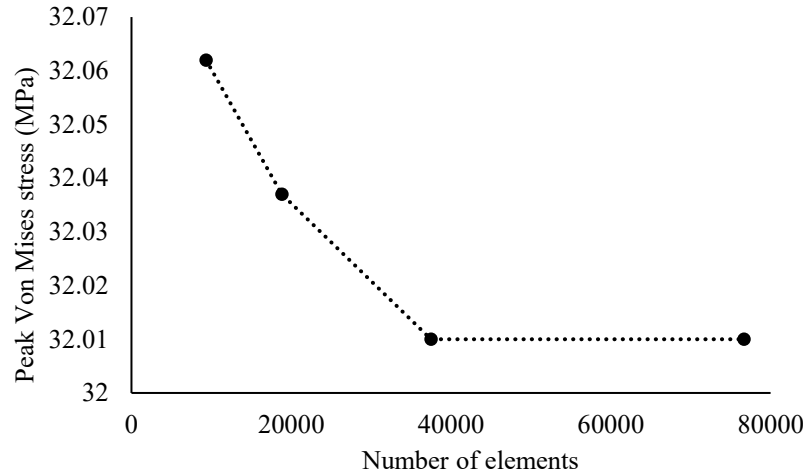
Figure 31. Mesh refinement on dogbone numerical simulation, showing convergence of peak Von Mises stress.

3.3.3 Results and discussion

The stress-strain curves measured in the experiments are shown in Figure 32. Dogbone 1 was shown to deviate greatly from the other three and the theoretical and numerical results. It is likely due to a fault of the experiment rather than a measurement error. Possible explanations include material defects, specimen warping, pre-loading effects, or improper experiment calibration. Nonetheless, it was deemed to be an anomalous misrepresentation and thus discarded from the analysis.
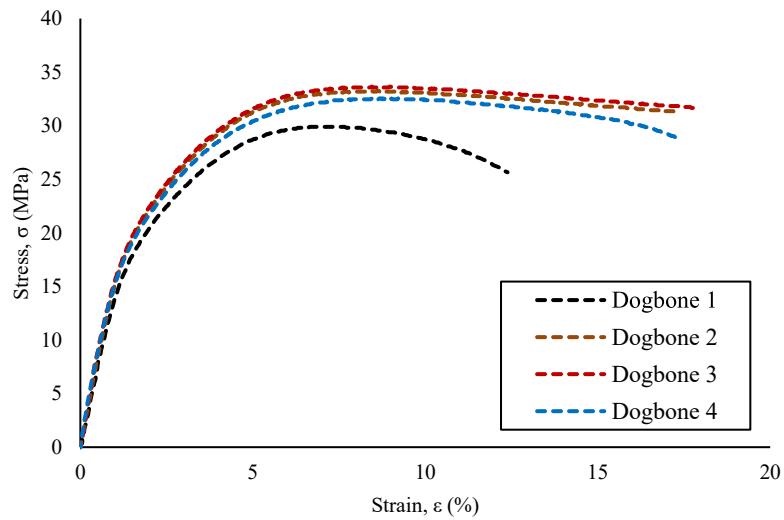
Figure 32. Stress-strain curve comparison of dogbone tensile experiments.

The measured parameters from dogbone tests 2 to 4 are listed in Table 15. The reported uncertainty was the standard deviation. There was high repeatability for the yield stress and yield strain measurements, showing only ± 0.6 MPa (± 2% of mean) and ± 0.07% elongation (± 1% of mean) uncertainty respectively. The uncertainty of the elastic modulus measurement was ± 0.13 GPa (± 7% of mean). It was significantly greater than the yield stress and strain measurements because it measures the slope of the two and their associated errors accumulate in the modulus measurement. It also takes measurements at low strain regions, which are prone to higher uncertainty as it is more difficult for any measurement system to detect small changes in length compared to large ones.

Table 15. Resultant measured parameters of dogbone tensile experiments.

Characteristics	Dogbone 2	Dogbone 3	Dogbone 4	Average
Area (mm^2)	32.63	32.69	30.92	-
Max load (N)	1091.4	1102.8	1019.9	-
Yield stress (MPa)	33.3	33.7	32.5	33.2 ± 0.6
Yield strain (%)	8.46	8.47	8.58	8.50 ± 0.07
Elastic modulus (GPa)	1.67	1.90	1.88	1.82 ± 0.13

The average of the results was compared to the manufacturer's specifications and the numerical simulation in Table 16. The manufacturer's values provided were a minimum, and the experimental results for all parameters were greater than the provided values. The measured yield stress was greater by 1.2 MPa (4%), the yield strain was greater by 0.5% elongation (6%), and the elastic modulus was greater by 4.2 GPa (30%). The results from both the numerical and experimental simulations show overall agreement between with the expected values. However, the measured modulus of elasticity was significantly higher than expected. This may not be an erroneous measurement, as the manufacturer's specifications were given as minimums.

Table 16. Comparison of analysis methods for dogbone tensile testing.

Characteristics	Expected	Numerical	Experimental
Yield stress (MPa)	32	32.0	33.2 ± 0.6
Yield strain (%)	8	7.98	8.50 ± 0.07
Elastic modulus (GPa)	1.4	-	1.82 ± 0.13

3.3.4 Uncertainty analysis

In order to understand the potential sources of measurement error, the components of the measurement system in the experiment were assessed. For the preliminary studies, the specimens were measured with a digital caliper (58-6800-4, Mastercraft) that had a reported accuracy of 0.02 mm and a resolution of 0.01 mm, resulting in a total estimated uncertainty of 0.025 mm. The estimations for the uncertainties of the MABTA (force) and the imaging system (displacement) are detailed in Section 3.2.3. The specimens of this experiment are assumed to satisfy plane stress conditions. Thus, the in-plane uncertainty would be more appropriate than the out-of-plane. The in-plane measurements were not taken and were instead estimated as one quarter of the out-of-plane uncertainty.

The stress was calculated using the measured force and area as shown by Equation (7). As the width and thickness were an average of five measurements along the testing length, the uncertainty for each measurement was the maximum difference to the mean measurement plus the accuracy of the caliper. The uncertainty for the area measurement was calculated as shown in Equation (8),

$$\frac{U_A}{A} = \sqrt{\left(\frac{U_w}{w}\right)^2 + \left(\frac{U_t}{t}\right)^2} \tag{8}$$

which then allowed the uncertainty of the stress measurement to be calculated as in Equation (9),

$$\frac{U_\sigma}{\sigma} = \sqrt{\left(\frac{U_F}{F}\right)^2 + \left(\frac{U_A}{A}\right)^2} \tag{9}$$

where the uncertainty in the force measurement was estimated as described in Section 3.2.3. The yield stress measurement uncertainty of the system is summarized in Table 17. The estimated yield stress uncertainty was relatively small and consistent across each test, the largest being $\pm$ 0.7 MPa ($\pm$ 2.3%). The area measurement was the more significant contributor to the uncertainty. Improvements to the yield stress measurements can be made by implementing a more accurate geometric measurement tool.

Table 17. Estimates for uncertainties of yield stress measurement and measured components of yield stress, showing the uncertainty as the absolute value and as the relative value in parenthesis.

Uncertainty	Dogbone 2	Dogbone 3	Dogbone 4
Yield stress (MPa)	**33.3 ± 0.6 (1.7%)**	**33.7 ± 0.6 (1.9%)**	**32.5 ± 0.7 (2.3%)**
Force (N)	1087 ± 14 (1.2%)	1100 ± 17 (1.2%)	1006 ± 13 (1.2%)
Area (mm²)	32.6 ± 0.4 (1.2%)	32.7 ± 0.5 (1.5%)	30.9 ± 0.6 (1.9%)
Width (mm)	*6.61 ± 0.04 (0.6%)*	*6.62 ± 0.04 (0.5%)*	*6.36 ± 0.08 (1.3%)*
Thickness (mm)	*4.93 ± 0.05 (1.0%)*	*4.94 ± 0.07 (1.4%)*	*4.96 ± 0.07 (1.5%)*

The strain was measured by the imaging system as a change in length. The change in length was equal to the sum of the displacements of the endpoints. This can be expressed by Equation (10),

$$\varepsilon = \frac{\Delta L}{L_0} = \frac{x_1 + x_2}{L_0} \qquad (10)$$

where:

ε is the strain,
ΔL is the change in length,
x_1 is the displacement of one endpoint, and
x_2 is the displacement of the other endpoint.

The strain uncertainty estimation can be simplified as shown below,

$$\frac{U_\varepsilon}{\varepsilon} = \sqrt{\left(\frac{U_{\Delta L}}{\Delta L}\right)^2 + \left(\frac{U_{L_0}}{L_0}\right)^2}$$

$$\frac{U_\varepsilon}{\varepsilon} = \sqrt{\left(\frac{\sqrt{U_{x_1}^2 + U_{x_2}^2}}{L_1 - L_0}\right)^2 + \left(\frac{U_{L_0}}{L_0}\right)^2}$$

and with $U_{x_1} = U_{x_2} = U_x$,

$$\frac{U_\varepsilon}{\varepsilon} = \sqrt{\left(\frac{\sqrt{2U_x^2}}{L_1 - L_0}\right)^2 + \left(\frac{U_L}{L_0}\right)^2}$$

$$\frac{U_\varepsilon}{\varepsilon} = \sqrt{\frac{2U_x{}^2}{(L_1 - L_0)^2} + \frac{U_L{}^2}{L_0{}^2}}$$

$$\frac{U_\varepsilon}{\varepsilon} = \sqrt{\frac{2U_x{}^2}{(L_1 - L_0)^2} + \frac{U_L{}^2}{L_0{}^2}}$$

$$U_\varepsilon = \frac{\cancel{L_1 - L_0}}{L_0} \times \frac{1}{L_0\cancel{(L_1 - L_0)}} \sqrt{2U_x{}^2(L_0{}^2) + U_L{}^2(L_1 - L_0)^2}$$

and for engineering strain, $L_1 \approx L_0$, so $L_0{}^2 \gg (L_1 - L_0)^2$,

$$U_\varepsilon = \frac{1}{L_0{}^2} \times \sqrt{2U_x{}^2(L_0{}^2) + \cancel{U_L{}^2(L_1 - L_0)^2}}$$

which results in the final simplification shown in Equation (11),

$$U_\varepsilon = \frac{\sqrt{2}U_x}{L_0} \tag{11}$$

Testing on dogbones 2 and 3 were conducted prior to the improved image synchronization. Thus, the images within each pair were not exactly matched with one another. The delay between the images was estimated to be 0.1 s. The displacement rate of each point marking the ends of the gage length was not the same as the loading rate. Realistically, both gage ends are moving at different rates of unknown magnitudes in the same direction, as shown in Figure 33 (a). The simplified model shown in Figure 33 (b) was assumed to be a reasonable approximation that can be consistently applied to all experiments. Thus, the point displacement of each gage length end was estimated as half the loading rate. For a loading rate of 0.1 mm/s, and a delay between an image pair of 0.1 s the displacement uncertainty due to asynchronization was estimated as 0.005 mm.
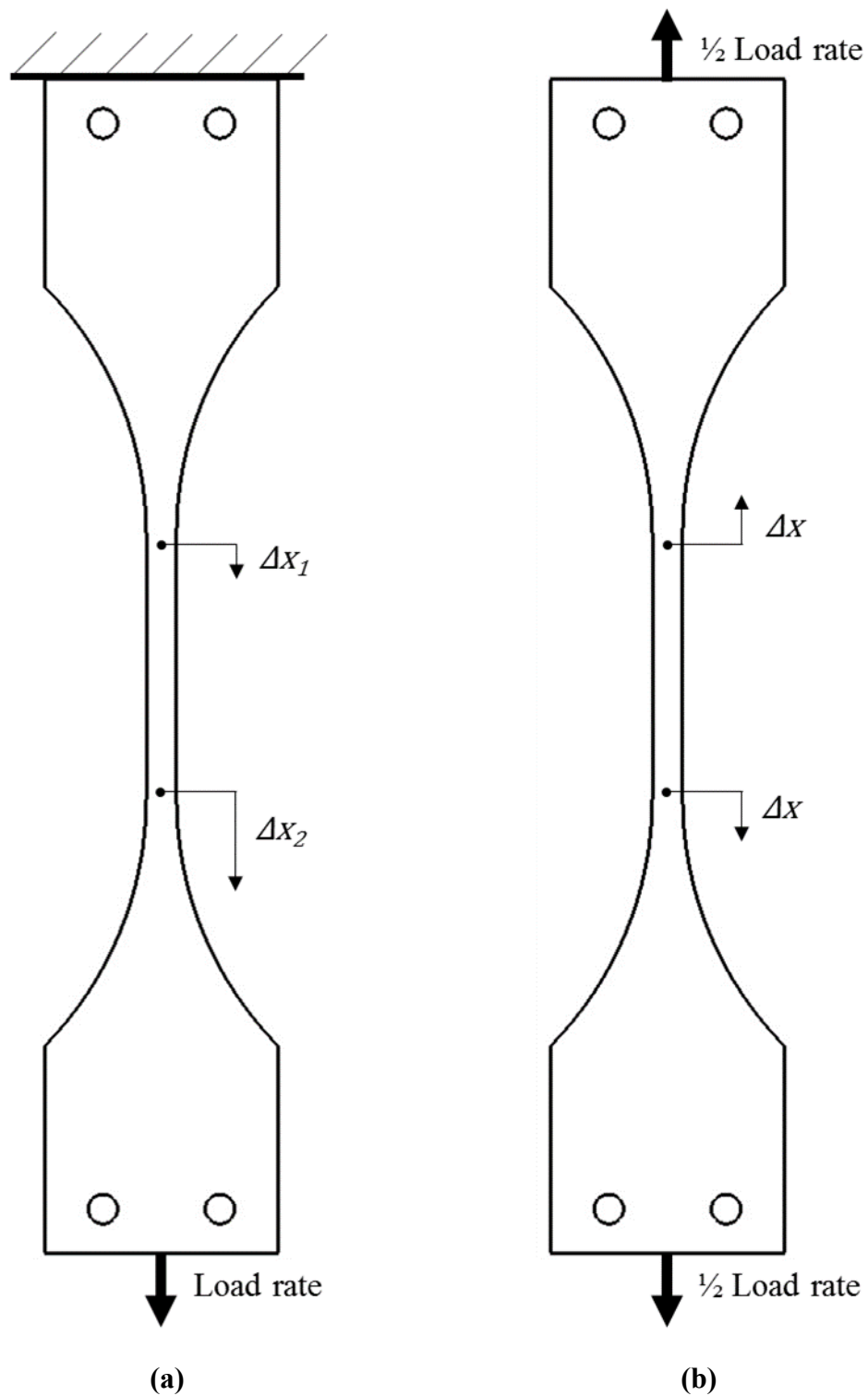
Figure 33. Comparison of **(a)** realistic displacement of gage length end points and **(b)** simplified model assumed in uncertainty calculations.

The uncertainties involving the yield strain measurement were estimated and compared between each of the experiments as shown in Table 18. For all tests, the estimated uncertainties of the measurements were very small, the largest being ± 0.03% strain (± 0.3% relative uncertainty). As previously mentioned, only dogbone 4 was tested with the improved synchronized imaging method detailed in Section 3.2.2. Dogbone 4 was determined to have the lowest estimated yield strain uncertainty in part due to the image synchronization. However, the improvement in relative uncertainty was minute regarding the yield strain. The out-or-plane uncertainty from the rigid body motion analysis proved to be a larger factor. Improvements in speckle pattern quality for dogbone 3 would result in higher measurement quality.

Table 18. Estimates for uncertainties of yield strain measurement and measured components of yield strain, showing the uncertainty as the absolute value and as the relative value in parenthesis.

Uncertainty	Dogbone 2	Dogbone 3	Dogbone 4
Yield strain (% strain)	**8.46 ± 0.01 (0.1%)**	**8.47 ± 0.03 (0.3%)**	**8.58 ± 0.01 (0.1%)**
Length (mm)	63.24 ± 0.02 (0.04%)	60.58 ± 0.06 (0.10%)	62.24 ± 0.01 (0.02%)
Synchronization (mm)	*± 0.005 (0.01%)*	*± 0.005 (0.02%)*	-
In-plane (mm)	*± 0.003 (0.005%)*	*± 0.009 (0.015%)*	*± 0.002 (0.003%)*

For the measurement of the elastic modulus in the dogbone tensile tests, the slope of the stress-strain curve between 0.05% strain and 0.25% strain was used. This can be expressed by Equation (12),

$$E = \frac{\Delta\sigma}{\Delta\varepsilon} = \frac{\sigma_{0.25\%} - \sigma_{0.05\%}}{\varepsilon_{0.25\%} - \varepsilon_{0.05\%}} \tag{12}$$

The uncertainty estimate for the modulus of elasticity measurement then can be represented by Equation (13),

$$\frac{U_E}{E} = \sqrt{\left(\frac{U_{\Delta\sigma}}{\Delta\sigma}\right)^2 + \left(\frac{U_{\Delta\varepsilon}}{\Delta\varepsilon}\right)^2} \tag{13}$$

For the force difference uncertainty measurement, the approximation can be expressed by Equation (14),

$$\frac{U_{\Delta\sigma}}{\Delta\sigma} = \frac{\sqrt{U_{\sigma_{0.25\%}}^2 + U_{\sigma_{0.05\%}}^2}}{\sigma_{0.25\%} - \sigma_{0.05\%}} \tag{14}$$

The stress values at 0.25% and 0.05% strain are known, and the uncertainties of those stress measurements can be calculated using Equation (9) as previously described. Upon closer examination of the strain measurement uncertainty, Equation (11) had previously shown that the strain measurement uncertainty is dependent on the length measurement uncertainty and the original length of the gage area, both of which are constant. This allows the strain measurement to be simplified as follows,

$$\frac{U_{\Delta\varepsilon}}{\Delta\varepsilon} = \frac{\sqrt{U_{\varepsilon_{0.25\%}}^2 + U_{\varepsilon_{0.05\%}}^2}}{\varepsilon_{0.25\%} - \varepsilon_{0.05\%}}$$

$$\frac{U_{\Delta\varepsilon}}{\Delta\varepsilon} = \frac{\sqrt{2U_\varepsilon^2}}{0.25\% - 0.05\%}$$

finally leading to the uncertainty estimation given by Equation (15),

$$\frac{U_{\Delta\varepsilon}}{\Delta\varepsilon} = \frac{\sqrt{2}U_\varepsilon}{0.2\%} \tag{15}$$

where the values for U_ε for each experiment are the same as those previously calculated and listed in Table 18.

Using the previously derived uncertainty estimation equations, the uncertainties for the elastic modulus measurements were calculated and listed in Table 19. In general, the relative uncertainty in the elastic modulus measurements was greater than the relative uncertainty of the yield stress and yield strain measurements. The calculations show that the largest contributor to the elastic modulus measurement uncertainty was the strain measurement, as expected. This is because the absolute uncertainty of the strain measurement is constant, causing the relative uncertainty to be much greater at low strain measurements. The yield strain measurement was at $8.50 \pm 0.07\%$ strain, whereas the strain measurements for the elastic modulus were up to two orders of magnitude less than that:

0.05% and 0.25% strain. This means that even miniscule reductions to the absolute uncertainty of the strain measurement can have significant impact on the elastic modulus measurements. Measuring at higher strain values would also improve the modulus measurements, though is not permitted as per the standard for the polypropylene material used in this experiment. Thus, to increase the quality of the elastic modulus measurements, improvements to the strain measurements should be prioritized.

Table 19. Estimates for uncertainties of elastic modulus measurement and measured components of elastic modulus, showing the uncertainty as the absolute value and as the relative value in parenthesis.

Uncertainty	Dogbone 2	Dogbone 3	Dogbone 4
Elastic modulus (GPa)	**1.67 ± 0.15 (9.0%)**	**1.90 ± 0.37 (19.7%)**	**1.89 ± 0.07 (3.6%)**
ΔStress (MPa)	**3.41 ± 0.07 (1.9%)**	**3.84 ± 0.07 (1.7%)**	**3.78 ± 0.07 (1.8%)**
at 0.05% strain (MPa)	*0.79 ± 0.05 (5.8%)*	*0.61 ± 0.05 (1.0%)*	*1.11 ± 0.05 (4.4%)*
Force (N)	25.7 ± 1.5 (5.8%)	19.9 ± 1.5 (1.0%)	34.2 ± 1.5 (4.4%)
Area (mm^2)	32.6 ± 0.04 (0.1%)	32.7 ± 0.03 (0.1%)	30.9 ± 0.08 (0.3%)
at 0.25% strain (MPa)	*4.19 ± 0.05 (1.1%)*	*4.45 ± 0.05 (7.5%)*	*4.89 ± 0.05 (1.0%)*
Force (N)	136.8 ± 1.5 (1.1%)	145.3 ± 1.5 (7.5%)	151.1 ± 1.5 (1.0%)
Area (mm^2)	32.6 ± 0.04 (0.1%)	32.7 ± 0.03 (0.1%)	1.11 ± 0.08 (0.3%)
ΔStrain (% strain)	**0.20 ± 0.02 (8.8%)**	**0.20 ± 0.06 (19.6%)**	**0.20 ± 0.01 (3.1%)**
at 0.05% strain	*0.05 ± 0.01 (24.9%)*	*0.05 ± 0.03 (55.4%)*	*0.05 ± 0.01 (8.7%)*
at 0.25% strain	*0.25 ± 0.01 (5.0%)*	*0.25 ± 0.03 (11.1%)*	*0.25 ± 0.01 (1.7%)*

The overall measurement uncertainty of the imaging system can be improved for better elastic modulus measurements. Implementing higher quality speckle patterns is one approach towards this goal. In this study, dogbone 3 had the worst speckle pattern and the greatest out-of-plane displacement uncertainty. The in-plane displacement uncertainty for dogbone 3 was 0.012 mm compared to 0.002 mm for dogbone 4. As a result, the relative uncertainty of the elastic modulus measurement for dogbone 3 was 16.1% greater than that of dogbone 4, demonstrating the impact of speckle pattern quality on small strain measurements.

To a lesser but nonetheless significant extent, better image synchronization can improve the quality of the elastic modulus measurement. In the yield strain measurement, the measurement uncertainty for dogbone 4 was only 0.1% less than that of dogbone 2, as

listed in Table 18. But for the elastic modulus, the measurement uncertainty for dogbone 4 was 5.4% less than that of dogbone 2. If the same amount of asynchronization was assumed for dogbone 4 as the others in the uncertainty approximation, the relative uncertainty estimate would have increased by 3.6% (from 3.6% to 7.2%). If image synchronization happens to be unavailable for an experiment, the error in asynchronization within an image pair can be reduced by decreasing the load rate of the system. This would reduce the amount of displacement between images in a set. However, the reduced load rate must still ensure failure of the test specimen within the given time frame specified by standards. It was for this reason that the upgrade was implemented in the first place and is recommended for experiments using a DIC system.

Increasing the image magnification of the DIC system in the experiment is another potential improvement to the measurements. This can be achieved simply by moving the cameras closer to the subject. By doing so, the speckle parameters can be adjusted and optimized in the images without needing to physically modify them on the specimens. Also, DIC operates by observing displacements in the image space, then converting the pixel displacements to physical displacements. Assuming that the image scale is the only parameter that changes in the DIC system, the pixel displacement uncertainty would remain the same. By increasing the magnification, and thus increasing the image scale (*i.e.*, the pixel-to-mm ratio), a lower physical displacement uncertainty is attained for the same pixel displacement uncertainty.

However, there are inherent constraints associated with changing the system magnification. In this test, the material was plastic and needed to be loaded to failure. This means that the entire gage length must be in the field of view of the cameras for the duration of the test, limiting the amount of magnification. Reducing the length of the specimen to accommodate an increase in magnification has a negative impact. The amount of magnification and the length of the testing region must be balanced. The approach of this study was to create speckle patterns with an average speckle diameter between 3-5 pixels at the maximum magnification that allowed for the entire gage region to be viewed for the duration of the experiment. However, controlling the speckle creation process can be difficult as evidenced by the undersized speckles on dogbone 3 that generated much lower quality results.

3.3.5 Summary

A set of dogbone tensile tests were conducted with the designed DIC system as a first step and initial assessment of the experimental design and the methods of the numerical simulation. A numerical simulation of the experimental conditions was performed prior to the experiment. Then, a set of experiments were performed, from which data was collected and used to calculate the measured yield stress, yield strain, and elastic modulus of a polypropylene dogbone specimen. The experimental results were compared with the material specifications and the results of the numerical simulation, and reasonable agreement was shown amongst the three. The experimental results were greater than the numerical simulation and the manufacturer's specifications. But because the specifications were provided as minimum values, the small deviations of the experiment results were deemed acceptable.

An uncertainty analysis was conducted on the experiment to assess potential areas of improvement. The uncertainty in the yield stress measurements was quite low and comparable to the experiment results. Minor improvements can be made by using more precise tools to measure the geometry of the test specimen. For the yield strain measurements, the uncertainty was also quite low and in agreement with the experiment results. The quality of these measurements was solely dependent on the DIC system; improving the quality of the speckle pattern or image synchronization can produce better results. However, the most critical area for improvement was revealed by the high uncertainty in the elastic modulus results. The experimental setup showed difficulties in measuring at very low strains. And because the elastic modulus needed to be measured at extremely small strains, there was high uncertainty associated with the elastic modulus measurements. For this reason, minimizing the uncertainty in strain measurements was deemed crucial. The newly implemented image synchronization method was demonstrated to be a significant improvement. The speckle pattern quality was also shown to have significant effects on the quality of measurements at low strains.

The performance of the experimental design under simple conditions was validated and its areas of weakness were thoroughly assessed. The next step was to increase the complexity of the system and evaluate the numerical and experimental methods under more demanding conditions.

3.4 Single-edge notched tension testing

The second set of experiments were single-edge notched tension (SENT) tests. The purpose of these tests was to assess the experimental system in its capacity to measure crack opening. The general setup of this experiment is shown in Figure 34.
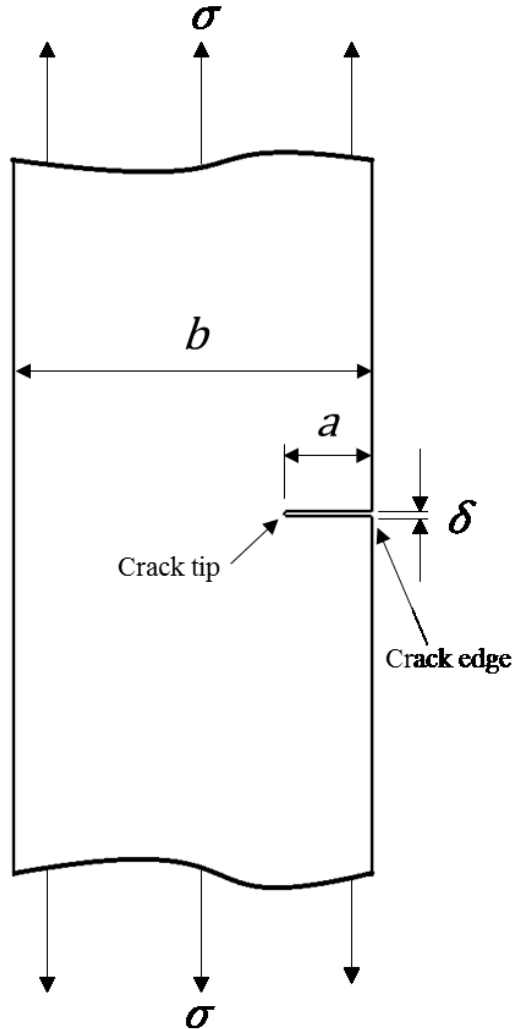
Figure 34. General setup for SENT experiment.

As with the dogbone tensile testing, the theoretical, numerical, and experimental analyses were validated against one another in this study. The same commercial numerical simulation software and polypropylene material were used as with the dogbone experiment. The main parameters of interest were the crack edge opening, δ, and the crack

tip strain, ε_{tip}. The expected value of the crack edge opening can be calculated using Tada's formula [147],

$$\delta = \frac{4\sigma a}{E'} V_1 \left({a}/{b} \right) \tag{16}$$

where $V_1 \left({a}/{b} \right)$ is represented by the empirical formula,

$$V_1 \left({a}/{b} \right) = \frac{1.46 + 3.42 \left(1 - \cos\frac{\pi a}{2b} \right)}{\left(\cos\frac{\pi a}{2b} \right)^2}$$

where:
   a is the crack length,
   b is the width of the specimen,
   σ is the tensile load on the specimen, and
   E' is the elastic constant (equal to E for plane strain).

The expected value of the crack tip strain can be calculated using the stress intensity factor (SIF) approach, which operates under the linear-elastic assumption. It is represented as,

$$\sigma_{xx} = \sigma_{yy} = \sigma_{tip} = \frac{K_I}{\sqrt{2\pi r}}$$

and converting to strain,

$$\varepsilon_{tip} = \frac{K_I}{E\sqrt{2\pi r}} \tag{17}$$

where the r is the distance along the crack center away from the crack tip, K_I is the SIF represented as,

$$K_I = \sigma\sqrt{\pi a}\, F \left({a}/{b} \right)$$

and $F \left({a}/{b} \right)$ is represented by the empirical formula by Tada [147],

$$F \left({a}/{b} \right) = \sqrt{\frac{2b}{\pi a} \tan\frac{\pi a}{2b}} \cdot \frac{0.752 + 2.02 + 0.37 \left(1 - \sin\frac{\pi a}{2b} \right)^3}{\left(\cos\frac{\pi a}{2b} \right)^2}$$

3.4.1 Experimental setup

The experimental setup for the SENT test was the same as with the dogbone tensile test shown in Figure 27, but with the SENT specimen in place of the dogbone (refer to Appendix F for engineering drawings). The geometrical measurements of the SENT specimens are listed in Table 23. The edge-crack was manufactured using the University of Alberta mechanical engineering department's waterjet cutter; the width of the crack was equal to the waterjet cutter kerf of 0.015" (or 0.381 mm). The width and thickness of each specimen were measured using the same approach as the previous experiment.

The DIC system geometry was also the same as the dogbone experiment (Table 12); the camera stereo angle was about ± 25° and the Scheimpflug angle was set to 4° for both cameras. The first two tests were conducted prior to the hardware triggering implementation at a standoff distance of about 550 mm. Tests 3 and 4 were conducted with hardware triggering at a standoff distance of about 650 mm. A white speckle pattern on a flat black coat was applied to each specimen, as shown in comparison to one another in Figure 35. The same commercial image correlation software was used in this experiment as the dogbone testing. The shape function it uses is an affine transformation and the images were processed with 23-pixel subsets at 11-pixel steps. A sliding minimum subtraction was used to pre-process the images to enhance the correlation.

Rigid body out-of-plane displacement was performed to quantify the DIC system uncertainty, and morphological analysis was used to study and characterize the speckle patterns of each specimen as shown in Figure 35 and listed in Table 20. SENT 2 was measured to have the least speckle size variation and, as expected resulted in the lowest pixel uncertainty. However, all the measured uncertainties were relatively low, and none deviated from the rest significantly. All speckle patterns created in this set of tests were relatively similar, hence the minor differences in measurement uncertainty.

| SENT 1 | SENT 2 | SENT 3 | SENT 4 |
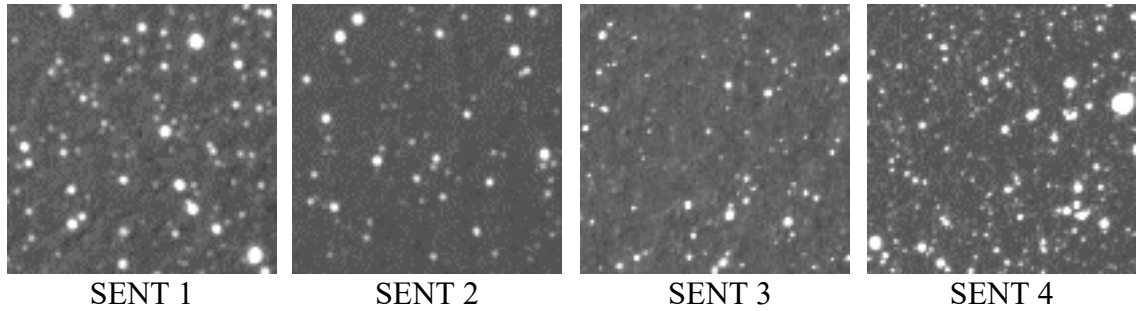
Figure 35. Comparison of SENT speckle patterns used in morphological analysis for uncertainty quantification.

Table 20. Morphological and uncertainty analysis of SENT speckle patterns.

Characteristics	SENT 1	SENT 2	SENT 3	SENT 4
Subset size	21	21	21	21
Density (speckles per subset)	2.33	2.39	1.96	2.52
Diameter (pixels)	2.70	2.73	2.68	2.67
Variation (IQR as % of mean)	38.2	26.7	38.5	38.6
Uncertainty (mm)	0.0060	0.0053	0.0051	0.0052
Scale (pixel/mm)	18.94	18.94	24.97	24.90
Uncertainty (pixels)	**0.113**	**0.101**	**0.127**	**0.130**

The SENT specimens were loaded at 0.05 mm/s to a maximum load of 2000 N. Strains and deformations on the specimen surface were measured by the cameras in the DIC system. These measurements were then used to calculate the crack edge opening that occurred during the experiment, as well as the strain at a distance, r, from the crack tip. The forces measured by the load cell were not used in the calculations. This is because the grip holes were predicted and observed to undergo significant stresses, failing before the crack. Therefore, they would not represent the tensile load applied to the crack region. Instead, the strain measured by the DIC system on the specimen was used to represent the general loading on the specimen. For the crack edge opening, Equation (16) can be modified as follows,

$$\delta = \frac{4\sigma a}{E'} V_1 \left(a/b \right)$$

and with $E' = E$ for the plane strain case,

$$\delta = 4\varepsilon a \cdot V_1\left(\frac{a}{b}\right)$$

where ε is the strain measured at a region representing the tensile load on the crack edge. This can be any region far enough away from the crack with a uniform strain across the width of the specimen to mimic the SENT conditions portrayed in Figure 34. The experimental measurements of crack edge displacement, δ, can be plotted as a function of the strain from loading, ε, with the slope yielding the measurement of the crack edge opening constant, $V_1\left(\frac{a}{b}\right)$, to be compared with the expected empirical value from literature. This is represented by Equation (18),

$$V_1\left(\frac{a}{b}\right) = \frac{\Delta\delta}{\Delta\varepsilon} \cdot \frac{1}{4a} \tag{18}$$

The same procedure can be applied to the crack tip strain by manipulating Equation (17),

$$\varepsilon_{tip} = \frac{K_I}{E\sqrt{2\pi r}}$$

$$\varepsilon_{tip} = \frac{\sigma\sqrt{\pi a}\, F\left(\frac{a}{b}\right)}{E\sqrt{2\pi r}}$$

and then reducing to,

$$\varepsilon_{tip} = \varepsilon\sqrt{\frac{a}{2r}} F\left(\frac{a}{b}\right)$$

The measured crack tip strain, ε_{tip}, can be plotted against the loading strain, ε, to attain the slope and extract the experimental value for the SIF constant, $F\left(\frac{a}{b}\right)$, with the value from literature. This is represented by Equation (19),

$$F\left(\frac{a}{b}\right) = \frac{\Delta\varepsilon_{tip}}{\Delta\varepsilon}\sqrt{\frac{2r}{a}} \tag{19}$$

A distance from the crack tip, *r*, of approximately 10% of the crack length was chosen for measurements. This is because the further from the crack tip, the more deviation occurs with the SIF approach [148]. However, regions too close to the crack tip were found to be heavily influenced by image noise from the crack itself. This can be caused by the crack itself registering as background (black) or the black paint shedding from plastic deformation at the crack tip and introducing white to the image. The exact distance was dictated by the strain scalar measurement closest to the desired location. Two MATLAB scripts were written and used; one for measuring crack edge displacements (see Appendix G) and the other for extracting strain measurements at the desired proximity from the crack tip (see Appendix H).

3.4.2 Numerical simulation

The SENT test numerical simulation was setup using the solver settings listed in Table 21. The boundary conditions and are shown in Figure 36. As with the test in Section 3.3.1, a non-linear model was implemented with polypropylene as the material. The upper holes were treated as fixed hinges and the lower set of holes were displaced downwards at a rate of 0.05 mm/s, same as in the experiment. The numerical simulation software generated the mesh, with the parameters listed in Table 22. Mesh independence was verified, as shown in Figure 37, using the mesh refinement approach.

Table 21. Summary of solver settings for SENT numerical simulations.

Attribute	Value
Specimen	SENT
Mechanics	Nonlinear static
Boundary conditions	Upper bolt holes: fixed hinge
Loading conditions	Lower bolt holes: displacement-based, 0.05 mm/s downwards
Software	Solidworks Simulation 2017
Solver	Direct sparse solver (Implicit)
Algorithms	Newton-Raphson
Convergence criteria	0.1%
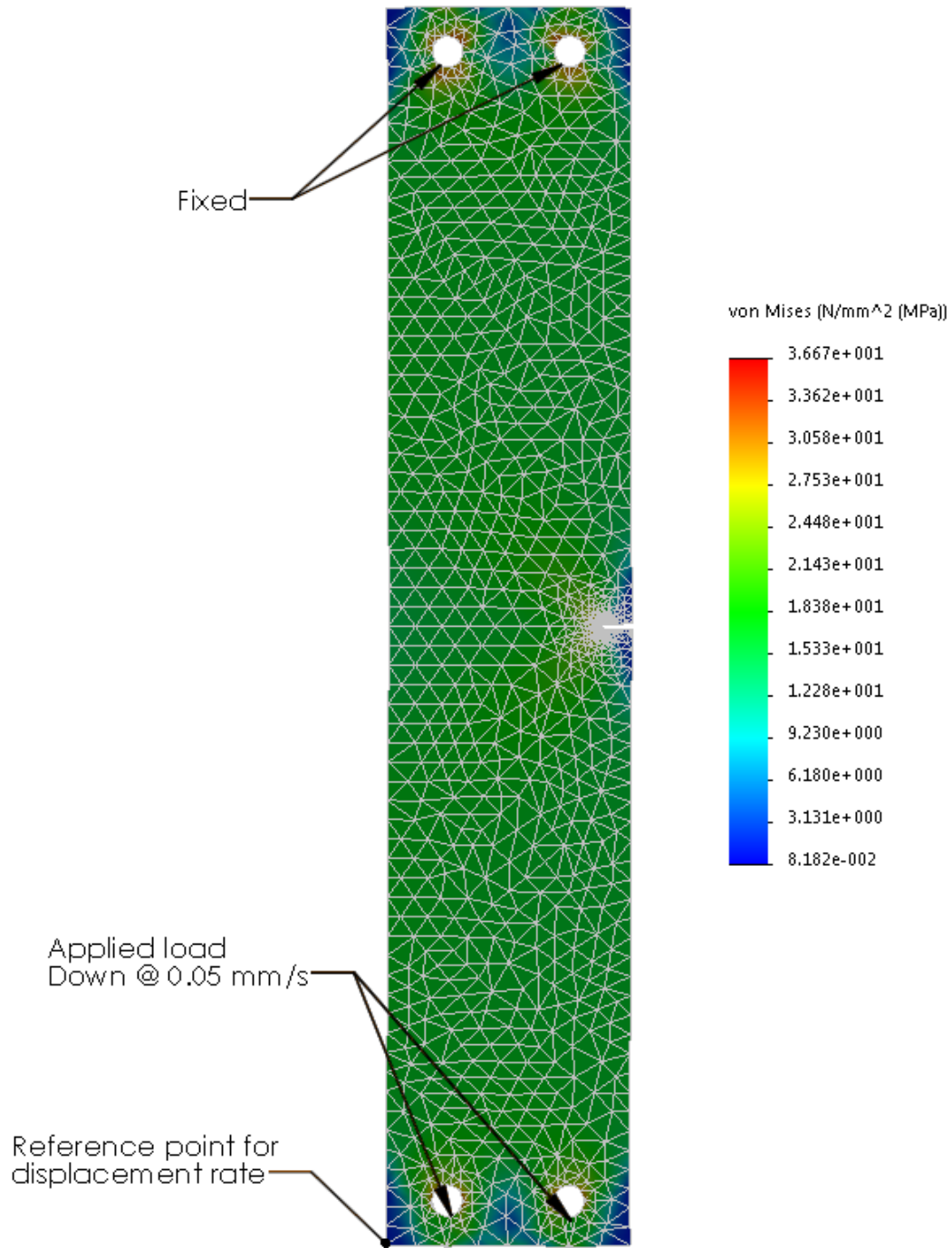
Figure 36. Numerical simulation setup for SENT test, showing final mesh, stress distribution, and boundary and loading conditions.

Table 22. SENT numerical simulation mesh settings and results per iteration.

Mesh	Iteration 1	Iteration 2	Iteration 3
Mesher	Curvature-based	Curvature-based	Curvature-based
Jacobian points	4	4	4
Mesh control	-	-	Bolt holes, crack
Max. element size (mm)	10	5	5
Min. element size (mm)	2	1	1
Number of nodes	5872	14407	36823
Number of elements	3031	7975	23255
Max. aspect ratio	16.017	14.481	5.971
Aspect ratio < 3 (%)	96.6	97.7	99.5
Aspect ratio < 10 (%)	0.396	0.15	0
Max Stress (MPa)	37.267	36.744	36.674
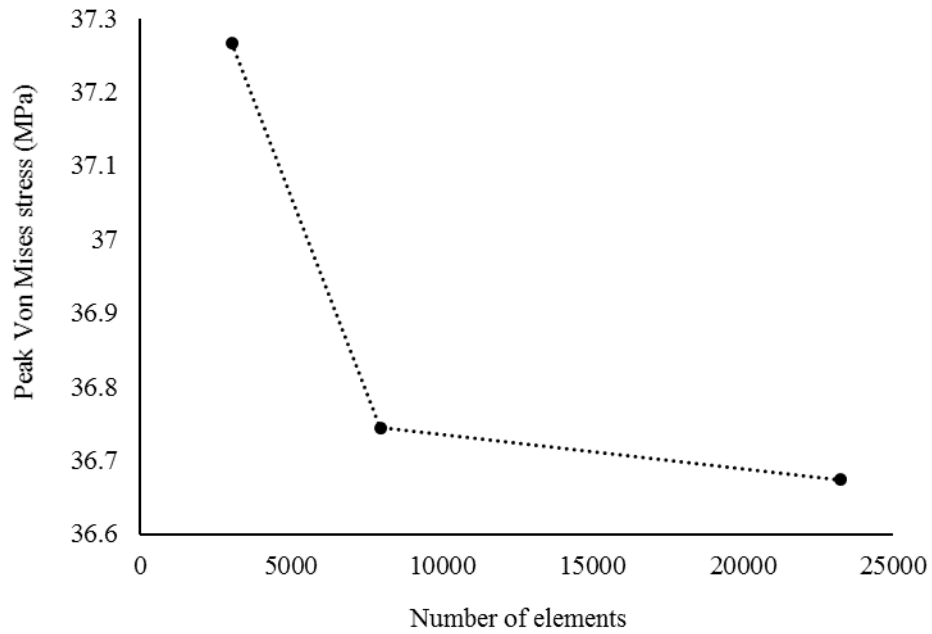
Figure 37. Mesh refinement on SENT numerical simulation, showing convergence of peak Von Mises stress.

3.4.3 Results and discussion

3.4.3.1 Crack edge opening

A comparison of the numerical simulation results with the theoretical analysis for crack edge opening is shown in Figure 38 (a) as the relative difference between the results as a function of the tensile load strain. As the numerical simulation analyzes higher tensile loads, the relative error escalates exponentially. At 0.5% strain from loading, the relative error remains below 5%. This is also the approximate point at which the numerical node at the crack tip exceeds the yield stress of the material, as shown in Figure 38 (b). The theoretical calculation using the SIF approach assumes a linear-elastic material, which the polypropylene material used is not. Before yielding occurs, at about 0.3% loading strain, the loading curve of the material can be approximated as linear elastic. Therefore, the numerical simulation was considered comparable to the theoretical analysis only up to 0.3% loading strain.
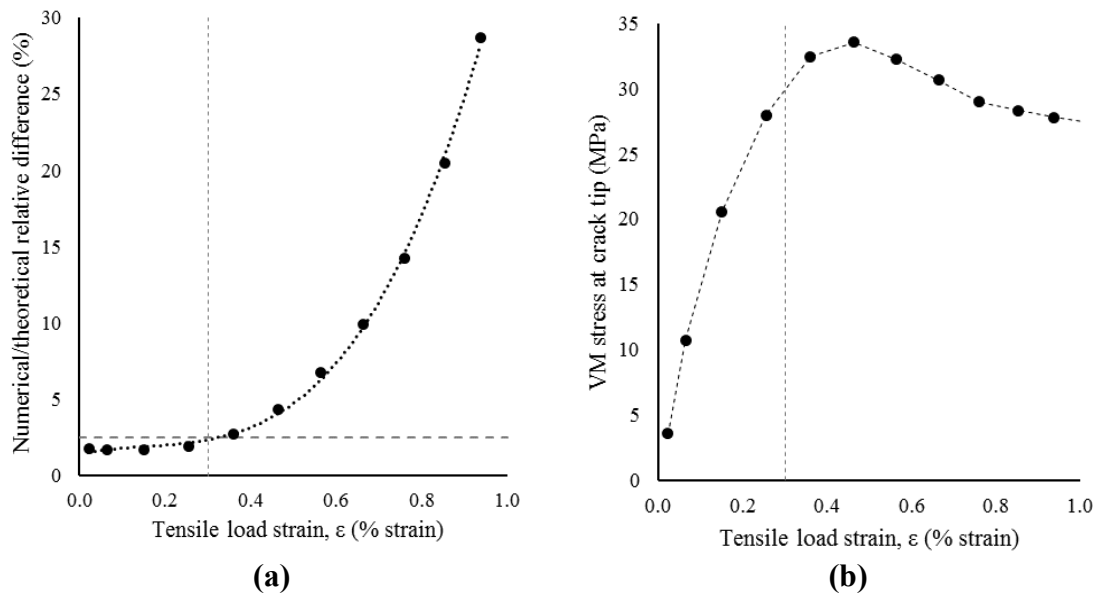
Figure 38. Numerical simulation results, showing **(a)** relative error compared to theoretical calculation (less than 5% at 0.50% tensile load strain), and **(b)** yielding at crack tip near 0.50% tensile load strain.

The numerical simulation value of the crack edge opening constant was acquired by from the plot shown in Figure 39. The graph represents Equation(16) (18) rearranged such that the slope represents the measured crack edge opening function, $V_1\left(a/b\right)$, which was equal to 1.63. This is in close agreement with the theoretical value of 1.59 for the given

geometry. Small discrepancies can be attributed to the material non-linearity of the region tested. The simulation values beyond 0.3% tensile load strain could not be compared to the theory as they are well into the non-linear region. They were instead compared with the experimental measurements.
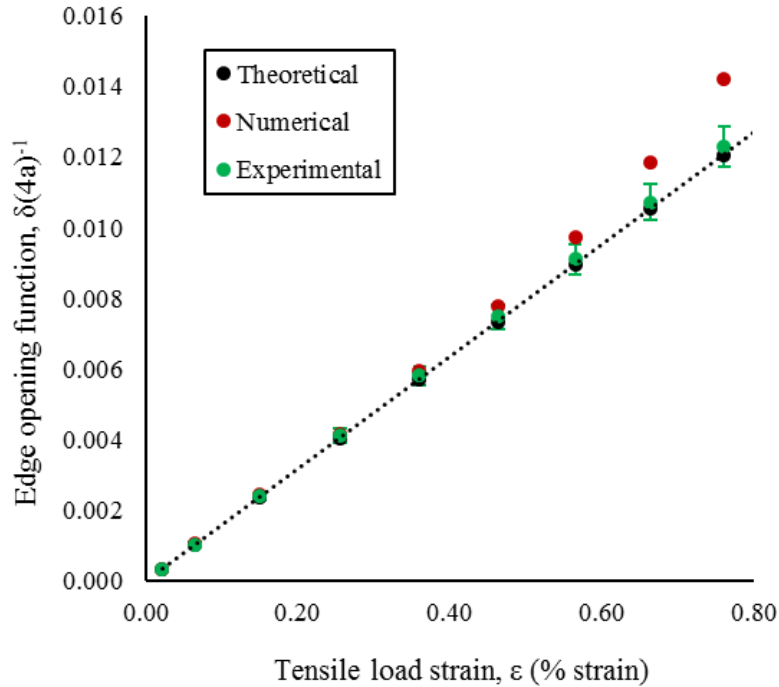
Figure 39. Edge opening-load strain curve for SENT numerical simulation.

The results from the experiment are listed in Table 23. The values for $V_1\left(^a/_b\right)$ for each test were acquired from the slope of the plot of shown in Figure 39. From the experiments, it was determined to be 1.62 ± 0.08. All experiments showed a high degree of linearity (as roughly characterized by the coefficient of determination, R^2). The discrepancy amongst the measurements is small but can be observed to follow trends in the geometry. SENT 1 was the widest and resulted in the largest crack edge opening constant. SENT 3 resulted in the lowest $V_1\left(^a/_b\right)$ value but was measured to be 0.2% larger than the smallest specimens. However, it was the thinnest specimen, which may have contributed to it having the lowest $V_1\left(^a/_b\right)$ value. This means that the plane-strain assumption may not be fully satisfied and variances in thickness may contribute to skew in results.

Table 23. Resultant crack edge measurements for SENT specimens.

Parameter	SENT 1	SENT 2	SENT 3	SENT 4	Average
Thickness (mm)	4.99	5.01	4.92	4.93	4.96 ± 0.04
Width, b (mm)	50.8	50.4	50.5	50.4	50.5 ± 0.2
Crack length, a (mm)	6.35	6.35	6.35	6.35	6.35 ± 0.025
$V_1\left(a/b\right)$	1.72	1.59	1.54	1.61	1.62 ± 0.08
Coeff. determination, R^2	0.999	0.998	0.999	0.999	-

The theoretical, numerical, and experimental results are compared in Table 24. There is overall strong agreement between the three values. The numerical and experimental results more strongly agree with each other than with the theoretical results. This is likely due to the non-linearity being accounted for in the numerical and experimental but not in the theoretical. However, the closeness indicates that the testing was indeed conducted in a fairly linear region. Another possible source of discrepancy is the lack of precracking of the specimen. Precracking was skipped as it requires fatigue loading at a slow rate over a long period of time which can prove time consuming [148].

Table 24. Comparison of analysis methods or crack edge opening for SENT testing.

Parameter	Theoretical	Numerical	Experimental
$V_1\left(a/b\right)$	1.59	1.63	1.62 ± 0.08

3.4.3.2 Crack tip strain

In the numerical simulation, the crack tip strain was observed at an element 0.82 mm from the crack tip. The calculated values of strain at this location were plotted as a function of the tensile load strain in Figure 40. As with the previous section analyzing the crack edge opening results, the simulation was considered valid only for the linear elastic region which was approximated to be up to 0.3% tensile load strain. The plot represents a rearranged version of Equation (19), where the slope represents the constant $F\left(a/b\right)$. It was calculated to be 1.14, which somewhat agrees with the theoretical value of 1.23. Crack tip measurements are extremely sensitive to location, such that any unaccounted for offset in either in-plane direction can significantly affect the measured value. In a finite element

model, this is likely to impact the solution as the measurements apply to an area rather than a point. As shown in Figure 41, the centroid of the observed element may not represent the measurement at that exact point as it must account for the rest of the area. An average measurement of the element may yield inaccuracies. A potential improvement in the approach would be to implement smaller elements in the numerical solver. But the results show that assessment of strain measurements around the crack tip using a SIF approach should be made with careful consideration.
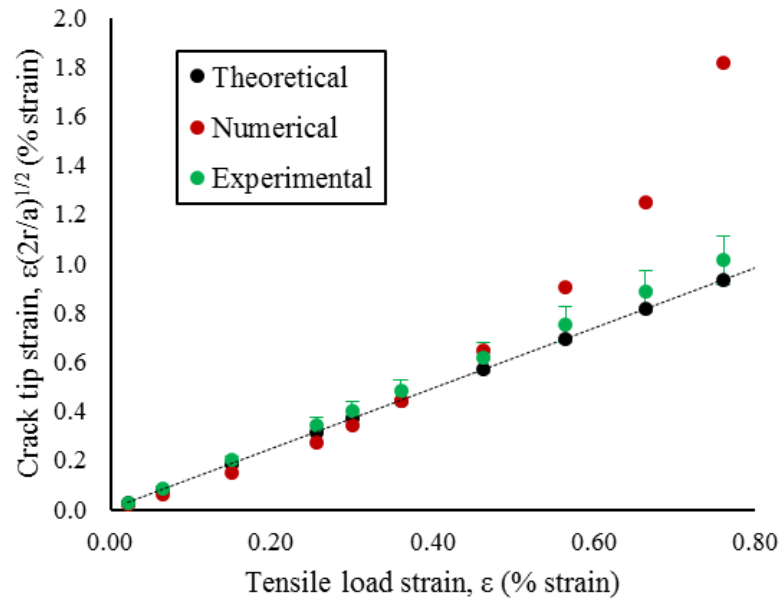
Figure 40. Crack tip-load strain curve for SENT numerical simulation.
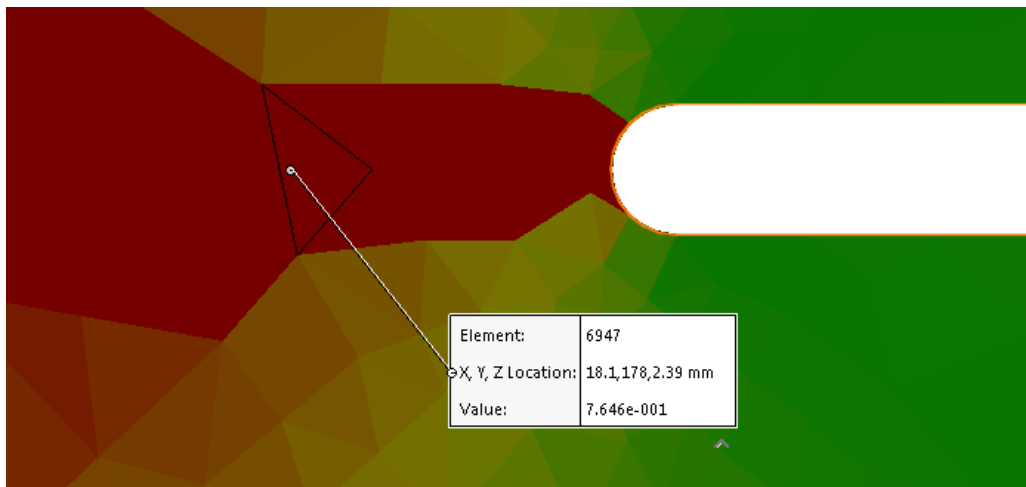
Figure 41. Crack tip strain numerical simulation, showing how element area can skew results.

For the experiment, the distances from the crack tip, r, were taken as the location of the strain measurement scalar respective to the crack tip. The image processing software calculates the strain measurement at a subset by using the difference between the displacement vectors of its immediate neighbors [149]. As Figure 42 shows, for measuring the strain in the y-direction, the y-displacement vectors for the subsets directly above and below are used to calculate ε_{yy} for the subset of interest. This means that the gage length of the strain measurement is effectively $2 \times$ the subset size.
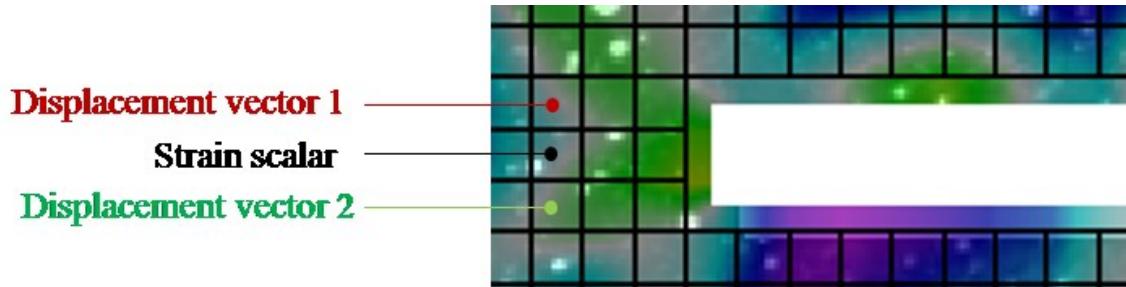
Figure 42. Calculation method for crack tip strain using image processing software.

Using the r and ε_{tip} values, $F\left(a/b\right)$ was measured by plotting the crack tip strain measurements as a function of the tensile load strain as shown in Figure 40 for each specimen. The crack tip strain measurements are listed in Table 25. The value of $F\left(a/b\right)$ was measured to be 1.33 ± 0.13, which is in agreement with the theoretical value of 1.23. All plots were very linear, as quantified by the R^2 value. The discrepancies in the distance from the crack tip of the measurement showed no effect on the agreement for each specimen. SENT 3 and 4 were closer to the expected value than 1 and 2. The difference between the pairs is that SENT 3 and 4 were conducted with the image synchronization method, whereas 1 and 2 used the previous asynchronistic software triggering. Like the crack edge opening measurement, stereo camera synchronization may have a significant effect on the strain measurement.

Table 25. Resultant crack tip strain measurements for SENT specimens.

Parameter	SENT 1	SENT 2	SENT 3	SENT 4	Average
Thickness (mm)	4.99	5.01	4.92	4.93	4.96 ± 0.04
Width, b (mm)	50.8	50.4	50.5	50.4	50.5 ± 0.2
Crack length, a (mm)	6.35	6.35	6.35	6.35	6.35 ± 0.025
Distance from tip, r (mm)	0.83	0.71	0.71	0.80	0.76 ± 0.06
$F\left(a/b\right)$	1.36	1.50	1.20	1.27	1.33 ± 0.13
Coeff. determination, R^2	0.990	0.984	0.995	0.994	-

Table 26 compares the theoretical, numerical, and experimental analysis of the crack tip strain for the SENT specimen testing. Compared to the crack edge opening results, there is more discrepancy between the values. This is likely due to the uncertainty in strain measurements being inherently greater than the displacement measurements used in the crack edge opening measurements. Another strong possibility for the source of disagreement is the material of the specimen. The SIF approach has been used for plastics with methods very similar to those used for metals [150]. However, because ductile non-linear plastics are rate-dependent in behavior, the validity of the method is not guaranteed for non-metals [148]. The method also does not apply to cases where yielding and non-linear viscoelasticity are present at relatively large distances from the crack tip [148]. This can explain why strain measurements too near the crack tip result in greater disagreement. Also, forgoing the precracking step may have been much more significant in the crack tip measurements than the crack edge measurements. But again, it was skipped as it would have been too time-consuming of a process for a preliminary study. For future tests, this aspect should be investigated more thoroughly.

Table 26. Comparison of analysis methods of crack tip strain for SENT testing.

Parameter	Theoretical	Numerical	Experimental
$F\left(a/b\right)$	1.23	1.14	1.33 ± 0.13

3.4.3.3 Non-linear analysis

The numerical and experimental results for an alternate SENT specimen were compared beyond the region of linear assumption. This sample is henceforth referred to as the thin SENT specimen (where b was only equal to about 19.5 mm) as the geometry was relatively thinner than the initial tests (where b was 50.5 mm). It was necessary to test a thinner specimen so that failure would occur at the crack instead of the grips. Firstly, the linear region (0% to 0.3% loading strain) was compared as before. The comparison of experimental results, numerical simulation results, and theoretical calculations is listed on Table 27. Agreement in the linear region with the theory would provide confidence for the assessment of the non-linear region for the numerical and experimental results. Strong agreement was shown with both crack edge opening and crack tip strain measurements, as the values for $V_1\left(a/b\right)$ and $F\left(a/b\right)$ are in close proximity with both theoretical and numerical values.

Table 27. Comparison of analysis methods for linear region of thin SENT testing.

Parameter	Theoretical	Numerical	Experimental
Thickness (mm)	*	*	4.90
Width, b (mm)	*	*	19.52
Crack length, a (mm)	*	*	6.35
$V_1\left(a/b\right)$	2.50	2.46	2.42
Crack tip distance, r (mm)	-	0.71	0.70
$F\left(a/b\right)$	1.75	1.75	1.78

*Same value as experimental.

Figure 43 shows the relative difference between the experiment measurements and numerical simulation in its entirety (linear and non-linear regions included) for both the crack edge and crack tip measurements. For each, the values for the relative differences were normalized respective to the measurement set. The crack tip set showed large relative deviation from the start, which is expected as comparatively small measurements are made. For both measurement comparison sets, the deviation decreases between the 0.2% to 0.8% region but reaches a peak at about 1% strain. This large discrepancy is due to the simulation not accounting for crack propagation and the associated energy release from the

phenomenon. Figure 44 shows this progression between the 0.8% and 1% loading strain region for thin SENT 2. The crack growth observed in the experiment did not occur in the simulation. Another potential contributing factor is the inability of the numerical simulation to account for the microstructural behavior of the fracture stress. Especially with more ductile materials, structural debonding can drastically affect the loading profile of a specimen.
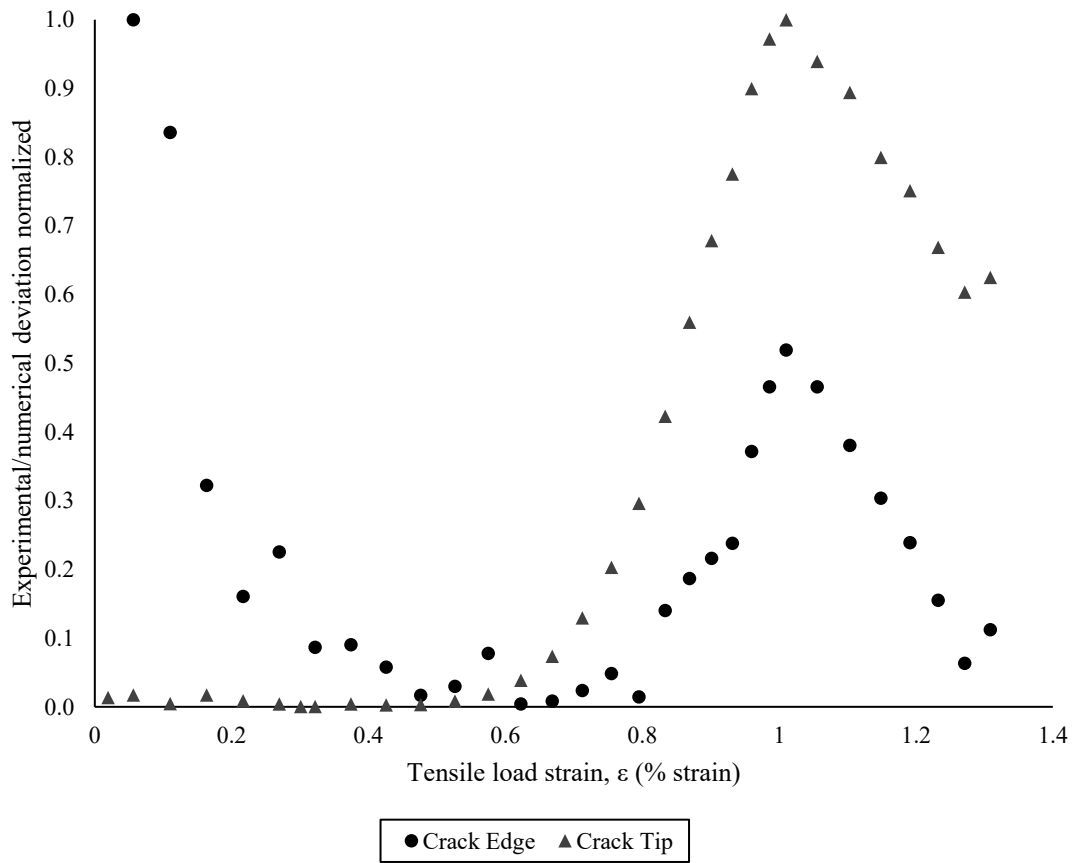
Figure 43. Comparison of experiment and numerical simulation for thin SENT specimen beyond linear region.
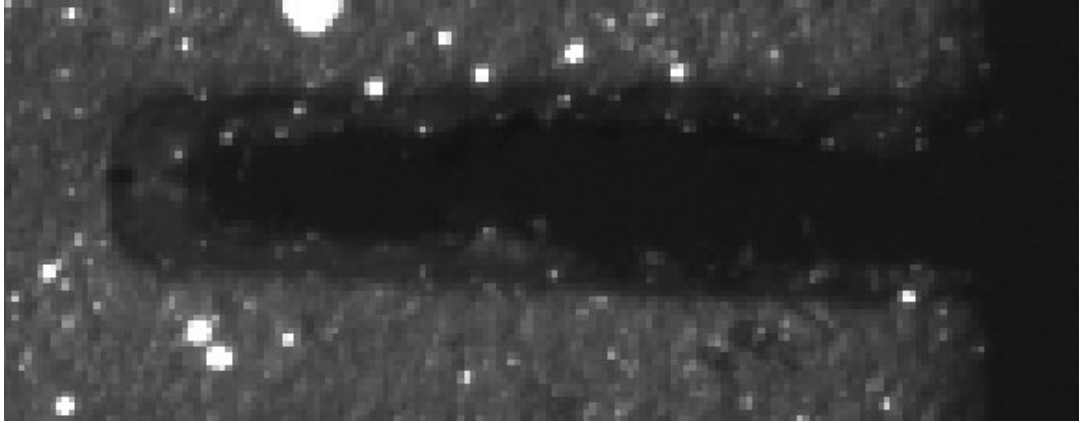
0.8% load strain
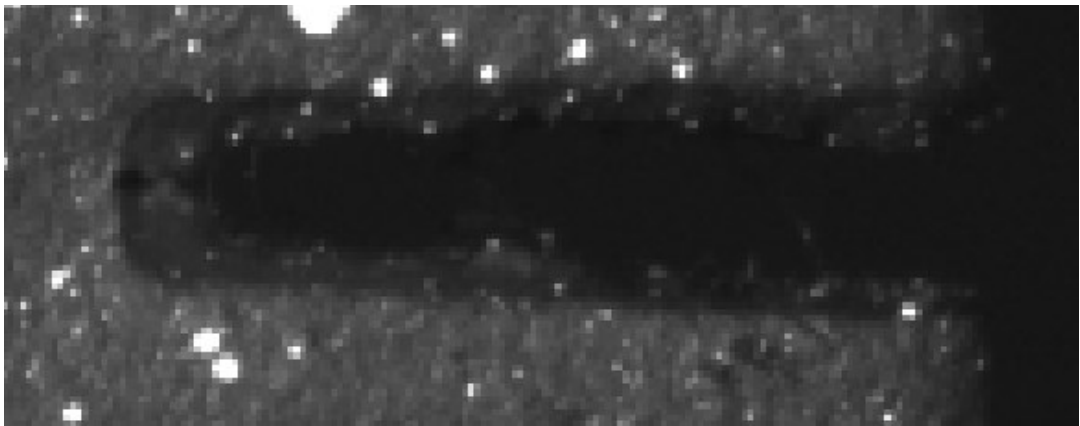
0.9% load strain
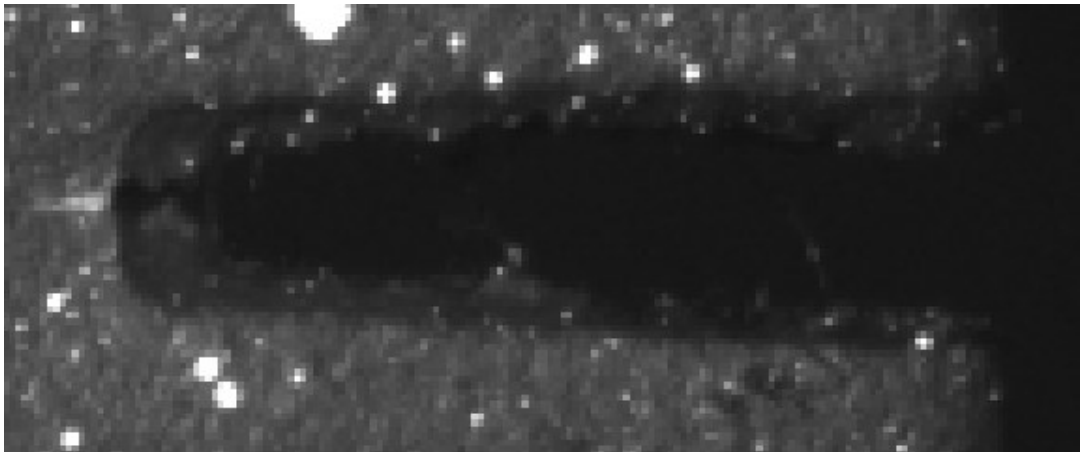
1.0% load strain

Figure 44. Crack propagation between 0.8% and 1.0% load strain of thin SENT 2, showing propagation through incremental stages of loading.

3.4.4 Uncertainty analysis

The uncertainty analysis of the SENT experiments revealed potential weaknesses and areas of improvement in the experimental system. The uncertainty in the crack length, a, was assumed to be 0.025 mm in compliance with the provided engineering drawings for manufacturing (see Appendix F). As with the dogbone experiments, in-plane uncertainty was estimated to be one quarter of the out-of-plane displacement uncertainties listed in Table 20 for the SENT specimens. The load rate of the experiment was 0.05 mm/s, and the synchronization delay was about 0.1 s amongst a pair of images. Because the specimen is fairly uniform and the crack under observation was at half the specimen length, the displacement uncertainty due to asynchronization was estimated to be 0.0025 mm.

The uncertainty in the measurement from the crack edge opening constant, $V_1\left(a/b\right)$, was estimated from Equation (18) as,

$$\frac{U_{V_1}}{V_1\left(a/b\right)} = \sqrt{\left(\frac{U_{\Delta\delta}}{\Delta\delta}\right)^2 + \left(\frac{U_{\Delta\varepsilon}}{\Delta\varepsilon}\right)^2 + \left(\frac{U_a}{a}\right)^2} \tag{20}$$

As the slope and difference-based measurements are simply $y_2 - y_1$, the associated measurement uncertainties can be reduced as so,

$$U_{\Delta y} = \sqrt{U_{y1}^2 + U_{y2}^2} = \sqrt{2}U_y$$

The gap opening was measured as the difference between two displacement measurements. The gap opening slope uncertainty can be reduced accordingly,

$$\frac{U_{\Delta\delta}}{\Delta\delta} = \frac{\sqrt{2}U_\delta}{\Delta\delta} = \frac{\sqrt{2}\sqrt{2}U_x}{\Delta\delta} = \frac{2U_x}{\Delta\delta}$$

Similarly, the strain slope uncertainty can be simplified using the process above and the uncertainty estimation for strain from Equations (11) and (15),

$$\frac{U_{\Delta\varepsilon}}{\Delta\varepsilon} = \frac{\sqrt{2}U_\varepsilon}{\Delta\varepsilon} = \frac{\sqrt{2}\times\left(\frac{\sqrt{2}U_x}{L_0}\right)}{\Delta\varepsilon} = \frac{2U_x}{\Delta\varepsilon L_0} \tag{21}$$

where a gage length, L_0, of 15 mm was used in all specimens to measure the loading strain. The virtual strain gage and was positioned favoring the unloaded edge at an appropriate distance away, as shown in Figure 45. This was to keep the measurement of the loading strain independent from that due to the change in stress flow due to the crack.
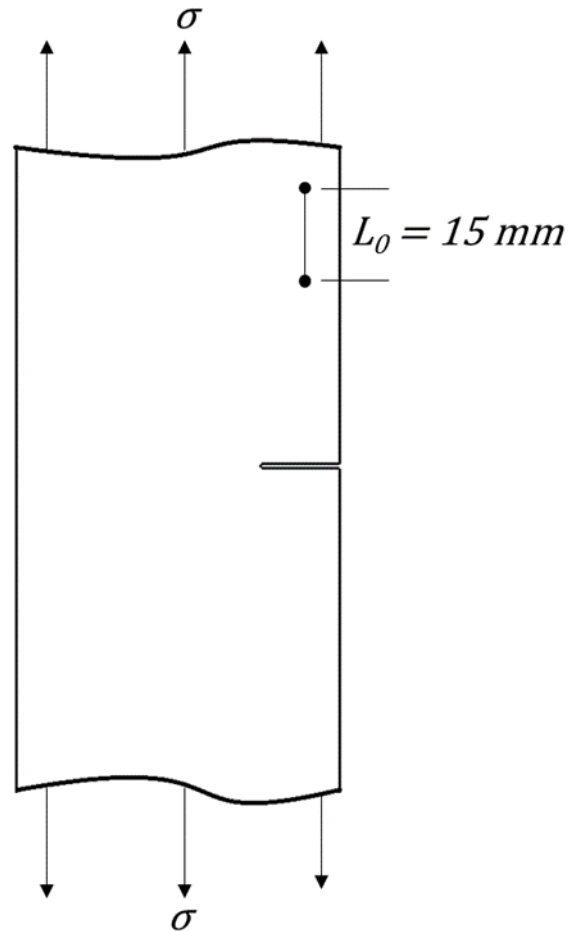
Figure 45. Placement of strain gage on SENT specimen to measure strain from general loading.

From Equation (20), the uncertainties of each component of the crack edge opening measurement were estimated and compared on Table 28. The best and worst cases of measurement uncertainty were examined. SENT 1 had marginally the worst speckle pattern and was tested with software camera triggering. SENT 3 had the best speckle pattern and was tested using synchronized hardware camera triggering. The relative uncertainty for the measurements was 18.8% for SENT 1 and 6.2 % for SENT 3. Crack length had very minor contributions to the measurement uncertainty. However, the exclusion of the precracking

procedure introduces unquantifiable errors that should be kept in mind. The loading strain measurement was the largest contributing factor to uncertainty. Image asynchronization was a large contributing factor, resulting in approximately 16% higher uncertainty in SENT 1 for the $V_1\left(a/b\right)$ measurement. For this reason, it is recommended to use image synchronization whenever possible. If not possible, testing at a slower loading rate would reduce the uncertainty due to non-synchronization. However, plastics tend to be rate dependent, so this should be kept in mind when adjusting the load rate.

Table 28. Estimates for uncertainties of measurement of crack edge opening constant, and components of measurement, showing the uncertainty as the absolute value and as the relative value in parenthesis.

Uncertainty	SENT 1	SENT 3
Displacement, x (mm)	± 0.0040	± 0.0013
In-plane (mm)	*± 0.0015*	*± 0.0013*
Synchronization (mm)	*± 0.0025*	-
Edge opening, $\Delta\delta$ (mm)	0.131 ± 0.008 (6.1%)	0.117 ± 0.003 (2.2%)
*Loading strain, $\Delta\varepsilon$ (%)	0.30 ± 0.05 (17.8%)	0.30 ± 0.02 (5.8%)
Crack length, a (mm)	6.35 ± 0.025 (0.4%)	6.35 ± 0.025 (0.4%)
Crack edge opening constant, $V_1\left(a/b\right)$	**1.72 ± 0.32 (18.8%)**	**1.54 ± 0.10 (6.2%)**

*Gage length, L_0 = 15 mm for SENT 1 and 3.

For additional improvements to the quality of the measurements in this test, strain is the crucial area of focus. Increasing the gage length is a potential approach. However, a gage that is too large may enter the area of influence of the crack. Increasing the FOV can accommodate larger gage lengths but would result in smaller magnification which, for an identical image with the same pixel uncertainty, would result in higher uncertainty of physical measurements. Alternately, the use of extension tubes could decrease the FOV and reduce the physical measurement uncertainty for the same pixel image. However, referring to Figure 45, this would then reduce the specimen area unaffected by the crack in the FOV, potentially affecting the load strain measurement. This can be addressed with a separate load measurement (*i.e.*, strain gages or load cell). In essence, there are compromises to consider when adjusting the system for optimal measurement conditions.

For the crack tip measurements, the uncertainty of the SIF constant, $F\left(\frac{a}{b}\right)$, was estimated from Equation (19) as,

$$\frac{U_F}{F\left(\frac{a}{b}\right)} = \sqrt{\left(\frac{U_{\Delta\varepsilon,tip}}{\Delta\varepsilon_{tip}}\right)^2 + \left(\frac{U_{\Delta\varepsilon,load}}{\Delta\varepsilon_{load}}\right)^2 + \left(\frac{U_a}{a}\right)^2 + \left(\frac{U_r}{r}\right)^2} \qquad (22)$$

The uncertainty for the load strain measurements is the same as Equation (21). The uncertainty in the crack tip strain measurements are similarly represented, but the gage length, L_0, is twice the size of a subset. This is because the correlation software used the displacement vectors of the two closest neighboring subsets in the direction of strain measurement specified to attain the strain measurement of the subset of interest, as shown in Figure 42. There was uncertainty in the measurement for the distance from the crack tip, r, as the strain scalar is a representation of the entire area within the subset. A measured strain is placed at the center of a subset, but this may not match the center of the correlation area, especially for subsets with uneven speckle distribution. Those may cause the correlation center to shift to the sides. Therefore, the uncertainty of r was estimated to be approximately one quarter of a subset.

Equation (22) was used to estimate the uncertainties of SENT 1 and 3 with the previously stated assumptions. The overall and component uncertainties are listed in Table 29. For SENT 1, the estimated relative uncertainty was 59.7%; for SENT 3, it was 35.2%. The crack length proved to be a minimal source of uncertainty. But as previously mentioned, the lack of precracking may have an unseen effect on the experiment. The crack tip strain measurement was estimated to have the highest uncertainty in both cases. The loading strain measurement was less significant in SENT 3 than SENT 1. Implementation of image synchronization in SENT 3 showed to be a marked reduction in strain measurement uncertainty, same as the previous experiments. Increasing the magnification would also reduce the physical measurement uncertainty of an image but would reduce the area within the FOV that is unaffected by the crack for measuring the load strain. Measuring the load separately is a possible approach to this issue.

Table 29. Estimates for uncertainties of measurement of crack tip SIF constant and components of measurement, showing the uncertainty as the absolute value and as the relative value in parenthesis.

Uncertainty	SENT 1	SENT 3
Displacement, x (mm)	± 0.0040	± 0.0013
In-plane (mm)	*± 0.0015*	*± 0.0013*
Synchronization (mm)	*± 0.0025*	-
Tip distance, r (mm)	0.83 ± 0.26 (31.8%)	0.71 ± 0.20 (28.2%)
*Crack tip strain, $\Delta\varepsilon_{tip}$ (%)	0.76 ± 0.36 (47.3%)	0.76 ± 0.15 (20.3%)
**Loading strain, $\Delta\varepsilon$ (%)	0.30 ± 0.05 (17.8%)	0.30 ± 0.02 (5.8%)
Crack length, a (mm)	6.35 ± 0.025 (0.4%)	6.35 ± 0.025 (0.4%)
SIF constant, $F\left(a/b\right)$	**1.30 ± 0.78 (59.7%)**	**1.20 ± 0.42 (35.2%)**

*Gage length, $L_{0,\,tip}$ = 2 × subset size ($L_{0,\,tip}$ = 2.22 mm for SENT 1 and 1.68 mm for SENT 3).
**Gage length, $L_{0,\,load}$ = 15 mm for SENT 1 and 3.

Reductions in the uncertainty of the crack tip strain measurements are possible. It is estimated to be high because the measurements are of low strains. The observed strains were small in part due to the limited region of elastic loading of the polypropylene. Testing different materials with linear elastic regions that reach into higher strains would also allow for better measurements. Also, the gage length for the crack tip measurement was relatively small (2.22 mm for SENT 1; 1.68 mm for SENT 3). Larger gage lengths would reduce the uncertainty but would decrease the resolution as well. This may not be desirable in this case as the strain measurements are highly sensitive near the crack tip. At smaller distances from the crack tip, the strain is higher; measuring these regions would decrease the relative uncertainty of this measurement. However, decreasing the distance to the tip would increase the relative uncertainty in the distance from the crack tip. This would be favorable in the case of SENT 1 as the crack tip strain had a much greater associated measurement uncertainty than the tip distance. However, for SENT 3, this would likely increase the overall uncertainty. A balance should be considered in this regard.

The main source of uncertainty with regards to the crack tip distance was due to the ambiguity of the location of the measurement. For subsets with excellent speckle distribution, it can be assumed that the center of the correlation are aligns with that of the subset itself. However, with subsets where speckles are askew, the subregion of the subset with high speckle density would dominate the correlation and the measurement would be

representative of the center of that subregion as opposed to the entire subset. Using smaller subsets would decrease the uncertainty due to center ambiguity but would also increase the overall displacement uncertainty as smaller subsets typically do. Measuring at greater crack tip distances would also reduce the relative uncertainty of this measurement. However, in using the SIF approach for crack loading quantification, it has been shown that measurement error scales with distance from the crack tip [148]. The closest distance to the crack tip that yields the smallest reasonable uncertainty estimate should be used. However, crack edge opening measurements have less uncertainty due to the nature of the DIC system and would be better suited for quantifying crack behavior using this setup.

3.4.5 Summary

To analyze the capabilities of the experimental setup in examining cracked specimens, a set of SENT experiments were carried out. Theoretical analysis was performed for a baseline of comparison. Then, numerical and experimental simulations were conducted and compared with one another as well as to the theoretical analysis to assess the validity of each method. Two aspects of crack testing were focused on: the crack edge opening displacement, and the strain at the crack tip. The respective empirical constants published in literature [147], $V_1\left(a/b\right)$ and $F\left(a/b\right)$, were the parameters for comparison of all three methods for the linear elastic region. Strong agreement of all methods and high experimental repeatability was observed for the crack edge gap opening. For the crack tip strain, there was agreement but to a lesser extent. One possibility cause is the exclusion of precracking from this experiment. The crack tip strain would be more sensitive to this effect than the crack edge gap measurements. Another possibility is the use of the SIF as the approach. It has been used in other studies, but is more applicable to metals than plastics, as metals are less rate-dependent and more linear than plastics. Thus, it may be a source of error and discrepancy between analysis methods.

For the non-linear region, only the numerical and experimental results were compared, as the SIF approach was only applicable to the linear region. General agreement was observed between the two up until the point of crack initiation. The numerical simulation did not account for the energy release due to crack propagation and became highly deviant from the experimental observations. In the future, theoretical comparisons

may be conducted by performing J-integral testing [148]. It was not conducted in this investigation due to the requirement of multiple specimens per test and the limited supply available at this time. Also, the crack extension measurements are taken post-loading, which would not be an effective way to assess this DIC system.

Future experiments involving crack measurements can be improved from this study. A major obstacle was that relatively low strains were measured. Materials with linear elastic regions that extend into higher strains would be more accurately measured in a study of this type. Also, adjustments to the imaging system can improve the experiment. Currently, the captured images are used to measure both the loading area and the crack region. A greater magnification would reduce the uncertainty of the physical measurement. The magnification could be increased (with lens extension tubes, for example) for a more localized view of the crack region if another system was measuring the load applied to the specimen. Using strain gages at the loading region is one possibility. Alternatively, designing and implementing new test grips that do not slip or cause premature yielding at the grip site would allow for the forces to be measured directly by the load cell.

This study also showed that minor adjustments can be implemented to accommodate the needs of different experiments. When implementing a gage for measuring the strain due to tensile loading, the maximum length of the gage was balanced with the maximum region unaffected by the crack presence. Also, the crack tip distance was selected in this experiment to be as close to the crack tip as possible while maintaining reasonable uncertainty regarding the location of measurement. Smaller crack tip distances would allow for higher strains and less error from the SIF approach but would increase the relative uncertainty of the crack tip distance which is highly sensitive. It was assumed that 0.30% load strain represented the linear region of the polypropylene in this experiment. Examining greater strains would reduce the relative uncertainty of the strain measurements but may also reduce the validity of the linear elastic assumption. These aspects can be tweaked to more optimally meet the conditions of similar but modified experiments.

By carrying out this SENT experiment study, the strengths, limitations, adjustability, and areas of improvement were assessed. The measurement system was deemed viable for measuring crack mechanics under these conditions. The knowledge gained from this study could then be applied to more complex fracture mechanics.

3.5   Conclusion

An existing mechanical experiment setup was modified to function as a DIC system. The components, setup, and usage of the system was detailed. The testing apparatus was then assessed by conducting experiments and comparing the results to numerical simulations and theoretical analysis. First, a set of dogbone tensile tests were conducted, examining the measurement of the material properties: yield stress, yield strain, and elastic modulus. Strong agreement was observed for all parameters among all three analysis methods (theoretical, numerical, and experimental).

Second, a set of SENT experiments were carried out. The crack edge opening and the crack tip strain were of interest. Both aspects showed reasonable agreement in the linear region among the three analysis methods. The theoretical, numerical, and experimental crack edge constant measurements were within 2% of one another; for the crack tip strain, within 8%. Crack edge openings of approximately 0.1 mm were measured with an estimated error of 0.003 mm and crack tip strains of 0.76% were measured with errors of 0.15% strain. In the non-linear region (strains greater than 3%), where the theoretical analysis became invalid, the numerical and experimental results showed good agreement up to the point of crack initiation and growth. This demonstrated that the numerical simulation did not account for the energy release consequential to crack growth, which should be considered in analyses moving forward. Although the crack edge opening and crack tip strain were not able to be validated beyond the 3% region, the DIC system should still be measuring accurate displacements and strains.

The limitations of the experiments were assessed, and areas of improvement were recognized. Adjustments to the current system and recommended implementations of new components and approaches were provided. It was found that the measurement uncertainty associated with the crack edge opening measurement was much smaller than that of the crack tips train measurements. Crack edge openings as small as 0.03 mm could be measured with less than 10% uncertainty. Therefore, it was the preferred measurement for characterizing crack motion of a fractured pelvis in the subsequent study. Experimental study of pelvic loading.

Chapter 4: Experimental study of pelvic loading

4.1 Introduction

4.1.1 Background

In this study, a biomechanical test simulation of a pelvis was designed and analyzed. Mechanical analysis of pelvic loading is agreed to be a useful approach in studying the pelvis for potential clinical application [11]. Currently, there is no universal standard for how to conduct a biomechanical pelvis experiment. There are many commonalities across studies in existing literature, and Aziz et al. has amalgamated them into a guideline of how to conduct such an experiment [151]. However, because every study investigates different aspects of the pelvis, it is still very difficult to compare results to literature. Therefore, extra steps may be required for validation of results.

Part of the difficulty for comparisons of results is due to the breadth of variation between cadaveric pelvic specimens. These often impose large amounts of uncontrollable variation on an experiment which often cause results to be statistically insignificant [91]. A study by Culemann et al. investigated both synthetic and cadaveric specimens, attaining statistical significance for the former but not the latter [77]. This is due to the high degree of homogeneity regarding synthetic specimens. Though they may not be exact replicates of cadaveric specimens, they have been shown to be reasonable representations [86], [152], [153].

To ascertain validity of a cadaveric pelvic simulation, studies often self-validate by creating a FE model and comparing the numerical simulation to their own experiment. Many studies implement strain gages at locations of interest predicted by the FE models and compare the values between the two [62], [63], [87]. Ghosh et al. demonstrated the viability of DIC by comparing measurements of the DIC system to those of strain gages and their own FE model [60]. These experiments in these studies are typically the simplest scenario of loading an intact pelvis or hemipelvis.

Other studies are more concerned with fractured pelvises and the assessment of fixation techniques currently used. As there are many different types of pelvic fracture, studies often focus on the various techniques of one fracture type and compare the fixation methods available towards the fracture of interest. The parameter of quantification is often

fracture displacement [40], [67], [72], [76], [94]. In two separate studies, Simonian et al. examined various methods of fixing iliac wing fractures [40] and T-type fractures [72], showing that there was no statistical difference in the fracture displacement under loading across the available techniques for either fracture type. On the contrary, in a more recent study, Kourkoulis et al. showed a difference in 3D fracture displacement of current methods of fixing T-type fractures using DIC, though the sample size was limited [79]. This may be due to the more recent study being conducted after the development of locking plates, which have a different mechanical behavior than conventional plates [39], [67], [94]. This demonstrates that comparisons across studies can be difficult due to statistical variance, specimen availability, specimen variation, and how long ago the study was conducted.

Some studies investigate the mechanical impact of pelvic fixation methods. In many surgery cases, the fracture fixation implant bears much of the loads which an intact pelvis would normally see. This can result in reduced bone resorption and loss in bone density, an affect known as stress shielding [36], [154]. Studies have shown that pelvic reinforcement implants can significantly affect the loading profile of a pelvis [55], [69], [90]. It has also been shown that the material of the implant also affects the extent of stress shielding on the pelvis [66], [155]. Different fixation techniques can also have various effects on stress shielding, such as the use of locking plates versus conventional plates [39], [67].

In this study, the strains of a pelvis in response to mechanical loading were observed for biomechanical understanding and validation. Comparisons to other studies examining strain fields of composite hemipelvis models was difficult still, as the limited number of studies that exist examine widely different parameters. In composite model studies, Ghosh et al. [60] and Small et al. [156] elected to quantify their results using von Mises strain. Their reason for doing so is mainly for a more direct and concise comparison to an FE model for validation. However, in this study, a more specific mechanical assessment was desired. The 1st and 3rd, or maximum tensile and minimum compressive, 3D principal strains were examined to understand the maximum tensile and compressive loading respectively in three dimensions. Many cases, such as a study by Girardi et al. [86], use strain gages to measure surface strains of a pelvis. However, as strain gages cannot measure

3D loading, the maximum and minimum principal strains normal to the surface are measured. In studies by Ghosh et al. [60] and Dickinson et al. [66], strain gages were used as a basis for comparison and validation. Logically, the DIC results from those investigations were also presented as maximum and minimum principal strain fields normal to the surface for comparison sake. Furthermore, this study targeted pelvic strain measurement at the ilium, whereas the previously mentioned DIC studies focused on a small area superior to the acetabulum. To the author's knowledge, the maximum tension and compression induced on the ilium of a composite hemipelvis had not yet previously been examined before this study.

Biomechanical pelvic testing was conducted in a previous study at the University of Alberta [144]. The purpose was to investigate the effect of pelvic fracture on the strain field of a pelvis, comparing it to an intact one. The main difficulties of the study were its sample size and the validation of the results. Only two tests were conducted due to the difficulties in setup and the cost of materials. One test was of an intact pelvis and another of a fractured. This was partly because the method used to fix the pelvis was cement potting. Both the assembly and disassembly processes are time-consuming, reducing the possible rate of testing. This study intended to improve upon these areas by creating a setup that can time and cost effectively conduct experiments. The setup was validated using the similar methods to those in the previous section of this thesis.

The validation approach for this study can be deconstructed into logical steps. First, an intact pelvis experiment was examined to assess how representative the experiment was regarding anatomical biomechanics. As 1st and 3rd principal strains of pelvic loading have not yet been investigated, numerical simulations were performed in this study for a basis of comparison. Boundary conditions analogous to single-leg stance in a human body were compared to those imposed on the pelvic specimen in the experiment to show that the experimental setup did not significantly alter the anatomical biomechanics. The numerical simulation of the experiment was then compared to the experimental results to assess the accuracy of the numerical calculation. After proving the experimental setup for an intact pelvis, the fractured pelvis could then be tested to investigate how an iliac FFP can mechanically alter the normal conditions of a pelvis.

4.2   Methods and materials

4.2.1 Pelvic fixture design

A new pelvic fixture was designed to impose a fixed boundary condition at the SI joint. This was to replace the previous technique of potting with the intention of improving the ease of conducting experiments, the time it takes to assemble and disassemble the test, and the continual requirement of cement for each test. 3D-printing was the manufacturing method used for its ability to create parts with complex geometries. Also, the complex geometry of the hemipelvis causes difficulties in enforcing a rigid fixation at a specific loading angle. The design freedom associated with 3D-printing alleviates this concern.

A model was created in SolidWorks, shown in Figure 46, and 3D printed with polymer material (Polyjet Verogray RG3850, Stratasys Ltd.), with the properties listed in Appendix F. First, an assembly model of the MABTA and femur was created with the hemipelvis solid model oriented at the desired angle for single leg stance, 12° adduction. The hemipelvis was aligned with the axis and planes of the femur with one point-based mate. Then, a block of solid material was created around the SI joint of the hemipelvis. The interfering volume of the hemipelvis was Boolean subtracted from the volume of the block, generating a profile that conformed to the hemipelvis geometry. The block was then split into two parts with a 5 mm cut through the subtracted volume in a manner that minimized the concavity of the hemipelvis mold to allow for physical assembly. Material was removed for cost reduction as well as viewability for the DIC system. Bolt holes were created to allow the two parts of the fixture to clamp together and mount to the MABTA.

Figure 46. Model of 3D-printed pelvic fixture designed for experiment, showing the part as a solid and with translucency to show the clamping bolt holes and the SI joint conforming profile.

The benefits and viability of the newly designed pelvic fixture was assessed according to its ease of setup and repeatability. Depending on the accuracy of the 3D-printing method, the design was susceptible to nonconformity as well as issues with fixation rigidity. The former could cause assembly and disassembly difficulties whereas the latter could reduce the repeatability of the experiment due to inconsistent fixation. In terms of cost and materials, because the 3D-printed fixture could be reused for the specimen designed for (described below), it inherently is more cost effective than the potting method assuming a reasonable lifetime. Therefore, the capability of the fixture was determined by gauging the difficulty of setup as well as the amount of repeatability across experiments. Repeatability was determined through multiple testing in a single setup as well as through multiple setups. Testing of multiple specimens is recommended for future validation but was not available in this study due to cost.

4.2.2 Experimental setup

The experiment was setup as shown in Figure 47. A fourth-generation composite hemipelvis model (SKU #3409, Sawbones) was the test specimen for all experiments (see Appendix F for properties). As shown in Figure 48, one model was intact, the other was fractured at the greater sciatic notch towards the ilium to represent onset of an iliac wing FFP. Both models were painted flat black with white speckles like the previous experiments. The hemipelvis specimens were clamped with the designed fixture at the SI joint and the fixture was rigidly bolted to the MABTA frame. The mock femur was made of aluminum with a hemispherical surface to insert into the acetabulum of the hemipelvis model. To more evenly distribute the loading of the femur, a small square of soft, compressible foam was placed between the two, serving as a mutual contact interface.
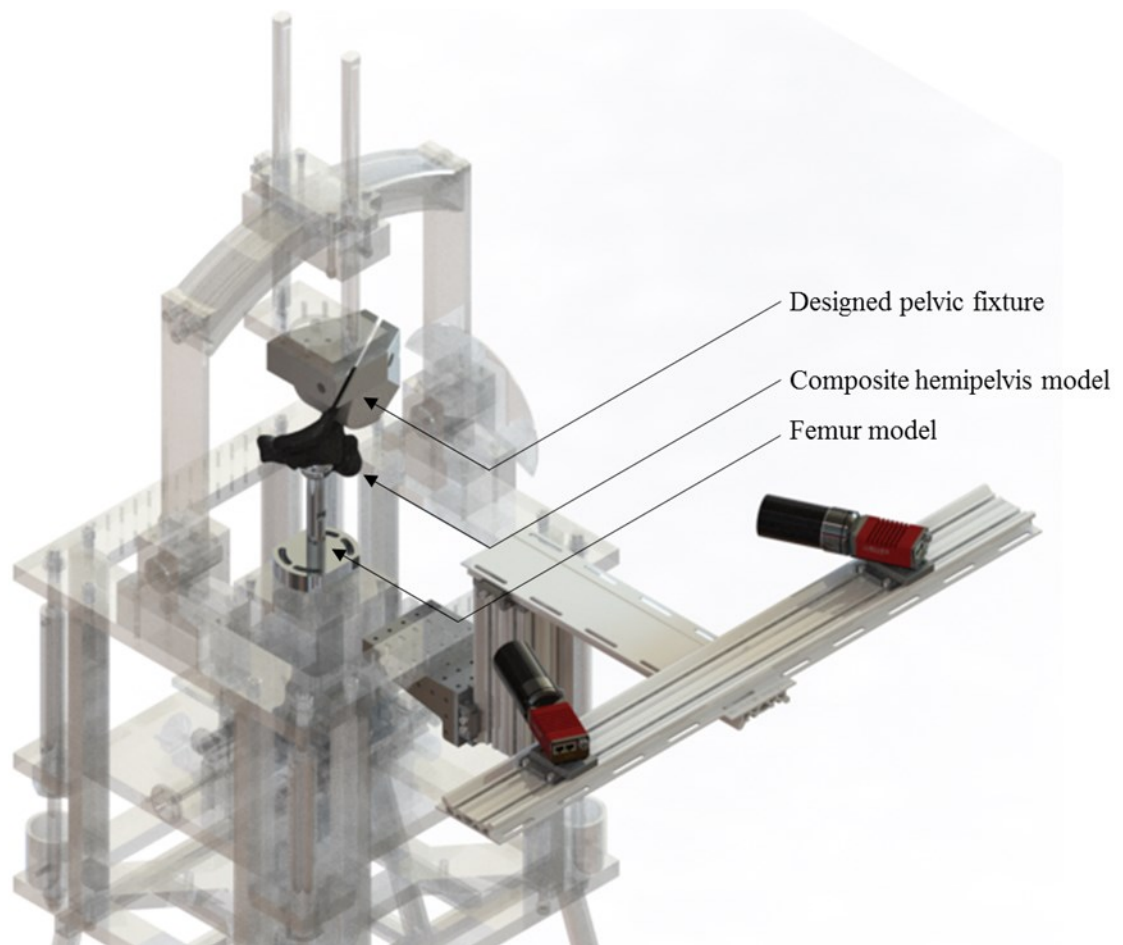
Figure 47. Setup of pelvic loading test, with MABTA displayed with translucency.

| (a) | (b) |
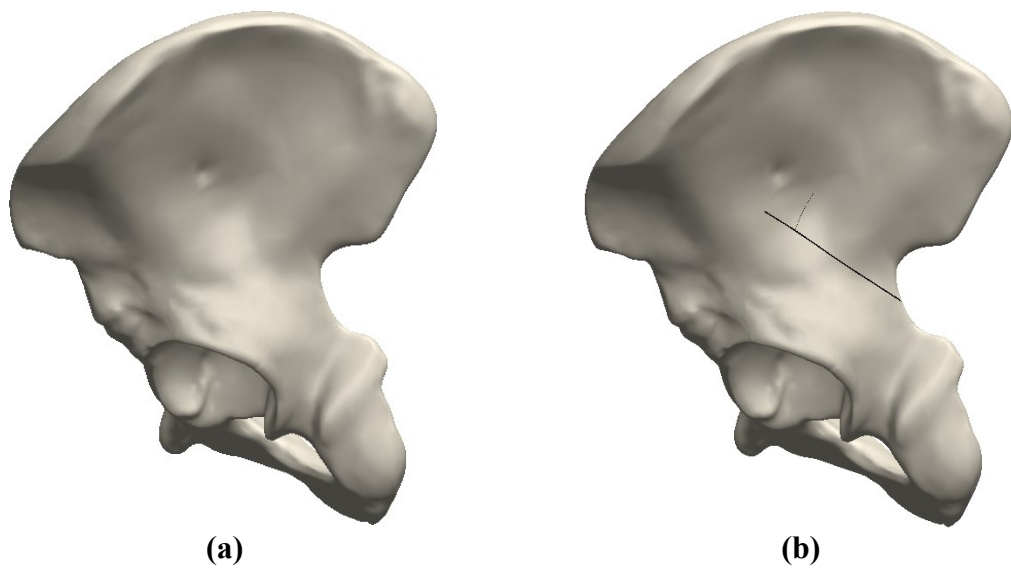
Figure 48. Pelvic specimens under examination, showing **(a)** the intact pelvis and **(b)** the fractured pelvis.

Once the specimens were set up, the cameras were adjusted for optimally capturing images. Due to the significant contouring of the pelvis, and limited depth of field, it was difficult to have the entire surface in focus; a setting that balanced the focus across the entire viewing surface was sought. The cameras were positioned at about ± 25° relative to the pelvis as it was setup in the MABTA with a Scheimpflug angle of 4°. The camera standoff distance was approximately 650 mm. An example of a typical image pair is shown in Figure 49. It shows some regions that are exclusive to one camera view, such as the outer edge of the greater sciatic notch in the right view; regions as such cannot be measured in the image correlation.
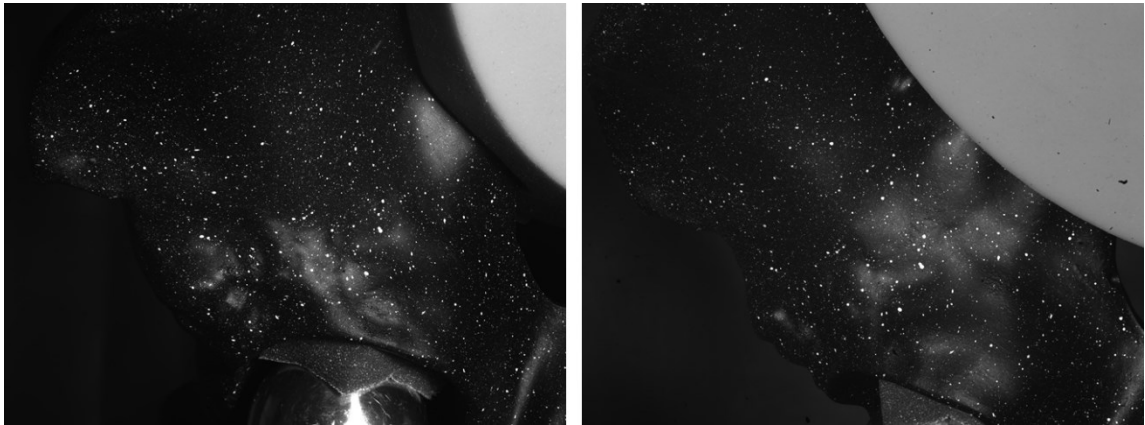
Figure 49. Field of view for a typical image pair in pelvic loading experiments, showing the left and right camera views respectively.

After setting up the cameras for the specimen in the test frame, rigid body out-of-plane displacement was performed to quantify the DIC system uncertainty similarly to the previous experiments. The rigid body motion was evaluated by placing the pelvis on a micrometer-controlled traversing stage at the approximate test location and displaced at known steps. The discrepancy to each step was the measurement uncertainty for each specimen. Figure 50 shows that the speckle pattern characteristics were location dependent. This is because of the surface curvature causing unevenness in illumination, making speckles in some regions darker than others. For the image correlation, the settings were geared towards the region of lowest speckle pattern quality, which was in the anterior-superior ilium region shown in Figure 50 (a). A subset size of 31 gave an appropriate

speckle density. Table 30 lists the morphological characteristics of each region, as well as the overall uncertainty based on the rigid body displacement of the specimen.
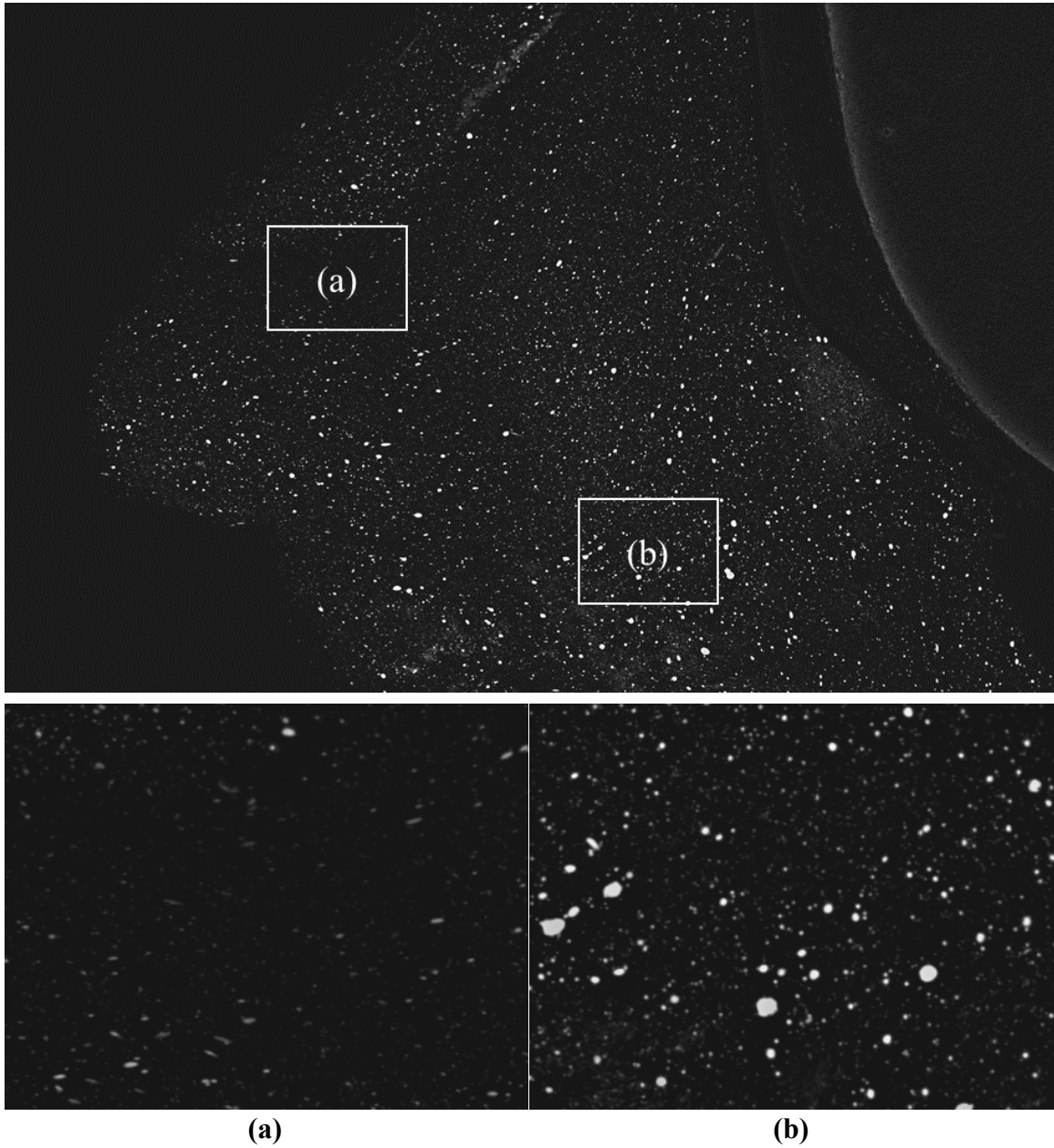
Figure 50. Pelvis morphological analysis, showing difference in speckle pattern quality at **(a)** the anterior-superior ilium and **(b)** the superior acetabulum.

Table 30. Morphological and uncertainty analysis of different regions of pelvis speckle pattern.

Characteristics	(a) Anterior-superior ilium	(b) Superior acetabulum
Subset size	31	31
Density (speckles per subset)	2.65	4.04
Diameter (pixels)	3.62	4.00
Variation (IQR as % of mean)	50.7	56.6
Uncertainty (mm)	0.00229	
Scale (pixel/mm)	25.36	
Uncertainty (pixels)	**0.059**	

As with the previous sections of this thesis, the same commercial image processing software was used to analyze the data. The image correlation settings are listed in Table 31. The commercial software uses an affine transformation algorithm, and the subsets were 31 pixels large and stepped at 15 pixels spaces. These parameters were based on the morphological analysis.

Table 31. Summary of image processing settings for pelvic loading tests.

Detail	Specification
Software	DaVis 8.4
Image filtering	Subtract sliding minimum
Subset size (pixels)	31
Step size (pixels)	15
Shape function	Affine transformation

The hemipelvis was loaded in a single-leg stance orientation which is an adduction angle of 12°, as shown in Figure 51. It was fixed at the SI joint but left free at the pubic symphysis. Most experiments impose a sliding support to the pubic symphysis as it is more representative of that contact point in the human body. However, it has been shown that leaving it unfixed, though causing differences in stress distribution, can still reasonably represent anatomical pelvic loading [95]. Doing so redirects stress that would normally flow through the ramus by removing the reaction force provided at the pubic symphysis; this must be taken into account. Multiple tests were conducted at various load rates to assess the sensitivity of the experiment to loading speed. The specimens were loaded to a

maximum of 500 N to prevent damage to the specimens and allow for reuse, a concern mainly for the fractured specimen. The vertical force applied into the acetabulum was measured by the MABTA load cell, and the surface displacements of the pelvis were measured by the cameras in the DIC system. All tests in this section used image synchronization to minimize error among image pairs. Once the image data were collected, image correlation was performed, using the settings in Table 31, and the 1st and 3rd principal strain fields were extracted for each test.
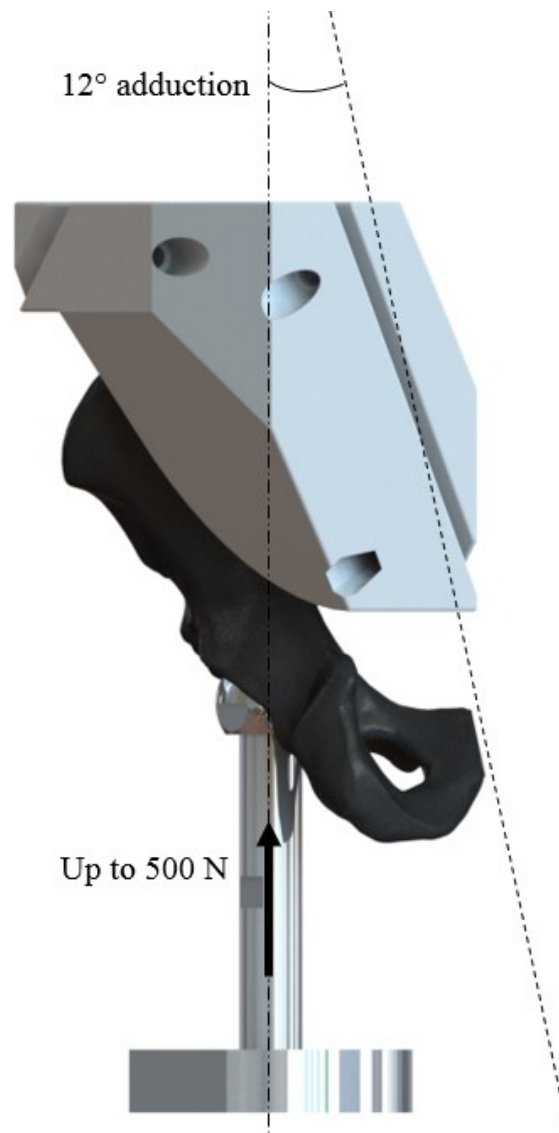
Figure 51. Posterior view, showing single-leg stance loading orientation of hemipelvis specimen in designed fixture as 12° adduction.

4.3   Intact pelvis

This section details the procedure by which the analysis of the intact pelvis loading scenario was conducted with the specimen shown in Figure 48 (a). Numerical simulations were performed and compared with experimental simulations to assess the behavior of the pelvis under the mechanical loading conditions and assess the sources of error and differentiation by comparing the results of the two analyses methods. For the experiments, six tests were analyzed to evaluate the repeatability of the experiment, comparing the 1st and 3rd principal strain fields measured in each test.

4.3.1   Numerical simulation

Numerical simulations were performed to provide a basis of comparison for the experimental simulation. The boundary conditions were varied between simulations to examine the potential sensitivity of the physical constraints of the biomechanical experiment as shown in Figure 52. The first was setup to most similarly represent pelvic loading in the human anatomy. This was achieved by fixing the surface of the SI joint and applying a sliding boundary to the pubic symphysis. The second excluded the pubic symphysis constraint to examine the effect on the loading profile of the hemipelvis. The third used a simplified model of the 3D-printed pelvic fixture, preventing penetration at the interface of the hemipelvis and the fixture, fixing the face of the fixture in contact with the MABTA, and including a sliding constraint on the pubic symphysis. This simulation was performed to determine the effect of the pelvic fixture on the simulation in comparison to the more anatomically realistic simulation. In this simulation, the clamping bolt holes were fixed to one another, causing the two parts of the fixture to be geometrically fixed to one another. However, it would deviate from the experiment if there was movement between the parts of the fixture. The fourth numerical simulation was the same as the third but excluded the pubic symphysis constraint to examine the significance of its effect.
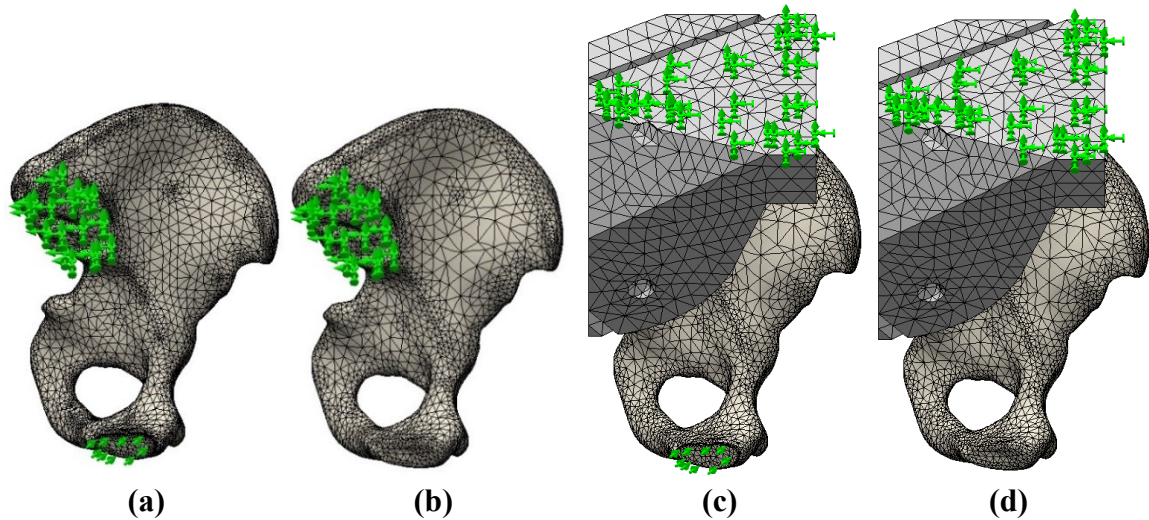
Figure 52. Boundary conditions examined in numerical simulations, showing **(a)** fixed SI joint and sliding pubic symphysis, **(b)** fixed SI joint and free pubic symphysis, **(c)** fixed MABTA-pelvic fixture interface and sliding pubic symphysis, and **(d)** fixed MABTA-pelvic fixture interface and free pubic symphysis.

Each simulation involved loading into the acetabulum in the same manner as with the experiment. For simplification purposes, the force was applied directly to the upper hemisphere of the acetabulum, rather than indirectly via the femur part. Regarding the hemipelvis specimen, the material properties used in the simulations are in Table 31. The model of the hemipelvis was taken from a CT scan of the composite model. This means that the material was treated homogenously, which is realistically not the case as there is both a cortical and cancellous layer in the model. The properties of the cortical layer were applied to the entire part, meaning that the stiffness of the hemipelvis was greater in the numerical simulation than the experimental. With the stiffness implemented conservatively high, a linear static model was used. The mesh settings are listed in Table 32, although mesh convergence was not pursued as the simulations were time-consuming and numerous. Due to time constraints, numerical simulations were performed only on the intact pelvis and not on the fractured pelvis.

Table 32. Summary of solver settings for intact pelvis numerical simulations.

Attribute	Value
Specimens	Intact pelvis (E = 16.7 GPa, σ_y = 93 MPa, ν = 0.3) Clamp (E = 2 GPa, σ_y = 50 MPa, ν = 0.394)
Mechanics	Linear static
Boundary conditions	(a) SI joint fixed, PS sliding (b) SI joint fixed (c) Pelvic fixture top surface fixed, PS sliding (d) Pelvic fixture top surface fixed
Loading conditions	12° adduction into upper acetabular hemisphere, total 500 N
Software	Solidworks Simulation 2017
Solver	FFEPlus (explicit)
Algorithms	Newton-Raphson
Convergence criteria	0.1%

Table 33. Intact pelvis numerical simulation mesh settings for each scenario.

Mesh	(a) SIJ + PS	(b) SIJ only	(c) Fixture + PS	(d) Fixture
Mesher	Curvature-based	Curvature-based	Curvature-based	Curvature-based
Jacobian points	4	4	4	4
Mesh control	-	-	-	-
Max. element size (in)	0.5	0.5	0.5	0.5
Min. element size (in)	0.1	0.1	0.1	0.1
Number of nodes	58344	64045	96021	97425
Number of elements	36704	40617	60757	61390
Max. aspect ratio	48.785	9.440	30.178	31.701
Aspect ratio < 3 (%)	97	98.6	98.1	97.6
Aspect ratio < 10 (%)	0.0845	0	0.0198	0.0472

The impact of the boundary conditions of simulation (a) differed from that of (b) in that removing the sliding constraint on the pubic symphysis diverted the loading that was formerly present at the superior ramus and pubis regions, as shown by Figure 53. There also is a slight increase in stress near the anterior iliac spine after the removal of the pubic symphysis constraint, as Figure 54 shows. Otherwise, the loading profiles were very similar. Areas of high stress in both simulations were on the iliac fossa near the SI joint

and at the greater sciatic notch. Also, both results had a stress propagation from the greater sciatic notch to the iliac crest similarly shaped to an iliac wing FFP. The miniscule effect of relaxing the pubic symphysis boundary condition is in congruence with Watson et al. [95], where it was observed that over-constraining the symphysis had a more severe impact on the accuracy of the simulation than under-constraining it.

(a)   (b)
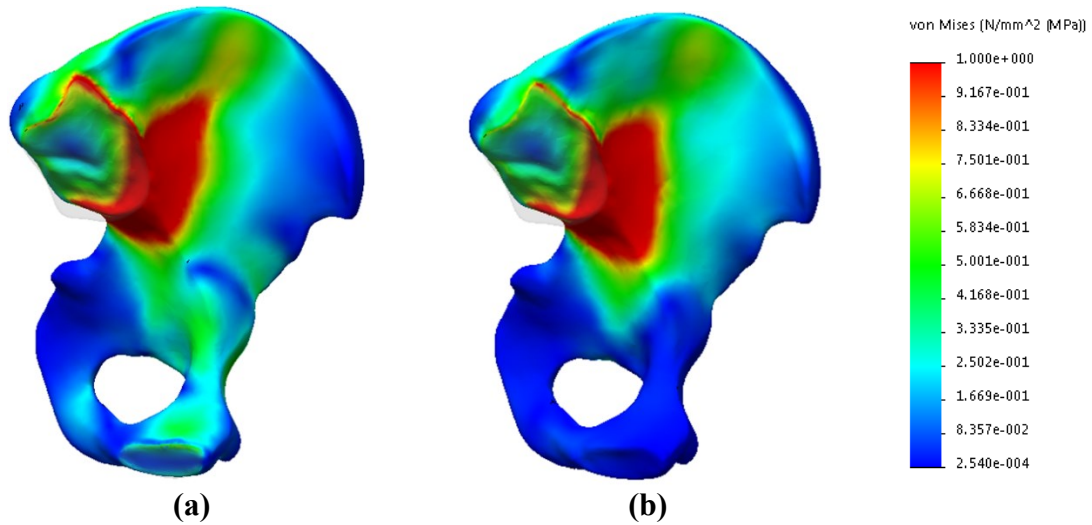
Figure 53. Pseudo-medial view for Von Mises stress results from **(a)** fixed SI joint and sliding pubic symphysis and **(b)** fixed SI joint and free pubic symphysis. The comparison shows the diversion of stress flow from the ramus and pubis due to the removal of the sliding constraint on the pubic symphysis.

(a)   (b)
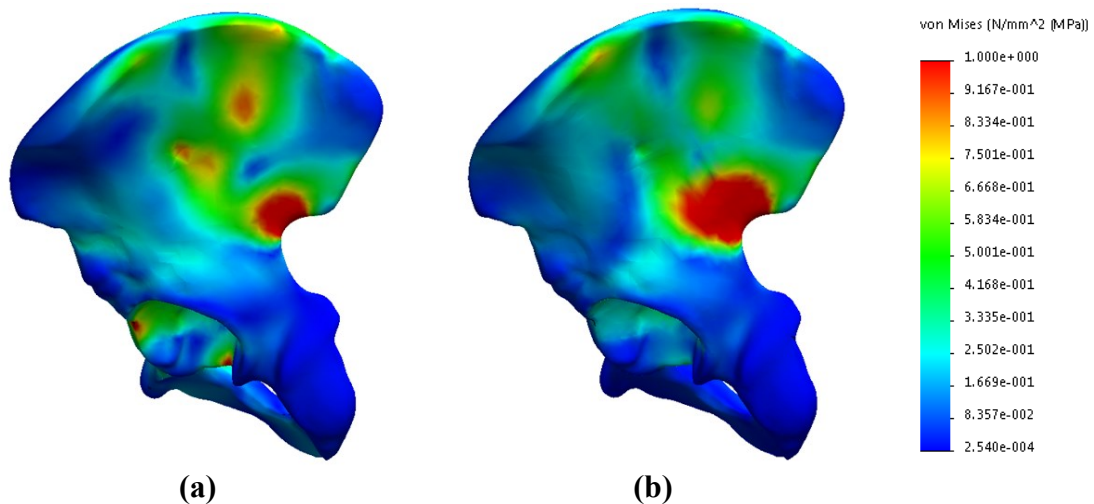
Figure 54. Pseudo-lateral view for Von Mises stress results from **(a)** fixed SI joint and sliding pubic symphysis and **(b)** fixed SI joint and free pubic symphysis. The comparison shows a slight increase in stress near the anterior superior iliac spine after removing the sliding constraint on the pubic symphysis.

When analyzing the instances in which the fixture was included in the simulation (shown in Figure 52 (c) and (d)), the removal of the pubic symphysis sliding constraint had a virtually negligible effect, as seen in Figure 55, suggesting that the sliding support had no mechanical impact. This may be due to the stiffnesses of the specimen and the fixture in the simulation being quite high. This would highly restrict the displacement of the specimen thus mitigating the effect of the sliding support. However, the stiffness is overestimated as the physical part has a cancellous bone component to it, so the simulation results could deviate from the experiment.

(a)   **(b)**
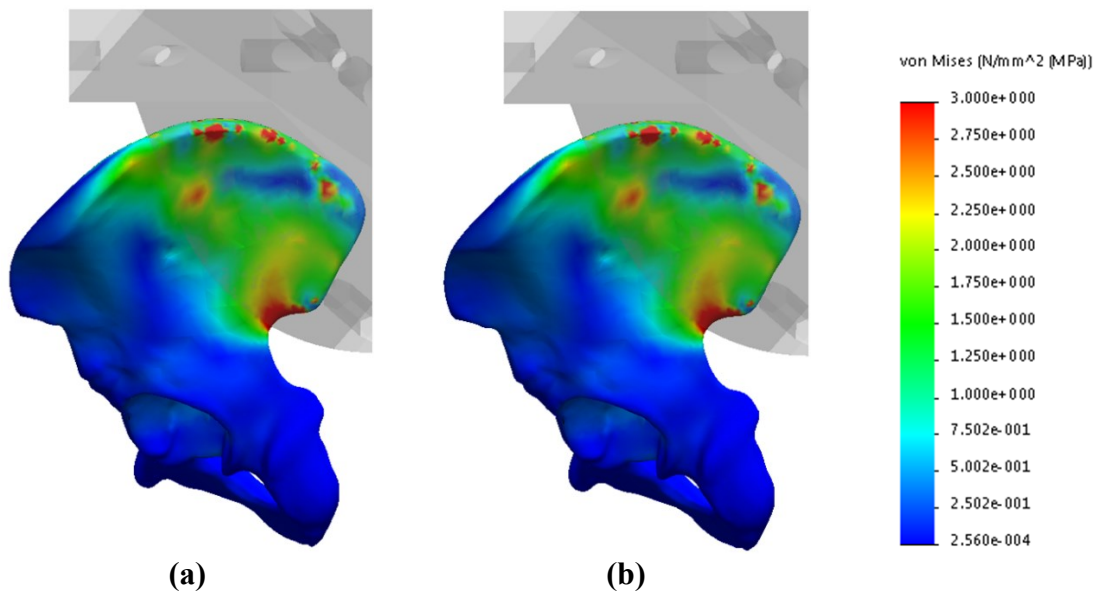
Figure 55. Pseudo-lateral view for Von Mises stress results from **(a)** pelvic fixture with sliding pubic symphysis and **(b)** pelvic fixture with free pubic symphysis. The comparison shows the two to be virtually identical.

In comparing the simulations with and without the pelvic fixture, there were greater stresses with the pelvic fixture particularly within the clamping region, as Figure 56 shows with a same-scale comparison. The inclusion of the fixture created a loading profile more similar to the free pubic symphysis case, showing relatively little stress in the superior ramus region. Both cases also showed higher stresses extending from the iliac crest to the anterior iliac spine. There was a posterior-superior shift of the stress propagation when including the fixture which can be seen by comparing Figure 55 to the non-fixture cases of Figure 54. A comparison of the displacements between the fixture and non-fixture cases in Figure 57 (a) and (b) respectively shows that the fixed location of the pelvis had moved

anteriorly from the SI joint. In Figure 57, both displacements were shown on a 0 to 0.05 mm scale; as there was rigid body movement of the pelvis in the fixture, the most representative range was estimated as 0.305 to 0.355 mm in Figure 57 (a). The change in the location of fixation suggests a less representative model using the fixture. However, the SI joint still exhibits little movement, suggesting that the simulation may still be reasonable, but the mechanical alteration should be considered. This is especially important with the DIC system because the fixture blocks the camera sightlines from viewing the loads at the site of consideration preventing detection of the altered mechanics.

(a)

(b)
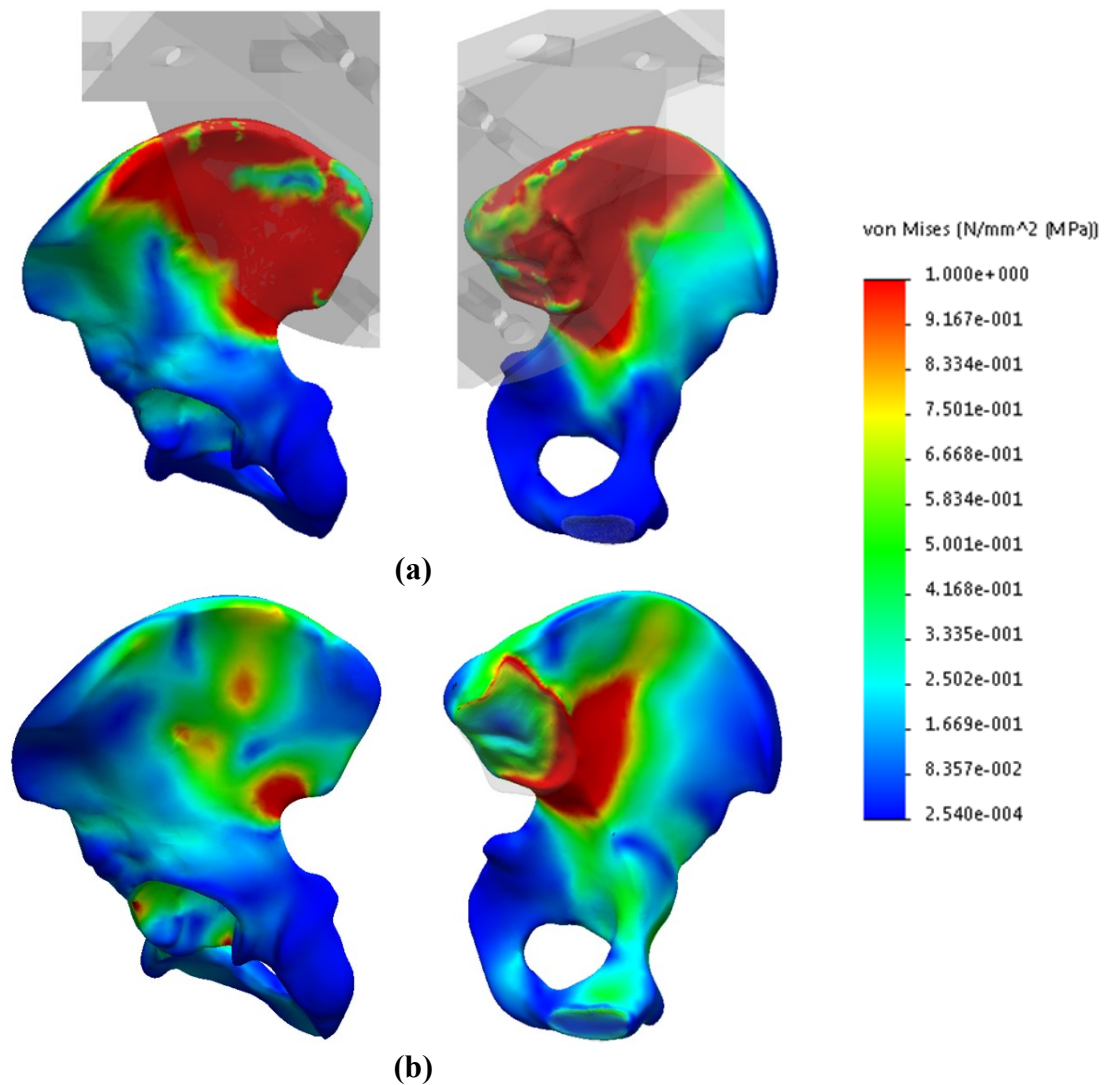
Figure 56. Comparison of pseudo-lateral and -medial views for Von Mises stress results from **(a)** pelvic fixture scenario and **(b)** fixed SI joint and sliding pubic symphysis. The comparison shows a higher stress in the clamping region within the pelvic fixture.

URES (mm)

3.550e-001
3.508e-001
3.467e-001
3.425e-001
3.383e-001
3.342e-001
3.300e-001
3.258e-001
3.217e-001
3.175e-001
3.133e-001
3.092e-001
3.050e-001

(a)

URES (mm)

5.000e-002
4.583e-002
4.167e-002
3.750e-002
3.333e-002
2.917e-002
2.500e-002
2.083e-002
1.667e-002
1.250e-002
8.333e-003
4.167e-003
0.000e+000

(b)
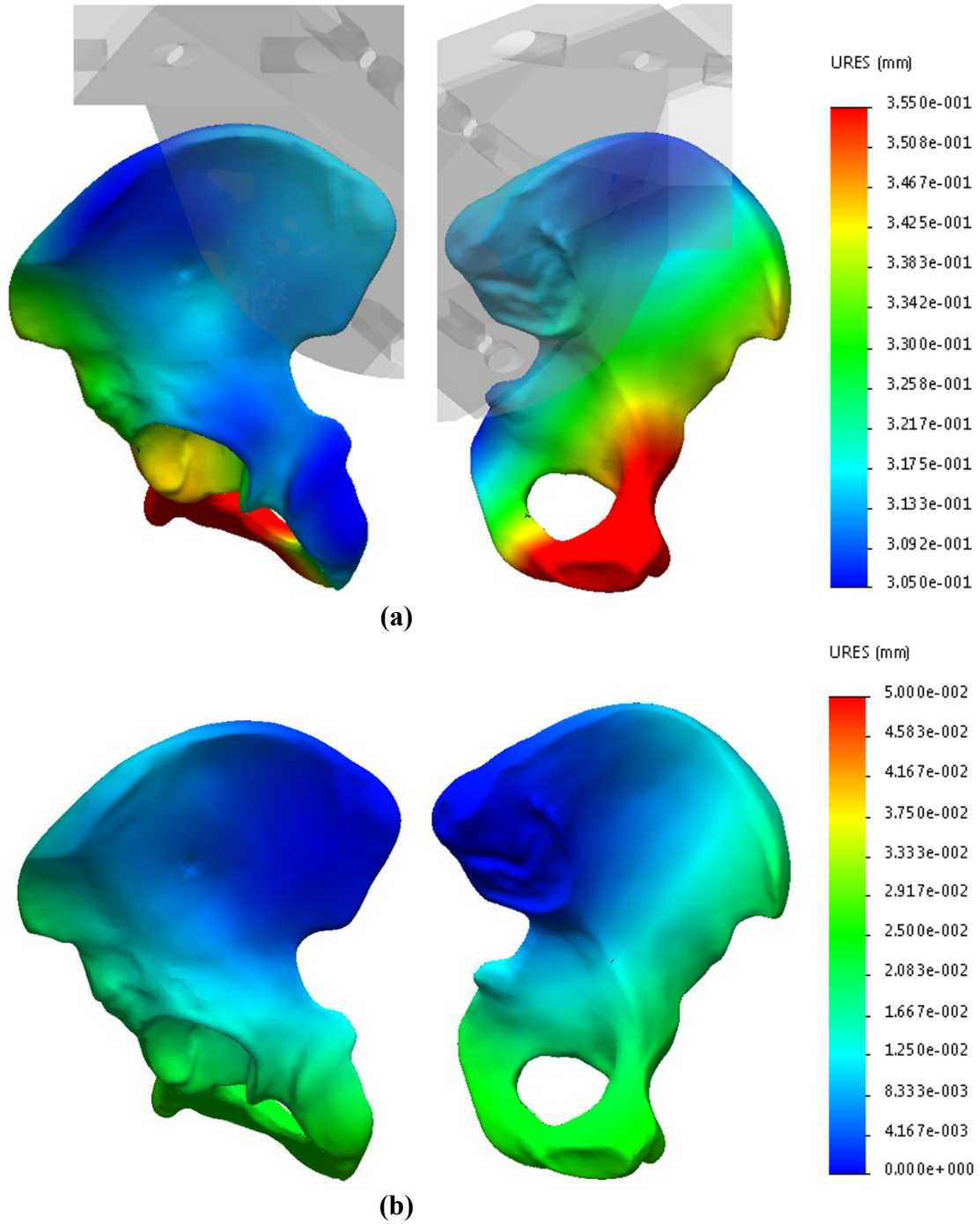
Figure 57. Comparison of pseudo-lateral and -medial views for resultant displacement results from **(a)** pelvic fixture and **(b)** fixed SI joint and sliding pubic symphysis. The comparison shows a difference in the fixation locations.

As the DIC system cannot measure stress directly, the strain fields of the test specimens were to be compared. The strains of interest were the minimum and maximum principal strains to understand the compressive and tensile loads experienced by the specimen. Figure 58 shows the numerical results for these values which served as a basis of comparison for the experimental results. Due to the deviations in the material properties between the simulation and experiment, differences in the strain magnitudes but similarities in the loading profile were anticipated.

(a)

(b)
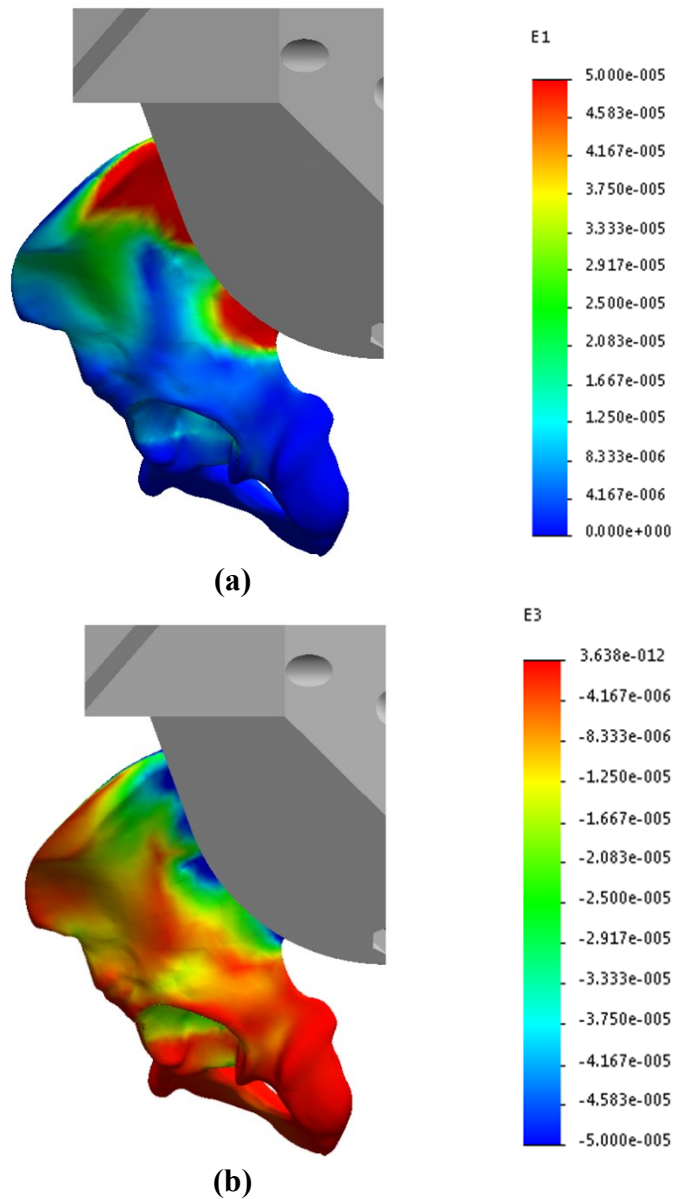
Figure 58. Numerical simulation results, showing **(a)** 1st principal strain and **(b)** 3rd principal strain.

4.3.2 Experimental simulation

In this section, strain measurements were extracted from local regions of the FOV in the experiment. This was done using software that was developed and detailed in Appendix H.

4.3.2.1 1ˢᵗ principal strain

The 1ˢᵗ principal strain fields measured from the intact pelvis loading experiment were examined to assess how the specimen was affected by tensile stresses. All experiments generated very similar loading profiles at maximum loading, all of which generally appear as shown in Figure 59. However, at the areas of high tensile strain – the greater sciatic notch, the iliac ala, and the iliac crest, as shown in Figure 59 – the strain values at maximum loading were quite variable between experiments, as compared in Table 34, with cases differing by about $\pm 45\%$. It may appear that higher load rates produced higher strain measurements, but the load rate was confounded with the clamping tightness in this set of experiments. The minimum setting of the torque wrench used could not be achieved without damage to the fixture. The clamping bolt torque did not exceed 5 ft-lb in any of the experiments.

Figure 59. Typical measured 1ˢᵗ principal strain field of intact pelvis at 500 N load with high strain regions labeled.

Table 34. Measured 1st principal strains at high strain regions at 500 N load for each intact pelvic loading test, all experiments combined, and numerical simulation results.

Case	Greater sciatic notch (με)	Iliac ala (με)	Iliac crest (με)	Details
Exp 1	14183	12656	-	*Load rate: 0.05 mm/s*
Exp 2	9097	8030	-	*Load rate: 0.05 mm/s* No foam, consecutive test
Exp 3	9888	8781	8328	*Load rate: 0.01 mm/s* Tightened clamp
Exp 4	4471	3443	2746	*Load rate: 0.01 mm/s* Tightest clamp
Exp 5	6613	5878	5708	*Load rate: 0.005 mm/s* Tightest clamp, sticky sheet
Exp 6	5500	4798	4530	*Load rate: 0.005 mm/s* Tightest clamp, sticky sheet, consecutive test
All Exp	**8292 ± 3553** **(± 43%)**	**7264 ± 3303** **(± 45%)**	**5328 ± 2342** **(± 44%)**	All experiment cases
Numerical	**84.3**	**43.5**	**92.9**	Pelvic fixture; no pubic symphysis boundary condition

As the clamping tightness of the fixture was increased, the measured strain values showed a decreasing trend. This may suggest that tightening the pelvic fixture clamp induced preloading on the specimen. A similar trend was observed between consecutive tests, specifically tests conducted without removing the specimen from the testing rig. It may have been that the loading of the pelvis in the first test forced the pelvis more rigidly into the pelvic fixture, resulting in the specimen starting in a tighter grip with higher preloading. To further investigate this theory, the starting images of experiments 5 and 6 were correlated to examine if there was any measurable preloading effect between the tests; Figure 60 displays the correlation results. As shown in Table 35, the measured difference at the maximum loading of each set and the correlation of the reference images of both sets were highly similar. This suggests that the difference in strain measurement was likely a result of the increased rigidity from the loading in the first experiment. In a greater context,

clamping tightness may be the main contributor to the variance in strain measurements. In Section 4.3.2.3, the repeatability was assessed by applying the appropriate preload.
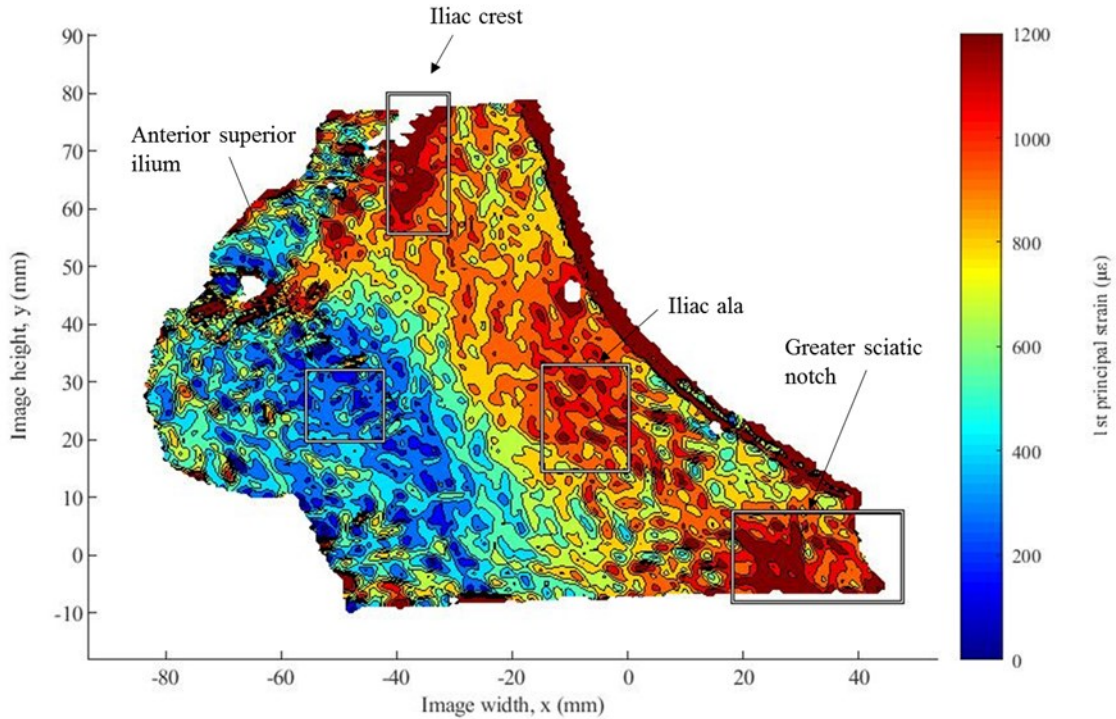
Figure 60. 1st principal strain map from correlation between reference images of experiments 5 and 6.

Table 35. Measured 1st principal strain – relationship between intact pelvis experiments 5 and 6, comparing difference between strain at maximum loading and result from correlation of the starting images of both sets.

Comparison	Greater sciatic notch ($\mu\varepsilon$)	Iliac ala ($\mu\varepsilon$)	Iliac crest ($\mu\varepsilon$)	Anterior superior ilium ($\mu\varepsilon$)
Difference at maximum load	1112	1080	1178	298
Correlation of reference images	1144	1037	1163	358
Relative difference	**-31 (3%)**	**43 (4%)**	**15 (1%)**	**-60 (20%)**

As opposed to the absolute strain measurements, comparisons of the relative magnitudes of the 1st principal strain fields of the experiments showed high agreement. These were used to compare with the numerical simulation results. The measurements at high strain locations were listed in Table 36 as a ratio to the measured strains at the anterior

superior ilium, a relatively low strain location as shown in Figure 59. Strong agreement can be observed across all tests. The relative strain ratio was 3.64 ± 0.27 (± 8%) at the greater sciatic notch, 3.14 ± 0.17 (± 5%) at the iliac ala, and 2.94 ± 0.36 (± 12%) at the iliac crest. The field of view in the first two tests did not include the iliac crest, so measurements could not be made at that region. In Figure 61 are examples of the strain ratios over time, showing a significant stretch up to the maximum loading where the strain ratios remain relatively constant. Experiments 3 and 6 are shown in Figure 61 (a) and (b) respectively; all experiments experience the same equilibrium. This suggests that within the limits of the experiment, the loading can be approximated as linear after a minimum threshold load. Zeroing the measurements at an appropriate preload would also address the variable clamping, but the relative strain ratios could provide comparison with the numerical simulation.

Table 36. Measured 1st principal strains at high strain regions at 500 N load for each intact pelvic loading test, all experiments combined, and numerical simulation results displayed as a ratio to 1st principal strain at anterior superior ilium.

Case	Greater sciatic notch	Iliac ala	Iliac crest	Details
Exp 1	3.44	3.07	-	*Load rate: 0.05 mm/s*
Exp 2	3.37	2.98	-	*Load rate: 0.05 mm/s* No foam, consecutive test
Exp 3	3.38	3.00	2.85	*Load rate: 0.01 mm/s* Tightened clamp
Exp 4	4.01	3.09	2.46	*Load rate: 0.01 mm/s* Tightest clamp
Exp 5	3.80	3.38	3.28	*Load rate: 0.005 mm/s* Tightest clamp, sticky sheet
Exp 6	3.82	3.33	3.15	*Load rate: 0.005 mm/s* Tightest clamp, sticky sheet, consecutive test
All Exp	**3.64 ± 0.27 (± 8%)**	**3.14 ± 0.17 (± 5%)**	**2.94 ± 0.36 (± 12%)**	All experiment cases
Numerical	**3.82**	**1.97**	**4.21**	Pelvic fixture; no pubic symphysis boundary condition

Figure 61. Ratios of 1st principal strains of intact pelvis at key locations to strain at anterior superior ilium as a function of load for **(a)** experiment 3 and **(b)** experiment 6. Relative loading profile asymptotes towards maximum loading of tests.

In comparison with the numerical simulations, the measured 1st principal strain fields of the experiments were orders of magnitudes beyond the results from the numerical simulations. This was expected as the hemipelvis was treated as homogenous cortical bone in the numerical simulation, making it much stiffer than in reality. However, in comparing the 1st principal strain fields of the numerical simulations, the experiment results were similar. There is a difference in position of the high strains, with the measured strain fields situated more anteriorly and inferiorly than the simulation, as shown by the comparison in Figure 62. The numerical simulation treats the pelvic fixture quite rigidly, but there was likely more clearance and movement within the clamping area in the experiment, causing the difference between the two. But as seen on Table 36, the strain ratios of the experiment are in close agreement with the simulation regarding the greater sciatic notch, with that of the iliac ala and iliac crest within the same magnitude.

(a)   **(b)**
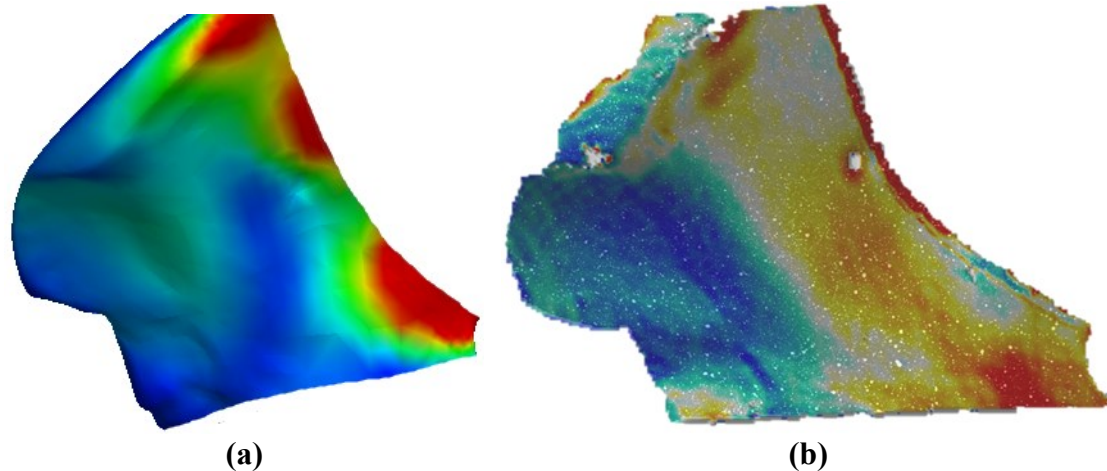
Figure 62. General comparison of 1st principal strain fields for **(a)** numerical simulation and **(b)** experimental measurements of intact pelvis.

There is also more loading in the superior acetabulum region in the experiment compared to any numerical simulation. The numerical simulations evenly distributed a unidirectional load across the upper hemisphere, but it may not be exactly so in the experiment. Potential loosening and displacement of the specimen within the fixture could cause relative rotation of the specimen resulting in an alteration in the loading orientation. Based on the loading conditions, any rotation would likely be in a general clockwise direction, meaning a smaller adduction angle. Figure 63 shows the results of a numerical simulation with an additional load with smaller adduction. As the load increases to 50 N then 100 N as shown in Figure 63 (a) and (b) respectively, the strain field becomes more similar to that measured and displayed in Figure 62 (b). This suggests that unevenness in distribution and misalignment of location may be responsible for the shift of the strain profile observed in the experiment.
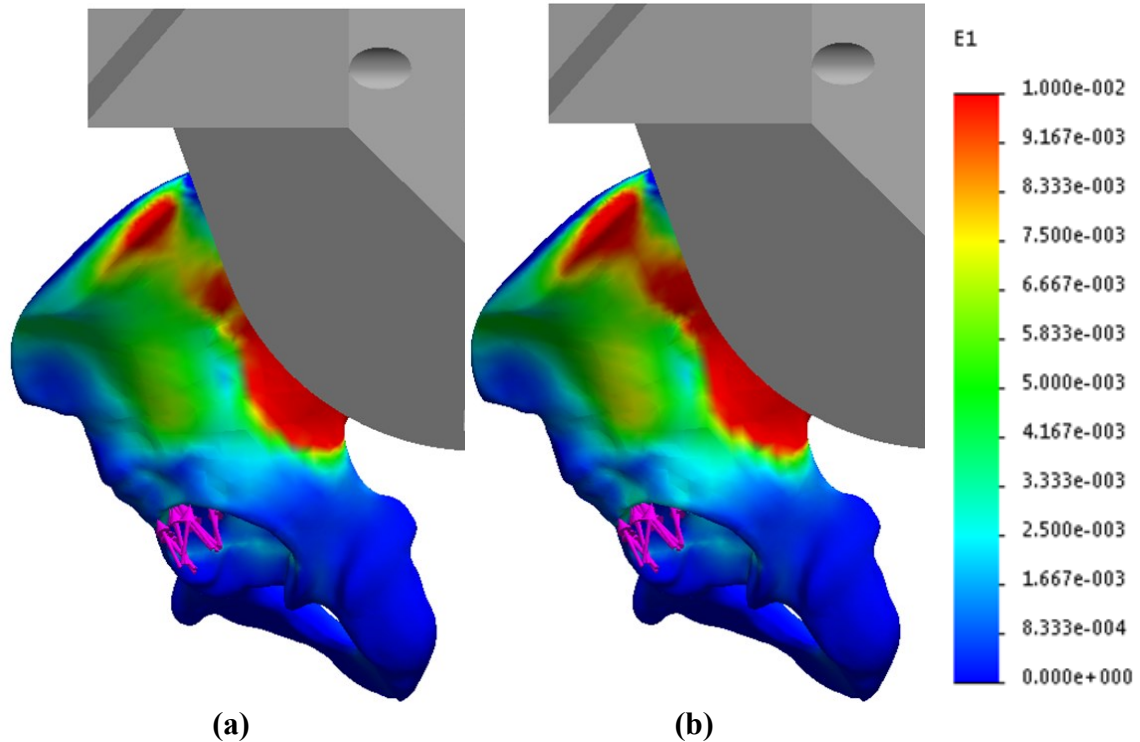
Figure 63. Numerical simulations of intact pelvis with additional force with smaller adduction angle than unidirectional 500 N load, showing 1st principal strain field for **(a)** an additional 50 N load and **(b)** an additional 100 N load.

4.3.2.2 3rd principal strain

The 3rd principal strain fields were also examined to investigate the compressive effects on the intact pelvis. Similar to the 1st principal strain measurements, the strain fields were similar across all experiments, appearing as that shown in Figure 64. In this case, the locations of high strain were at the anterior iliac crest and the anterior iliac spine, as shown in Figure 64. As listed in Table 37, there was a wide range of measured strain values at 500 N of loading for all experiments at the locations of interest. Table 38 displays a comparison of the strain measurement differences between experiments 5 and 6 at maximum loading versus the correlation of the starting images of both experiments. The similarity within the comparison can be explained like in the 1st principal strain study: preloading was imposed from the loading of the first experiment. Therefore, as previously stated, the repeatability was assessed after preloading in Section 4.3.2.3.
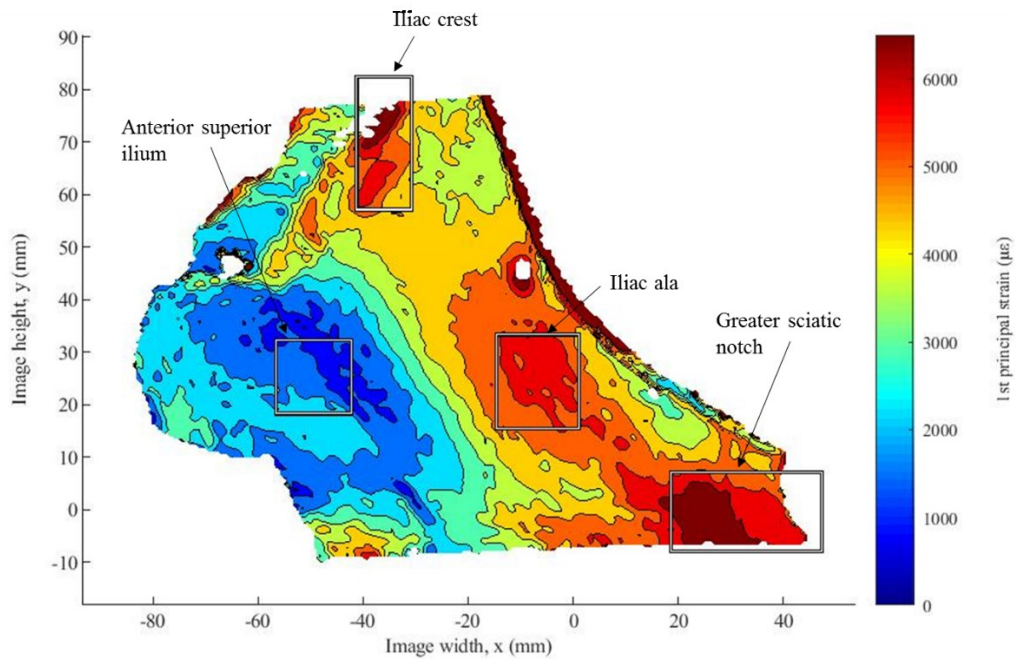
127
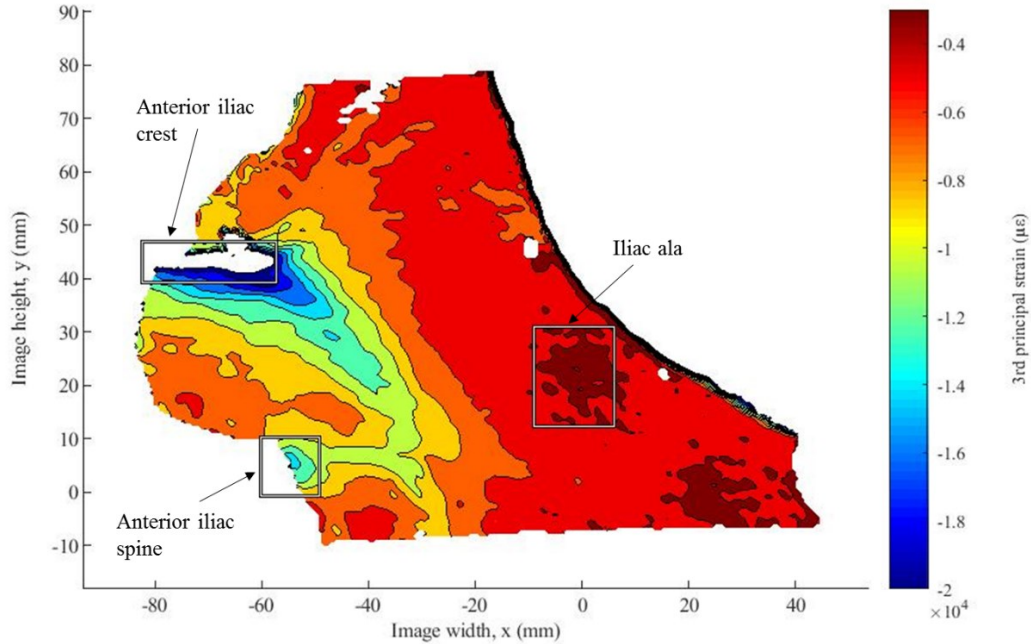
Figure 64. Typical measured 3rd principal strain field of intact pelvis at 500 N load with high strain regions labeled.

Table 37. Measured 3rd principal strains at high strain regions at 500 N load for each intact pelvic loading test, all experiments combined, and numerical simulation results.

Case	Anterior iliac spine (με)	Anterior iliac crest (με)	Details
Exp 1	-18485	-29291	*Load rate: 0.05 mm/s*
Exp 2	-12527	-18907	*Load rate: 0.05 mm/s* No foam, consecutive test
Exp 3	-12720	-28535	*Load rate: 0.01 mm/s* Tightened clamp
Exp 4	-6323	-11121	*Load rate: 0.01 mm/s* Tightest clamp
Exp 5	-10175	-19787	*Load rate: 0.005 mm/s* Tightest clamp, sticky sheet
Exp 6	-8390	-16283	*Load rate: 0.005 mm/s* Tightest clamp, sticky sheet, consecutive test
All Exp	**-8359 ± 4763 (± 57%)**	**-15772 ± 9586 (± 61%)**	All experiment cases
Numerical	**-10.9**	**-11.5**	Pelvic fixture; no pubic symphysis boundary condition

Table 38. Measured 3rd principal strain – relationship between intact pelvis experiments 5 and 6, comparing difference between strain at maximum loading and result from correlation of the starting images of both sets.

Comparison	Anterior iliac spine ($\mu\varepsilon$)	Anterior iliac crest ($\mu\varepsilon$)	Iliac ala ($\mu\varepsilon$)
Difference at maximum load	-1785	-3504	-518
Correlation of reference images	-1794	-3453	-565
Relative difference	**10 (1%)**	**-51 (1%)**	**47 (9%)**

Additionally, there was also high agreement when comparing relative strains at high strain locations. The 3rd principal strain measurement ratios are listed in Table 39, where it can be seen that there is strong agreement across the experiments for the 3rd principal strain field. Figure 65 shows that the strain ratios were constant for a significant range up to the test maximum loading for experiments 3 and 6, similarly to the 1st principal strain ratios. This was the case across all tests. The values are also similar to those resulting from the numerical simulation. The major difference was that the anterior iliac crest was predicted by the numerical simulation to have less strain than the measurements.

Table 39. Measured 3rd principal strains at high strain regions at 500 N load for each intact pelvic loading test, all experiments combined, and numerical simulation results displayed as a ratio to 3rd principal strain at iliac ala.

Case	Anterior iliac spine	Anterior iliac crest	Details
Exp 1	3.58	5.67	*Load rate: 0.05 mm/s*
Exp 2	3.58	5.40	*Load rate: 0.05 mm/s* No foam, consecutive test
Exp 3	3.26	7.30	*Load rate: 0.01 mm/s* Tightened clamp
Exp 4	3.31	5.82	*Load rate: 0.01 mm/s* Tightest clamp
Exp 5	3.3	6.43	*Load rate: 0.005 mm/s* Tightest clamp, sticky sheet
Exp 6	3.28	6.36	*Load rate: 0.005 mm/s* Tightest clamp, sticky sheet, consecutive test
All Exp	**3.38 ± 0.15 (± 4%)**	**6.16 ± 0.69 (± 11%)**	All experiment cases
Numerical	**3.07**	**3.25**	Pelvic fixture; no pubic symphysis boundary condition

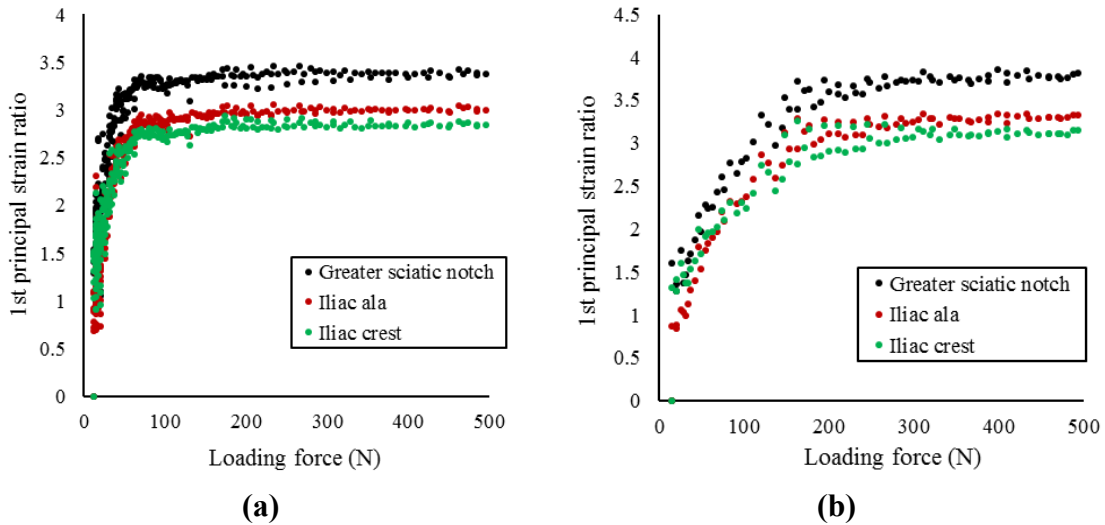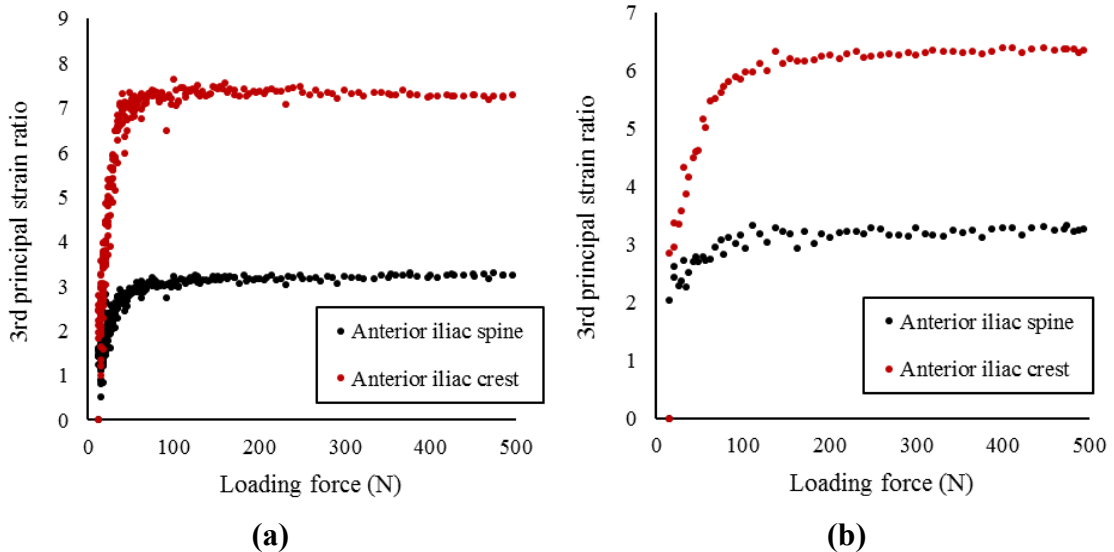**Figure 65.** Ratios of 3rd principal strains of intact pelvis at key locations to strain at iliac ala as a function of load for **(a)** experiment 3 and **(b)** experiment 6. Relative loading profile asymptotes towards maximum loading of tests.

The 3rd principal strain field had higher strain concentrations compared to the numerical simulation, as can be seen between Figure 66 (a) and (b) at the anterior iliac crest. One possible explanation for this is that the direction of the load is altered throughout the experiment due to deformation and movement within the test fixture. As shown in Figure 67, introducing a load at a smaller adduction angle can change the strain field shape. When the load was increased from 50 N to 100 N, shown in Figure 67 (a) and (b) respectively, the relative 3rd principal strains at the anterior iliac spine and anterior iliac crest increase. Also, the compressive strains at the greater sciatic notch and the inferior iliac ala are lower like that of the experiment as shown in Figure 66 (b). However, the strain at the superior iliac ala increase, suggesting that the introduced loads in the simulation may not represent the loading in the experiment. Nonetheless, it shows that differences in loading orientation is a possible explanation for differences between the numerical and experimental results.

(a)   **(b)**
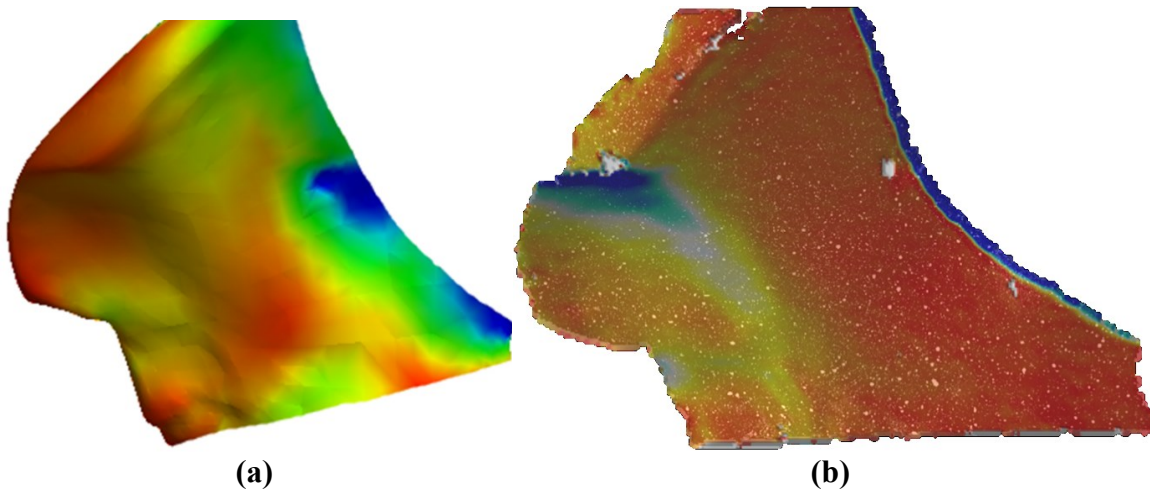
Figure 66. General comparison of 3rd principal strain fields for **(a)** numerical simulation and **(b)** experimental measurements of intact pelvis.
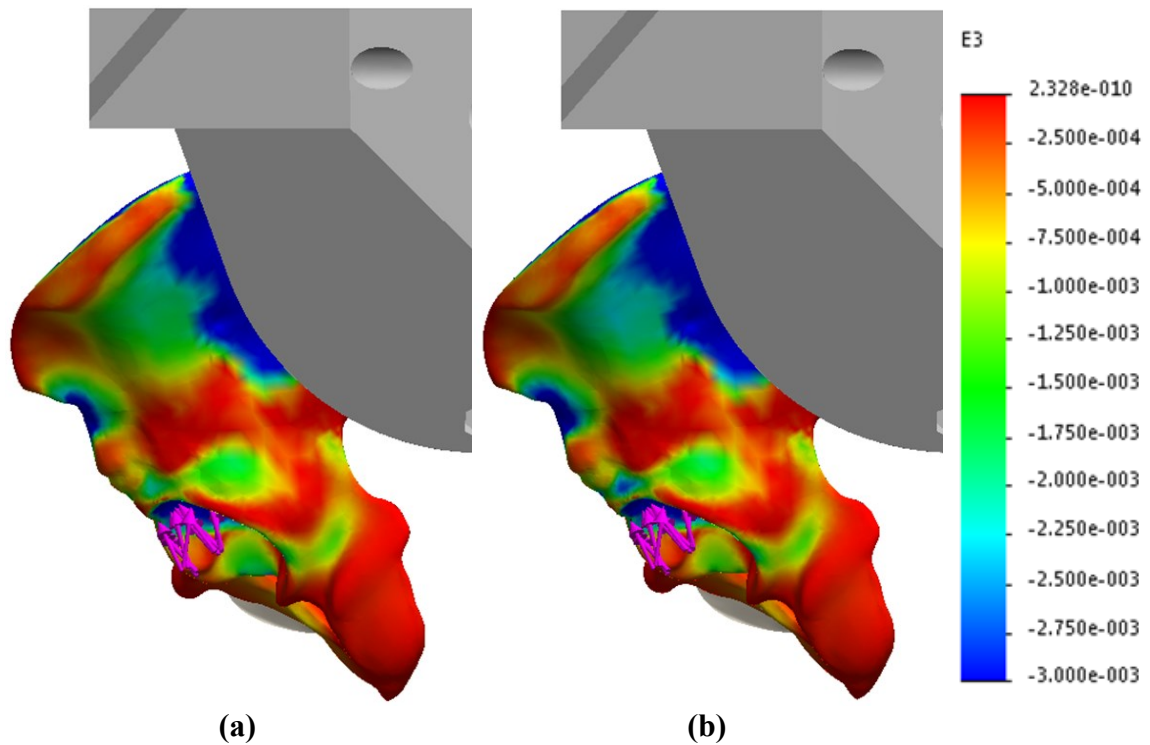
Figure 67. Numerical simulations of intact pelvis with additional force with smaller adduction angle than unidirectional 500 N load, showing 3rd principal strain field for **(a)** an additional 50 N load and **(b)** an additional 100 N load.

Another possible explanation is that there may be erroneous measurements at the anterior iliac crest in the experiment. It can be seen in Figure 50 (a) that the speckle pattern of the anterior iliac crest is the lowest quality of the specimen surface in view. Due to the surface curvature, the perspective of this region is at a significant angle and the illumination is particularly poor. This makes the anterior iliac crest highly susceptible to measurement error. High strains may be falsely detected.

4.3.2.3   Repeatability

To address the issue of the inconsistent preload, the measured strains at the ROIs were plotted as a function of the loading force for all test cases to observe trends. As shown by the example in Figure 68, it was found that after 100 N of loading, measurements in all test cases became much more linear and consistent. Therefore, the appropriate preload for this set of testing was deemed to be 100 N and all measurements were zeroed and compared at this value.
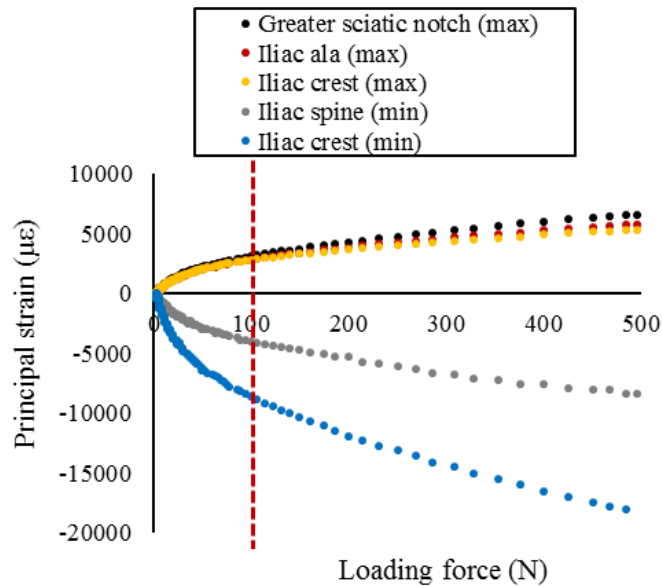
Figure 68. Typical strain vs. loading force profiles at ROIs, showing measurements for Exp 3.

The comparison provided in Figure 69 shows that across all 6 experiments, there was reasonable agreement between the measurements when examining the strains at the ROIs as a function of the loading force after preloading. One of the test cases (Exp 4) was shown to have an anomalous deviation which may have been due to significant overtightening of the specimen. The loading slope is not perfectly linear and appears to gradually reduce as the overall loading increases, meaning that the anomalous case may be representative of higher loadings and may not be comparable to the other cases. It was therefore excluded from the final determination of the repeatability listed in Table 40. From the five remaining cases, it was shown that the repeatability of the test setup was approximately 10% across the measurements.
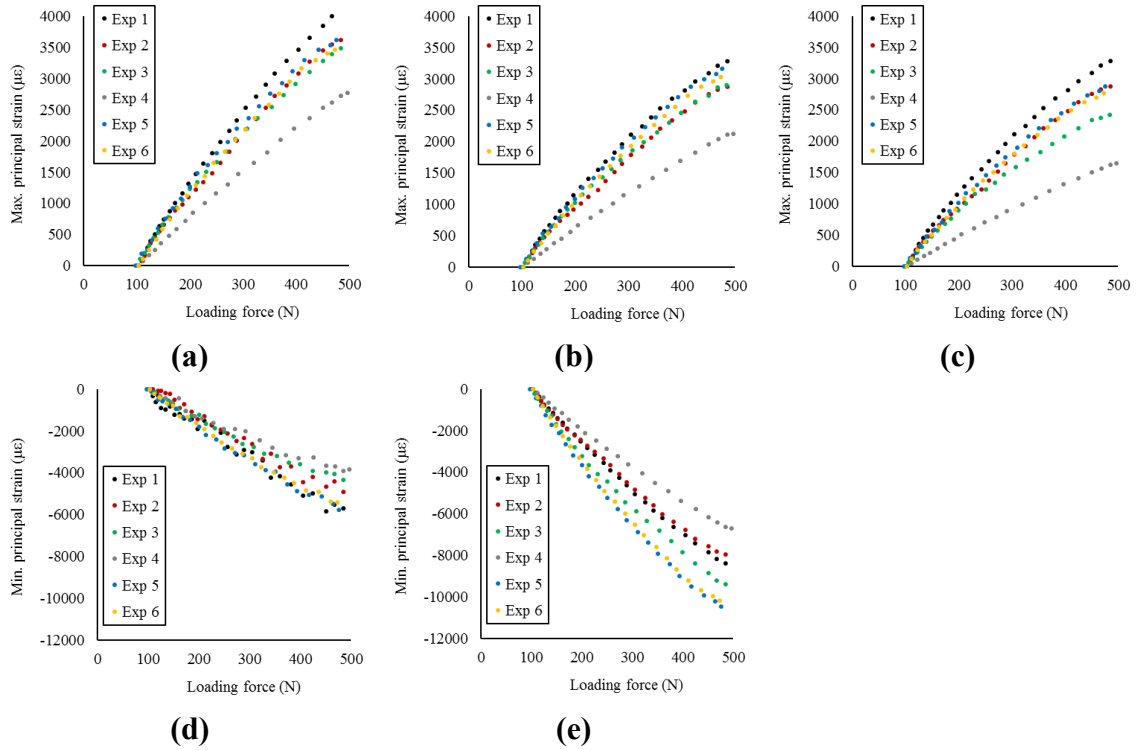
Figure 69. Comparison of strain vs. loading force plots at each ROI across all experiments for repeatability.

Table 40. Repeatability for measurements for all test cases and excluding the anomalous test case.

Region (principal strain)	All cases (με/N)	Excluding Exp 4 (με/N)
Greater sciatic notch (max)	$9.1 \pm 1.2 (\pm 13\%)$	$9.5 \pm 0.7 (\pm 7\%)$
Iliac ala (max)	$7.5 \pm 1.1 (\pm 14\%)$	$7.9 \pm 0.4 (\pm 6\%)$
Iliac crest (max)	$6.8 \pm 1.5 (\pm 21\%)$	$7.3 \pm 0.8 (\pm 11\%)$
Anterior iliac spine (min)	$-13.0 \pm 2.0 (\pm 15\%)$	$-13.6 \pm 1.4 (\pm 10\%)$
Anterior iliac crest (min)	$-22.9 \pm 3.7 (\pm 16\%)$	$-24.0 \pm 2.7 (\pm 11\%)$

There were many observed benefits provided from the designed pelvic fixture. Compared to the previous method of cement potting, the fixture designed for this experiment significantly facilitated the setup of a pelvic loading experiment. Assembly involves simply clamping the specimen in the 3D printed fixture instead of potting the specimen under a fume hood and waiting 24 hours for it to set. Disassembly simply involves loosening the clamp and removing the part, whereas the potting method necessitated a day-long process of removing the adhesive cement from the surface of the hemipelvis. Multiple experiments were conducted within a day on one specimen. As the

fixture was designed for the specified single-leg stance loading orientation, difficulties in specimen positioning were removed.

Nonetheless, there were drawbacks to using the designed fixture. The main issue was the movement of the hemipelvis relative to the clamp. There are numerous potential explanations for this. The computer model was created from a CT scan of the hemipelvis model (as opposed to one provided by the manufacturer) and deviations may have resulted from the process. There could also be deviations from this composite model from the scanned one. On the other hand, the 3D-printing process may be unable to sufficiently capture the complexity of the specimen surface. Any combination of these factors may have caused incongruence between the fixture and the specimen allowing for relative movement between the two.

Several approaches were taken to reduce the relative movement with the current design of the fixture. The use of a small piece of foam to distribute the load within the acetabular cup seemed to be ineffective at limiting displacement. A high-friction rubber sheet was inserted at the SI joint but also proved ineffectual. But as previously mentioned and shown in Table 34 and Table 37, tighter clamping resulted in lower measured strains. Tests conducted within the same setup showed the same effect, as the loading from previous experiments were believed to have imposed rigidity on the specimen within the fixture. This suggest that even though tightness can minimize relative displacement, it may introduce various amounts of preloading on the specimen. A standard bolt torque should be established for more consistent absolute measurements across tests. In this study, over-tightening resulted in damage to the clamp. The minimum setting on the torque wrench of 5 lbf-ft was not reached before minor damage occurred. These observations should be considered when assembling the specimen and fixture for an experiment.

Overall, the designed fixture was simple and easy to use. Though the raw strain measurements were variable, they were similar after zeroing at the preload. Inconsistencies could be addressed by redesigning the fixture with an increased interior clearance and accommodating the difference between the shape of the clamp and the hemipelvis using a compressible foam material. The use of a stronger, stiffer material for the fixture could also reduce movement of the specimen within. Consistency could also be improved by quantifying the clamping force (bolt torque) required to properly constrain the specimen.

4.3.3 Uncertainty analysis

The sources of uncertainty in this experiment were analyzed to assess where the measurements may be erroneous such that they could be understood and anticipated in the fractured pelvis experiments. For brevity sake, only experiment 6 was analyzed. Regarding both the 1st and 3rd principal strain measurements, the uncertainty was estimated individually per local area.

The strain quantifications were presented as a ratio to the low strain region, as shown in Figure 59 and Figure 64 for 1st and 3rd principal strains respectively. This yielded the equation,

$$SR_n = \frac{\varepsilon_n}{\varepsilon_{ref}} \tag{23}$$

where:

SR_n is the strain ratio at local area n,
ε_n is the strain measured at the high strain local area n, and
ε_{ref} is the strain measured at the low strain reference area.

The uncertainty propagation of the equation could then be estimated as,

$$\frac{U_{SR_n}}{SR_n} = \sqrt{\left(\frac{U_{\varepsilon_n}}{\varepsilon_n}\right)^2 + \left(\frac{U_{\varepsilon_{ref}}}{\varepsilon_{ref}}\right)^2} + \frac{U_{SR_{load}}}{SR_{load}} \tag{24}$$

where:

U_p is the estimated uncertainty of parameter, p,
SR_{load} is the strain ratio measured at the maximum load.

The uncertainty associated with SR_{load} was due to the ambiguity of preloading in the experiment. This means the measured maximum load of each test, 500 N, may not have been the true load of each experiment. As the strain ratios were constant for a section up to and including the maximum load, the associated uncertainty, $U_{SR_{load}}$, was the standard deviation of all measurements in the constant region.

For the strain measurements, both local and reference strain measurements had the same sources of uncertainty. One source of uncertainty was the DIC system. For a measurement within one subset, it could be quantified with out-of-plane rigid body displacement and the equation,

$$U_\varepsilon = \frac{\sqrt{2}U_x}{L_0}$$

where:

U_x is the uncertainty of measured displacement, and

L_0 is the gage length.

The equation represents the measurement uncertainty of one subset. From the morphological analysis and the subset size of this investigation, the uncertainty of a single subset strain measurement would be an estimated 1325 µε. However, in this study, the regions of interest contained multiple subsets. The gage length, L_0, was taken as the smallest length of a selected instead. The other source of uncertainty was the ambiguity of the area selection for the strain measurements. Minor differences were inevitable when specifying the area of measurement due to viewing angle differences between the tests. This component was quantified by repeating the procedure of selecting an area and measuring it, then calculating the standard deviation for all measurements. The overall uncertainty of a strain measurement could then be represented as,

$$U_\varepsilon = U_{DIC} + U_{area} \tag{25}$$

From the uncertainty analysis of the 1st principal strain measurements, the estimations listed in Table 41 show that the most prominent source of uncertainty was the strain measurement. This is because the strains measured in the experiment were extremely small and the field of view was relatively large, as it was desired to capture a big area of the hemipelvis. The window size was selected based on the speckle pattern morphological characteristics. A larger window size would have reduced the measurement uncertainty if desired, but at the cost of measurement resolution. For this experiment, larger window sizes would have been more optimal, as there were no discernable local strain gradients that would have been missed.

Table 41. Estimates for uncertainties of 1st principal strain ratios for intact pelvic testing, showing the uncertainty as the absolute value and as the relative value in parenthesis.

Uncertainty	Greater sciatic notch	Iliac ala	Iliac crest
Reference strain (µε)	**1282 ± 234 (18%)**	*	*
Area selection (µε)	*± 18 (1%)*	*	*
DIC system (µε)	*± 216 (17%)*	*	*
	(L_0 = 15 mm)		
Local ROI strain (µε)	**5582 ± 273 (5%)**	**4842 ± 230 (5%)**	**4770 ± 356 (7%)**
Area selection (µε)	*± 57 (1%)*	*± 14 (1%)*	*± 32 (1%)*
DIC system (µε)	*± 216 (4%)*	*± 216 (4%)*	*± 324 (6%)*
	(L_0 = 15 mm)	(L_0 = 15 mm)	(L_0 = 10 mm)
Strain ratio	**3.82 ± 0.79 (21%)**	**3.33 ± 0.70 (21%)**	**3.15 ± 0.70 (22%)**
Cumulative strain	*± 0.72 (19%)*	*± 0.63 (19%)*	*± 0.62 (19%)*
Load ambiguity	*± 0.07 (2%)*	*± 0.07 (2%)*	*± 0.08 (3%)*

*Same value for all cases.

It was also evident that more uncertainty varied from different areas of measurement. The reference region (the anterior superior ilium) had a higher relative uncertainty due to the measurement being smaller in magnitude. As a result, it was the highest source of uncertainty in the experiments. This uncertainty could be reduced by observing a larger area (*i.e.*, increasing the gage length). However, that would increase the ambiguity of the ROI boundaries. A balance between clearly defining a ROI and minimizing uncertainty is key.

Compared to the strain measurements, the other sources of uncertainty were small contributors. The variation in defining the local ROIs had a much smaller impact on the measured strain. In assessing the ambiguity of the loading force at the time of measurement, the strains across the linear region leading up to maximum loading were compared. Little variation occurred for a significant portion of the loading throughout the experiment. This also means that the exact force of the load at measurement is not overly significant within the loading limits of this experiment; the relationships are constant for a wide range of loading. Compared to the uncertainty contribution of the measurement of 1st principal strains by the system, all other sources of uncertainty have a relatively low impact on the measurement quality.

Similar observations were made when analyzing the uncertainty of 3rd principal strain field measurements. The estimated uncertainties for each local ROI are listed in Table 42. The DIC system that was measuring the strains was the primary source of uncertainty. The area selection and load ambiguity had comparatively insignificant impact. However, the uncertainties in the strain ratios were lower for the 3rd principal strains as the reference region had larger magnitudes of measurement, reducing the relative uncertainty. Therefore, it may be worthwhile to increase the maximum loading of the experiment, taking measurements of higher strains for a lower overall uncertainty.

Table 42. Estimates for uncertainties of 3rd principal strain ratios for intact pelvic testing, showing the uncertainty as the absolute value and as the relative value in parenthesis.

Uncertainty	Anterior iliac spine	Anterior iliac crest
Reference strain (µε)	**-2556 ± 234 (9%)**	*
Area selection (µε)	*± 18 (1%)*	*
DIC system (µε)	*± 216 (8%)*	*
	(L_0 = 15 mm)	
Local ROI strain (µε)	**-8911 ± 608 (7%)**	**-15865 ± 1277 (8%)**
Area selection (µε)	*± 284 (3%)*	*± 630 (4%)*
DIC system (µε)	*± 324 (14%)*	*± 647 (4%)*
	(L_0 = 10 mm)	(L_0 = 5 mm)
Strain ratio	**3.28 ± 0.45 (14%)**	**6.23 ± 0.85 (14%)**
Cumulative strain	*± 0.37 (12%)*	*± 0.76 (13%)*
Load ambiguity	*± 0.08 (2%)*	*± 0.09 (1%)*

*Same value for all cases.

In the experiment, higher discrepancy in results were observed in the local areas that were closer to the edge of the correlation field, such as the greater sciatic notch and the iliac crest. One reason is that the correlation algorithm quantifies strain at a subset as a function of its neighbors. At the edge of the correlation space, the subsets do not have neighbors on all sides of the subset. The strain is then calculated by the software using the neighbors available [149], which are those inwardly to the specimen surface. This effectively reduces the gage length of the strain measurement by half, thereby doubling the uncertainty of the subsets at the edge locations. This can be addressed by simply taking measurements a safe distance from the edge or reducing the subset size such that the edge is effectively reduced in size and allowing for measurements closer to the specimen edge.

It could also be that different areas were being measured due to changes in the FOV of the experiment.

At the iliac crest, the uncertainties in both 1st and 3rd principal strain measurements were notably higher than the other measurements. This is likely due to the poor quality of the speckle pattern at that location, as shown in Figure 50 (a). There are many available approaches that can address this concern. The specimen can be repainted to improve the speckle pattern, the camera field of view can be reangled or rescaled to better accommodate the specimen curvature, or the illumination can be improved to allow for a more even distribution of light to make the speckles equally viewable across the specimen surface.

There are other aspects of the experiment that likely affected the results, but they could not be properly quantified in the uncertainty estimation. The clamping tightness of the fixture was a likely source of uncertainty, but it could not be measured as no bolts reached the minimum limit of the torque wrench used. Also, the loading orientation could not be properly measured in this setup. It was roughly 12° adduction as per the design, but as shown earlier, small deviations to the loading angle may have large effects. Future experiments should seek to quantify the bolt torque and the loading orientation to better understand the sources of uncertainty within the experiment.

4.3.4 Summary

An experimental setup was designed to simulate single-stance loading of a composite hemipelvis model. By examining the 1st and 3rd principal strain fields under loading, the maximum tensile and compressive loads could be studied. The study revealed the successes and drawbacks of the system and the analysis approach. The designed pelvic fixture greatly facilitated the testing in terms of time and material resources. There were concerns with the probable movement of the specimen within the fixture. The tightness of the clamp was observed to have a significant effect on the magnitude of the measured strain values on the pelvis. It was observed that tightening the clamp had imposed preloading on the specimen, causing the measured strain values of more tightly clamped tests to appear noticeably smaller in magnitude. However, for all six tests conducted, the relative strain fields were very similar to one another. This parameter was useful for comparing the results to the numerical analysis, but zeroing the measurements at 100 N of preload showed repeatability

across the test cases and was more meaningful for comparing across experimental results. Therefore, in the fractured pelvis testing, the strains were analyzed after the application of preloading. The repeatability of this setup for pelvic loading simulations was observed to be approximately 10% across the experiments.

Preliminary numerical analysis was performed on the experimental setup for a baseline of comparison. First, it was compared with a simulation of the hemipelvis constrained at the SI joint and sliding at the pubic symphysis to mimic more realistic biomechanical conditions. It was observed that the numerical simulations were similar, both containing a high strain region connecting the iliac crest to the greater sciatic notch in the profile of an iliac FFP. However, there was a stress reduction at the ischial ramus in the simulation with the fixture, and the high strain regions on the ilium were located more posteriorly in comparison to the constrained hemipelvis simulation. It was observed that adjusting the direction of the load in the simulation created similar strain fields to those observed in the experiment, suggesting that the loading orientation varied from that intended. Deviations could also have arisen from the homogeneity of the specimen material (as only cortical bone), profile construction errors from the CT scan, or inaccuracies in the 3D-printing manufacturing. Future work should aim to more rigorously investigate numerical simulations with a more in-depth study and use a more representative model (such as one provided by the manufacturer).

From the uncertainty analysis of the system, it was observed that changes could be made to the strain measurement uncertainty to improve the overall quality of the experiment. The results of the intact pelvis experiment provide a baseline of expectations to build from. Knowledge of the high tensile and compressive strain areas can be used to optimize the field of view for more specific experiments in the future. Knowing the magnitudes of the strains to be measured can also help determine the parameters of the DIC system to increase the overall quality of measurements. The results of this experiment could then be used as a datum of comparison for the more complicated case of loading a fractured hemipelvis.

4.4 Fractured pelvis

In this section, a fractured composite hemipelvis specimen, shown in Figure 48 (b), was observed under the same mechanical loading conditions as the previous section with the intact hemipelvis. Numerical and experimental analyses were performed and compared to study the potential errors in both case with respect to realistically simulating the biomechanical loading conditions. The results were also compared with the previous intact hemipelvis study to understand how the fracture alters the biomechanics of the hemipelvis.

Three experiments were conducted on a fractured pelvis specimen to verify the repeatability. The displacement fields were examined to assess how the crack influences the movement of the pelvis. Then, the 1st and 3rd principal strain fields were observed to understand how the tensile and compressive loads on the pelvis were affected due to the presence of the fracture. And finally, the crack edge displacements were measured to determine the magnitude and direction of the fracture motion. They were quantified by the three fracture modes: opening (mode I), shearing (mode II), and tearing (mode III), as shown in Figure 70. From the results of the biomechanical testing, potential approaches to managing the fracture behavior were assessed.

| Mode I (opening) | Mode II (shearing) | Mode III (tearing) |
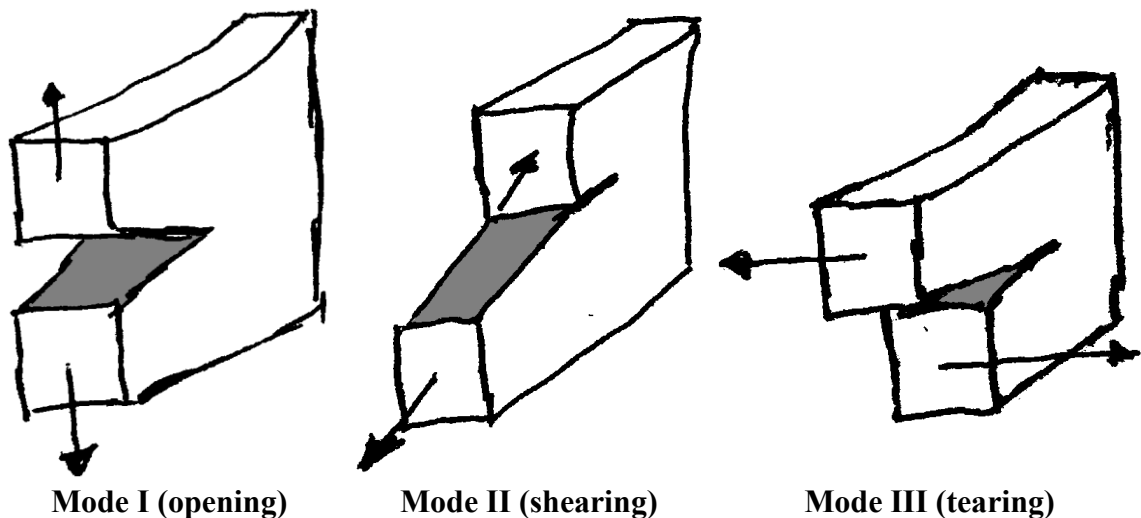
Figure 70. Comparison of the three modes of fracture: opening (mode I), shearing (mode II), and tearing (mode III).

4.4.1 Numerical simulation

4.4.1.1 Numerical simulation setup

The numerical simulation performed on the fractured hemipelvis case was conducted to provide a baseline comparison for experimental results. The reason was the same as the with the intact pelvis. However, theoretical calculations of mechanically loading a fractured specimen is much more complex than an intact pelvis. Therefore, the theoretical analysis was deemed to be not an option in this portion of the study. The specimen model itself was altered to mimic a pre-existing cracked specimen from a previous study, as shown in Figure 48 (b). As the exact geometry of the crack was not documented, manual estimations were made to approximately mimic the crack in the 3D model. There were two major visible cracks on the physical specimen. The primary one originated at greater sciatic notch and stretched to the middle of the iliac ala towards the iliac crest, similarly to an iliac FFP. A secondary crack branched from a point inferior to the primary crack tip at a near-perpendicular angle and traversed posteriorly and superiorly through the iliac ala.

The material properties for the specimen and fixture were the same as the intact simulation, as listed in Table 43. The fractured hemipelvis was within the clamp and the top surface of the clamp was fixed. To simulate single-leg stance, a 500 N force was applied into the upper acetabular hemisphere at a 12° adduction angle. The mesh settings of the numerical simulations are listed in Table 44. Due to limitations in time and scope, multiple iterations were not performed and convergence was not pursued in this set of simulations.

Table 43. Summary of solver settings for fractured pelvis numerical simulations.

Attribute	Value
Specimens	Fractured pelvis (E = 16.7 GPa, σ_y = 93 MPa, ν = 0.3) Clamp (E = 2 GPa, σ_y = 50 MPa, ν = 0.394)
Mechanics	Linear static
Boundary conditions	Pelvic fixture top surface fixed
Loading conditions	12° adduction into upper acetabular hemisphere, total 500 N
Software	Solidworks Simulation 2017
Solver	FFEPlus (explicit)
Algorithms	Newton-Raphson
Convergence criteria	0.1%

Table 44. Fractured pelvis numerical simulation mesh settings.

Mesh	Fractured hemipelvis
Mesher	Curvature-based
Jacobian points	4
Mesh control	-
Max. element size (in)	0.5
Min. element size (in)	0.1
Number of nodes	163563
Number of elements	105591
Max. aspect ratio	45.467
Aspect ratio < 3 (%)	97.2
Aspect ratio < 10 (%)	1.07

4.4.1.2　Comparison to intact numerical simulation

The relative displacement fields calculated by the numerical simulations were compared between the intact pelvis and the fractured pelvis, as shown in Figure 71. Note that the scale is relative as the intact pelvis case could not be solved with large displacements and thus yielded much smaller displacement values. In the x-, y-, and z-directions, the displacement fields contained a discontinuity at the primary crack in the fractured pelvis case. Superior to the crack, there was much less movement than the region inferior. This was expected as the specimen was fixed at the SI joint and the crack allowed freer motion of the inferior hemipelvis. In the x- and y-directions, shown in Figure 71 (a) and (b) respectively, the displacement fields were generally similar between the intact and fractured specimens. But in the z-direction, shown in Figure 71 (c) the displacement field was much more lateral inferior to the crack, suggesting that more out-of-plane motion in the lower portion of the hemipelvis had resulted due to the freedom of motion created by the presence of the fracture.
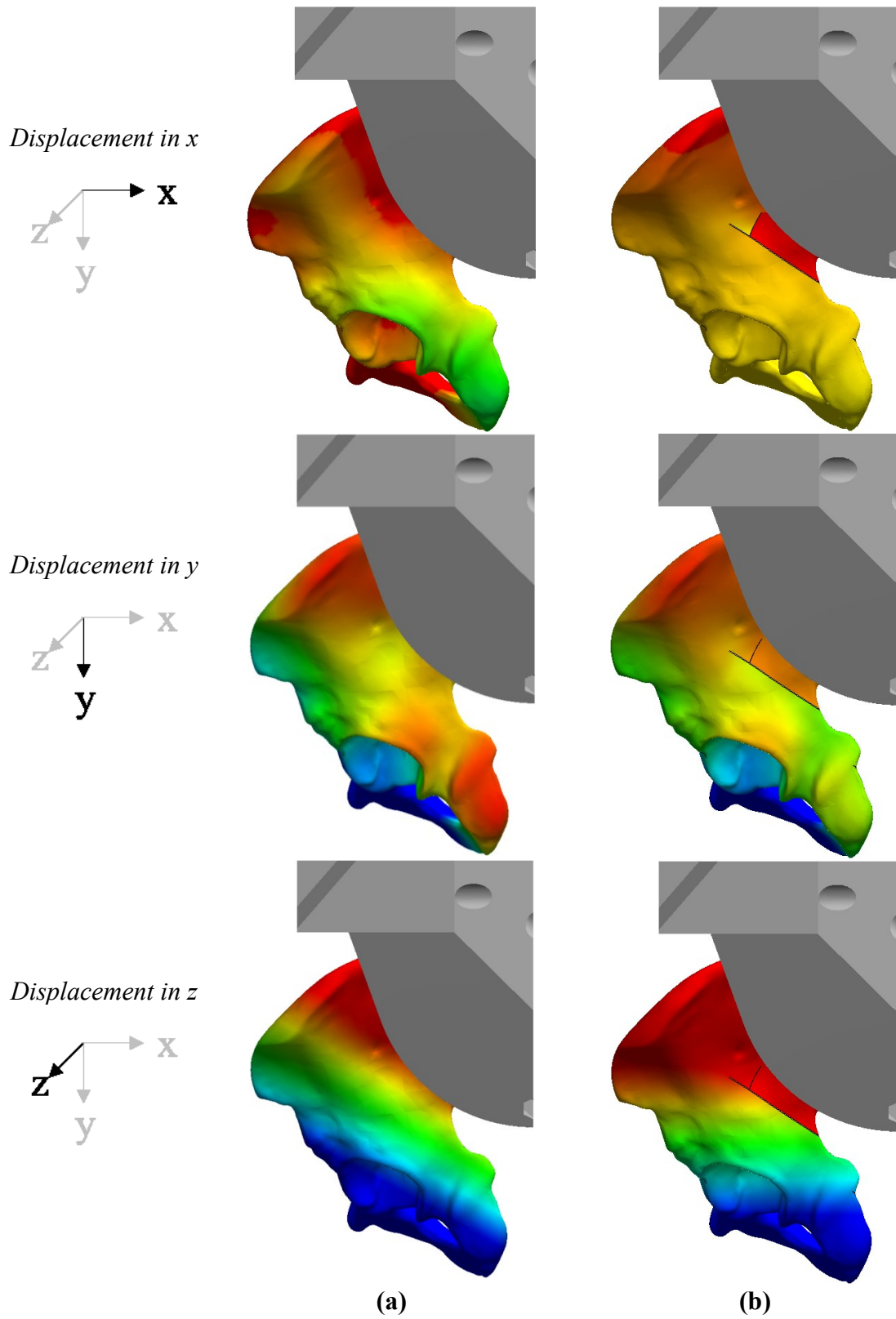
Figure 71. Numerical simulation results, comparing the x-, y-, and z-displacement fields of **(a)** the intact pelvis and **(b)** the fractured pelvis.

The 1st principal strain fields between the fractured and intact cases contained noticeable differences Figure 72. In the fractured scenario, the strain concentration localized at the greater sciatic notch was no longer there due to the presence of the primary crack edge. The highest strain localizations were at the crack tips instead. There was also another tensile stress region anterior to the primary crack tip, suggesting the direction of potential crack propagation in the loading scenario. Similar observations were made in studying the numerical simulation results of the 3rd principal strain fields Figure 73. The fractured specimen no longer contained high compressive stresses at the greater sciatic notch, similarly to the 1st principal strain case. The highest compressive strain was found at the primary crack tip, and high strains were observed to flow from the crack tip in two directions: 1) superiorly to the iliac crest and 2) anteriorly to the anterior-superior iliac spine. Also, in both 1st and 3rd principal strain field comparisons, strains induced by the pelvic fixture clamping were less significant in the fractured case compared to the maximum strains across the specimen.

(a)   (b)
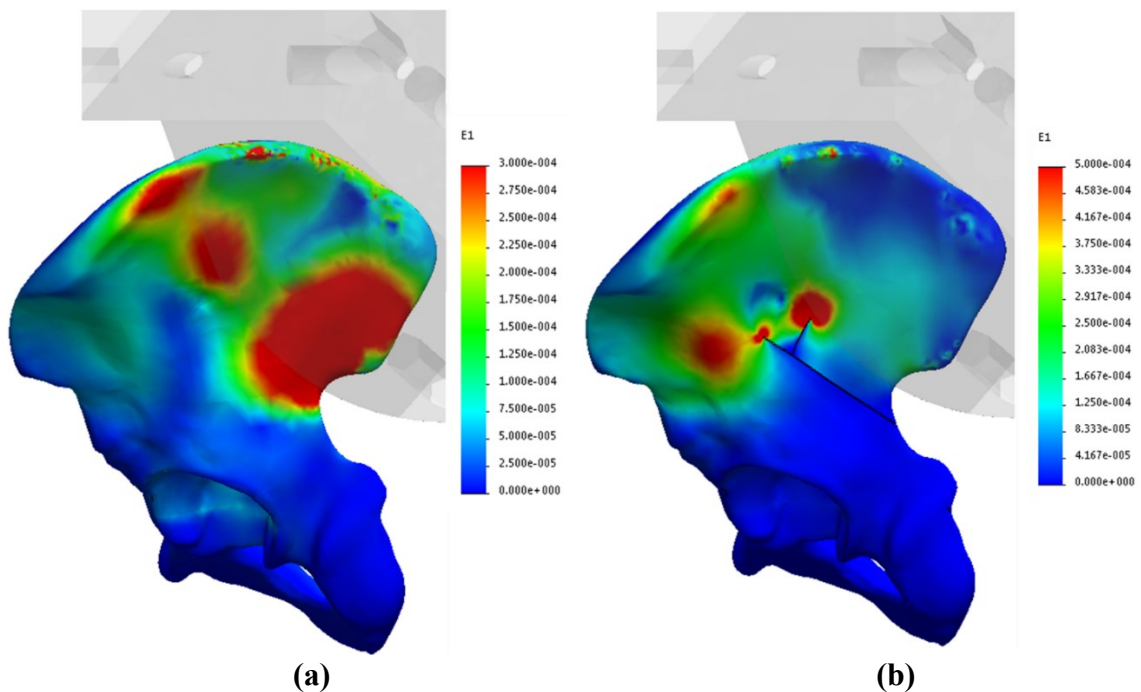
Figure 72. Numerical simulation results, comparing the 1st principal strain fields of **(a)** the intact pelvis and **(b)** the fractured pelvis.
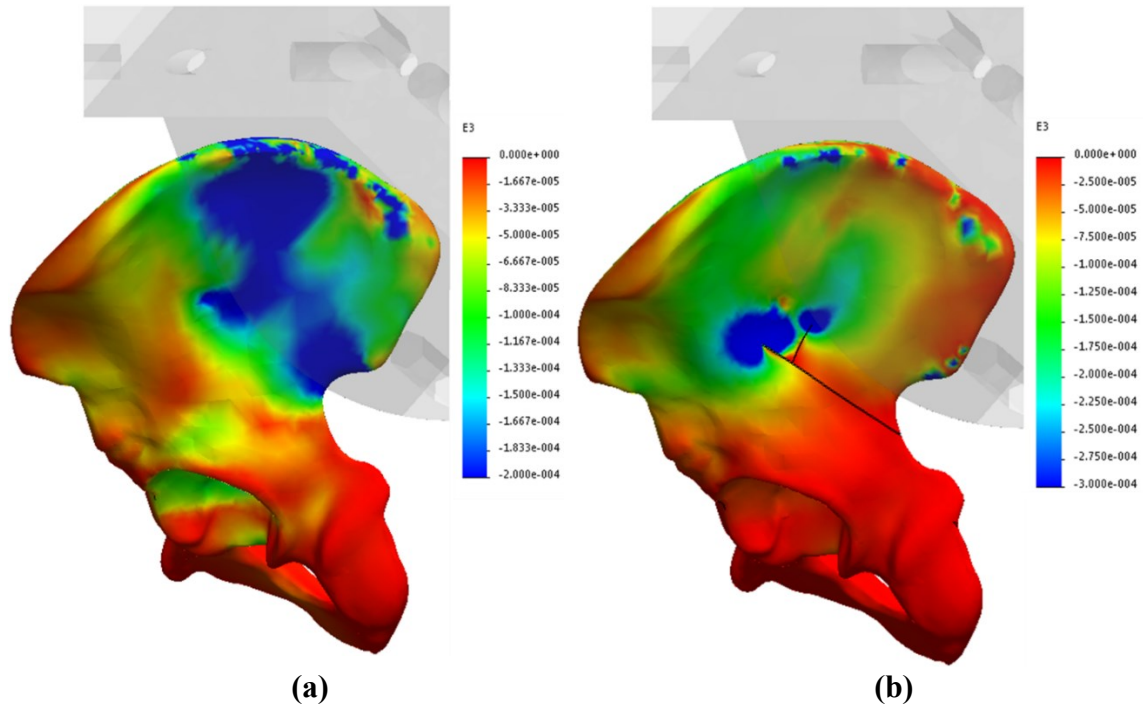
Figure 73. Numerical simulation results, comparing the 3rd principal strain fields of **(a)** the intact pelvis and **(b)** the fractured pelvis.

4.4.2 Experimental simulation

In this section, strain data were once again extracted from local regions of the FOV in the experiment using custom software (see Appendix H). Another program was developed to measure crack displacements as detailed in Appendix G.

4.4.2.1 Displacement

From the experiment, the measured displacement fields were observed in comparison with the intact experiment results, as shown in Figure 74. The displacements were greater by about a factor of 2, but the relative profiles were very similar between the intact and fractured pelvis cases. Like the numerical simulation comparison, the x- and y-displacement fields were closely matched with a minor discontinuity at the location of the crack in the fractured pelvis specimen. For the z-displacement field, the profile is more lateral within the region inferior to the primary crack. This was the same as the comparison of the numerical simulations of intact and fractured pelvis scenarios as the lack of constraint due to the crack allowed for more out-of-plane motion. However, the numerical simulation of the fractured case predicted more dominance in out-of-plane motion of the

147

inferior portion than was shown in the experiment. This may be due to a less rigid SI joint fixation occurring in the experiment, allowing for more in-plane motion of the specimen relative to the out-of-plane motion.
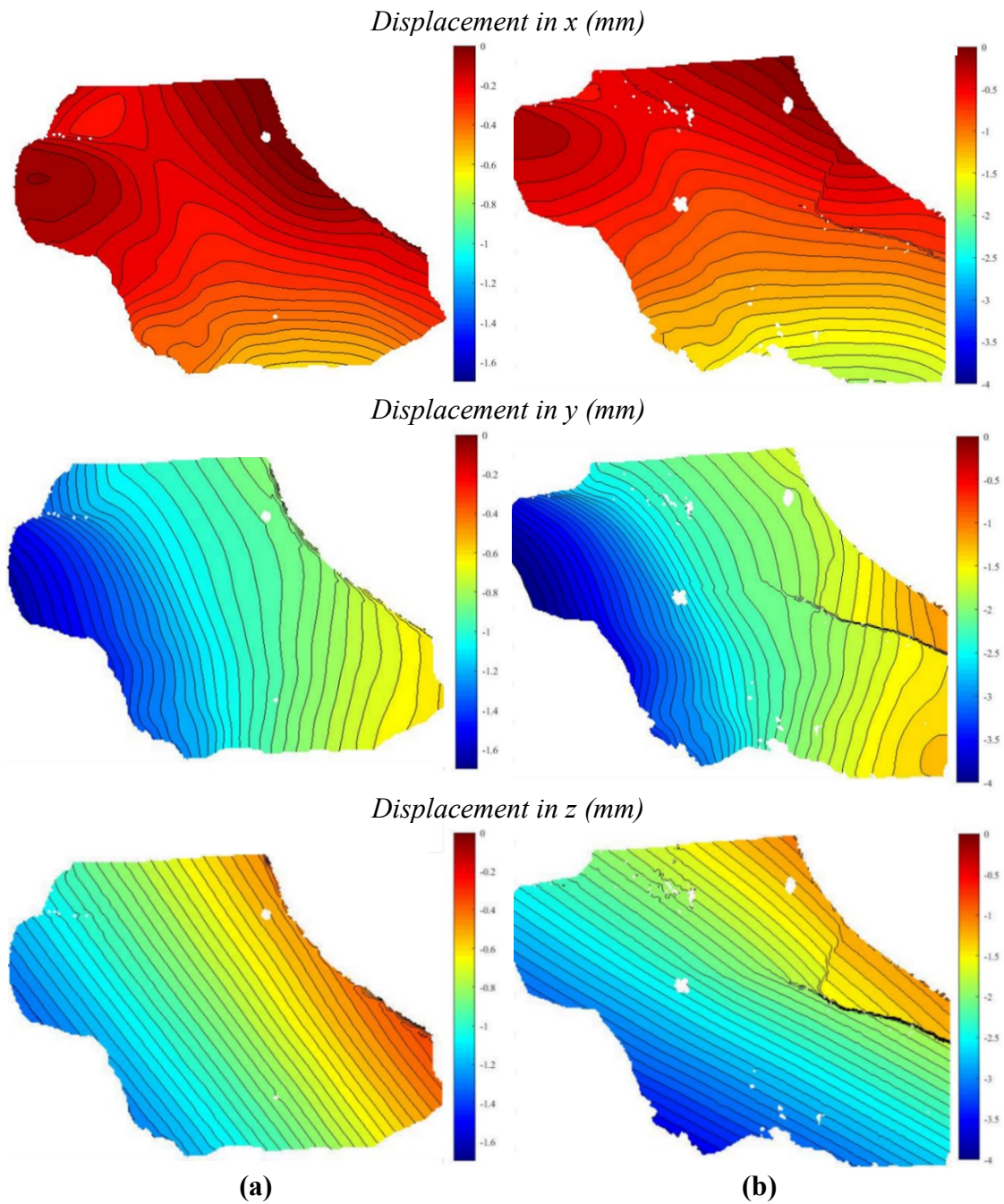
Figure 74. Experimental simulation results, comparing the x-, y-, and z-displacement fields of **(a)** the intact pelvis and **(b)** the fractured pelvis.

4.4.2.2 1st principal strain

In analyzing the 1st principal strain fields measured from the fractured pelvic testing, a similar approach was used as with the intact test analyses. The 1st principal strain fields were similar in profile across all fractured experiments and generally appear as shown in Figure 75. The high strain regions were the posterior acetabulum, the iliac ala, and the anterior inferior iliac spine for all test cases. As opposed to the intact case, the tensile strains at the iliac crest seemed to be less significant, though previously observed high strain regions were on the edge of the FOV in these tests. The empty space in the superior ilium was caused by image noise preventing measurements at that area. The sharp gradient lines of high 1st principal strains represent the crack movement on the specimen. They are measured as high tensile strains from the DIC results because the movement of points on a pair of crack edges relative to one another is extreme compared to two points on a continuous surface.

Figure 75. Typical measured 1st principal strain field of fractured pelvis at 500 N load with high strain regions labeled.

Similarly to the intact pelvis study, it was also found that the appropriate preload for this set of tests was 100 N by comparing the strain-load curves at the ROIs. It was found that there was less variation after zeroing the measurements at the preload, as shown in Table 45. The reasons are believed to be the same as the intact pelvis study in that the variable clamping tightness applied to the pelvis caused various levels of preloading which offset the strain values observed throughout each experiment. As shown in Figure 76, measurements at each high strain region zeroed after preloading were consistent across the experiments.

Table 45. Measured 1st principal strains at high strain regions at 500 N load for all fractured pelvic loading tests reported as raw values and after zeroing at 100 N preload.

Raw values (με)	Posterior acetabulum	Iliac ala	Anterior inferior iliac spine
Case 1	27550	21726	19756
Case 2	23386	17651	17910
Case 3	21825	16295	17123
All cases	**24254 ± 2959 (± 12%)**	**18557 ± 2827 (± 15%)**	**18263 ± 1352 (± 7%)**
Preloaded values (με)	Posterior acetabulum	Iliac ala	Anterior inferior iliac spine
Case 1	13062	10332	8647
Case 2	11502	8687	8870
Case 3	11117	8388	8318
All cases	**11894 ± 1030 (± 9%)**	**9135 ± 1047 (± 11%)**	**8612 ± 278 (± 3%)**
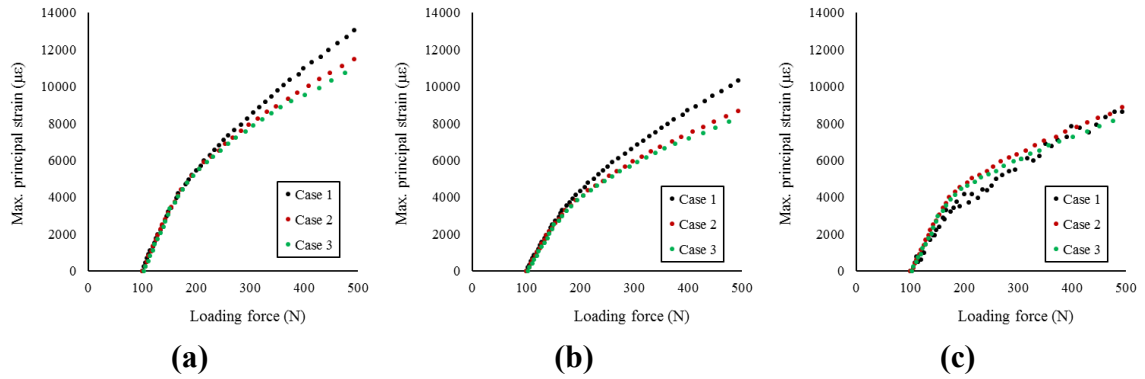
Figure 76. 1st principal strain measurements of fractured pelvis for all test cases zeroed at 100 N of preload at **(a)** the posterior inferior acetabulum, **(b)** the iliac ala, and **(c)** the anterior inferior iliac spine.

Compared to the results of the intact pelvis experiment, the locations of the strain regions were very similar, as shown in Figure 77. However, with the fractured pelvis experiment, the concentrations of tensile stress were heightened. Other areas of high stress were also decreased, such as the region superior to the crack and near the posterior acetabulum. This was directly due to the allowance of movement from the crack. The high tensile loads at the superior iliac ala and the iliac crest were also lessened as a result. Also, there were generally higher strains superior to the acetabulum due to the fracture.
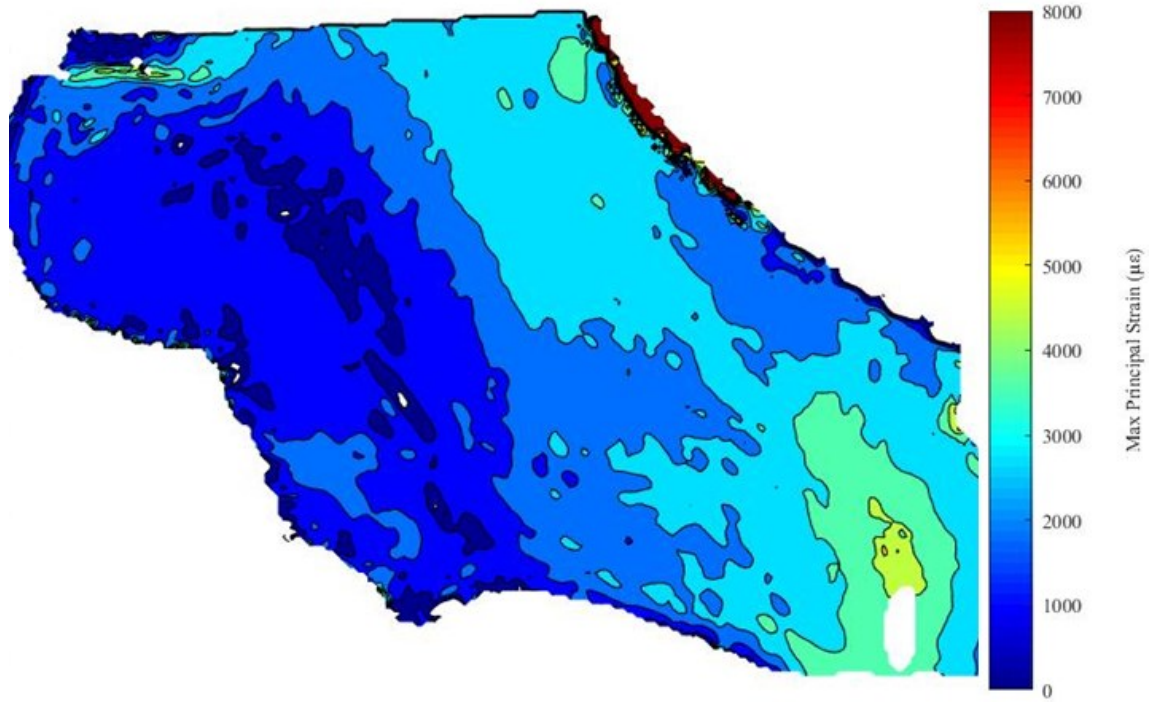
(a)
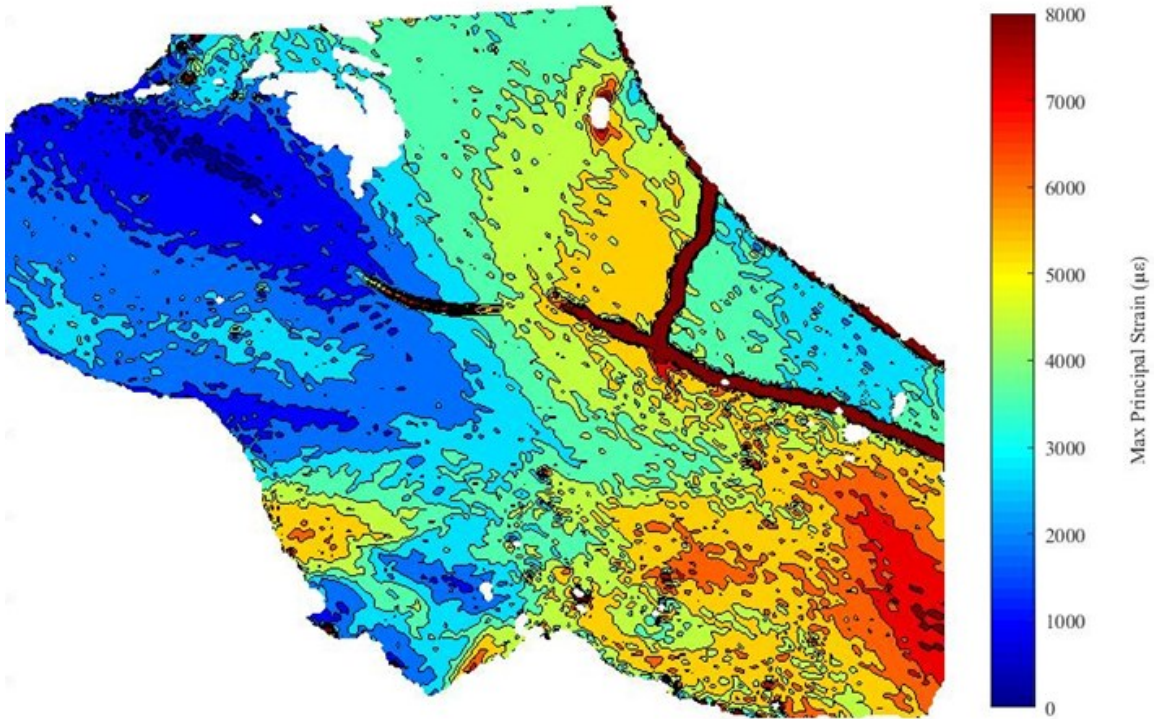
(b)

Figure 77. Comparison of 1st principal strain fields between **(a)** an intact pelvis and **(b)** a fractured pelvis.

For the experiments, the tensile loading at the anterior-superior iliac spine was more pronounced in the fractured pelvis specimen case than the intact as seen in Figure 77. However, this was not the case in the numerical simulations, as Figure 72 shows. This was due to the oversimplification of the loading condition used in the numerical simulations. To simulate the acetabular loading, the load was placed on the surface on the acetabulum directly. However, in the physical test, as the pelvis is displaced, it moves relative to the femur, which is fixed about the loading axis. As a result, the femur head applies a reaction force to the inside of the acetabulum which varies in terms of contact point, direction, and distribution throughout the experiment as the hemipelvis experiences relative displacement. This mechanism was not accounted for in the simplified numeric model, which explains the absence of high strains superior to the acetabulum in the numerical results. This hypothesis is supported by the observed increased local concentrations of the tensile loads in the superior acetabular regions in the fractured pelvis experiment results. In comparison to the intact pelvis, the greater out-of-plane displacements of this region cause the femur head to apply a greater reaction force from the inside of the acetabulum thereby increasing the tensile strains. The bending would occur about the point of contact, which would appear as the region bearing the minimum 1st principal strains.

Another significant difference between the numerical and experimental simulations of the fractured pelvis was that there were no distinct 1st principal strain concentrations at the crack tip in the experiment (Figure 77 (b)) as there were in the numerical analysis (Figure 72 (b)). One explanation is that the crack on the physical specimen was 3D in nature. It may have a variable profile in the out-of-plane direction, which was not implemented in the computer model. Given that the hemipelvis model was a composite of simulated cancellous and cortical bone, the 3D profile of the crack may play a significant role in the mechanical loading profile of the part. If so, a more geometrically accurate fracture model may be of high importance for future studies. As another possibility, the experiment measurement shows (Figure 77 (b)) that there was a microscopic crack detection in the middle of the ilium at the same region the numerical simulation predicted there to be high tensile strains. This suggests that the region may have already experienced yielding and a tiny crack may have already existed on the specimen before the experiment. Though it is practically invisible to human sight, the DIC system was able to observe this

phenomenon. Therefore, another error in the numerical modeling may simply be the exclusion of microfractures, something which should be acknowledged in futures studies. It could also be that the crack was simply growing throughout the experiment, and the numerical simulation did not account for crack growth and yielding. More detailed crack growth analysis should be explored in this scenario.

4.4.2.3   3rd principal strain

To understand the compressive loading experienced by the fractured pelvis specimen, analysis of the 3rd principal strains performed in an approach similar to that of the 1st principal strains. The 3rd principal strain fields for all specimens in this set of experiments were very similar to one another and appear as shown in Figure 78. For the minimum principal strain measurements, the greatest compressive strains were located near the anterior iliac crest. It was far beyond the limits of the used colormap such that it appears white. On the other hand, the cracks show up as white space as they extend beyond the colormap on the low compression end (towards zero). This was because in this loading scenario there was no crack closure, only crack widening. The final empty space, in the middle of the iliac ala, was due to the image noise as it was in the 1st principal strain field analysis. In this analysis, the regions more closely examined were the anterior superior iliac spine, the anterior superior acetabulum, and the anterior ilium, as shown in Figure 78.
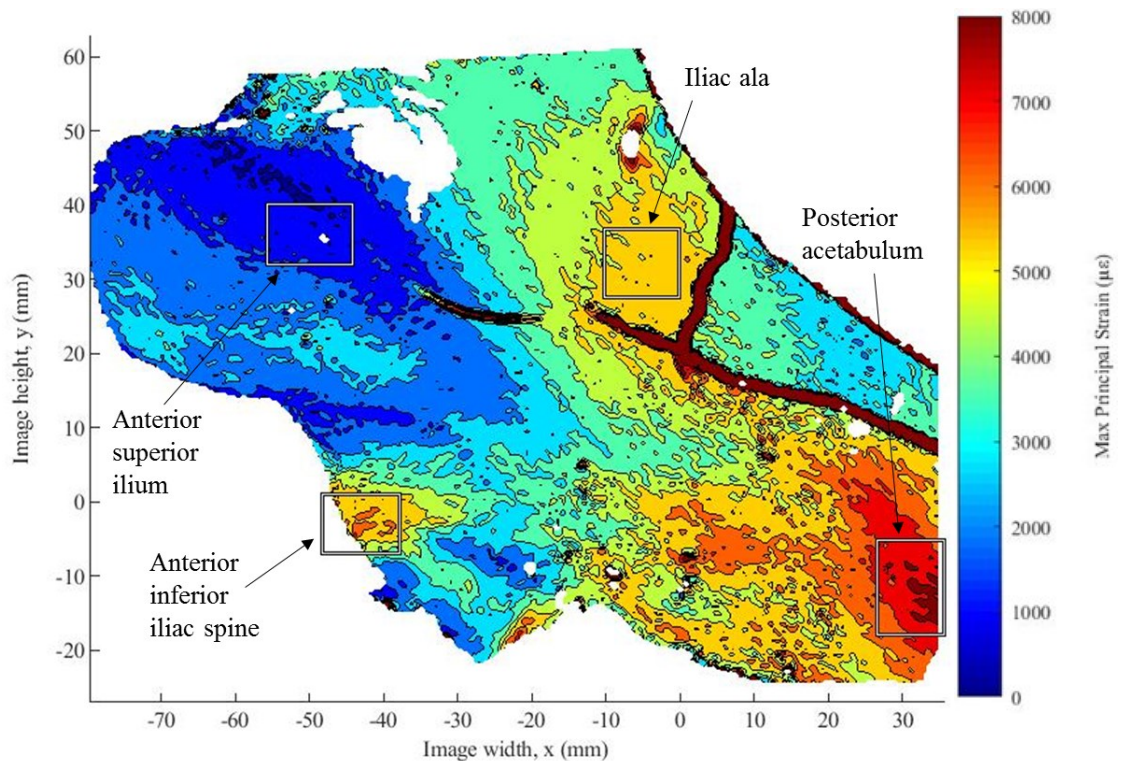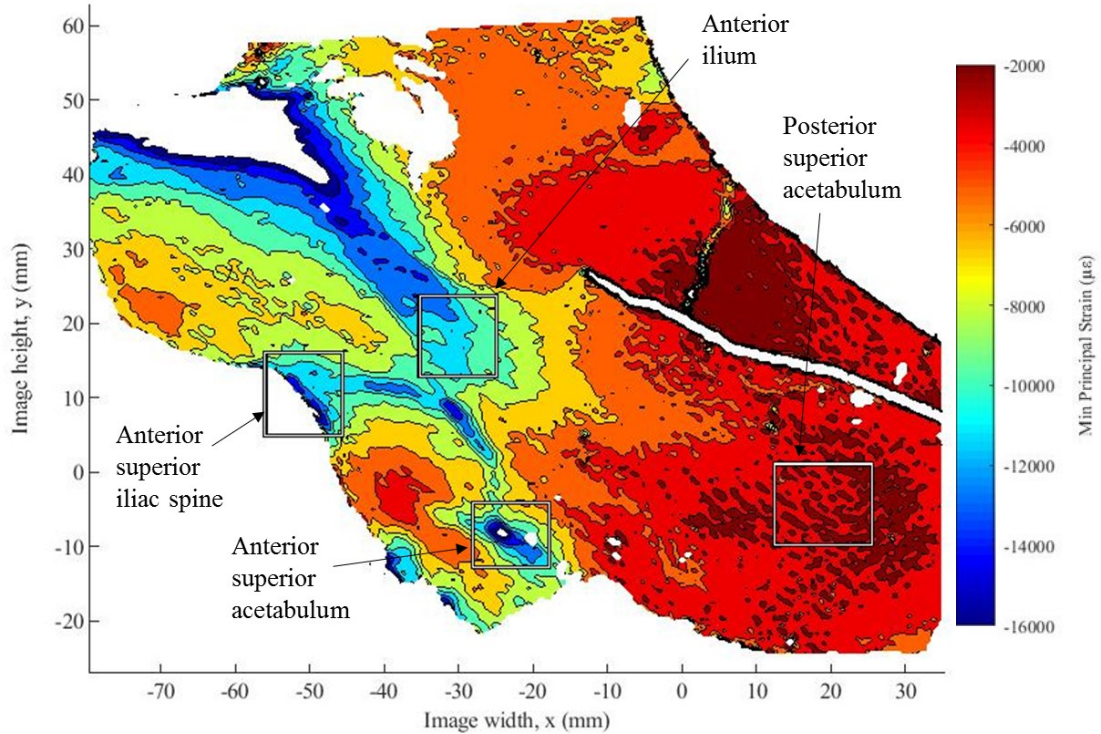
Figure 78. Typical measured 3rd principal strain field of fractured pelvis at 500 N load with high strain regions labeled.

The variation in the measured strain values across the three experiments performed on the fractured pelvis specimen was greater when observing the raw strain measurements compared to the measurements zeroed after a 100 N preload, as seen in the results listed in Table 46. Again, this was thought to be due to inconsistent preloading due to variations in clamping force of the specimen. Figure 79 shows that the comparison across all test cases after preloading are very similar, suggesting that 100 N was an appropriate value for the preload.

Table 46. Measured 3rd principal strains at high strain regions at 500 N load for all fractured pelvic loading tests reported as raw values and after zeroing at 100 N preload.

Raw values (µε)	Anterior superior iliac spine	Anterior superior acetabulum	Anterior ilium
Case 1	-40245	-33648	-36677
Case 2	-33345	-29194	-32063
Case 3	-32032	-27756	-30434
All cases	**-35207 ± 4412 (± 13%)**	**-30200 ± 3072 (± 10%)**	**-33058 ± 3238 (± 10%)**

| Preloaded values (µε)	Anterior superior iliac spine	Anterior superior acetabulum	Anterior ilium
Case 1	-18944	-16021	-17667
Case 2	-16372	-14515	-16127
Case 3	-16109	-14130	-15640
All cases	**-17142 ± 1566 (± 9%)**	**-14889 ± 999 (± 7%)**	**-16478 ± 1058 (± 6%)**
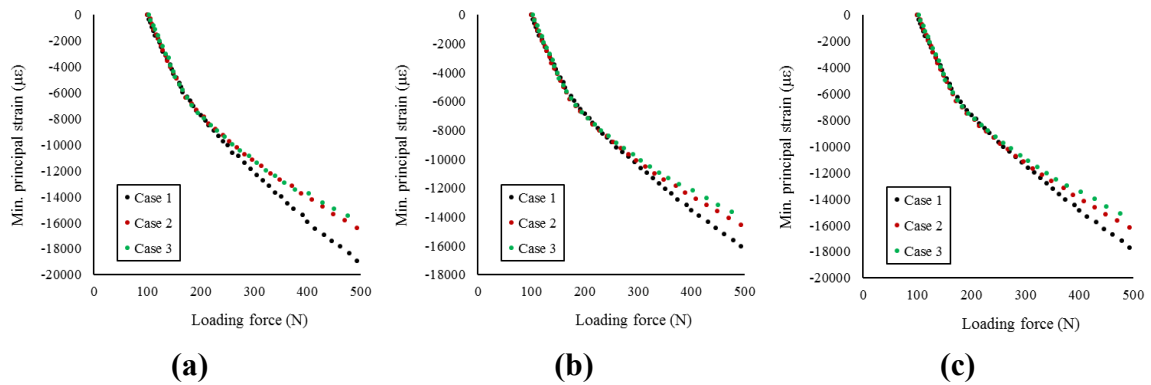
Figure 79. 3rd principal strain measurements of fractured pelvis for all test cases zeroed at 100 N of preload at **(a)** the anterior superior iliac spine, **(b)** the anterior superior acetabulum, and **(c)** the anterior ilium.

The comparison of the 3rd principal strain fields for the intact and the fractured specimens showed the two to be similar, as shown in Figure 80. In the fractured specimen case, the measured strain values were greater and more localized on both an absolute and relative scale. There is a similar "J-shape" profile running from the anterior superior iliac spine to the iliac crest, but at higher strain values. The compressive loading at the anterior iliac crest is comparatively much larger to the rest of the pelvis specimen in the fractured case. The increase is due to the greater allowance of relative displacement of sections of the pelvis resulting from the fracture.
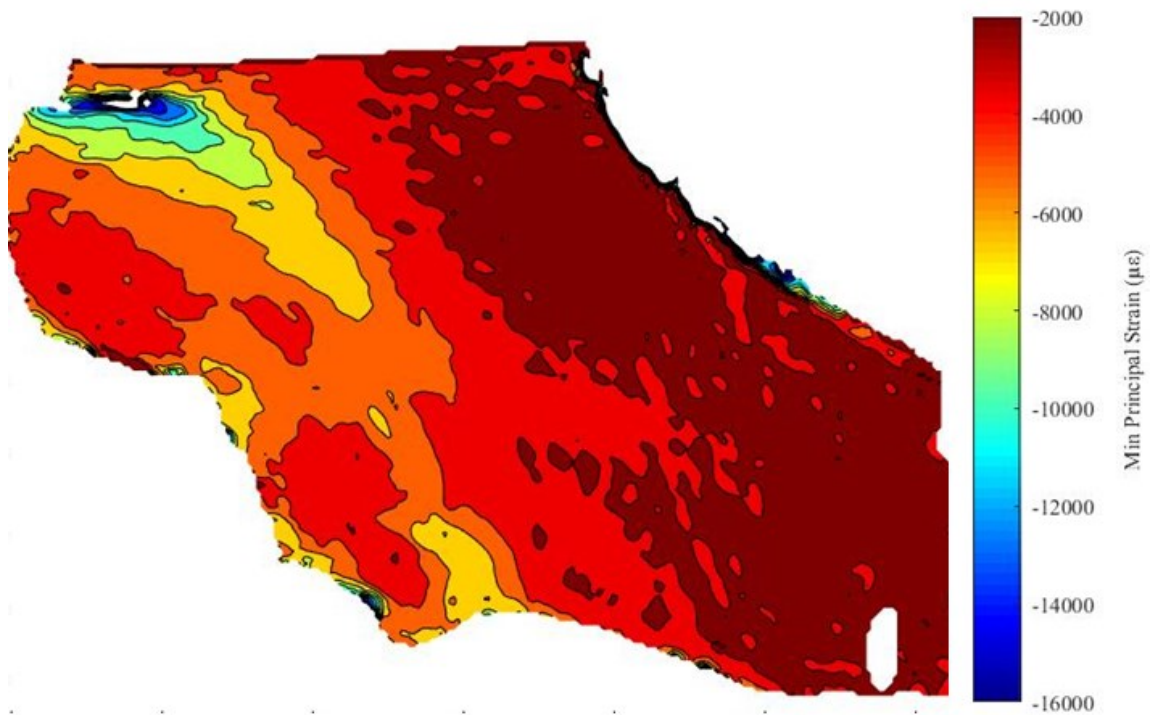
(a)
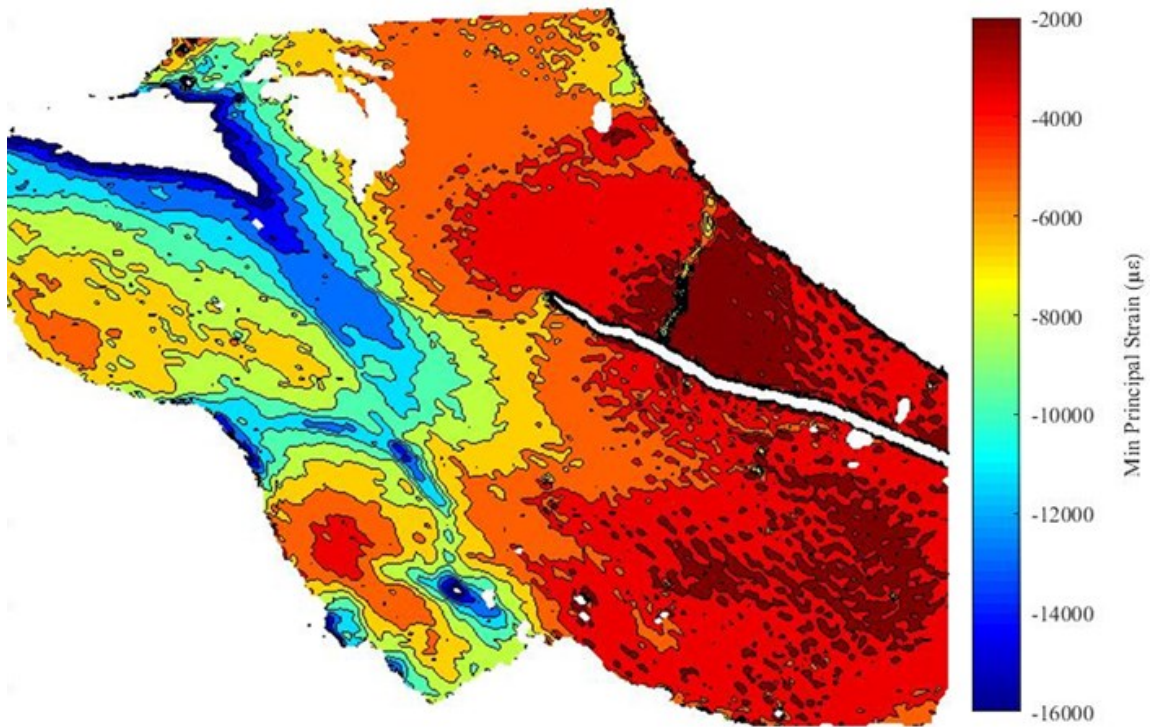
(b)

Figure 80. Comparison of 3rd principal strain fields between **(a)** an intact pelvis and **(b)** a fractured pelvis.

There is a local compressive loading superior to the acetabulum that was more prominent in the fracture case than the intact one. This further supports the previously proposed hypothesis that the femur head was applying a reactive force in response to the displacement of the inferior hemipelvis. The area of the high compressive stress also works in conjunction with the areas of the superior acetabulum showing high tensile loading in Figure 75 to locate the point of contact between the femur head and the interior acetabulum. It is at the local minimum 3rd principal stress (Figure 78). This means that the inferior pelvis is experiencing a significant bending moment in the y-direction about the contact point. Again, this phenomenon likely did not appear in the numerical simulations due to the oversimplification of the applied loading from the femur head.

Another significant difference in the intact and fractured pelvis 3rd principal strain fields can be seen anterior and inferior to the primary crack tip of the fractured specimen. There is a sharp gradient in compressive loading at this area extending from the crack tip anteriorly. The gradient also follows the detected crack widening observed in the 1st principal strain fields (Figure 75). This further supports the idea that a microscopic crack already existed here. The inferior edge of the crack may be compressing up against the inner surface while the superior edge is displacing upwards. This would explain why crack widening is detected in the 1st principal strain measurements (Figure 75) while compression is detected inferior to the crack (Figure 78). Additionally, the crack in the middle of the ilium extends one way towards the tip of the primary crack (from the greater sciatic notch) and in the other towards the iliac crest. This may be the predicted propagation direction of the crack under continued loading, which is representative of an iliac wing FFP. By observing the mechanical measurements of the experimental loading, it could be possible to predict future fracture behavior of the specimen, though this must be further investigated.

The absence of significant strains at the crack tip in the experiment results compared to the numerical simulations are believed to be for the same reasons provided in the 1st principal strain field analysis. In the case that the real crack is three-dimensional, the numerical model is an oversimplification. Also, assuming material homogeneity in the specimen causes more analytical error in assuming the out-of-plane crack profile. And the inability for the numerical simulations to account for crack yielding and propagation during loading may produce results that are greatly different from the physical experiment.

4.4.2.4   Crack edge opening

The DIC system which measured the displacement and strain fields of the pelvic experiment was simultaneously used to measure the fracture movement and characterize the fracture stability under single-leg stance loading conditions. From the measured displacement fields, a program was written to allow two points to be selected and the difference in displacements to be calculated between the them in all directions, as shown in Figure 81. When appropriately placed near crack edges, the results are the crack edge displacements in the x-, y-, and z-directions. Then, these displacements were converted from the image coordinate system to displacements relative to the crack profile, allowing for the determination of the crack movements in modes I, II, and III (Figure 70). This provided insight regarding both the magnitude and the nature of the crack opening, the latter referring to if the crack is widening, shearing, or tearing. Knowledge of crack behavior in this scenario could be used to predict and prevent crack propagation, as well as have clinical applications for fracture healing.
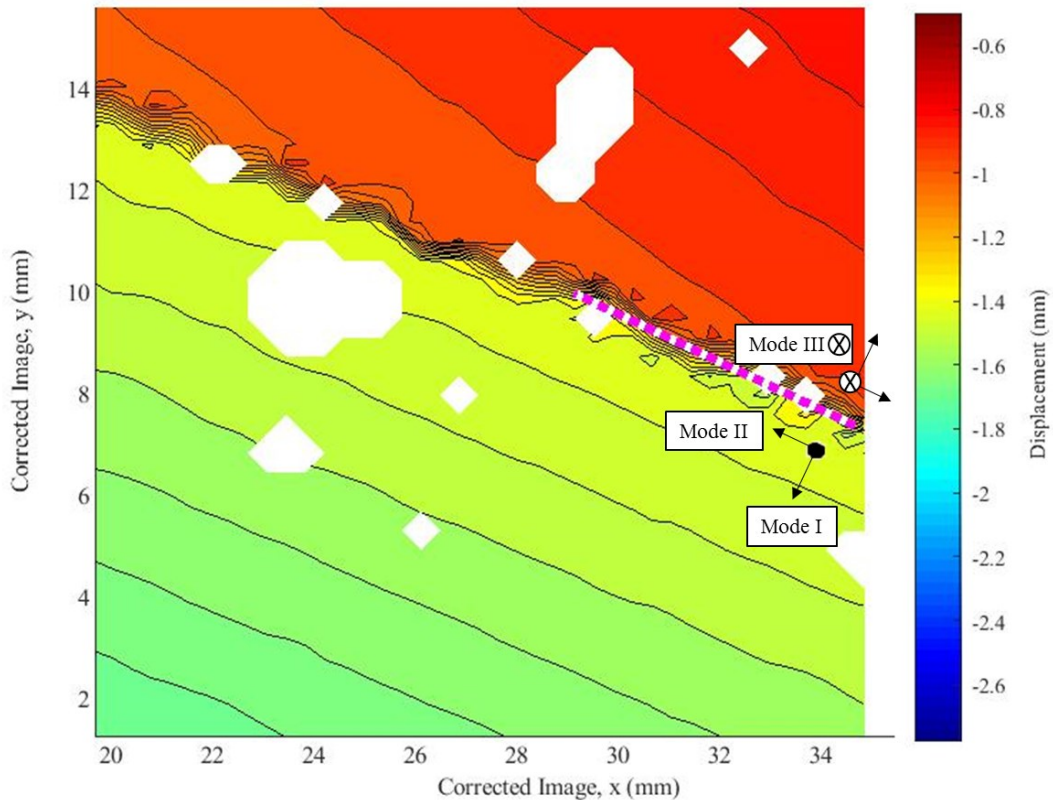
Figure 81. Points of measurement and orientation for crack displacement at greater sciatic notch edge.

As shown in Figure 82, the crack edge openings were observed at two locations: the greater sciatic notch for the primary crack, and the propagation point in the middle of the iliac ala along the primary crack where the secondary crack originates. For all three experiments, the crack opening measurements for each crack opening mode are shown in Figure 83 (a) and (b) plotted as a function of the loading force for the primary and secondary crack edges respectively. For the reasons previously described, the measurements were zeroed at 100 N of preload. All cases showed two regions of linearity with the same approximate transition point between the two regions. This point was estimated to be at approximately 170 N of loading for all tests. It can be seen in Figure 83 that the primary crack experiences greater displacements due to the load in comparison to the secondary crack. This means that the primary crack is generally less stable than the secondary crack in the conditions of the test.
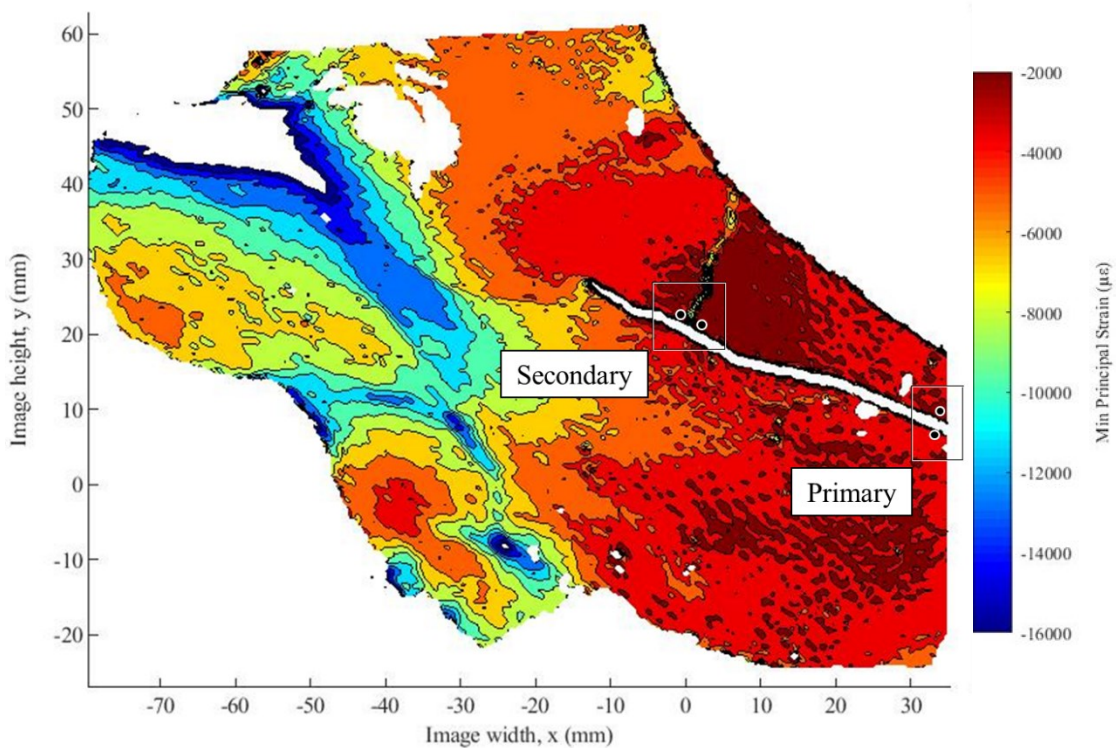
Figure 82. Locations on fractured pelvis of primary and secondary crack at the greater sciatic notch and propagating from the middle of the iliac ala respectively.
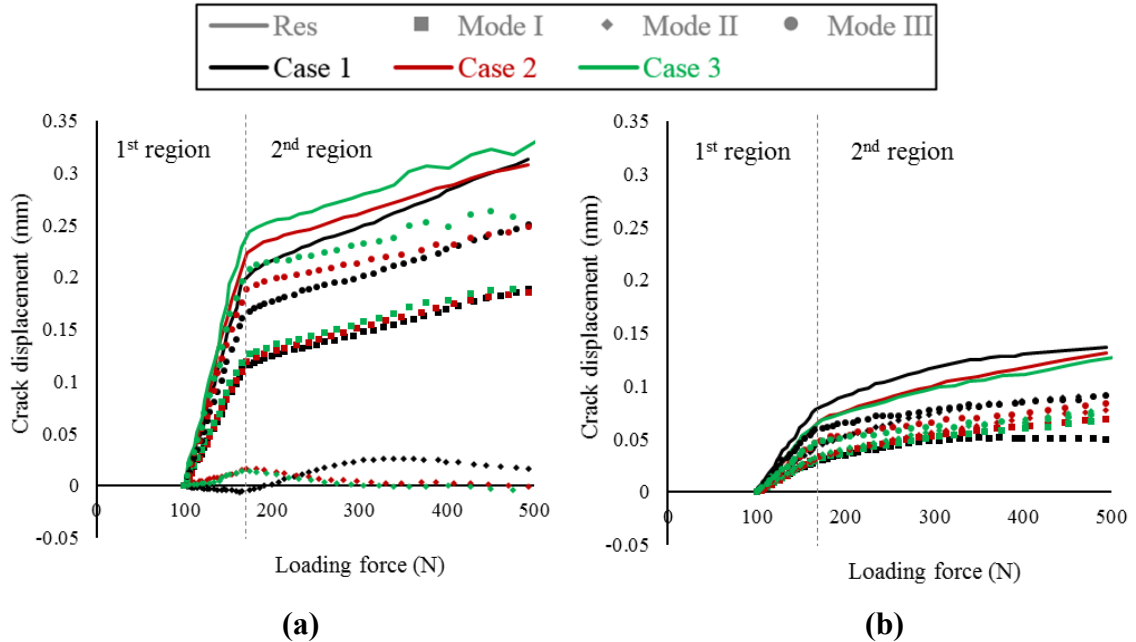
Figure 83. Crack displacements of fractured pelvis, showing modes I, II, and II, and the resultant displacement as a function of loading force for **(a)** the primary crack and **(b)** the secondary crack. First and second loading regions are divided at approximately 170 N of loading force.

In general, the measured crack displacements show consistency among all three experiments. However, in the first loading test, there was some erratic behavior in the early stages of loading. This was likely due to movement within the fixture which was not present in the second tests. It may have also caused the results of the first test to be less similar than the second and third. Table 47 lists the variation in measurements across the experiments for all crack opening modes and both loading regions, comparing the inclusion and exclusion of the first crack test. It showed that for the first case, the measured displacement for the secondary crack deviated from the other cases more than that of the primary crack. For both regions of the primary crack, the measurements were close in the cases including and excluding the first crack specimen, being at most 0.002 mm apart for the measured resultant crack displacement. But for the secondary crack, the variation for all three cases was 0.01 mm (or 5 times) higher than that excluding the first case. This suggests that the crack in the middle of the ilium may be more sensitive to boundary and loading conditions than the crack at the greater sciatic notch. For a weight-bearing rehabilitation plan, this means that the secondary crack requires more consideration and more detailed examination in determining the most suitable approaches.

Table 47. Measurement variation for mode I, II, and III, and resultant crack displacement for first and second loading regions of primary and secondary cracks of fractured pelvis. Comparison was made between the inclusion of all three tests and the exclusion of the first.

Variation *(Primary crack)*	First region		Second region	
	Cases 1, 2, 3	*Cases 2, 3*	*Cases 1, 2, 3*	*Cases 2, 3*
Mode I	0.008	0.016	0.003	0.003
Mode II	0.009	0.004	0.009	0.007
Mode III	0.032	0.032	0.009	0.011
Resultant	0.033	0.034	0.009	0.011
Variation *(Secondary crack)*	First region		Second region	
	Cases 1, 2, 3	*Cases 2, 3*	*Cases 1, 2, 3*	*Cases 2, 3*
Mode I	0.009	0.002	0.008	0.002
Mode II	0.003	0.002	0.011	0.002
Mode III	0.010	0.003	0.013	0.003
Resultant	0.013	0.003	0.017	0.003

All values presented in units of ± mm (% of mean).

The mechanical behavior of the primary crack was characterized in terms of the fracture mode and listed in Table 48. The displacement in each mode was reported as a percentage of the overall crack displacement. For the primary crack, mode III was most prominent, followed by mode I. There was relatively very little crack displacement in mode II. For fixation of this crack, providing rigidity against tearing should be the priority. In deciding upon a weight-bearing rehabilitation plan, these observations suggest that orienting loads posteriorly and at a greater adduction angle – a leg more in front and outwardly – may allow for the reintroduction of pelvic loads while encouraging crack closure instead of growth. This modified orientation is shown in Figure 84. On the other hand, it also implies that loading on the pelvis with a leg too inwardly may be detrimental to fracture propagation. Thus, leaning on or sidestepping in the direction of the fractured hemipelvis should be avoided during rehabilitation. More rigorous mechanical testing of these conditions should be performed before making such clinical recommendations.

Table 48. Contribution of each fracture mode towards resultant crack displacement for both loading regions of primary crack on fractured pelvis.

First region	Case 1	Case 2	Case 3	Average
Mode I	32.0	28.3	26.9	29.1
Mode II	0.1	0.5	0.3	0.3
Mode III	67.9	71.1	72.8	70.6
Second region	Case 1	Case 2	Case 3	Average
Mode I	35.8	36.3	33.4	35.2
Mode II	0.3	0.1	0.1	0.2
Mode III	63.9	63.6	66.5	64.7

All values presented as % of resultant crack displacement.
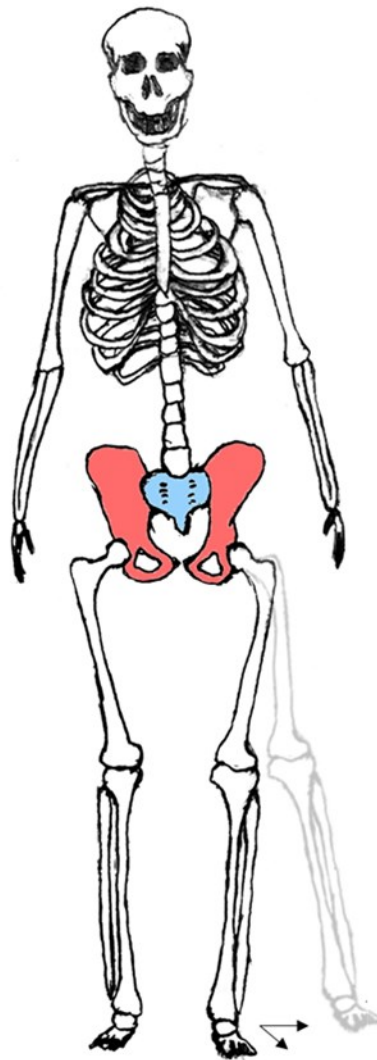
Figure 84. Rehabilitation for primary crack (leg forward and outward from single-leg stance).

163

For the secondary crack, branching posteriorly from the ilium, all crack displacement modes were more equal, as presented in Table 49. This suggests that its crack displacement profile is more complex than the primary crack. It would also explain why more deviation was observed between the experiments for this crack than the primary crack. The first crack specimen showed a lower mode I crack displacement in the second loading region than the other specimens. Again, this was likely due to differing boundary conditions from the movement within the fixture that was not present in the second and third cases. An optimal fixation approach is less straightforward with this crack, as movement is less predictable and more equal in all directions. It also creates difficulties in recommending rehabilitation for reintroducing loads to a fractured pelvis for healing. However, the raw crack displacement comparison between the primary and secondary cracks shown in Figure 85 suggests that the secondary crack may be comparatively insignificant. As the primary crack was observed to be less stable, a rehabilitation recommendation that addresses the primary crack may peripherally resolve the issue of the secondary crack. On the other hand, as the secondary crack experiences more complex motion and showed more sensitivity to the boundary conditions, it may become more significant in other scenarios and testing conditions and limits. Therefore, further examination is required to support such recommendations, but the biomechanical analytic process demonstrated in this research can be applied in these future studies.

Table 49. Contribution of each fracture mode towards resultant crack displacement for both loading regions of secondary crack on fractured pelvis.

First region	Case 1	Case 2	Case 3	Average
Mode I	14.1	23.7	22.7	20.2
Mode II	30.4	23.8	27.1	27.1
Mode III	55.5	52.5	50.2	52.7
Second region	Case 1	Case 2	Case 3	Average
Mode I	12.6	26.7	28.5	22.6
Mode II	43.8	34.0	36.5	38.1
Mode III	43.6	39.3	35.0	39.3

All values presented as % of resultant crack displacement.
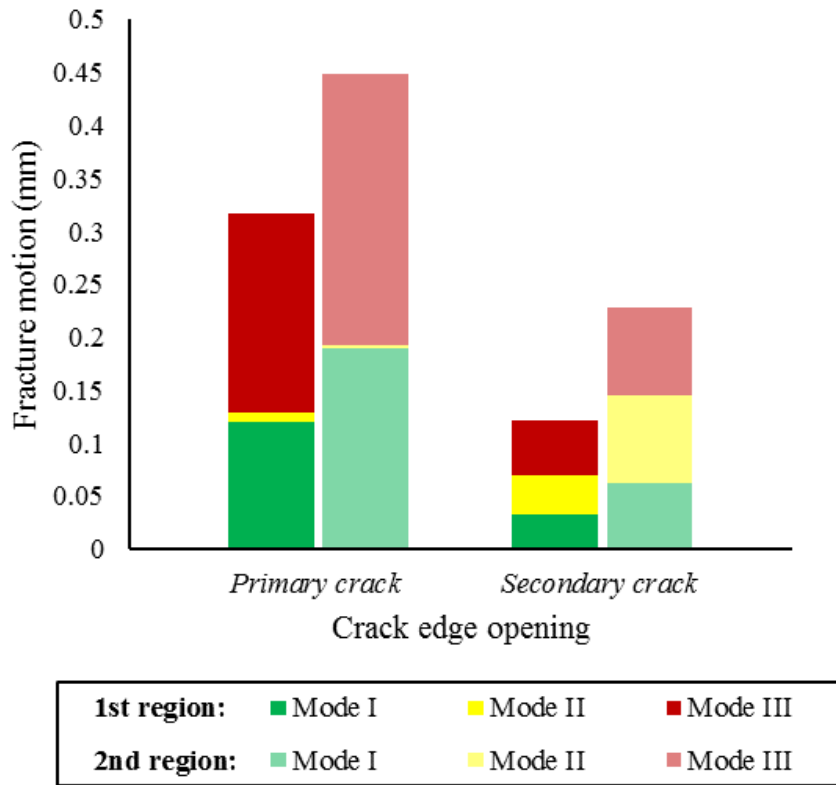
Figure 85. Comparison of raw crack displacements for all fracture modes between primary and secondary cracks.

The measurements of the crack displacements on the fractured hemipelvis were not exact; assumptions were required. For example, the fracture mode III was assumed to be the measured out-of-plane displacements on the pelvis in the test set up. This means that the surface of the specimen at the crack edge was assumed to be perpendicular to the cameras. However, this is unlikely as the curvature of the pelvic surface is pronounced, complex, and non-uniform throughout the entire FOV. Therefore, the z-displacements also contribute to modes I and II, just as the x- and y-displacements contribute to mode III. This may be addressed by utilizing the surface height data to understand the out-of-plane locations of the points used to measure the crack displacements to make 3D conversions of the displacements to crack modes. However, other concerns may take precedence over this, such as the fact that the specimen geometry and the crack profiles are very complex.

4.4.2.5 Crack tip strain

In the SENT testing performed earlier in this thesis, the two parameters of crack measurement were the crack edge opening and the crack tip strain. Regarding the latter, there were great difficulties finding application in the fractured pelvis scenario stemming from multiple reasons. For the SENT test, the geometry was controlled and specific and the specimen measurements (width, crack length, thickness, *etc.*) were known to greater precision as it was a much simpler case. Here, the complex geometry of the hemipelvis specimen makes it difficult to know the exact crack geometry. It also causes difficulty in controlling the loading direction respective to the crack. The cracking process was also more controlled in the SENT experiments; the fractured pelvis was used in a previous experiment and the crack geometry was not precisely formed then. Also, there is no standard for mechanical measurements of fracture pelvises unlike a simple edge-notched plate specimen. And despite the significantly higher levels of control in the SENT experiment, there was still a relatively high uncertainty associated with the crack tip strain measurement.

Nonetheless, there is still value associated with the crack tip strain, but it could not be used in this study. Future studies should pursue a more controlled fracturing of the specimen. As the SENT testing with the designed DIC system was shown to be effective, the hemipelvis specimen could be cracked and loaded to mimic the SENT conditions but for a more complex geometry. This would require initiating a small edge crack and loading the specimen in unidirectional tension normal to the crack. The greater sciatic notch would be a suitable location for the edge crack and the specimen could be approximated to have a semi-infinite width compared to the crack. Specifically, check if the results show a bean-shaped stress concentration at the crack tip, as it would suggest the viability of the approach in mechanically assessing a fractured pelvis. If successful, the crack length could be incrementally increased to determine the maximum length for which the loading scenario is valid. Trends in the increasing crack length and strain measurement distance from the crack tip could be used to determine an empirical SIF for a composite hemipelvis. This could then be used to establish more controlled and standard biomechanical analysis of pelvic fracture and provide a more quantifiable predictability to pelvic fracture growth.

4.4.3 Uncertainty analysis

The strain measurement uncertainty was estimated using the same approach as with the intact pelvis study (Section 4.3.3). The uncertainties for the 1st and 3rd principal strains are presented in Table 50. As the intact pelvis uncertainty analysis showed the strain measurement to be dominant and the area selection and load ambiguity to be comparatively insignificant, only the DIC strain measurement uncertainty was considered. The gauge length for all areas was estimated to be approximately 10 mm. It was shown that the measurement uncertainties from the fractured pelvis testing were definitively lower than the intact experiments even though a smaller effective gauge length was used. This was due to the strain measurement values being much higher in the former than the latter, causing the relative uncertainty to be smaller. This was also reflected in the measurement results as there was less discrepancy between the fractured pelvis testing.

Table 50. Estimates for uncertainties of 1st and 3rd principal strains after preloading for fractured pelvic testing, showing the uncertainty as the absolute value and as the relative value in parenthesis.

1st principal strain	Posterior acetabulum	Iliac ala	Anterior inferior iliac spine
Local ROI strain (με)	11894 ± 324 (3%)	9135 ± 324 (4%)	8612 ± 324 (4%)

3rd principal strain	Anterior superior iliac spine	Anterior superior acetabulum	Anterior ilium
Local ROI strain (με)	-17142 ± 324 (2%)	-14889 ± 324 (2%)	-16478 ± 324 (2%)

*Same value for all cases.

As for the crack edge openings, the measurement was the difference between the displacements of two points. The uncertainty in was estimated using the rigid body displacement uncertainty for the pelvis, U_x, and was expressed as,

$$U_\delta = \sqrt{U_{x_1}{}^2 + U_{x_2}{}^2} = \sqrt{2}U_x \qquad (26)$$

Thus, the uncertainty in the fracture displacement was estimated to be $\pm$ 0.003 mm. For more context, the minimum crack opening that could be measured with less than 10% uncertainty was 0.03 mm. This includes the measurements in modes I and II for the primary

crack in all modes for the secondary crack. Therefore, there is much confidence in these results and the ability of system to characterize the stability and mechanics of a pelvis.

Though the crack tip strain was not measured in these tests, the uncertainty analysis in Section 3.4.4 shows that the uncertainty in the crack tip strain measurement would be much greater than the other parameters of interest. It was reported to be approximately 35% in a 2D scenario. In 3D cases, the out-of-plane displacement uncertainty has been estimated to be up to four times the 2D scenario. Much of this uncertainty can be minimized by zooming in the FOV to the crack tip, ignoring the remaining area of the specimen. However, as the fractured pelvis contains an extremely complex geometry and crack profile, it may be difficult to determine exactly where the tip of the fracture is. Considering how sensitive the measurement is to the crack tip distance, this can introduce significant uncertainty. Therefore, it is recommended studying a known and controlled fracture profile before measuring and quantifying an unknown one, such as that of this experiment.

4.4.4 Summary

A fractured composite hemipelvis model was observed under single-leg stance loading conditions to observe how the fracture influences the biomechanics of a pelvis. First, numerical simulations were conducted on a fractured hemipelvis 3D model based on the loading setup in the experiment. When comparing the numerical results of the fractured specimen to the intact pelvis, it was found that the displacement profiles were generally very similar. The only major difference was in the z-displacements where more prominent out-of-plane motion was detected inferior to the greater sciatic notch fracture due to the freedom of movement introduced directly by the edge crack. Regarding the strain fields, for both the maximum and minimum principal strains, there was less significant loading in and around the clamping region in the fractured pelvis case. Instead, the high strain regions were localized at the crack tips of the solid model.

The experiment results were then compared with the numerical simulations and the intact pelvis experiment. The displacement fields showed similarity between the intact and fractured pelvis experiments with the z-displacement showing more prominence inferior to the greater sciatic notch fracture. Unlike the numerical simulations of each pelvic specimen, the strain fields were similar between the experiments. However, the 1st principal

strain field showed higher concentrations superior to the acetabulum in the fracture case. The same was observed for the 3rd principal strain measurements. In contrast, this trend did not occur in the numerical simulations and was reasoned to be due to the oversimplification of the application of force by the femur. In the numerical simulations, the load moved with the acetabulum instead of remaining along the loading axis and providing a reaction force in the acetabulum in response to the displacement of the hemipelvis. The crack tip strains that showed in the numerical simulations did not appear in the experiment results. This was likely due to oversimplifications and inaccuracies of the crack modeling in the software model rather than errors in the measurement system. More rigorous modeling should be pursued for a more insightful source of comparison for the experimental results.

Further comparison with the intact pelvis simulation showed how the fracture affected the mechanical profile of the pelvis. Along with heightened tensile and compressive strain concentrations, tension reduced at the region superior to the primary crack while compression increased at the iliac crest. Furthermore, a tertiary microscopic crack was detected near the primary crack tip by examining the strain fields, showing the capability of the system to capture mechanical phenomena on a very small scale.

The magnitude and direction of crack movement was also observed. It was found that the primary crack, originating at the greater sciatic notch, showed more consistent measurements across experiments than the secondary crack, originating midway through the primary crack and propagating posteriorly and superiorly across the ilium. This meant that the secondary crack was more sensitive to the boundary conditions than the primary crack. The primary crack displaced more than the secondary, meaning that it was less stable. It was dominated by mode I (opening) and mode III (tearing) movement. When fixing the pelvis, it would be beneficial to prevent motion in these directions. In weight-bearing rehabilitation, applying loads to counteract the motion would encourage crack reduction. The secondary crack showed more evenly distributed motion across all modes, causing ambiguity and difficulty in recommending fixation and rehabilitation techniques.

Nonetheless, it was demonstrated that with the crack measurement capabilities of the designed testing rig, the biomechanical analysis could potentially be used to recommend a quantified rehabilitation to address a pelvic fracture. Characterization of the fracture stability were made using measurements with less than 10% uncertainty.

4.5   Conclusion

A biomechanical study on a composite hemipelvis model was conducted to assess how the presence of a fracture can influence the mechanics of the specimen. The first step was to demonstrate the capabilities of the experiment using an intact pelvis. A numerical simulation was conducted to compare with the experimental results. By observing the 1st and 3rd principal strains, the tensile and compressive loading across the specimen surface was better understood, establishing a baseline scenario to compare the more complicated case of a fractured pelvis. In the presented set of tests, the measurement repeatability was approximately 10%. Therefore, the setup was reasonably consistent and deemed valid for testing fractured pelvises under the same experimental conditions.

The fractured pelvis test results were compared to the intact results to observe how the fracture alters the mechanics of the pelvis. The strain fields between intact and fracture scenarios were generally similar with the observation of expected differences, such as discontinuities at the cracks and shifts in the mechanical load distribution resulting from the fracture presence. This suggests that the experiments were repeatable and the mechanical variations observed were realistic. Furthermore, the strain field measurements captured the existence of a microscopic crack that responded to the compression of the specimen. This further demonstrated the strength of the DIC system in this experiment.

The displacement at the crack edges of the fractured pelvis specimens were measured to evaluate the mode and motion of the cracks. These results were used to anticipate how the fracture would be prone to displace within the loading scenario. Using the predictive information, potential approaches for pelvic repair or rehabilitation were presented.

This study extensively details a biomechanical experiment on a pelvis and demonstrates how the results can be used to better understand and improve the approaches to pelvic fractures. Future work includes more rigorous numerical modeling, studying different fractures, and examining different loading scenarios. These approaches all progress towards safer, stronger, and more specific recommendations of approaches to fixation and therapy regarding pelvic fracture.

Chapter 5: Conclusions and future work

5.1   Conclusions

The purpose of this thesis was to demonstrate how biomechanical experimental simulation can be used to analyze the mechanics and characterize the stability of a fractured pelvis. It involved the design, assembly, and validation of a test setup that would reasonably simulate mechanical loading of a hemipelvis in a single-leg stance configuration. The experiment components consisted of a DIC system that was integrated into an existing mechanical testing apparatus, known as the MABTA.

To understand the quality of the mechanical measurements, a preliminary study was performed on the DIC system. Procedures of how to effectively conduct a DIC experiment and how to quantify the uncertainty of the measurements by the system were studied and presented. A DOE study investigated the effects of speckle pattern quality in a DIC experiment were investigated. This was done by prescribing rigid body displacements in the out-of-plane direction of a set of different speckle patterns with controlled parameter variation and examining the bias and precision error in the DIC measurements to quantify the uncertainty. It was determined that a good speckle pattern consisted of 2-3 speckles per subset and an average speckle diameter of 3-5 pixel with minimal speckle size variation. The IQR of the measured speckle diameters of a pattern was shown to be an intuitive measure of speckle size variation. From this introductory investigation, the methods used to conduct the DIC experiment, the target speckle pattern characteristics, and the uncertainty quantification method was used thenceforth in the subsequent experiments of this study.

The imaging system was then integrated with the MABTA and reconfigured such that the optical and mechanical components of the entire experiment would extract data synchronously. In the following validation tests, it was shown that the image synchronization achieved with the designed test setup was a significant improvement to the quality of the extracted test data. The first and simplest of the validation tests was performed on dogbone specimens to understand the major sources of uncertainty in strain measurements of the designed experiment. The second set used the slightly more complex SENT testing to better comprehend the uncertainty involving fracture measurements. The

simpler case showed excellent agreement among the theoretical, numerical, and experimental analyses. However, the crack testing showed that a major issue of the numerical simulations was the inability to simulate crack yielding accurately, though the numerical results prior to yielding were in good agreement with the theory and experiment. The two simple scenarios used in the validation tests showed that the experimental setup yielded reasonable and expected results, providing confidence in the experiment design for more complex scenarios. The greatest source of uncertainty was the strain measurement, which were most troublesome at extremely small strain values. Adjustments to gauge length and image magnification were found to be the easiest ways of minimizing this uncertainty. On the other hand, crack edge opening measurement was associated with a lower uncertainty; openings as small as 0.03 mm could be measured with less than 10% uncertainty. With the test setup, this parameter was more meaningful and reliable for quantifying the mechanical behavior of a cracked specimen using this system. These insights were applied to the next set of experiments on a pelvic specimen.

With the grounds of understanding of the mechanical experiment provided by testing on the simpler cases, the complex problem of pelvic loading was investigated. It involved comparing numerical and experimental simulations of intact and fractured hemipelvis models to assess the potential inaccuracies of each of the analyses. The numerical simulations were determined to require further work as there were deviations resulting from oversimplification of the model and the boundary conditions. For the experimental loading simulation, the 1st and 3rd principal strains were measured for an understanding of the tensile and compressive loads experienced by the specimens. The test setup showed good repeatability, measured to be about 10% across the set of tests. The confidence in the system and the ideal targeted measurements gained from the intact pelvis testing was carried forth to the even further complicated mechanical problem of fractured pelvic loading.

The final set of experiments, conducted on a fractured hemipelvis model, were built upon the insights gained from testing incrementally more complex scenarios. Good repeatability was observed in both the strain and the crack opening measurements across all experiments. Compared to the intact hemipelvis experiment, the strain distributions were overall quite similar. The observed shifts in the mechanical loading profile were

expected to occur due to the fracture presence, suggesting that the measurements in the fractured pelvis loading simulation were reasonable. Additionally, the designed experimental setup showed a microscopic crack that responded to the compressive loading of the specimen. This demonstrated the capability of the system to measure extremely small mechanical phenomena and across the entire surface of the pelvis, making it a valuable tool in researching and understanding pelvic mechanics.

The fracture modes were then observed and characterized using crack edge opening measurements. For the specimen of this experiment, the primary crack was the unstable component, showing greater displacement due to loading than the secondary crack. Modes I and III (opening and tearing) were the main components of the primary crack displacement. The secondary crack had less consistent motion across tests and was more evenly distributed across all fracture modes. Though stable in this set of experiments, it could become more prominent in other loading scenarios or limits. The measurements used to characterize the fracture stability had an associated uncertainty of less than 10%. This means that not only is there much confidence in the results presented in this work, but also in the ability of the designed system to characterize the mechanics and stability of a fractured pelvis.

5.2   Future Work

Certain areas within the research presented in this thesis require further improvement and investigation. One of the major components is the numerical analyses. As the cases increased in complexity, the issues within the numerical simulation increased in count and significance. A more complex software should be used in future studies, perhaps one that can properly simulate yielding and crack propagation as well as the acetabular loading conditions. Also, a more accurate hemipelvis model should be acquired or created. This refers to a model with both cortical and cancellous bone and with a crack profile that is more exact to the tested specimen. More in-depth anatomical conditions could also be studied for a stronger basis of comparison. For example, the simulation of a full pelvic girdle under single-stance loading could be conducted and compared to the hemipelvis model to assess the effects of the simplification of the latter case. Implementing

ligamentous forces in the simulation would also provide insight as to how to make the hemipelvis model testing more anatomically realistic.

There is still room for further experimentation on pelvic specimens as well. Variations on the tests would provide more insight regarding pelvic biomechanics. Other cracks should be examined to further validate the application of biomechanical testing to a real pelvic facture. Also, a simpler crack with a known geometry and profile should be tested for a more controlled assessment of the numerical analyses. An approximation of a SENT test using the hemipelvis model could potentially allow for an empirical SIF for a more mechanical quantification of the fracture. Other specimens could also be experimented on, such as models from other manufacturers, fractured hemipelvis models fixed with instrumentation, and cadaveric pelvic specimens.

Future work should more strongly emphasize the clinical application aspect of this study. For example, in recommending a fixation technique based on the mechanical behavior, other common loading scenarios should be examined, such as double-leg stance or fatigue loading. Or for assessing weight reintroduction for rehabilitation, a series of experiments should be conducted to determine the exact loading orientation to promote crack closure and discourage further propagation. Also, the in vivo behavior and the biological responses to the mechanical phenomenon observed using the pelvic models should be considered heavily. As the entire purpose of this research is to promote the health and well-being of those affected by pelvic fracture, assessment of the real-life application should always be the main focus of the research.

References

[1] E. Hernlund *et al.*, "Osteoporosis in the European Union: Medical management, epidemiology and economic burden: A report prepared in collaboration with the International Osteoporosis Foundation (IOF) and the European Federation of Pharmaceutical Industry Associations (EFPIA)," *Arch. Osteoporos.*, vol. 8, no. 1–2, 2013.

[2] J. A. Kanis, "Diagnosis of osteoporosis," *Osteoporos. Int.*, vol. 7, no. SUPPL. 3, 1997.

[3] L. Alexeeva *et al.*, "Assessment of fracture risk and its application to screening for postmenopausal osteoporos," *World Heal. Organ. - Tech. Rep. Ser.*, no. 843, pp. 1–129, 1994.

[4] R. Factors, "Consensus development conference: Prophylaxis and treatment of osteoporosis. Copenhagen. 1990," *Am. J. Med.*, vol. 90, pp. 107–110, 1991.

[5] M. Soubrier *et al.*, "Insufficiency fracture. A survey of 60 cases and review of the literature," *Jt. Bone Spine*, vol. 70, no. 3, pp. 209–218, 2003.

[6] G. Dodge and R. Brison, "Low-impact pelvic fractures in the emergency department," vol. 12, no. 6, 2010.

[7] R. M. F. Hill, C. M. Robinson, and J. F. Keating, "Fractures of the pubic rami," vol. 83, no. November, 2001.

[8] W. A. Van Dijk, M. Poeze, S. H. Van Helden, P. R. G. Brink, and J. P. A. M. Verbruggen, "Ten-year mortality among hospitalised patients with fractures of the pubic rami," *Injury*, vol. 41, no. 4, pp. 411–414, 2010.

[9] J. Taillandier, F. Langue, M. Alemanni, and E. Taillandier-heriche, "Mortality and functional outcomes of pelvic insufficiency fractures in older patients," vol. 70, pp. 287–289, 2003.

[10] W. A. Van Dijk, M. Poeze, S. H. Van Helden, P. R. G. Brink, and J. P. A. M. Verbruggen, "Ten-year mortality among hospitalised patients with fractures of the pubic rami," *Injury*, vol. 41, no. 4, pp. 411–414, 2010.

[11] M. Tile, D. L. Helfet, and J. F. Kellam, *Fractures of the Pelvis and Acetabulum*. Philadelphia, UNITED STATES: Wolters Kluwer Health, 2003.

[12] a Cappozzo, F. Catani, U. Della Croce, and A. Leardini, "Position and orietnation in space of bones during movement," *Clin. Biomech.*, vol. 10, no. 4, pp. 171–178, 1995.

[13] U. Della Croce, A. Cappozzo, and D. C. Kerrigan, "Pelvis and lower limb anatomical landmark calibration precision and its propagation to bone geometry and joint angles," *Med. Biol. Eng. Comput.*, vol. 37, no. 2, pp. 155–161, 1999.

[14] P. M. Rommens and A. Hofmann, "Comprehensive classification of fragility fractures of the pelvic ring: Recommendations for surgical treatment," *Injury*, vol. 44, no. 12, pp. 1733–1744, 2013.

[15] A. R. Burgess *et al.*, "Pelvic ring disruptions: effective classification system and treatment protocols.," *J. Trauma*, vol. 30, no. 7, pp. 848–56, Jul. 1990.

[16] G. F. Pennal, M. Tile, J. P. Waddell, and H. Garside, "Pelvic disruption: assessment and classification.," *Clin. Orthop. Relat. Res.*, no. 151, pp. 12–21, 1980.

[17] T. Nusselt, H.-M. Klinger, W. Schultz, and M. H. Baums, "Fatigue stress fractures of the pelvis: A rare cause of low back pain in female athletes," *Acta Orthop. Belg.*, vol. 76, no. 6, pp. 838–843, 2010.

[18] P. M. Rommens and A. Hofmann, "Comprehensive classification of fragility fractures of the pelvic ring: Recommendations for surgical treatment," *Injury*, vol. 44, no. 12, pp. 1733–1744, 2013.

[19] H. Finiels, P. J. Finiels, J. M. Jacquot, and D. Strubel, "Fractures of the sacrum due to bone deficiency a meta- analysis of 508 cases ," *Press. Medicale*, vol. 26, no. 33, pp. 1568–1573, 1997.

[20] D. Wagner, C. Ossendorf, D. Gruszka, A. Hofmann, and P. M. Rommens, "Fragility fractures of the sacrum: how to identify and when to treat surgically?," *Eur. J. Trauma Emerg. Surg.*, vol. 41, no. 4, pp. 349–362, 2015.

[21] R. H. Daffner and H. Pavlov, "Stress fractures: Current concepts," *Am. J. Roentgenol.*, vol. 159, no. 2, pp. 245–252, 1992.

[22] K. J. Koval *et al.*, "Pubic Rami Fracture: A Benign Pelvic Injury?," *J. Orthop. Trauma*, vol. 11, no. 1, pp. 7–9, 1997.

[23] M. P. Herman *et al.*, "Sacral Insufficiency Fractures After Preoperative Chemoradiation for Rectal Cancer: Incidence, Risk Factors, and Clinical Course," *Int. J. Radiat. Oncol. Biol. Phys.*, vol. 74, no. 3, pp. 818–823, 2009.

[24] M. Karataş, C. Başaran, E. Özgül, Ç. Tarhan, and A. M. Ağildere, "Postpartum sacral stress fracture: An unusual case of low-back and buttock pain," *Am. J. Phys. Med. Rehabil.*, vol. 87, no. 5, pp. 418–422, 2008.

[25] D. Resnick and J. Guerra Jr., "Stress fractures of the inferior public ramus following hip surgery," *Radiology*, vol. 137, no. 2, pp. 335–338, 1980.

[26] W. J. Launder and D. S. Hungerford, "Stress fracture of the pubis after total hip arthroplasty," *Clin. Orthop. Relat. Res.*, vol. No. 159, pp. 183–185, 1981.

[27] I. Oh and J. A. Hardacre, "Fatigue fracture of the inferior pubic ramus following total hip replacement for congenital hip dislocation," *Clin. Orthop. Relat. Res.*, vol. No. 147, pp. 154–156, 1980.

[28] D. S. Meredith, F. Taher, F. P. Cammisa Jr., and F. P. Girardi, "Incidence, diagnosis, and management of sacral fractures following multilevel spinal arthrodesis," *Spine J.*, vol. 13, no. 11, pp. 1464–1469, 2013.

[29] C. Schizas and N. Theumann, "An unusual natural history of a L5-S1 spondylolisthesis presenting with a sacral insufficiency fracture," *Eur. Spine J.*, vol. 15, no. 4, pp. 506–509, 2006.

[30] R. H. Daffner and H. Pavlov, "Stress fractures: Current concepts," *Am. J. Roentgenol.*, vol. 159, no. 2, pp. 245–252, 1992.

[31] K. B. Freedman, F. S. Kaplan, W. B. Bilker, B. L. Strom, and R. A. Lowe, "Treatment of osteoporosis: Are physicians missing an opportunity?," *J. Bone Jt. Surg. - Ser. A*, vol. 82, no. 8, pp. 1063–1070, 2000.

[32] L. Marmor, "Stress fracture of the pubic ramus simulating a loose total hip replacement," *Clin. Orthop. Relat. Res.*, vol. No. 121, pp. 103–104, 1976.

[33] W. C. Peh *et al.*, "Imaging of pelvic insufficiency fractures.," *RadioGraphics*, vol. 16, no. 2, pp. 335–348, Mar. 1996.

[34] C. Rangger, A. Kathrein, M. C. Freund, T. Klestil, and A. Kreczy, "Bone bruise of the knee. Histology and cryosections in 5 cases," *Acta Orthop. Scand.*, vol. 69, no. 3, pp. 291–294, 1998.

[35] D. Schapira, D. Militeanu, O. Israel, and Y. Scharf, "Insufficiency fractures of the pubic ramus," *Semin. Arthritis Rheum.*, vol. 25, no. 6, pp. 373–382, 1996.

[36] R. Huiskes, H. Weinans, and B. van Rietbergen, "The Relationship Between Stress Shielding and Bone Resorption Around Total Hip Stems and the Effects of Flexible Materials The Relationship Between Stress Shielding and Bone Resorption Around Total Hip Stems and the Effects of Flexible Materials," *Clin. Orthop. Relat. Res.*, no. December, pp. 124–134, 1992.

[37] J. L. Lewis, M. J. Askew, R. L. Wixson, G. M. Kramer, and R. R. Tarr, "The influence of prosthetic stem stiffness and of a calcar collar on stresses in the proximal end of the femur with a cemented femoral component," *J. Bone Jt. Surg. - Ser. A*, vol. 66, no. 2, pp. 280–286, 1984.

[38] J. D. Bobyn, E. S. Mortimer, A. H. Glassman, C. A. Engh, J. E. Miller, and C. E. Brooks, "Producing and avoiding stress shielding: Laboratory and clinical observations of noncemented total hip arthroplasty," *Clin. Orthop. Relat. Res.*, no. 274, pp. 79–96, 1992.

[39] K. A. Egol, E. N. Kubiak, E. Fulkerson, F. J. Kummer, and K. J. Koval, "Biomechanics of Locked Plates and Screws," *J. Orthop. Trauma*, vol. 18, no. 8, pp. 488–493, Sep. 2004.

[40] P. T. Simonian, M. L. C. Routt, R. M. Harrington, and A. F. Tencer, "The unstable iliac fracture: A biomechanical evaluation of internal fixation," *Injury*, vol. 28, no.

7, pp. 469–475, 1997.

[41] S. C. Mears, E. G. Sutter, S. J. Wall, D. M. Rose, and S. M. Belkoff, "Biomechanical comparison of three methods of sacral fracture fixation in osteoporotic bone," *Spine (Phila. Pa. 1976).*, vol. 35, no. 10, pp. E392–E395, 2010.

[42] A. C. Gupta *et al.*, "Percutaneous sacroplasty," *J. Neurointerv. Surg.*, vol. 4, no. 5, pp. 385–389, 2012.

[43] M. D. Waites, S. C. Mears, A. M. Richards, J. M. Mathis, and S. M. Belkoff, "A biomechanical comparison of lateral and posterior approaches to sacroplasty," *Spine (Phila. Pa. 1976).*, vol. 33, no. 20, pp. E735–E738, 2008.

[44] J. D. Bastian, M. J. B. Keel, P. F. Heini, U. Seidel, and L. M. Benneker, "Complications related to cement leakage in sacroplasty," *Acta Orthop. Belg.*, vol. 78, no. 1, pp. 100–105, 2012.

[45] S. M. Barber, A. D. Livingston, and D. A. Cech, "Sacral radiculopathy due to cement leakage from percutaneous sacroplasty, successfully treated with surgical decompression," *J. Neurosurg. Spine*, vol. 18, no. 5, pp. 524–528, 2013.

[46] S. V Bukata, "Systemic administration of pharmacological agents and bone repair: What can we expect," *Injury*, vol. 42, no. 6, pp. 605–608, 2011.

[47] P. Peichl, L. A. Holzer, R. Maier, and G. Holzer, "Parathyroid hormone 1-84 accelerates fracture-healing in pubic bones of elderly osteoporotic women," *J. Bone Jt. Surg. - Ser. A*, vol. 93, no. 17, pp. 1583–1587, 2011.

[48] D. K. Dittmer and R. Teasell, "Complications of immobilization and bed rest. Part 1: Musculoskeletal and cardiovascular complications.," *Can. Fam. Physician*, vol. 39, no. 1, pp. 1428–1437, 1993.

[49] R. Teasell and D. K. Dittmer, "Complications of immobilization and bed rest. Part 2: Other complications.," *Can. Fam. Physician*, vol. 39, no. June, pp. 1440–1442, 1445, 1993.

[50] M. Babayev, E. Lachmann, and W. Nagler, "The controversy surrounding sacral insufficiency fractures to ambulate or not to ambulate?," *Am. J. Phys. Med. Rehabil.*, vol. 79, no. 4, pp. 404–409, 2000.

[51] P. M. Rommens, D. Wagner, and A. Hofmann, "Osteoporotic fractures of the pelvic ring ," *Z. Orthop. Unfall.*, vol. 150, no. 3, pp. e107–e120, 2012.

[52] H. P. Geiselhart and T. Abele, "Total instability of the pelvic ring as a result of increasing unsufficiency fractures ," *Unfallchirurg*, vol. 102, no. 8, pp. 656–661, 1999.

[53] L. Graham-Gotis *et al.*, "Sacral insufficiency fractures in the elderly," *J. Bone Jt. Surg. - Ser. B*, vol. 76, no. 6, pp. 882–886, 1994.

[54] A. S. Greenwald and J. J. O'Connor, "The transmission of load through the human hip joint," *J. Biomech.*, vol. 4, no. 6, pp. 507–528, 1971.

[55] D. Lionberger, P. S. Walker, and J. Granholm, "Effects of prosthetic acetabular replacement on strains in the pelvis," *J. Orthop. Res.*, vol. 3, no. 3, pp. 372–379, 1985.

[56] M. Ries, J. Pugh, J. Choy Au, J. Gurtowski, and R. Dee, "Cortical pelvic strains with varying size hemiarthroplasty in vitro," *J. Biomech.*, vol. 22, no. 8–9, 1989.

[57] H. A. C. Jacob, A. H. Huggler, C. Dietschi, and A. Schreiber, "Mechanical function of subchondral bone as experimentally determined on the acetabulum of the human pelvis," *J. Biomech.*, vol. 9, no. 10, pp. 625-626,IN1-IN2,627, 1976.

[58] Y. Yoshioka and R. Shiba, "A study on the stress analysis of the pelvis by means of the three-dimensional photoelastic experiments," *J. Japanese Orthop. Assoc.*, vol. 55, no. 2, pp. 209–222, 1981.

[59] A. W. Miles and P. B. McNamee, "Strain gauge and photoelastic evaluation of the load transfer in the pelvis in total hip replacement: The effect of the position of the axis of rotation," *Proc. Inst. Mech. Eng. Part H J. Eng. Med.*, vol. 203, no. 2, pp. 103–107, 1989.

[60] R. Ghosh, S. Gupta, A. Dickinson, and M. Browne, "Experimental Validation of Finite Element Models of Intact and Implanted Composite Hemipelvises Using Digital Image Correlation," *J. Biomech. Eng.*, vol. 134, no. 8, p. 081003, 2012.

[61] J. M. García, M. Doblaré, B. Seral, F. Seral, D. Palanca, and L. Gracia, "Three-dimensional finite element analysis of several internal and external pelvis fixations.," *J. Biomech. Eng.*, vol. 122, no. 5, pp. 516–522, 2000.

[62] A. E. Anderson, C. L. Peters, B. D. Tuttle, and J. A. Weiss, "Subject-Specific Finite Element Model of the Pelvis: Development, Validation and Sensitivity Studies," *J. Biomech. Eng.*, vol. 127, no. 3, p. 364, 2005.

[63] M. Dalstra, R. Huiskes, and E. L. van, "Development and validation of a three-dimensional finite element model of the pelvic bone," *J.Biomech.Eng*, vol. 117, no. 0148-0731 (Print), pp. 272–278, 1995.

[64] Z. Hao, "The Effect of Boundary Condition on the Biomechanics of a Human Pelvic Joint Under an Axial Compressive Load: A Three-Dimensional Finite Element Model," *J. Biomech. Eng.*, vol. 133, no. 10, p. 101006, 2011.

[65] V. B. Shim, R. P. Pitto, R. M. Streicher, P. J. Hunter, and I. A. Anderson, "Development and Validation of Patient-Specific Finite Element Models of the Hemipelvis Generated From a Sparse CT Data Set," *J. Biomech. Eng.*, vol. 130, no. 5, p. 051010, 2008.

[66] A. S. Dickinson, A. C. Taylor, and M. Browne, "The influence of acetabular cup material on pelvis cortex surface strains, measured using digital image correlation,"

J. Biomech., vol. 45, no. 4, pp. 719–723, 2012.

[67]   R. Mehin, B. Jones, Q. Zhu, and H. Broekhuyse, "A biomechanical study of conventional acetabular internal fracture fixation versus locking plate fixation.," *Can. J. Surg.*, vol. 52, no. 3, pp. 221–228, 2009.

[68]   D. R. Sparks, D. P. Beason, B. S. Etheridge, J. E. Alonso, and A. W. Eberhardt, "Contact pressures in the flexed hip joint during lateral trochanteric loading," *J. Orthop. Res.*, vol. 23, no. 2, pp. 359–366, 2005.

[69]   S. A. Olson, B. K. Bay, M. W. Chapman, and N. A. Sharkey, "Biomechanical consequences of fracture and repair of the posterior wall of the acetabulum Biomechanical Consequences of the Posterior of Fracture and Repair of the Acetabulum *," *J. Bone Jt. Surg.*, vol. 77, pp. 1184–1192, 1995.

[70]   T. Pohlemann, M. Angst, E. Schneider, R. Ganz, and H. Tscherne, "Fixation of transforaminal sacrum fractures: A biomechanical study," *J. Orthop. Trauma*, vol. 7, no. 2, pp. 107–117, 1993.

[71]   T. A. Schildhauer, W. R. Ledoux, J. R. Chapman, M. B. Henley, A. F. Tencer, and J. L. Chip Routt, "Triangular osteosynthesis and iliosacral screw fixation for unstable sacral fractures: A cadaveric and biomechanical evaluation under cyclic loads," *J. Orthop. Trauma*, vol. 17, no. 1, pp. 22–31, 2003.

[72]   P. T. Simonian, M. L. C. Routt, R. M. Harrington, and A. F. Tencer, "The Acetabular T-Type Fracture," *Clin. Orthop. Relat. Res.*, vol. NA;, no. 314, p. 234???240, 1995.

[73]   K. Yinger, J. Scalise, S. A. Olson, B. K. Bay, and C. G. Finkemeier, "Biomechanical comparison of posterior pelvic ring fixation," *J. Orthop. Trauma*, vol. 17, no. 7, pp. 481–487, 2003.

[74]   Y. Agarwal, S. Doebele, M. Windolf, T. Shiozawa, B. Gueorguiev, and F. M. Stuby, "Two-leg alternate loading model - A different approach to biomechanical investigations of fixation methods of the injured pelvic ring with focus on the pubic symphysis," *J. Biomech.*, vol. 47, no. 2, pp. 380–386, 2014.

[75]   V. B. Shim, J. Böshme, P. Vaitl, C. Josten, and I. A. Anderson, "An Efficient and Accurate Prediction of the Stability of Percutaneous Fixation of Acetabular Fractures With Finite Element Simulation," *J. Biomech. Eng.*, vol. 133, no. 9, p. 094501, 2011.

[76]   Y. Zhang, Y. Tang, P. Wang, X. Zhao, S. Xu, and C. Zhang, "Biomechanical comparison of different stabilization constructs for unstable posterior wall fractures of acetabulum. A cadaveric study," *PLoS One*, vol. 8, no. 12, 2013.

[77]   U. Culemann *et al.*, "Different stabilisation techniques for typical acetabular fractures in the elderly-A biomechanical assessment," *Injury*, vol. 41, no. 4, pp. 405–410, 2010.

[78]   M. Karanika, D. Georgiou, S. Darmanis, A. Papadogoulas, E. D. Pasiou, and S. K.

Kourkoulis, "Assessing osteosynthesis techniques for pelvic fractures using Digital Image Correlation," *Procedia Struct. Integr.*, vol. 2, pp. 1252–1259, 2016.

[79]   S. K. Kourkoulis, S. Darmanis, Papadogoulas, and E. D. Pasiou, "3D-DIC in the service of orthopaedic surgery: Comparative assessment of fixation techniques for acetabular fractures," *Eng. Fract. Mech.*, vol. 183, pp. 125–146, 2017.

[80]   A. H. Sutton, Michael , Jean-José, Orteu Schreier, *Image Correlation for Shape, Motion and Deformation Measurements*, vol. 53, no. 9. 2009.

[81]   Singh AK, Sharma RC, Sharma RK, and Musmade DM, "Challenges in Cadaver Availability for Learning and Research in Medical Sciences," *Int. J. Med. Clin. Res.*, vol. 2, no. 2, pp. 976–5530, 2011.

[82]   J. Elfar, R. M. G. Menorca, J. D. Reed, and S. Stanbury, "Composite bone models in orthopaedic surgery research and education," *J. Am. Acad. Orthop. Surg.*, vol. 22, no. 2, pp. 111–120, 2014.

[83]   J. Elfar, R. M. G. Menorca, J. D. Reed, and S. Stanbury, "Composite bone models in orthopaedic surgery research and education," *J. Am. Acad. Orthop. Surg.*, vol. 22, no. 2, pp. 111–120, 2014.

[84]   R. M. Meneghini, C. Meyer, C. A. Buckley, A. D. Hanssen, and D. G. Lewallen, "Mechanical stability of novel highly porous metal acetabular components in revision total hip arthroplasty," *J. Arthroplasty*, vol. 25, no. 3, pp. 337–341, 2010.

[85]   L. Cristofolini, M. Viceconti, A. Cappello, and A. Toni, "Mechanical validation of whole bone composite femur models," *J. Biomech.*, vol. 29, no. 4, pp. 525–535, 1996.

[86]   B. L. Girardi, T. Attia, D. Backstein, O. Safir, T. L. Willett, and P. R. T. Kuzyk, "Biomechanical comparison of the human cadaveric pelvis with a fourth generation composite model," *J. Biomech.*, vol. 49, no. 4, pp. 537–542, 2016.

[87]   A. S. O. Leung, L. M. Gordon, T. Skrinskas, T. Szwedowski, and C. M. Whyne, "Effects of bone density alterations on strain patterns in the pelvis: Application of a finite element model," *Proc. Inst. Mech. Eng. Part H J. Eng. Med.*, vol. 223, no. 8, pp. 965–979, 2009.

[88]   Y. Jia *et al.*, "Digital image measurement of specimen deformation based on CCD cameras & Image J software : An application to human pelvic biomechanics," *Inf. Opt. Photonics Technol. II*, vol. 6837, no. 04, pp. 1–10, 2007.

[89]   Z. Salo, M. Beek, D. Wright, and C. Marisa Whyne, "Computed tomography landmark-based semi-automated mesh morphing and mapping techniques: Generation of patient specific models of the human pelvis without segmentation," *J. Biomech.*, vol. 48, no. 6, pp. 1125–1132, 2015.

[90]   E. Varga, T. Hearn, J. Powell, and M. Tile, "Effects of method of internal fixation of symphyseal disruptions on stability of the pelvic ring," *Injury*, vol. 26, no. 2, pp.

75–80, 1995.

[91]   Singh AK, Sharma RC, Sharma RK, and Musmade DM, "Challenges in Cadaver Availability for Learning and Research in Medical Sciences," *Int. J. Med. Clin. Res.*, vol. 2, no. 2, pp. 976–5530, 2011.

[92]   C. Zeng, W. Xing, Z. Wu, H. Huang, and W. Huang, "A combination of three-dimensional printing and computer-assisted virtual surgical procedure for preoperative planning of acetabular fracture reduction," *Injury*, vol. 47, no. 10, pp. 2223–2227, 2016.

[93]   X. Chen *et al.*, "Accurate fixation of plates and screws for the treatment of acetabular fractures using 3D-printed guiding templates: An experimental study," *Injury*, vol. 48, no. 6, pp. 1147–1154, 2017.

[94]   K. Khajavi, A. T. Lee, D. P. Lindsey, P. Leucht, M. J. Bellino, and N. J. Giori, "Single column locking plate fixation is inadequate in two column acetabular fractures. A biomechanical analysis," *J. Orthop. Surg. Res.*, vol. 5, no. 1, pp. 1–6, 2010.

[95]   P. J. Watson, A. Dostanpor, M. J. Fagan, and C. A. Dobson, "The effect of boundary constraints on finite element modelling of the human pelvis," *Med. Eng. Phys.*, vol. 43, pp. 48–57, 2017.

[96]   M. Cimerman and A. Kristan, "Preoperative planning in pelvic and acetabular surgery: The value of advanced computerised planning modules," *Injury*, vol. 38, no. 4, pp. 442–449, 2007.

[97]   M. J. Rudert *et al.*, "A New Sensor for Measurement of Dynamic Contact Stress in the Hip," *J. Biomech. Eng.*, vol. 136, no. 3, p. 035001, 2014.

[98]   W. H. Peters and W. F. Ranson, "Digital Imaging Techniques In Experimental Stress Analysis," *Opt. Eng.*, vol. 21, no. 3, Jun. 1982.

[99]   T. C. Chu, W. F. Ranson, and M. A. Sutton, "Applications of digital-image-correlation techniques to experimental mechanics," *Exp. Mech.*, vol. 25, no. 3, pp. 232–244, 1985.

[100]   H. A. Bruck, S. R. McNeill, M. A. Sutton, and W. H. Peters, "Digital image correlation using Newton-Raphson method of partial differential correction," *Exp. Mech.*, vol. 29, no. 3, pp. 261–267, 1989.

[101]   M. Sutton, C. Mingqi, W. Peters, Y. Chao, and S. McNeill, "Application of an optimized digital correlation method to planar deformation analysis," *Image Vis. Comput.*, vol. 4, no. 3, pp. 143–150, 1986.

[102]   P. Synnergren and M. Sjödahl, "A stereoscopic digital speckle photography system for 3-D displacement field measurements," *Opt. Lasers Eng.*, vol. 31, no. 6, pp. 425–443, 1999.

[103] P. Synnergren, "Measurement of three-dimensional displacement fields and shape using electronic speckle photography," *Opt. Eng.*, vol. 36, no. 8, p. 2302, 1997.

[104] A. S. Dickinson, A. C. Taylor, H. Ozturk, and M. Browne, "Experimental Validation of a Finite Element Model of the Proximal Femur Using Digital Image Correlation and a Composite Bone Model," *J. Biomech. Eng.*, vol. 133, no. 1, p. 014504, 2011.

[105] G. Okotie, S. Duenwald-Kuehl, H. Kobayashi, M.-J. Wu, and R. Vanderby, "Tendon Strain Measurements With Dynamic Ultrasound Images: Evaluation of Digital Image Correlation," *J. Biomech. Eng.*, vol. 134, no. 2, p. 24504, Mar. 2012.

[106] M. Hokka, N. Mirow, H. Nagel, M. Irqsusi, S. Vogt, and V.-T. Kuokkala, "In-vivo deformation measurements of the human heart by 3D Digital Image Correlation," *J. Biomech.*, vol. 48, no. 10, pp. 2217–2220, 2015.

[107] G. W. Melenka and J. P. Carey, "Experimental analysis of diamond and regular tubular braided composites using three-dimensional digital image correlation," *J. Compos. Mater.*, vol. 51, no. 28, pp. 3887–3907, Feb. 2017.

[108] S.-H. Tung and C.-H. Sui, "Application of digital-image-correlation techniques in analysing cracked cylindrical pipes," *Sadhana*, vol. 35, no. 5, pp. 557–567, 2010.

[109] S. G. Shah and J. M. C. Kishen, "Fracture Properties of Concrete-Concrete Interfaces Using Digital Image Correlation," *Exp. Mech.*, vol. 51, no. 3, pp. 303–313, 2011.

[110] S. A. Hall *et al.*, "Discrete and continuum analysis of localised deformation in sand using X-ray μCT and volumetric digital image correlation," *Geotechnique*, vol. 60, no. 5, pp. 315–322, 2010.

[111] F. Hild and S. Roux, "Digital image correlation: From displacement measurement to identification of elastic properties - A review," *Strain*, vol. 42, no. 2, pp. 69–80, 2006.

[112] S. Avril *et al.*, "Overview of identification methods of mechanical parameters based on full-field measurements," *Exp. Mech.*, vol. 48, no. 4, pp. 381–402, 2008.

[113] G. Vendroux and W. G. Knauss, "Submicron deformation field measurements: Part 1. Developing a digital scanning tunneling microscope," *Exp. Mech.*, vol. 38, no. 1, pp. 18–23, 1998.

[114] G. Vend Roux and W. G. Knauss, "Submicron deformation field measurements: Part 2. Improved digital image correlation," *Exp. Mech.*, vol. 38, no. 2, pp. 86–92, 1998.

[115] B. Gencturk, K. Hossain, A. Kapadia, E. Labib, and Y.-L. Mo, "Use of digital image correlation technique in full-scale testing of prestressed concrete structures," *Meas. J. Int. Meas. Confed.*, vol. 47, no. 1, pp. 505–515, 2014.

[116] J. S. and J. Sirohi, "Measurement of the deformation of an extremely flexible rotor

blade using digital image correlation," *Meas. Sci. Technol.*, vol. 24, no. 6, p. 65203, 2013.

[117] P. Reu, "Calibration: 2D Calibration," *Exp. Tech.*, vol. 37, no. 5, pp. 1–2, 2013.

[118] P. Reu, "Calibration: Stereo Calibration," *Exp. Tech.*, vol. 38, no. 1, pp. 1–2, 2014.

[119] R. B. Abernethy, R. P. Benedict, and R. B. Dowdell, "ASME Measurement Uncertainty," *J. Fluids Eng.*, vol. 107, no. 2, p. 161, 1985.

[120] ASME/ANSI PTC 19.1, "Test Uncertainty," 2013.

[121] M. A. Sutton, J. J. Orteu, H. W. Schreier, and P. Reu, "Introduction to digital image correlation: Best practices and applications," *Exp. Tech.*, vol. 36, no. 1, pp. 3–4, 2012.

[122] R. Bigger *et al.*, "A Good Practices Guide for Digital Image Correlation," Oct. 2018.

[123] D. Lecompte *et al.*, "Quality assessment of speckle patterns for digital image correlation," *Opt. Lasers Eng.*, vol. 44, no. 11, pp. 1132–1145, 2006.

[124] B. Pan, Z. Lu, and H. Xie, "Mean intensity gradient: An effective global parameter for quality assessment of the speckle patterns used in digital image correlation," *Opt. Lasers Eng.*, vol. 48, no. 4, pp. 469–477, 2010.

[125] P. L. Reu, "A Study of the Influence of Calibration Uncertainty on the Global Uncertainty for Digital Image Correlation Using a Monte Carlo Approach," *Exp. Mech.*, vol. 53, no. 9, pp. 1661–1680, 2013.

[126] H. Haddadi and S. Belhabib, "Use of rigid-body motion for the investigation and estimation of the measurement errors related to digital image correlation technique," *Opt. Lasers Eng.*, vol. 46, no. 2, pp. 185–196, 2008.

[127] M. Bornert *et al.*, "Assessment of digital image correlation measurement errors: Methodology and results," *Exp. Mech.*, vol. 49, no. 3, pp. 353–370, 2009.

[128] B. Pan, H. M. Xie, B. Q. Xu, and F. L. Dai, "Performance of sub-pixel registration algorithms in digital image correlation," *Meas. Sci. Technol.*, vol. 17, no. 6, pp. 1615–1621, 2006.

[129] S. Yaofeng and J. H. L. Pang, "Study of optimal subset size in digital image correlation of speckle pattern images," *Opt. Lasers Eng.*, vol. 45, no. 9, pp. 967–974, 2007.

[130] P. Reu, "All about speckles: Speckle Size Measurement," *Exp. Tech.*, vol. 38, no. 6, pp. 1–2, Nov. 2014.

[131] G. Crammond, S. W. Boyd, and J. M. Dulieu-Barton, "Speckle pattern quality assessment for digital image correlation," *Opt. Lasers Eng.*, vol. 51, no. 12, pp. 1368–1378, 2013.

[132] P. Reu, "All about speckles: Aliasing," *Exp. Tech.*, vol. 38, no. 5, pp. 1–3, 2014.

[133] P. Zhou and K. E. Goodson, "Subpixel displacement and deformation gradient measurement using digital image/speckle correlation (DISC)," *Opt. Eng.*, vol. 40, no. 8, p. 1613, Aug. 2001.

[134] J. Park, S. Yoon, T. H. Kwon, and K. Park, "Assessment of speckle-pattern quality in digital image correlation based on gray intensity and speckle morphology," *Opt. Lasers Eng.*, vol. 91, no. November 2016, pp. 62–72, 2017.

[135] D. C. Montgomery, *Design and Analysis of Experiments*. USA: John Wiley & Sons, Inc., 2006.

[136] G. W. Melenka, J. S. Schofield, M. R. Dawson, and J. P. Carey, "Evaluation of dimensional accuracy and material properties of the MakerBot 3D desktop printer," *Rapid Prototyp. J.*, vol. 21, no. 5, pp. 618–627, 2015.

[137] P. G. Benardos and G. C. Vosniakos, "Prediction of surface roughness in CNC face milling using neural networks and Taguchi's design of experiments," *Robot. Comput. Integr. Manuf.*, vol. 18, no. 5–6, pp. 343–354, 2002.

[138] V. Elango and L. Karunamoorthy, "Effect of lighting conditions in the study of surface roughness by machine vision - An experimental design approach," *Int. J. Adv. Manuf. Technol.*, vol. 37, no. 1–2, pp. 92–103, 2008.

[139] P. L. Reu, "Experimental and Numerical Methods for Exact Subpixel Shifting," *Exp. Mech.*, vol. 51, no. 4, pp. 443–452, 2011.

[140] W. Thielicke and E. J. Stamhuis, "PIVlab – Towards User-friendly, Affordable and Accurate Digital Particle Image Velocimetry in MATLAB," *J. Open Res. Softw.*, vol. 2, Oct. 2014.

[141] P. Reu, "Calibration : Care and Feeding of a Stereo-rig," vol. 38, pp. 1–2, 2014.

[142] G. Lionello and L. Cristofolini, "A practical approach to optimizing the preparation of speckle patterns for digital-image correlation," *Meas. Sci. Technol.*, vol. 25, no. 10, pp. 1–9, 2014.

[143] J. L. Dressler, "Development of the Multi-Axis Biomechanical Testing Apparatus to Experimentally Measure In-Vitro Stresses on Knee Cortex under Gait Level Loads," University of Alberta (M.Sc. Thesis), 2008.

[144] H. Nazeri, "An investigation of the strain field and inter-fragmentary movement of a broken hemi-pelvis," University of Alberta (M.Sc. Thesis), 2015.

[145] ASTM International, "Standard test method for tensile properties of plastics," *ASTM Int.*, vol. 08, pp. 46–58, 2003.

[146] ISO 527-1:2012, "Plastics — Determination of tensile properties — Part 1: General principles."

[147] H. Tada, P. C. Paris, and G. R. Irwin, *The Stress Analysis of Cracks Handbook, Third Edition*. Three Park Avenue New York, NY 10016-5990: ASME, 2000.

[148] T. L. Anderson, *Fracture Mechanics*. CRC Press, 2017.

[149] LaVision, *DaVis 8.2 Software*. Göttingen: LaVision GmbH, 2014.

[150] D. R. Moore, J. G. Williams, and A. Pavan, *Fracture Mechanics Testing Methods for Polymers, Adhesives and Composites*, 1st ed., vol. 7. Oxford: Elsevier, 2001.

[151] M. S. R. Aziz, E. H. Schemitsch, and R. Zdero, *Biomechanical Testing of the Intact and Surgically Treated Pelvis*. Elsevier Inc., 2016.

[152] S. P. Väänänen, S. Amin Yavari, H. Weinans, A. A. Zadpoor, J. S. Jurvelin, and H. Isaksson, "Repeatability of digital image correlation for measurement of surface strains in composite long bones," *J. Biomech.*, vol. 46, no. 11, pp. 1928–1932, 2013.

[153] L. Cristofolini, M. Viceconti, A. Cappello, and A. Toni, "Mechanical validation of whole bone composite femur models," *J. Biomech.*, vol. 29, no. 4, pp. 525–535, 1996.

[154] J. D. Bobyn, E. S. Mortimer, A. H. Glassman, C. A. Engh, J. E. Miller, and C. E. Brooks, "Producing and avoiding stress shielding: Laboratory and clinical observations of noncemented total hip arthroplasty," *Clin. Orthop. Relat. Res.*, no. 274, pp. 79–96, 1992.

[155] R. M. Meneghini, C. Meyer, C. A. Buckley, A. D. Hanssen, and D. G. Lewallen, "Mechanical stability of novel highly porous metal acetabular components in revision total hip arthroplasty," *J. Arthroplasty*, vol. 25, no. 3, pp. 337–341, 2010.

[156] S. R. Small, M. E. Berend, L. A. Howard, D. Tunç, C. A. Buckley, and M. A. Ritter, "Acetabular Cup Stiffness and Implant Orientation Change Acetabular Loading Patterns," *J. Arthroplasty*, vol. 28, no. 2, pp. 359–367, 2013.

Appendix A: Scheimpflug setup

A.1   Overview

A Scheimpflug adapter is an optical component that allows cameras to capture an angular plane of focus, as opposed to a parallel. Under normal conditions, flat surfaces that are viewed at an angle are difficult to be entirely in focus. Inserting a Scheimpflug adapter between the lens and the sensor allows for the correction of the plane of focus to be in line with the angled flat surface. This is particularly beneficial for a stereo DIC system because the drawback of losing even focus across a specimen surface due to camera angling is compensated for. The following content details how the Scheimpflug system was determined in this thesis and how to repeat the procedure.

A.2   Determining Scheimpflug geometry

To determine if the components are adequate to achieve the desired imaging setup, a preliminary analysis of the optical system should be conducted under thin lens conditions as shown in Figure A-1. The estimated standoff distance is determined using the relationship,

$$\frac{w_{sensor}}{v} = \frac{w_{FOV}}{u}$$

where:
v is the lens length, and
u is the standoff distance.

Typically, the lens length and sensor width are known and the desired field of view is prescribed to allow for the calculation of the standoff distance. If the physical setup is limited, the standoff distance may be prescribed. And if the system is being designed for purchase, the lens length may be the calculated parameter. It should be noted that the calculations are estimations, as the lens length is not the only contributor to the system focal length. Also, the geometric parameters alter when the Scheimpflug adapter is introduced. But if the basic calculations can satisfy the conditions of the test, the Scheimpflug geometry can be more easily determined. The thin lens standoff distance, u, can be used to estimate the standoff distance in the following Scheimpflug system.
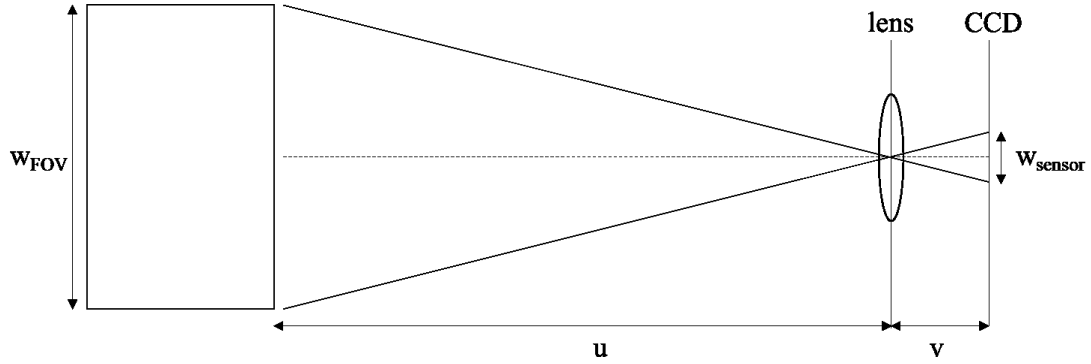
Figure A-1. Thin lens approximation for preliminary assessment of imaging setup.

The geometry for the Scheimpflug optical system is much more complex, with a simplified version shown in Figure A-2. The relationship between the main components in the Scheimpflug principle are,

$$\tan \psi = \frac{u'}{f} \sin \theta$$

where:

ψ is the Scheimpflug angle,
u' is the distance along the optical axis between the lens and the target,
f is the lens focal length, and
θ is the angle between the camera and the target viewing surface.

The distance between the sensor plane and the lens plane along the optical axis, v', can be represented as,

$$\tan \psi = \frac{v'}{v' \cos \theta - f} \sin \theta$$

This then allows for the standoff distance, y, and the distance between cameras, x, to be determined using trigonometric relationships,

$$y = \cos \psi \, (u' + v')$$
$$x = 2 \times \sin \psi \, (u' + v')$$

188
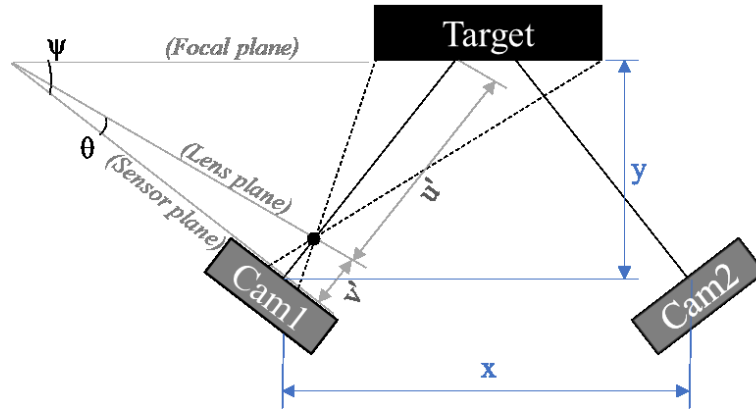
Figure A-2. Geometric relationships in Scheimpflug setup.

The parameters to be determined are dependent on the constraints of the setup. The stereo angle is most likely prescribed and may be dependent on the extent of curvature on the surface, which can limit the areas of the surface viewable by both cameras. Also, the balance between in-plane and out-of-plane measurement quality can dictate how small or large the stereo angle should be. Otherwise, some Scheimpflug adapters are non-adjustable, fixing the respective parameter. And if space is an issue, the standoff distance or the camera spacing may be prescribed and the Scheimpflug or stereo angles to be determined.

A.3　Camera focus

After setting up the Scheimpflug imaging system to the desired geometry, the cameras can be focused for optimal subject viewing. However, this process is different from the regular straight-view camera system. The focus distance shown on the lens does not correspond to the distance between the lens and the object in a Scheimpflug setup. Manual adjustments and judgements must be made while viewing the image. Adjustments to the depth of focus also are different, as shown in Figure A-3. Changing the aperture size (by changing the lens f/#) in a straight image shown in Figure A-3 (a) shows that the resizing of the depth of focus is in line with the viewing target. But with a Scheimpflug adapter, changes to the aperture size cause the depth of focus to change size obliquely and shift angularly as shown in Figure A-3 (b). Once the adjustments are made, testing can be performed. Until all desired tests are completed, the physical camera system should remain undisturbed.
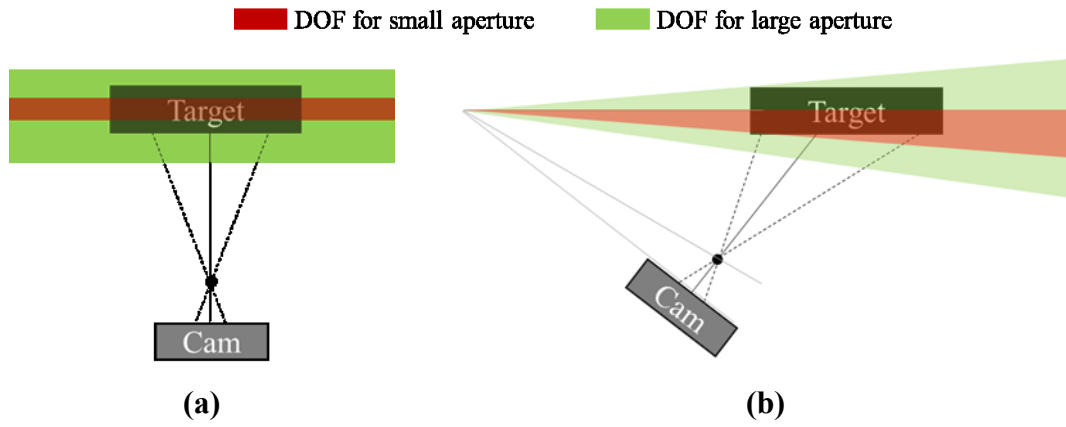
Figure A-3. Comparison of depth of field adjustments, showing **(a)** normal view, and **(b)** Scheimpflug adapter view.

Appendix B: Speckle Morphology

B.1   Overview

A MATLAB program with the filename "DIC_SpeckleMorphology.m" was developed to morphologically analyze a speckle pattern. The main interface is shown in Figure B-1. This appendix will detail how the program works and how to use it.
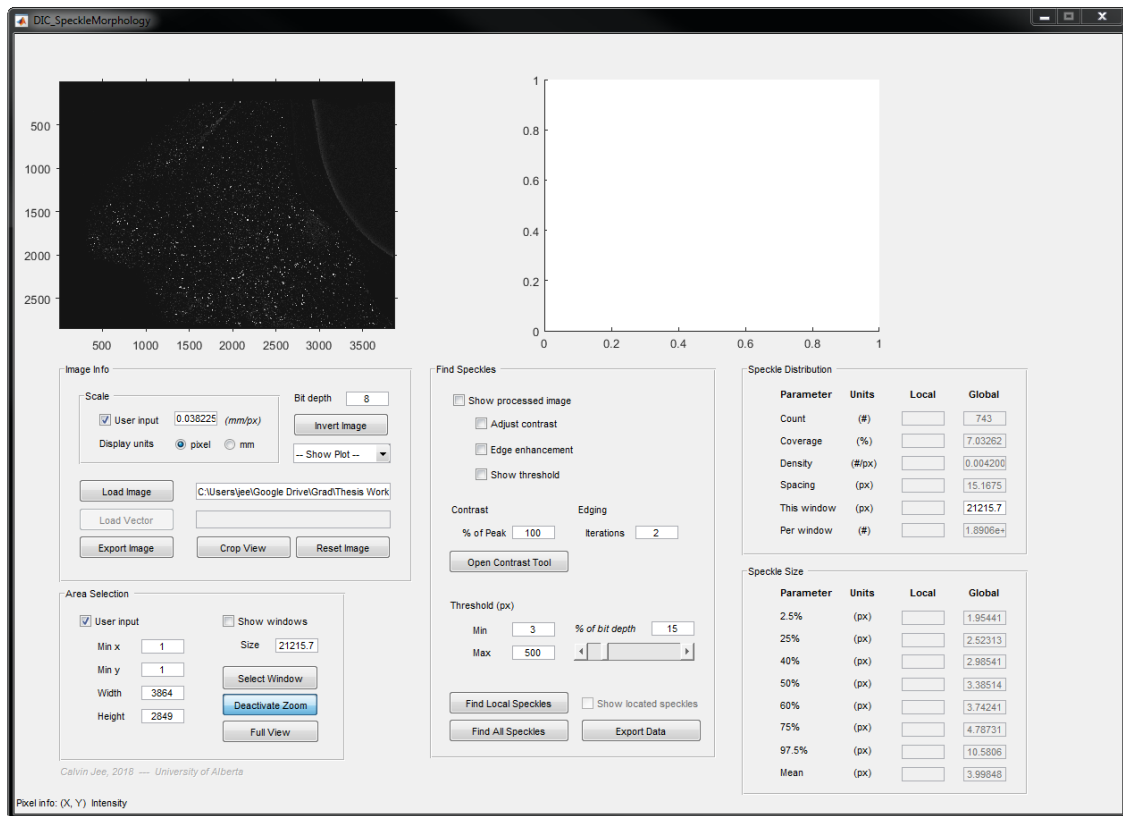
Figure B-1. Interface of MATLAB program developed to morphologically analyze speckle patterns.

B.2   Image setup

The first step is to press the "load image" button and load the image to be analyzed. Currently, the program can handle .im7 or .tif files. Once loaded, the image will display on the left plot axes of the interface. The image must be white speckles on a black background. If the loaded image is the opposite, press the "invert image" button to enable the program to proceed.

Using the tool in the "area selection" section, adjust the visible image to show the area to be analyzed. This is necessary for images which contain background noise. Once the desired view is attained, press the "crop view" button to limit the analysis to the region displayed on the image axes. If a different field of view is desired, the original image can be recovered by pressing the "reset image" button. Otherwise, the image can now be filtered and analyzed.

B.3 Image filtering

Image filtering is performed to aid the MATLAB program to separate the speckles from one another or from background noise. In the current iteration of the program, the processing options are limited. It should also be noted that the processing functions are time consuming, especially with large images. It is recommended to crop a small section of an image and determine ideal processing settings, then apply them to the full view.

When the "adjust contrast" box is checked, global contrasting will be applied to the image. This is based on the "contrast → % of peak" field, in which the intensity floor is shifted to the peak as per the value in the field as shown in Figure B-2. This allows for finer control over of filtering and thresholding, as the range of intensity values is maximized. It is recommended to always select this option.
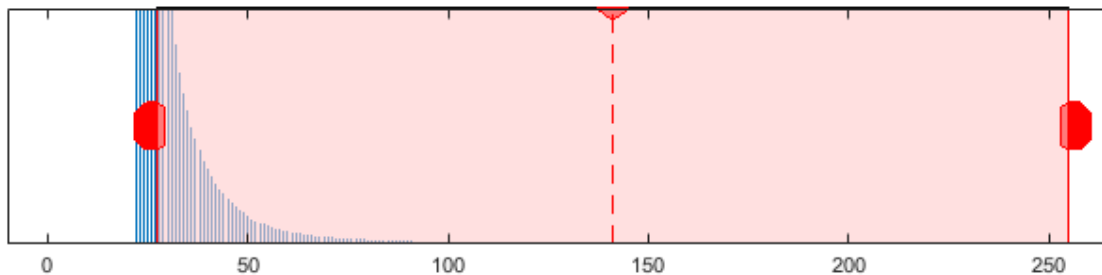
Figure B-2. Intensity distribution plot, showing movement of intensity floor to improve global contrast.

When the "edge enhancement" box is checked, local contrasting will be applied. This is dictated by the "edging → iterations" field. In this stage of image editing, the image is sharpened, then a sequence of dilation, erosion, and local Laplacian filtering is conducted to the number of iterations specified. The parameters used in these image processing functions were set based on trial and error but can be edited directly in the file named

192

"preEdge.m". This option is useful for distinguishing speckles that are clumped and have soft edge, as they can normally be combined and treated as larger speckles. It is not needed for speckle patterns with well-defined edges. And in cases where there are very low contrast speckles that are essentially noise, local contrasting may treat them as real speckles. Local contrasting should be used carefully for the best morphological result.

Thresholding is the final step of the image processing before morphological analysis can be conducted. In this step, the image is binarized, making detected speckles completely white and the background completely black. This allows the program to locate and characterize the speckles unambiguously. The minimum and maximum determine the limits of the sizes of features considered to be speckles in terms of pixel count. Then, the "% of bit depth" value specifies the minimum intensity, given as a percentage of the full intensity range of the image, for a pixel to be made white with all other pixels below the cutoff converted to black. Basically, it separates speckles from background noise. The morphological analysis to be conducted is based on the threshold image. To ensure that it is a reasonable representation of the original image, the "show processed image" checkbox can be toggled to compare the two, as shown in Figure B-3.

<center>(a)   (b)</center>
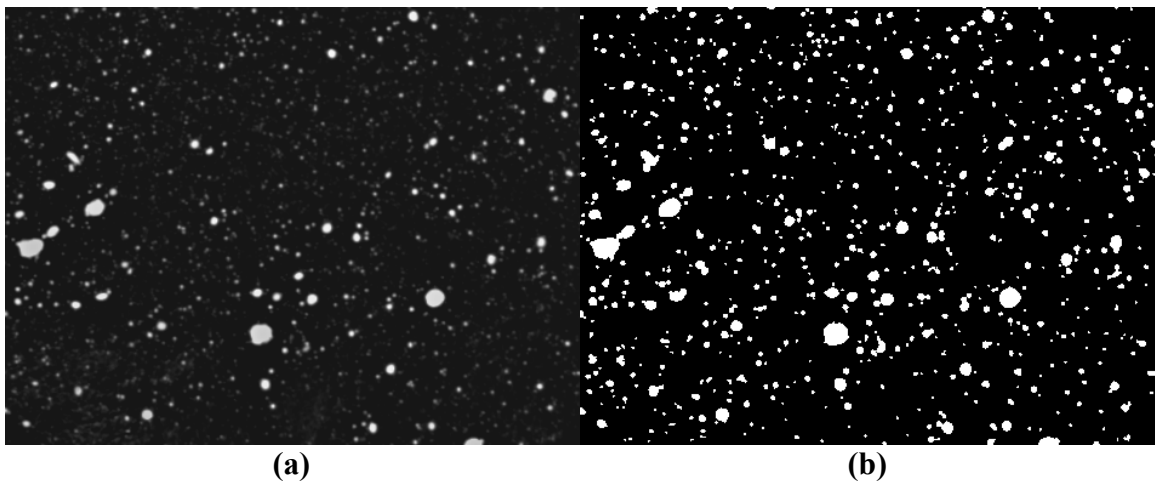
Figure B-3. Morphological analysis of a speckle pattern, showing **(a)** the original image and **(b)** the final threshold image to be analyzed.

B.4 Extracting data

Once the image is finalized, the "find all speckles" button can be pressed to run the morphological analysis. The program counts the speckles and records the size and location of each speckle. All parameters under the "speckle distribution" and "speckle size" sections are calculated based on those values. Within the "show plot" dropdown, selected results can be displayed on the axes on the right of the interface. If the results are satisfactory, they can be saved to a text file by pressing the "export data" button.

Appendix C: Using the cameras

C.1   Hardware

C.1.1 Camera components

Table C-1 lists the components required to run the cameras in the imaging system.

Table C-1. List of components in imaging system required to run cameras.

Cameras
GX-3300, Allied Vision
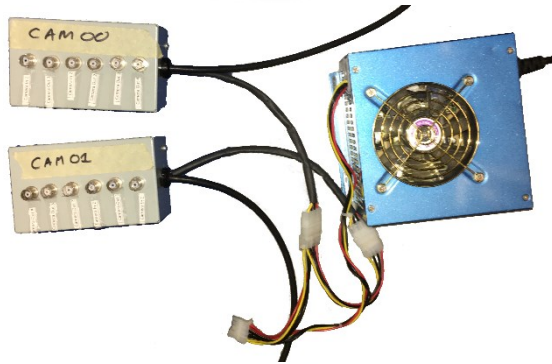
Power supply unit (PSU)
EG425P-VE, Enermax
(Sends power through camera boxes to cameras)
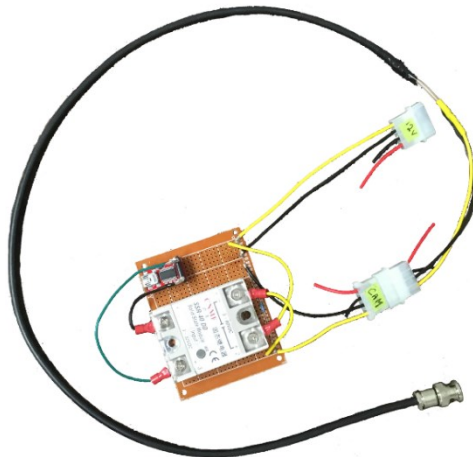
Trigger circuit board
*Custom design
(connects trigger power from PSU to cameras; connects to MABTA computer for trigger signal)

GigE card
PRO/1000 PT, Intel®
(connects cameras to imaging computer)

C.1.2 Optics and optomechanics

The optical components are shown assembled and affixed to the multi-axis biomechanical testing apparatus (MABTA) in Figure C-1. The subassembly components are detailed and labeled in the assembly drawing in Figure C-2.
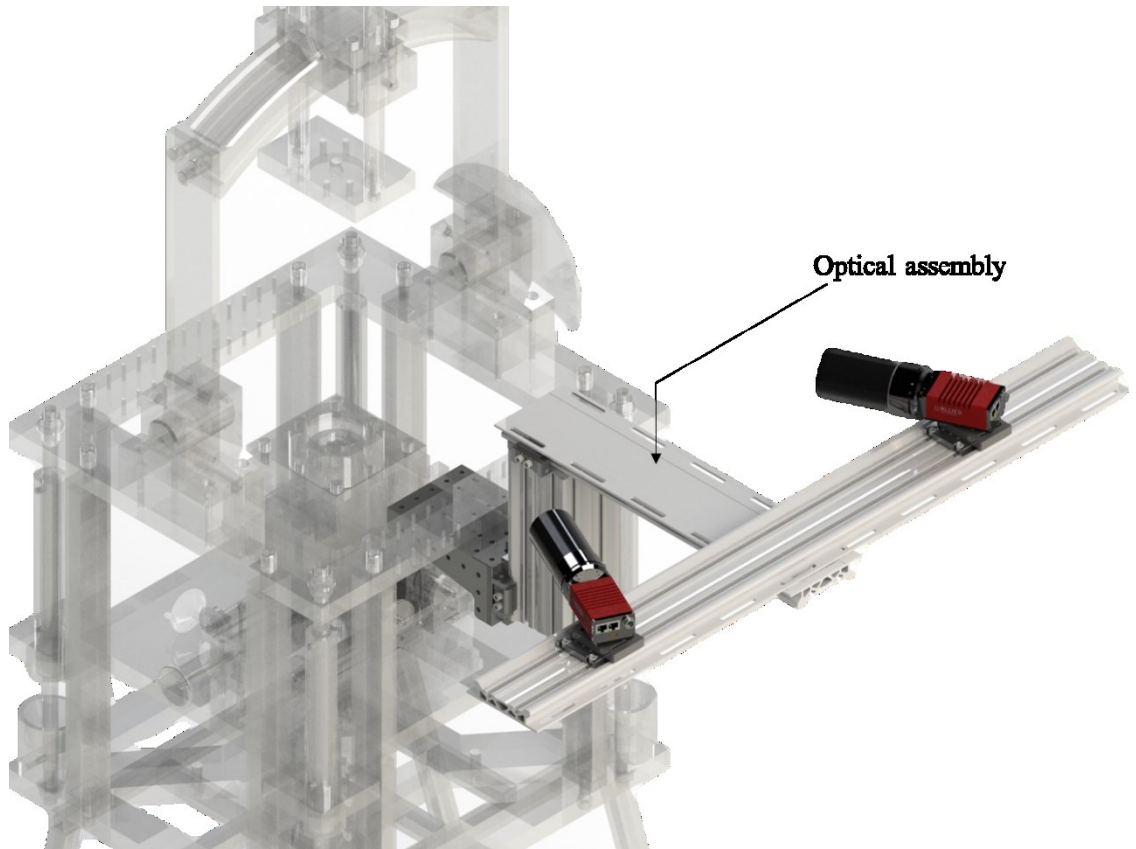
Figure C-1. Mounting of optical assembly onto MABTA (displayed with translucency).

ITEM NO.	PART NUMBER	Manufacturer	SW-Author(Author)	QTY.
1	Rail_95mm_1side_L1000 (XT95SP-1000)	Thorlabs	Thorlabs	1
2	Rail_95mm_1side_L500 (XT95SP-500)	Thorlabs	Thorlabs	1
3	Rail Carriage_95mm (XT95P11)	Thorlabs	Thorlabs	2
4	Rail_95mm_L250 (XT95-250)	Thorlabs	Thorlabs	1
5	Bracket_90deg (AP90RL)	Thorlabs	Thorlabs	1
6	Rail Plate_95mm (XT95P12)	Thorlabs	Thorlabs	2
7	Spacer_0.5in (BA2S6)	Thorlabs	Thorlabs	2
8	Camera Assembly (AV-GX3300)	-	Calvin Jee	2
	GX3300 F-Mount	Allied Vision	Allied Vision	1
	Camera Lens (80 mm) (f#2.8, Arax)	Arax	Calvin Jee	1

The Department of Mechanical Engineering
UNIVERSITY OF ALBERTA

TITLE

Optical Assembly

MODEL BY (Last Save): Calvin Jee (2018-11-28)
DRAWING BY (Last Save): Calvin Jee (2018-11-28)
SUPERVISOR (Checked?): Dr. Kajsa Duke ( )

SIZE B | ORDER NO. - | MASS: 3418.56 g | REV 1

SCALE: 1:4 | SHEET 1 OF 1

SPEED CODE: -
COMMENTS:

UNLESS OTHERWISE SPECIFIED:
DIMENSIONS ARE IN MM
TOLERANCES:
ANGULAR: ± 0.5°
LINEAR
X = ± 0.5
X.X = ± 0.1
X.X.X = ± 0.025
SURFACE FINISH 0.6 μm
DO NOT SCALE DRAWING

MATERIAL: -

FILE NAME: _Optical Assembly

Figure C-2. Assembly drawing, showing all components used in the imaging system.

197

C.1.3 Other imaging components

Table C-2 lists other necessary imaging components to use the cameras for a DIC experiment.

Table C-2. List of other essential components in imaging system.

Illumination
CN-600SA, Nanguang Photo & Video
Systems Co.
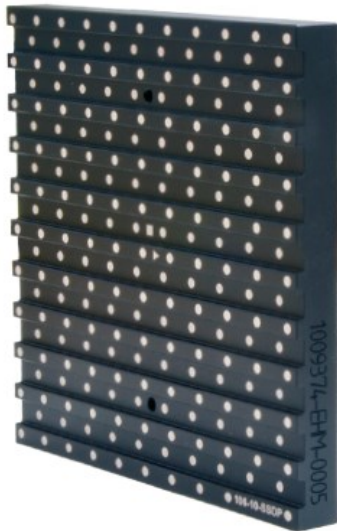
Calibration plate
Type 22, LaVision GmbH

Airbrush gun
PCMT70536, Porter Cable
(used to paint speckles on test specimens)

C.2 Software

The main interface for the camera control software, entitled StereoCam, is shown in Figure C-3.
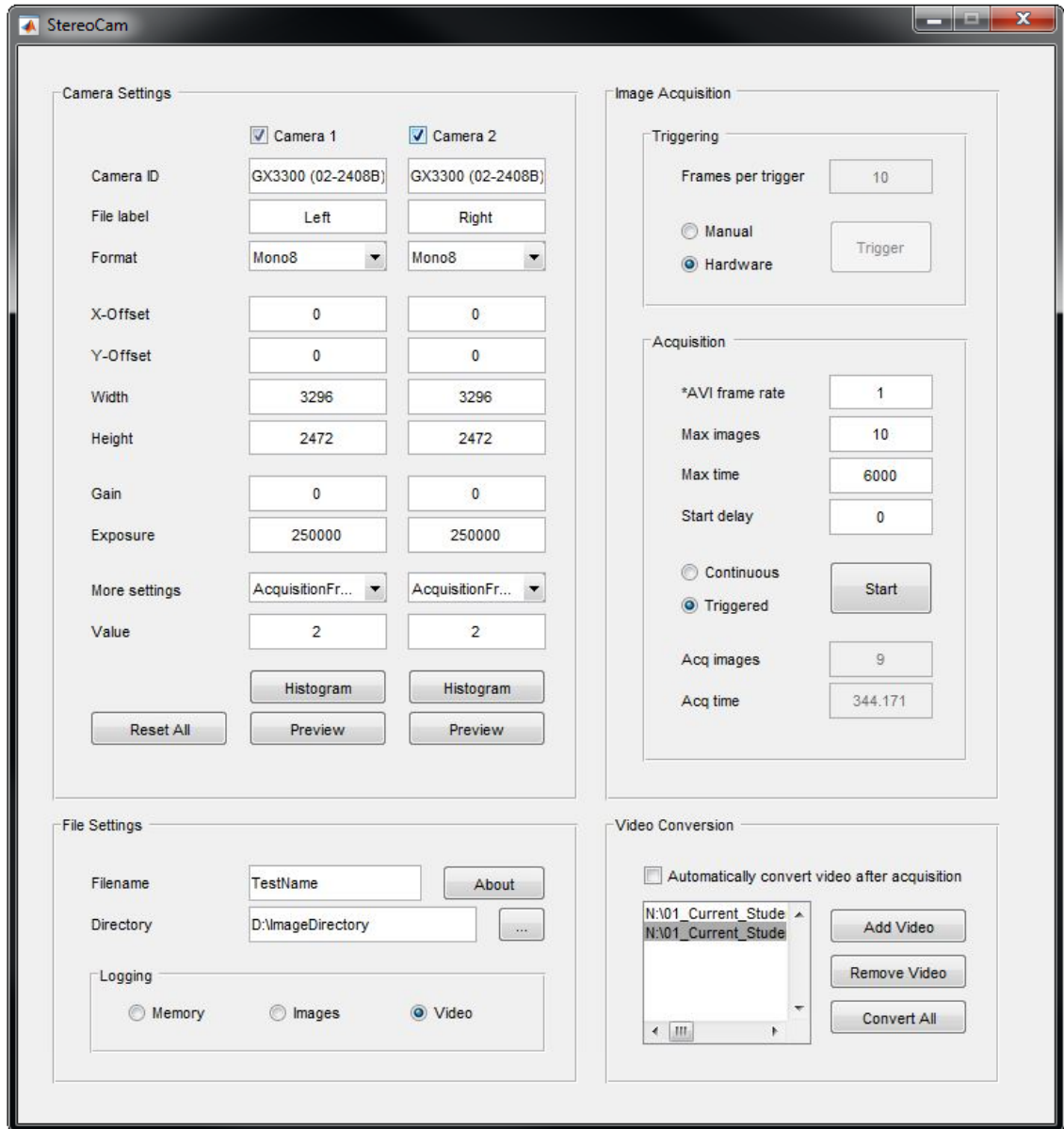
Figure C-3. MATLAB program created for stereo camera control.

C.2.1 Loading cameras

First, the camera(s) involved in the image acquisition must be loaded into the software. This is done by clicking the checkbox for either camera 1 or 2, which will then prompt the user to select a detected camera to load. Once loaded, the camera settings can be adjusted to specifications. The region of interest (ROI) parameters (x-offset, y-offset, width, and height) and the brightness settings (gain and exposure) are displayed and readily adjustable. Smaller images require less computational power to handle, leaving ROI adjustability desirable in situations where large chunks of the camera field of view (FOV) are not of interest. Gain should be set to 0 in most cases, as more gain increases the intensity of all pixels in the image but does not increase contrast. This means that the image processing correlation is not improved by increasing gain.

More settings are available than those displayed upfront. However, because different cameras have different programming protocols, settings from some cameras may be unavailable to others. For example, hardware triggering is available for the GX-3300 camera, but not for generic webcams. The option of displaying all adjustable settings available was considered but passed on as some cameras have hundreds of parameters and would be overwhelming for any user. Therefore, key parameters are coded into the program for each camera. For the GX-3300, frame rate, binning, and packet size are adjustable through this interface. If other settings are deemed crucial in the future, the code can easily be adjusted to add them to the interface dropdown list.

Currently, the StereoCam software can handle generic webcams and the GX-3300 cameras. Again, because of the wide variety of camera handling protocols, many cameras must be individually programmed. To add another camera to the software, copy an existing camSet_*cameraName*.m file and modify the tags and values to fit with the camera of interest. Save the script as camSet_*newCamera*.m and modify the camSet.m file to include the new camera, as shown in Figure C-4.

```
% Update camera settings -- refers to individual camera update scripts
function cam = camSet(cam, varargin)

...
```

```
% update based on camera being used
switch cam.ID
    case 'GX3300 (02-2408B)'
        cam = camSet_GX3300(cam, tag, val);
    case 'Microsoft LifeCam Studio'
        cam = camSet_MSLifeCam(cam, tag, val);
    case 'Logitech HD Webcam C270'
        cam = camSet_LogitechC270(cam, tag, val);
    case 'Integrated Webcam'
        cam = camSet_XPSwebcam(cam, tag, val);

    case '*newCamera*'
        cam = camSet_*newCamera*(cam, tag, val);

    otherwise
        cam.Gain = '-';
        cam.Exp = '-';
end
```

Figure C-4. Instructions for how to program compatibility for a new camera into StereoCam.

C.2.2 Logging options

The StereoCam program allows the user to specify the method of collecting and saving image data. The three options available are 1) memory logging, 2) image (or disk) logging, and 3) video logging. There are different benefits and applications for each of these methods. Logging to memory allows for a higher frame rate to be achieved. However, because data is being stored in the computer's limited random-access memory (RAM), there is a limit on the number of images collected. Also, if the program or computer crashes during image acquisition, all images held in RAM are lost.

The second method is by disk logging. When an image is captured during an experiment, it is immediately saved to the disk drive. This provides data safety, as a computer or software crash does not cause data loss. However, immediately saving each image to the disk drive is a very slow process and limits the highest achievable image acquisition rate.

The last logging method is video logging. This method opens a .avi file and writes images to that file as they are captured by the cameras. Each image is a frame in the video file. This allows images to be captured at a high acquisition rate, though not as high as with the memory logging method. Also, it preserves the images to the disk within the video file, meaning data loss does not occur in the event of a program or computer crash. After the data acquisition, the images must be extracted from the video file, which can be a very time-consuming process. Conversion from a video file to a set of images is a feature of the StereoCam program.

C.2.3 Trigger options

There are two options for the camera timing of the image acquisition: 1) manual (or software) triggering, or 2) hardware triggering. With manual triggering, the MATLAB program sends the trigger signal to the cameras whenever the "trigger" button is pressed during the experiment and records the time of the trigger. This method is very user-friendly and grants the experimenter easy control of the cameras during an experiment through the StereoCam program. However, there are asynchronicity issues with this method when used with two cameras. The software trigger is sent to the cameras one after another causing a time delay between the two cameras that can reach up to 0.1 seconds.

For synchronized stereo camera image acquisition, it is recommended to use the hardware triggering method. To do this, the hardware must be connected properly as demonstrated by Figure C-5. Each camera trigger box must be connected to the power supply unit (PSU) by the LP4 cables and to the respective camera by the 12-pin Hirose connector to supply power to the cameras. The trigger circuit board must be connected to the PSU by the input LP4 cable (marked by "12 V") to ready the transmission of the 12 V signal that triggers the camera image capture. The output LP4 connector is connected to a custom-made LP4 to BNC cable. The BNC connector of this cable is connected to a BNC-T-piece which splits through two BNC cables on the output end. Each of these cables would carry the 12 V signal to a camera trigger box when triggered, commanding the camera to which it is connected to capture an image. Finally, in order to control the sending of the trigger signal, the trigger circuit board must be connected to the external signaling device (such as the MABTA computer) from the breakout board (FTDI Basic-5V, SparkFun) with

202

a Mini USB to USB cable. When the signaling device sends a 5 V signal, the trigger circuit board allows the 12 V from the power supply through to the cameras, triggering an image capture.
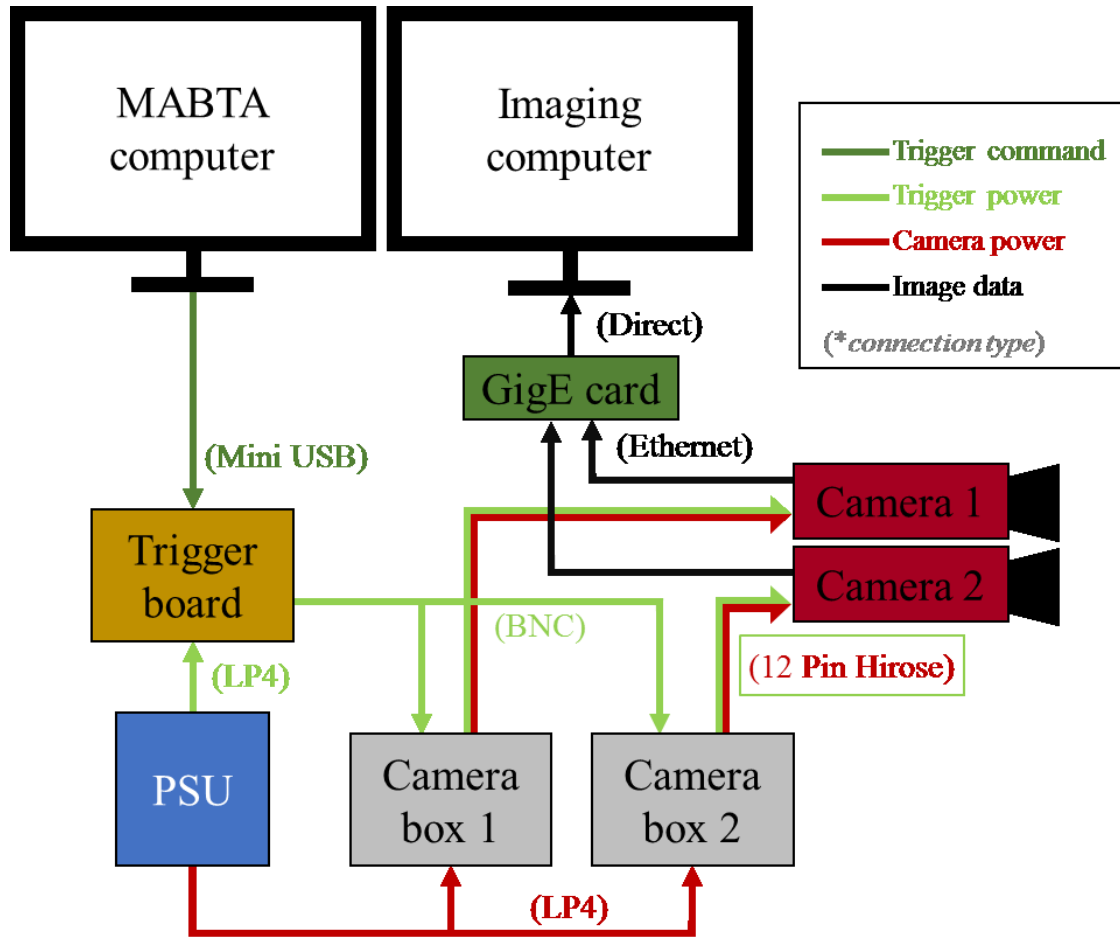
Figure C-5. Signal diagram for image acquisition with camera hardware triggering via MABTA control.

C.2.4 Image acquisition

Once all the settings are specified appropriately, the software can be used to set up and collect image data. Simultaneous stereo camera previewing is one of the capabilities of the program. This facilitates the positioning of the ROI of the test specimen to be optimal with the both camera FOVs. Additionally, a histogram snapshot can be captured with the software, allowing for a quick quantitative assessment of the image qualities from the

distribution of the intensity levels. Final adjustments can then be made to the FOV, brightness, or other camera parameters.

After fine-tuning the settings, the camera system should be ready for image acquisition. The maximum number of images and the time limit can be set for the acquisition to prevent acquiring more images than necessary. The image acquisition mode can be set to "continuous" or "triggered". With the "continuous" mode, the cameras are triggered by software at the very start of the test and continue capturing images at a fixed specified acquisition rate until the completion of the test. If the "triggered" mode is used, images will be captured whenever the cameras are triggered (either manually or with hardware). A delay can also be specified if the user wishes, which starts the acquisition a specified number of seconds after the start button is pressed. The test is stated by pressing the "start" button on the main panel showed in Figure C-3. For the duration of the test, StereoCam will display the number of images acquired and how long the acquisition has been running for. Once the acquisition is complete, either by reaching a maximum image count or time limit or by pressing the "stop" button, the images can be found in the directory specified by the user.

As a final note, if errors are occurring in the StereoCam program, try the following approaches: 1) reduce the frame rate of the camera, 2) reduce the packet size, or 3) reduce the region of interest.

Appendix D: DIC Uncertainty

D.1   Overview

Shown in Figure D-1 is the MATLAB program developed to quantify the uncertainty of a DIC system. This section details how the program works and how to use it. Note that the program only reads .vc7 files, so only DaVis image correlation software can be used is required to extract displacement fields.
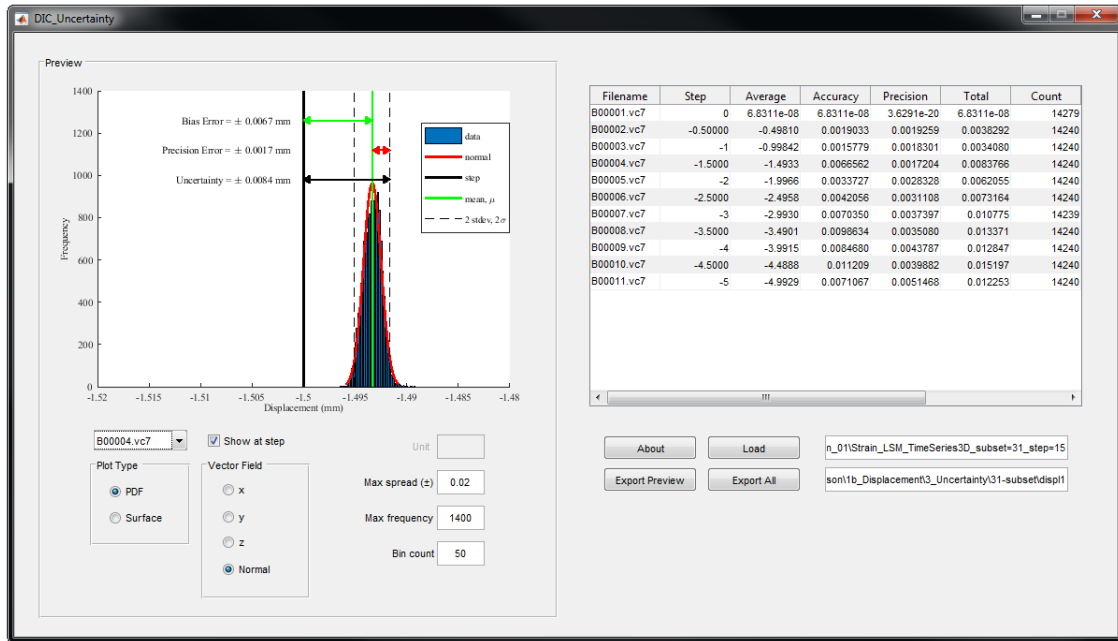
Figure D-1. Interface of MATLAB program developed to quantify uncertainty of a DIC system.

D.2   Rigid body displacement

Unidirectional rigid body displacements must first be measured and correlated by the imaging system to attain the vector fields used to quantify the measurement uncertainty. The test specimen must first be displaced at known steps, each being captured by the imaging system. This thesis examined rigid body displacements in the out-of-plane direction, but in-plane steps can be measured as well. After collecting the displacement images, image correlation must be performed on the images to attain the displacement field measured by the camera system. The resultant .vc7 files can then be loaded into this program to analyze the system uncertainty.

D.3   Uncertainty quantification

The program extracts the measured displacement vectors in the x-, y-, and z- directions relative to the imaging system's coordinates. The DIC coordinate system may not match with that of the physical displacements. However, since the displacements were unidirectional, the resultant vector, or the norm, corresponds to the physical displacements as there was no theoretical displacement in other directions. Thus, it is the norm of the vector that is used by the program. The prescribed displacement steps can be entered into the table (in the step column), allowing for the bias error to be determined for each step. Based on the distribution of the measurements, the precision error is calculated. Combining the two yields the total uncertainty of the system for the physical setup and correlation settings used in the specific set of displacement measurements.

D.4   Data presentation

The data can be presented in three forms: as values listed in a table, as a probability density function (PDF) plot, or as a surface plot. The table allows for transferring the results to other programs for analysis. As shown in Figure D-2 (a), the PDF displays the distribution of the measurement and shows the bias error, precision error, and the uncertainty of the overall image. Figure D-2 (b) demonstrates how the surface plot shows how uncertainty varies across the specimen surface. The "export preview" button saves the currently previewed plot to the user-specified location. The "export all" button saves the table, the PDF plots, and the surface plots to the user-specified folder. As a word of warning, in the current edition, the filenames are fixed which may cause previous exported files to be overwritten if they haven't been renamed.
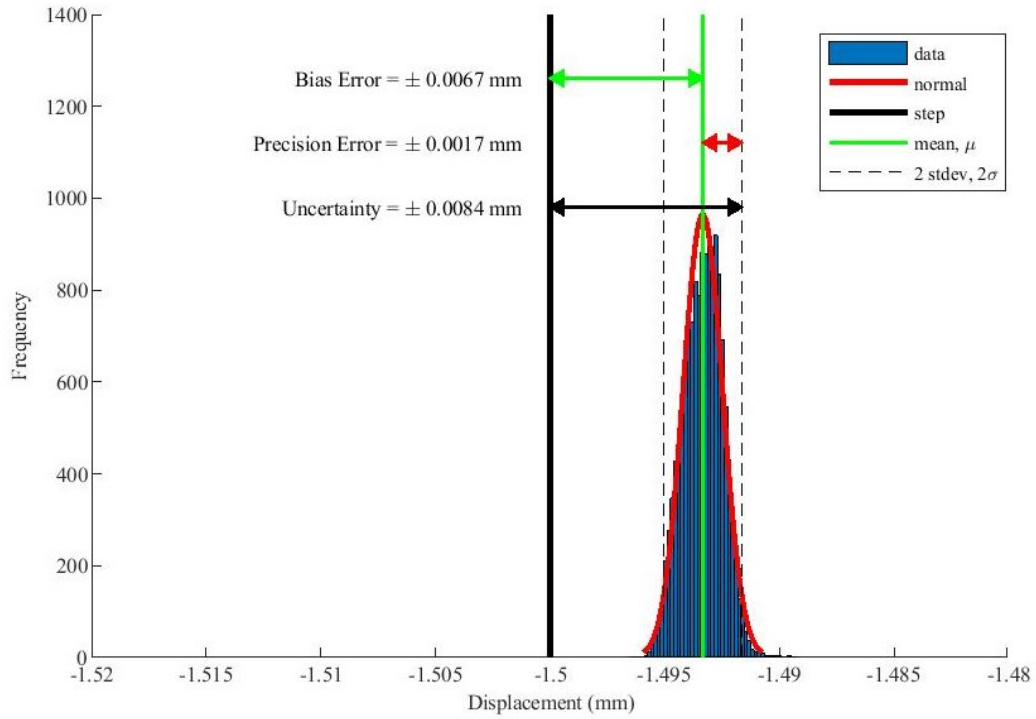
(a)
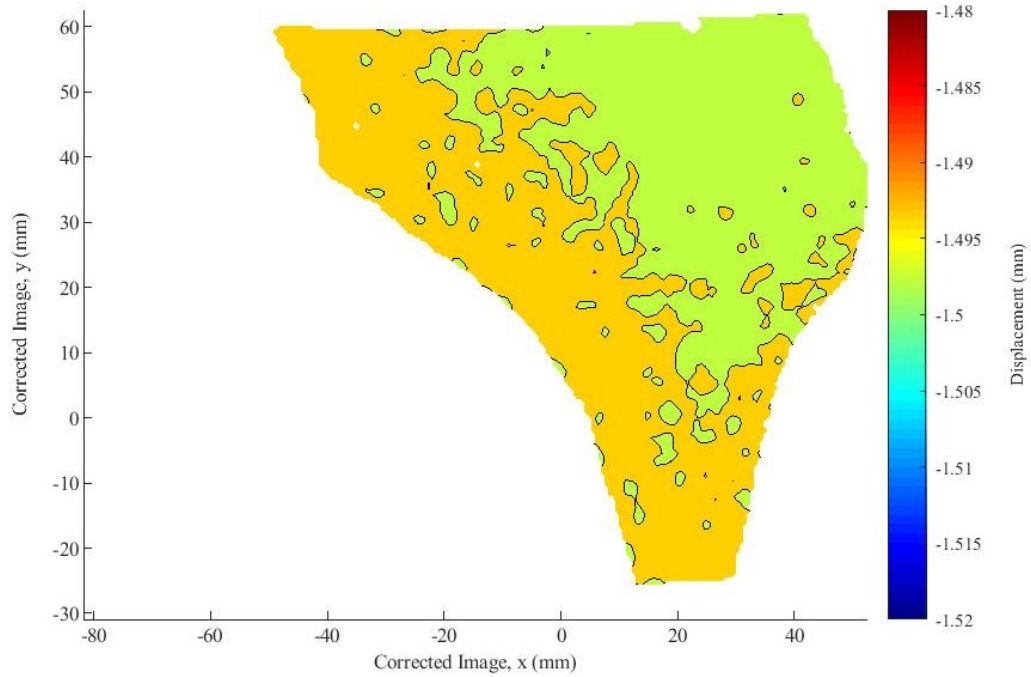
(b)

Figure D-2. DIC uncertainty quantification, showing measurement uncertainty **(a)** as a probability distribution and **(b)** as a profile across the specimen surface.

Appendix E: Using the MABTA

This appendix serves as a manual on how to use the multi-axis biomechanical testing apparatus (MABTA) to conduct loading experiments. The MABTA is shown below in Figure E-1.
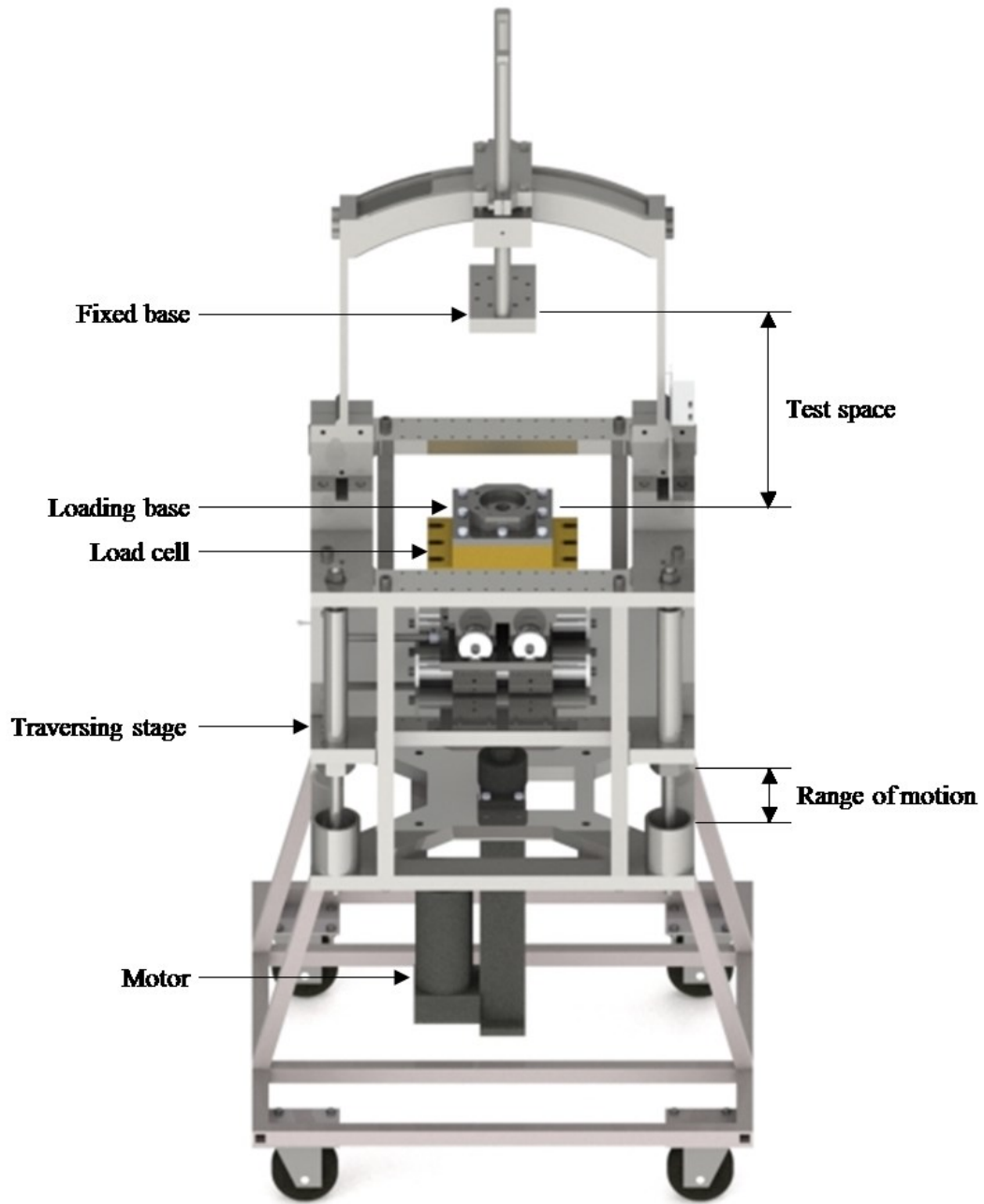
Figure E-1. Multi-axis biomechanical testing apparatus (MABTA) diagram.

E.1   Hardware

Ensure that all components listed in Table E-1 are plugged in, turned on, and connected. Ensure that the strain gage amplifier is on for at least 1 hour before use to allow it to warm up.

Table E-1. List of components in MABTA.

Load Cell
MC6-6-2000, AMTI

Strain Gage Amplifier
MSA-6 MiniAmp, AMTI
(connects to load cell to MABTA computer)

Motor
EC3BK32-5005B-150-MF3-FT1E-PB, IDC

Servo amplifier
Servostar S30661, Kollmorgen
(connects motor to MABTA computer)

E.2   Software

E.2.1 Starting up

Once all MABTA components to be used in the experiment are turned on and connected, start up the MABTA control program. The software will prompt for a starting position; read and enter the measurement from the ruler as shown in Figure E-2 below. This is a safety measure that prevents the motor from exceeding the limits of its range of motion. After the starting position is entered, the main panel shown in Figure E-3 is accessible and the MABTA can be controlled by the user.
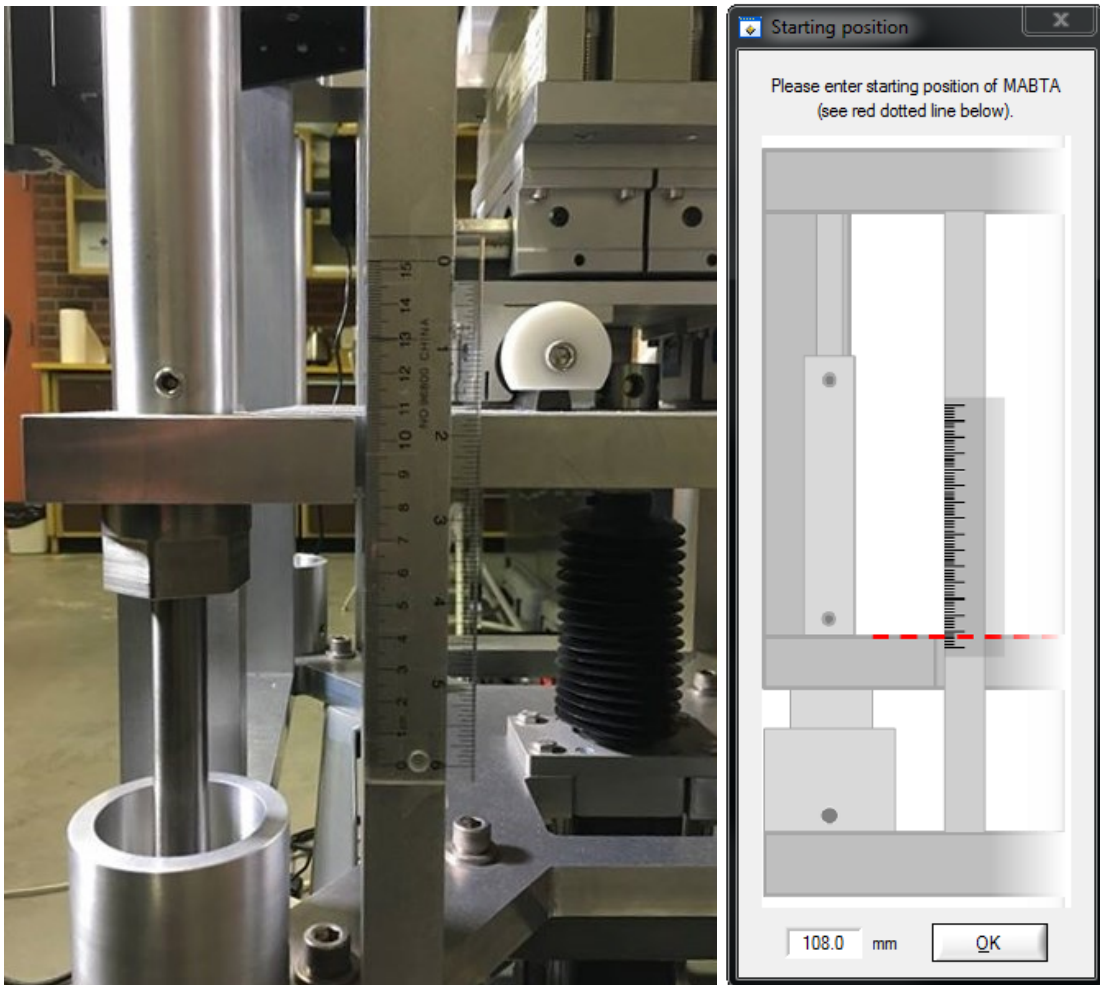
Figure E-2. MABTA control software safety implementation for motor range of motion.
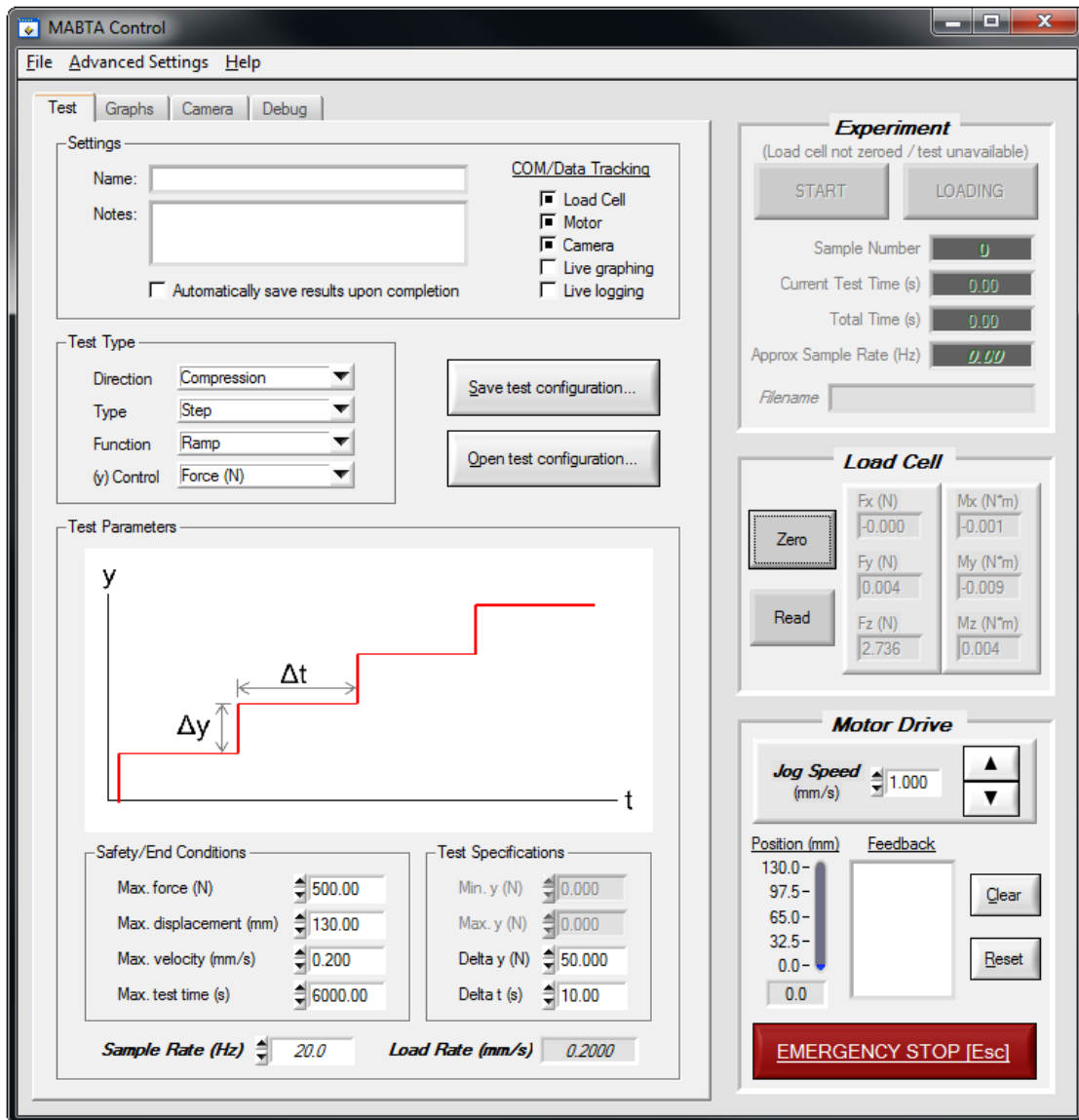
Figure E-3. MABTA control software, main panel.

E.2.2 Connecting devices

Upon loading, the MABTA control software connects the hardware to serial and USB ports defined by the default settings. If there are issues with the hardware connections, check the settings under Advanced Settings → COM settings. Ensure that the proper ports are selected for the respective hardware.

E.3   Setting up an experiment

E.3.1 Data collection settings

In the main panel shown in Figure E-3, check the boxes in the settings section for the instrumentation to collect data in the experiment. Typically, the load cell and motor are checked. If an external camera system is used, the camera is checked as well. The live graphing option allows monitoring of measured positions and loads during an experiment. Once set, the graphs cannot be switched during the experiment as it interferes with the timing of the sampling (ensure that the desired graphs are set prior to starting the experiment). If the live logging option is checked, measured data is written to a text file when measured during the experiment. This means that in the event of a computer or software crash, the data collected up to that point is saved. Note that live graphing and live logging requires computational resources which may reduce the maximum achievable sample rate. If live logging is not used, the results can be set to save automatically or manually to a text file in the same way after the test is finished.

E.3.2 Safety and end conditions

The physical limitations of the components, such as the maximum load allowed by the load cell and motor, are safeguarded by the MABTA control program. The software is instructed to prevent the machine from exceeding 0.8 times the manufacturer's limit for each component. If any of these limitations are reached during an experiment, the program stops the experiment and unloads the specimen. Otherwise, the experimenter can specify the ending conditions of the experiment from the main panel shown in Figure E-3. These include maximum force, displacement, velocity, and time. If any of these user-prescribed values are reached during an experiment, the test is concluded and the specimen unloading begins.

E.3.3 Test settings

To define the type of experiment to be conducted by the software, choose the appropriate fields referring to direction, type, function, and y-control on the main panel shown in Figure E-3. Depending on the version of the software, not all test combinations may be available. The two direction options are compression (moving the loading stage upwards) and tension

(moving the loading stage downwards). The y-control is the parameter that determines the conditions of the test. Currently, y can be set such that the tests are force- or displacement-based.

There are two loading types: continuous and step. With continuous, the MABTA loads the specimen at a constant rate specified by the user as $\Delta y/\Delta t$. The loading continues until an end condition is met. With step loading, the specimen is loaded at a constant rate until meeting the step condition, specified by the user as Δy. The step is held until the hold condition, Δt, is met. During a step loading test, the user can also manually start or end a load step.

Function defines the test trajectory. Ramp is the most common, in which loading occurs in a linear fashion with respect to y until the end condition is met. In a hold test, loading is performed until the hold condition is met. The MABTA then holds the position until an end condition is met. With cyclic loading, the MABTA motor oscillates to achieve a wave function regarding the y parameter. For example, with displacement-based cyclic loading, the MABTA moves up and down, changing directions whenever a prescribed upper or lower limit is reached.

The control values of the experiment are set in the test specifications section of the MABTA control software in Figure E-3. The prescription of values depends on which test type is specified. For example, in a displacement-based step-ramp compression test, the Δy defines the position step intervals, the Δt defines the step duration, and the maximum velocity specifies the loading rate between steps. The load rate field can be consulted as a final review for the loading in the test based on the user-input. The sample rate applies to measurements taken by the load cell and motor, but not the camera. Section E.3.4 below provides more details on how to set the image data collection with the MABTA control software. For quick access, the settings of any test configurations can be saved and later opened.

E.3.4 Camera settings

The MABTA control software has been upgraded to indirectly communicate with cameras. Note that the software does not collect or process any images from the camera. It simply sends an electrical trigger signal to the cameras, commanding them to capture an image.

Doing so requires the trigger circuit board shown in Figure E-4. The circuit board connects to the MABTA computer via USB using a breakout board (FTDI Basic-5V, SparkFun) and relays a signal sent by the computer to the cameras. Another machine is required to save images captured from the camera. This reduces the stress on the computer controlling the MABTA, allowing it to collect loading and position data at a higher and more reliable sample rate. For more information on how to set up the image collection computer, see Appendix C.
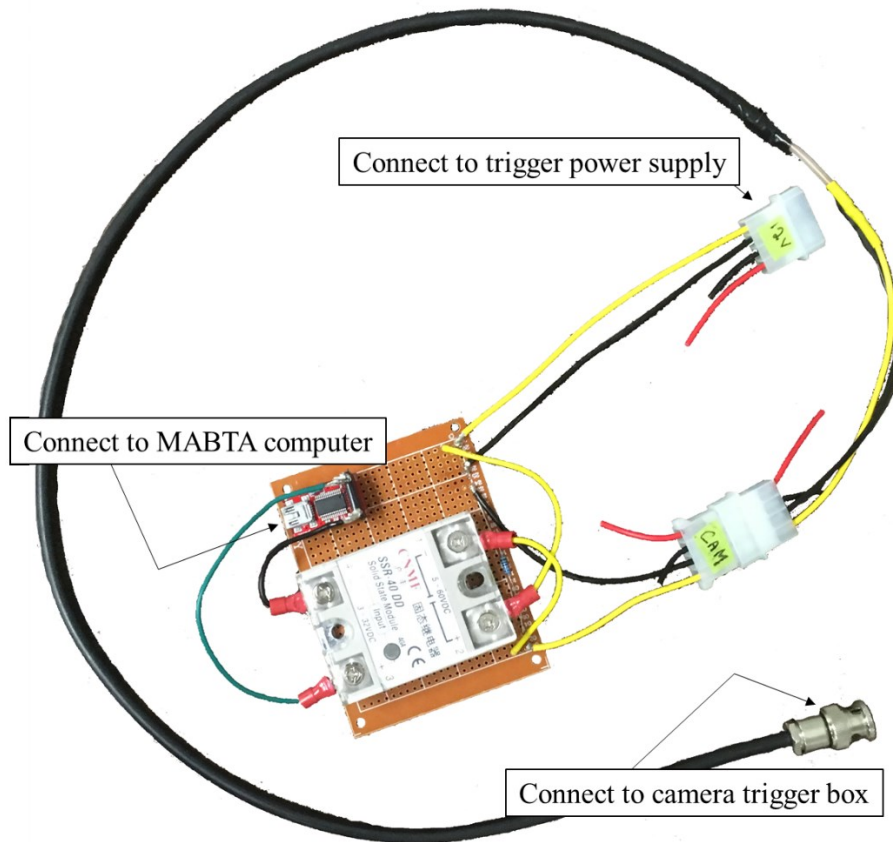
Figure E-4. Circuit board sending signal from MABTA to cameras to trigger an image capture.

If the trigger circuit board is connected to the MABTA, the camera functions will become available. The settings for triggering the cameras can be set in the "camera" tab of the MABTA control software shown in Figure E-5. During an experiment in which the camera function is enabled, the MABTA will follow the protocols specified here. Trigger rate will set the rate of image acquisition if the cameras are separately specified to capture one image per trigger. Ensure that the camera frame rate is greater than the trigger rate (set

on the camera control software). Three experiment trigger conditions are available. The "continuous" setting triggers the cameras constantly throughout the experiment. The "throughout step" setting triggers the cameras only while a step is held. Lastly, the "end of step" setting causes the cameras to capture one image per held step just before loading is resumed. In most cases, the trigger ON-level should be high and a trigger duration of 10 ms is sufficient. Before starting an experiment with camera triggering, it is recommended to test the trigger to verify its function.
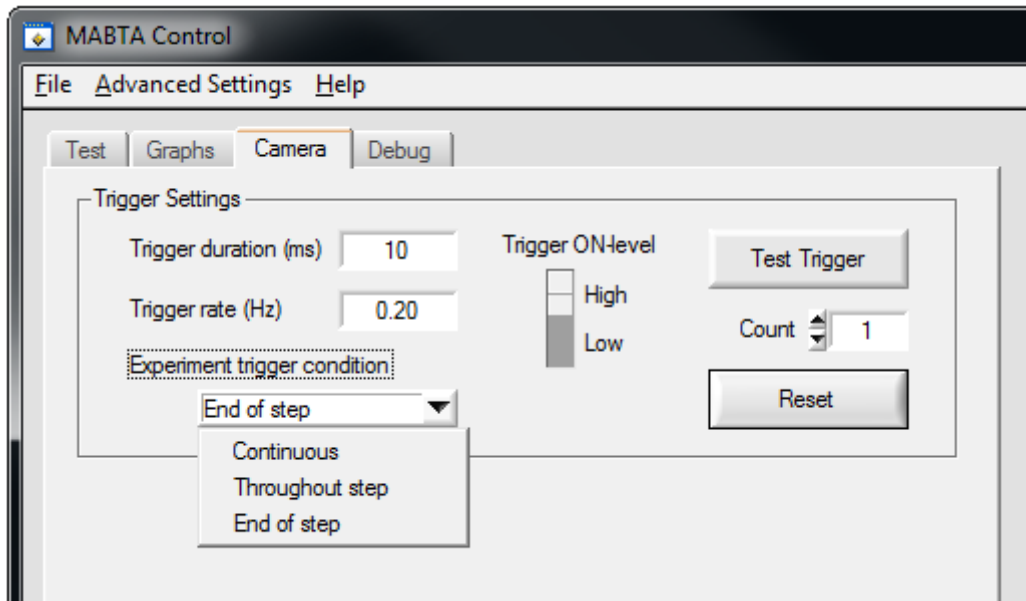
Figure E-5. Settings for trigger signal sent from MABTA control to cameras.

E.4   Running an experiment

E.4.1 Preparing the experiment

First, set up the loading stage of the MABTA with any components (clamps, jigs, *etc.*) that are to be used in the experiment. Then, press the "zero" button in the load cell section of the main control panel shown in Figure E-3. Check to see if the loads are at zero with the "read" button. Cross check the position reading in the motor section of the main panel to the ruler measurement on the MABTA to ensure that the software has properly located the motor position. Then, jog the motor to adjust the test space to accommodate the size and shape of the test specimen. Set up the test specimen on the MABTA and perform any

necessary pre-loading. Then, zero the load cell again with respect to the experiment (load cell must not be reading for experiment to start). Perform a final check of the test settings before starting the experiment.

E.4.2 Conducting the experiment

When ready, press the "start" button on the main panel shown in Figure E-3 to begin the experiment. The MABTA control software will carry out the test in accordance to the user specifications. If live graphing is enabled, monitor the data as it is collected to ensure that the experiment is going as planned and data is being collected properly. At any point, the experiment can be manually ended with the "stop" button. During a step loading experiment, a step can be preemptively started or ended by the user before the step condition has been met by pressing the "loading/holding" button.

Once the experiment has automatically or manually reached the end, the specimen unloading process is initiated. During this phase, the motor is moved at the specified load rate in the opposite direction that it was last moving until the load cell reads the initial zero load state. In an emergency, the "emergency stop" button will stop the motor immediately. As a last resort, the plug for the MABTA power can be disconnected.

E.4.3 Finishing the experiment

The data collected from the experiment is saved to a .txt file in the user-specified directory. If live logging was enabled during the experiment, results were saved in real time with the experiment. This uses more computing power but saves data in the event of a program or system crash. If the box labeled "automatically save results upon completion" was checked, the data is written to a txt. File immediately after completing the experiment in the location specified before starting the experiment. If neither of these cases apply, the results must be manually saved (File → Save or Save as) else they are lost upon closing the program. When finished all experiments in a session, be sure to turn off all components, mainly the MABTA motor, the load cell signal amplifier, and the cameras.

Appendix F: Material Specifications

F.1   Material specifications

Table F-1 lists the material specifications for the polypropylene (PP-DWST, SIMONA®) used in the experiments.

Table F-1. Material specifications for polypropylene in experiment.

		SIMONA® PP-DWU AlphaPlus®	SIMONA® PP-DWST	SIMONA® PPs	SIMONA® PP-C
Technical data					
Density, g/cm³, DIN EN ISO 1183		0.915	0.905	0.950	0.910
Yield stress, MPa, DIN EN ISO 527		33	32	32	26
Elongation at yield, %, DIN EN ISO 527		8	8	8	7
Tensile modulus of elasticity, MPa, DIN EN ISO 527		1,700	1,400	1,600	1,200
Impact strength, kJ/m², DIN EN ISO 179		no break	no break	no break	no break
Notched impact strength, kJ/m², DIN EN ISO 179		9	7	6	45
Ball indentation hardness, MPa, DIN EN ISO 2039-1		70	70	70	50
Shore hardness D, DIN EN ISO 868		72	70	72	67
Mean coefficient of linear thermal expansion, K^{-1}, DIN 53752		1.6×10^{-4}	1.6×10^{-4}	1.6×10^{-4}	1.6×10^{-4}
Thermal conductivity, W/m · K, DIN 52612		0.22	0.22	0.22	0.22
Fire behaviour, DIN 4102		normal flammability	normal flammability	low flammability 2 to 20 mm	normal flammability
Dielectric strength, kV/mm, DIN IEC 60243-1		52	58	22	52
Specific surface resistance, Ohm, IEC 60093		10^{14}	10^{14}	10^{14}	10^{14}
Volume resistivity (annular electrode), Ohm · cm, DIN 53482		$> 10^{16}$	$> 10^{16}$	$> 10^{16}$	$> 10^{16}$
Tracking resistance (KC method), V, DIN 53480		> 600	> 600	> 600	> 600
Permittivity, DIN 53483	at 300 – 1,000 Hz	2.3	2.1	2.3	2.3
	at $3 \cdot 10^5$ Hz	2.2	2.2	2.2	2.2
Dielectric loss factor, DIN 53483	at 300 Hz	$< 3 \times 10^{-4}$	3×10^{-4}	$<3 \times 10^{-4}$	$< 3 \times 10^{-4}$
	at 1,000 Hz	5×10^{-4}	3×10^{-4}	5×10^{-4}	5×10^{-4}
	at $3 \cdot 10^5$ Hz	$< 3 \times 10^{-4}$	3×10^{-4}	$< 3 \times 10^{-4}$	$< 3 \times 10^{-4}$
Crystalline melting range (calorimetric), K (°C), DIN 52328		433 – 438 (160 – 165)	433 – 438 (160 – 165)	433 – 438 (160 – 165)	433 – 438 (160 – 165)
Temperature range, °C		0 to +100	0 to +100	0 to +100	−20 to +80
Chemical resistance		excellent in contact with many acids, alkalis and solvents			
Physiologically safe	BfR	✓	✓		✓
	EU	✓	✓		
	FDA	✓	✓		✓

Table F-2 lists the material properties of the pelvic fixture designed and implemented in the experiment (Polyjet Verogray RG3850, Stratasys Ltd.).

217

Table F-2. Material specifications for polyjet veroygray RG3850 used in 3D printed pelvic fixture.

Property	ASTM	Units	Metric	Units	Imperial
Tensile strength	D-638-03	MPa	50-65	psi	7250-9450
Elongation at break	D-638-05	%	10-25	%	10-25
Modulus of elasticity	D-638-04	MPa	2000-3000	psi	290,000-435,000
Flexural Strength	D-790-03	MPa	75-110	psi	11000-16000
Flexural Modulus	D-790-04	MPa	2200-3200	psi	320,000-465,000
HDT, °C @ 0.45MPa	D-648-06	°C	45-50	°F	113-122
HDT, °C @ 1.82MPa	D-648-07	°C	45-50	°F	113-122
Izod Notched Impact	D-256-06	J/m	20-30	ft lb/inch	0.375-0.562
Water Absorption	D-570-98 24hr	%	1.1-1.5	%	1.1-1.5
Tg	DMA, E»	°C	52-54	°F	126-129
Shore Hardness (D)	Scale D	Scale D	83-86	Scale D	83-86
Rockwell Hardness	Scale M	Scale M	73-76	Scale M	73-76
Polymerized density	D792	g/cm3	1.17-1.18		
Ash content VeroGray, VeroWhitePlus	USP281	%	0.23-0.26	%	0.23-0.26
Ash content VeroBlackPlus	USP281	%	0.01-0.02	%	0.01-0.02

Table F-3 lists the material properties of the hemipelvis specimen (SKU #3409, Sawbones) used in the experiment.

Table F-3. Material specifications for pelvic specimen used in experiments.

Cortical bone (short fiber filled epoxy)	ASTM	Units	Metric	Units	Imperial
Density		g/cc	16.4	lb/in^3	0.0592
Tensile strength					
Longitudinal	D638	MPa	93.0	psi	13500
Transverse	D638	MPa	106	psi	15400
Tensile modulus					
Longitudinal	D638	GPa	10.0	ksi	1450
Transverse	D638	GPa	16.0	ksi	2320
Compressive strength	D695	MPa	157	psi	22800
Compressive modulus	D695	GPa	16.7	ksi	2420
Cancellous bone (rigid polyurethane bone)	ASTM	Units	Metric	Units	Imperial
Density					
Solid		g/cc	0.270	lb/in^3	0.00975
Cellular		g/cc	0.320	lb/in^3	0.0116
Compressive strength					
Solid	D1621	MPa	5.40	psi	783
Cellular	D1621	MPa	6.00	psi	870
Compressive modulus					
Solid	D1621	GPa	0.137	ksi	19.9
Cellular	D1621	GPa	0.155	ksi	22.5
Poisson Ratio	D1621		0.30		0.30

F.2   Specimen geometry

The drawings below show the geometry of the true shape of the dogbone specimen, the waterjet cutting shape of the dogbone specimen, and the single edge notch tension (SENT) specimen shape in Figure F-1, Figure F-2, and Figure F-3 respectively.
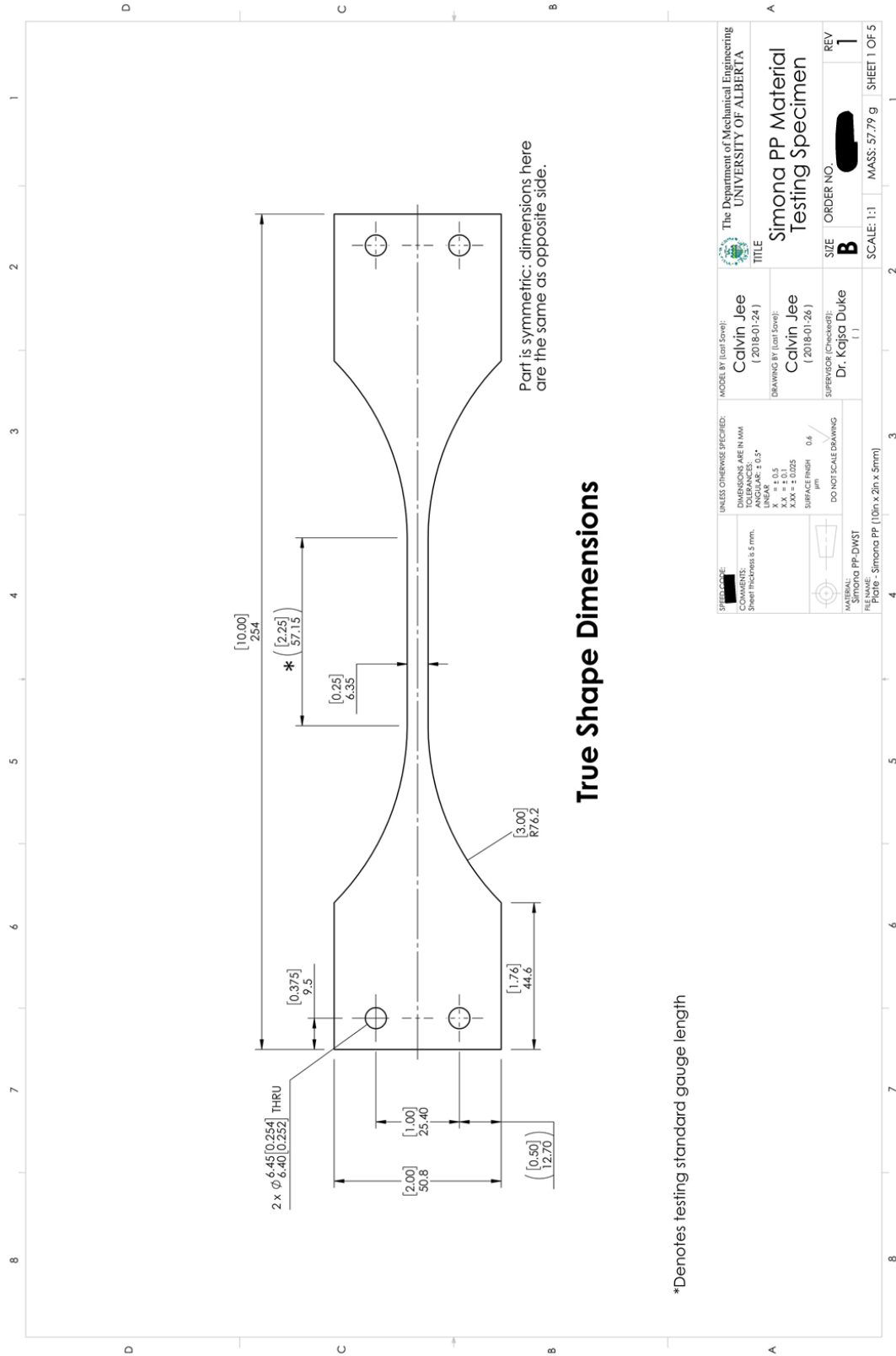
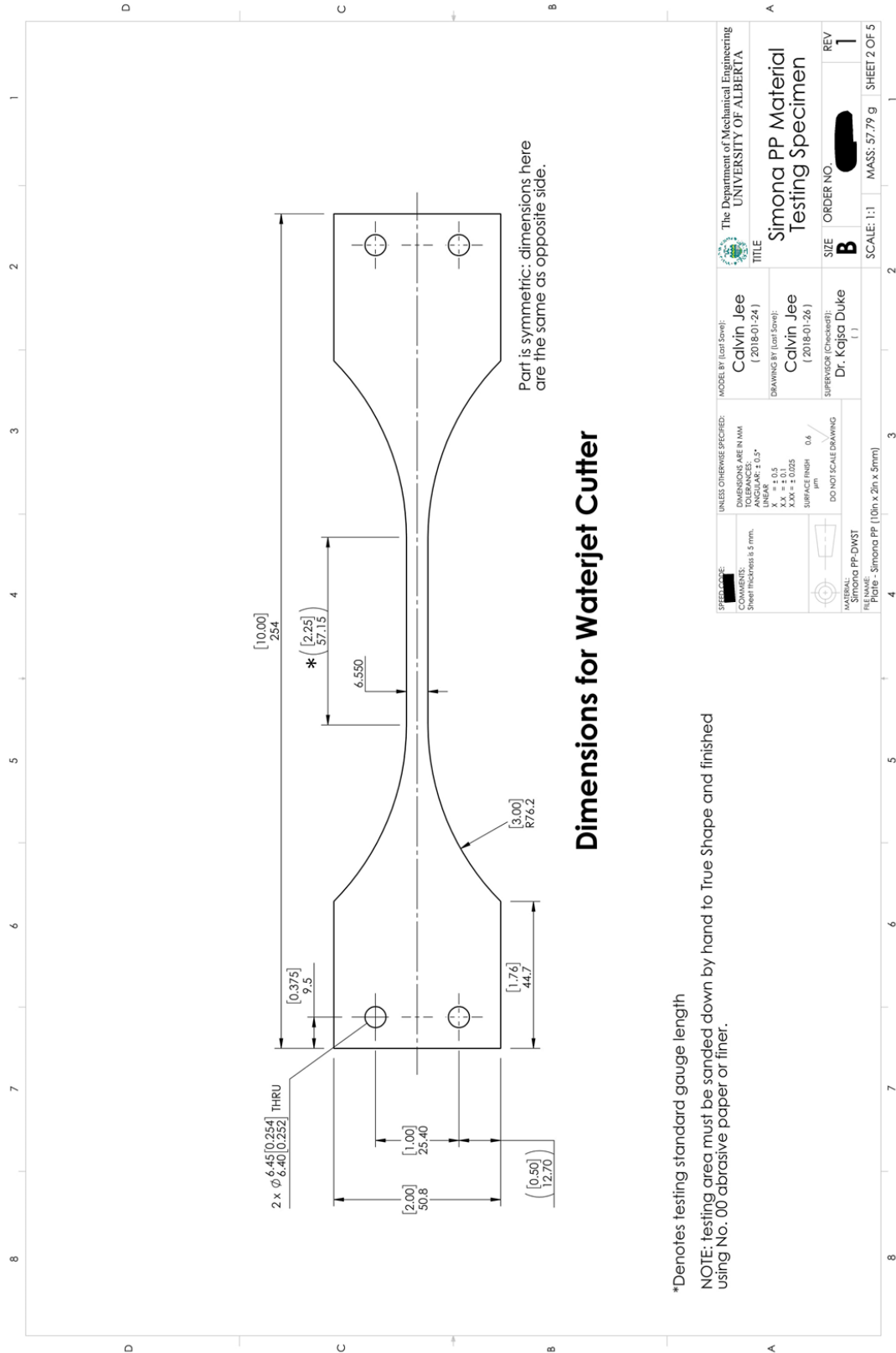**Figure F-1.** Final dimensions of polypropylene dogbone specimen.

Figure F-2. Waterjet cutter dimensions for polypropylene dogbone specimen.
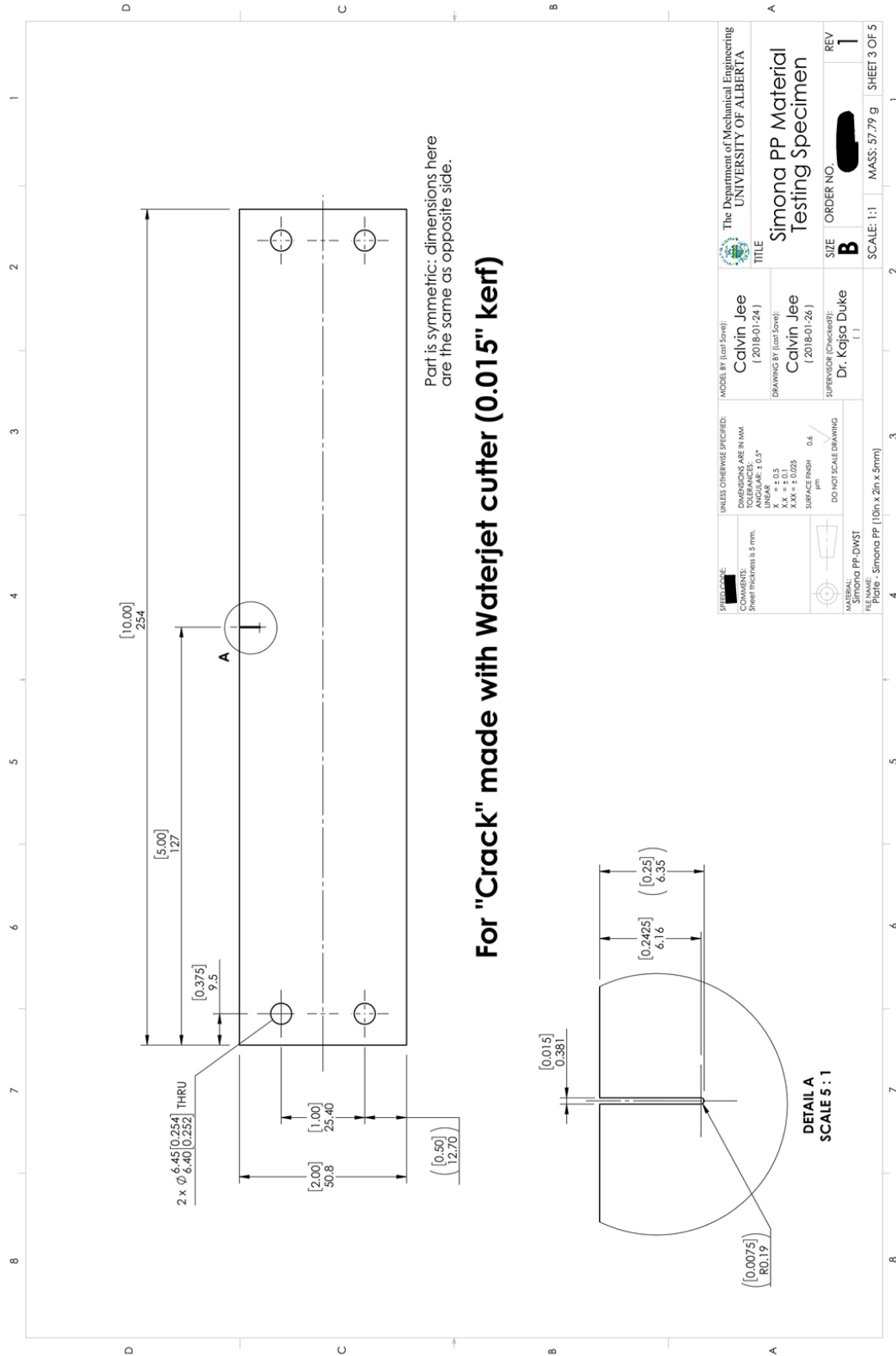
221

Figure F-3. Dimensions for polypropylene SENT specimen.

Appendix G: Crack opening

G.1   Overview

Figure G-1 shows the MATLAB program that was created to measure the displacement of a crack. It operated on .vc7 files from image correlation results produced by DaVis 8.4 software. One of the main motivations behind creating this program was the limited number of licenses available for accessing DaVis; this program allowed the data to be analyzed externally so others could access the DIC software. The other was the amount of control the program allowed for in terms of defining the crack, the points of measurement, and extracting the values for an entire image correlation set.
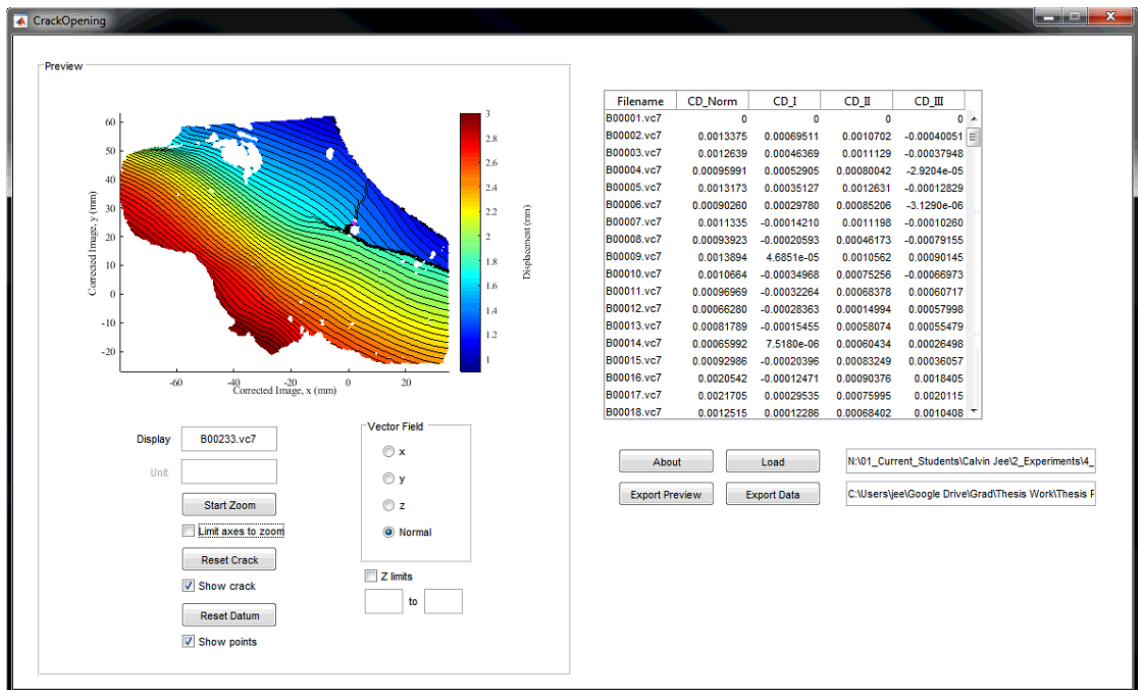

Figure G-1. Interface of MATLAB program developed to measure crack displacements from extracted displacement fields using DaVis 8.4 image correlation software.

G.2   Handling data

Click the "load" button to import the data set to be analyzes. Only .vc7 files are read, as they contain the displacement vectors extracted from the image correlation. Once loaded, any displacement field within the set can be viewed by clicking on it in the table. The x-, y-, and z-displacements can also be shown in addition to the overall resultant

displacements. The Z limits option, when checked, allows the user to set the colormap scale. The "start zoom" button allows control over the field of view to more easily discern the crack on the displacement field. When the "lock axes to zoom" option is checked, the current FOV is kept constant when browsing within the data set or switching between the x-, y-, z-, and resultant displacement fields. At any point, it can be unlocked to zoom out to the full view. This is particularly beneficial in facilitating the crack definition process detailed below.

G.3   Extracting crack measurements

After the desired data set is loaded, the following user operations allows for the displacement fields to be converted into crack openings. The results are the magnitudes of the crack displacements in the three fracture modes shown in Figure G-2, which are opening, shearing, and tearing. The resultant crack displacement is also calculated.
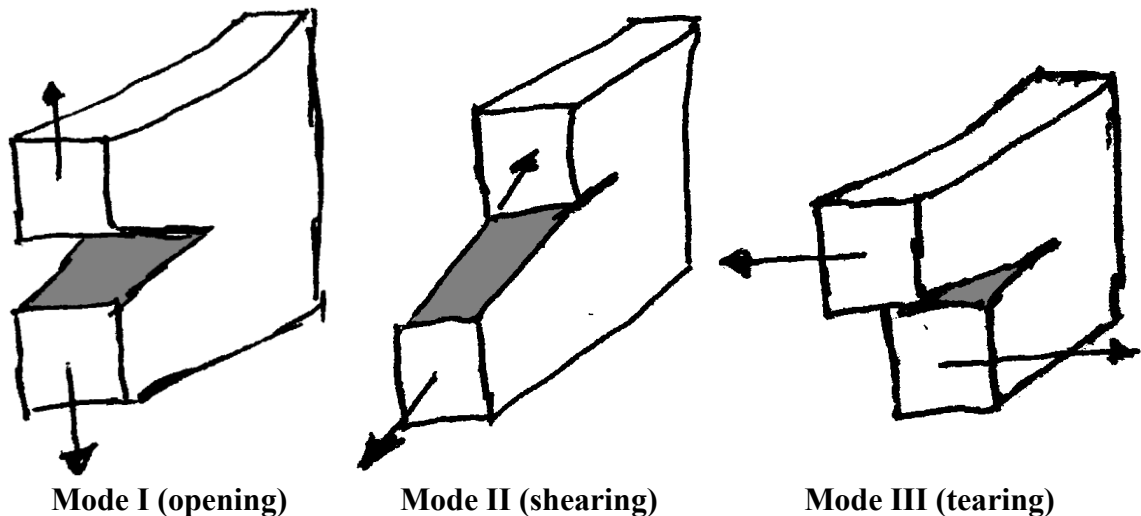

| Mode I (opening) | Mode II (shearing) | Mode III (tearing) |

Figure G-2. The three modes of fracture: opening (mode I), shearing (mode II), and tearing (mode III).

To do so, the crack and the points of measurement must be defined. First, press the "define crack" button. This will request the two endpoints of the crack to be defined by the user, as shown in Figure G-3. The crack edge should be selected first to produce positive results in mode I crack widening. Next, press the "select datum" button to define the points of measurement about the defined crack. In this step, the point representing one edge is selected as a reference point. A complimentary point is then located opposite the user-

defined crack at a distance equal and perpendicular to the reference point, as shown in Figure G-3. The reference point is displayed as black and the complimentary as white. This is mainly important for understanding the direction of movement in modes II and III as negative values may imply crack opening in the direction opposite to the defined coordinates as opposed to crack closure. In mode I, for a properly defined coordinate system, negative values always represent crack closure. After the crack and datums are defined, the crack displacements are calculated and presented in the data table.
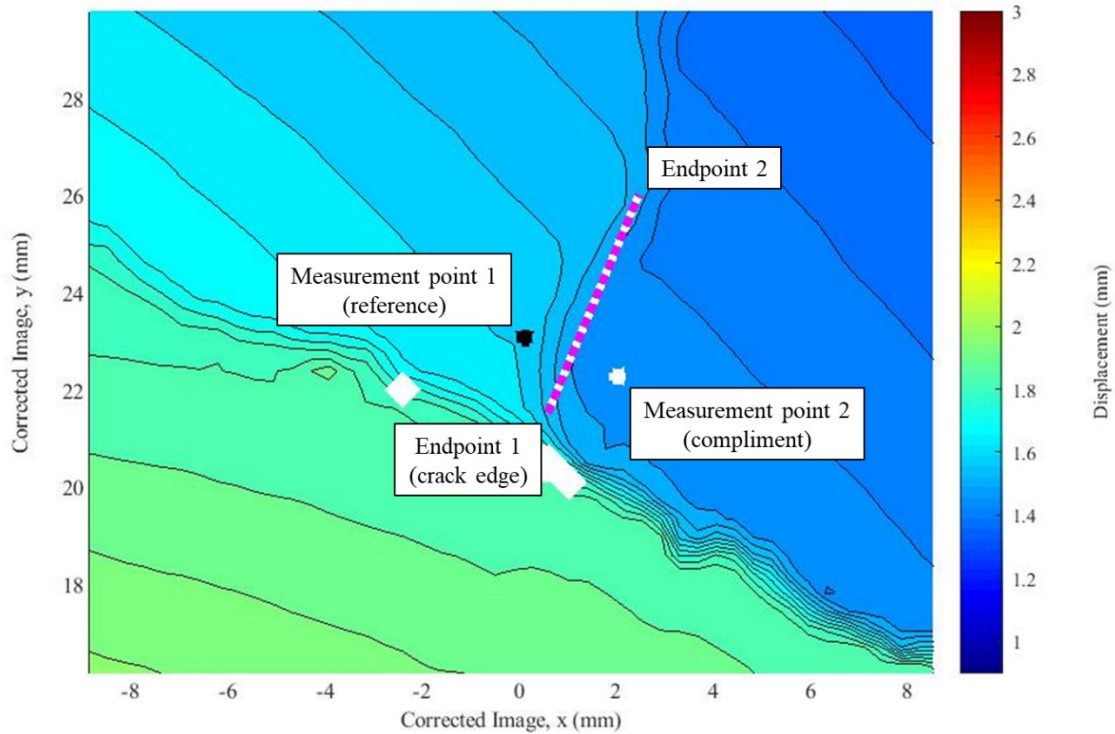

Figure G-3. The procedure for defining the crack and the datums for measuring the crack displacements.

The measured x-, y-, and z-displacements from the imported data are used to calculate the crack displacements in all fracture modes at the defined measurement points. It does so by converting the x- and y- displacements to the opening and shearing directions of the crack while assuming that the z-displacements are fully representative of out-of-plane crack movement (*i.e.*, tearing). However, this assumes that the viewing surface is perfectly flat, which is typically untrue. For this study, the approximation was deemed reasonable, and approaches for addressing this issue were considered in the following section.

The calculated crack displacements can be exported via the "export data" button, creating a .txt file with all the crack measurements for the user-defined crack for the entire data set. The "export preview" button allows for a .jpg file to be saved of whatever is displayed in the GUI axes, including the zoomed-in FOV, the crack definition, and the measurement points.

G.4   Future work

The program in its current state reads displacement fields and utilizes the data to calculate crack measurements. However, it can be improved to interpret displacement fields with greater purpose, depending on what the application may be. For example, implementing area-based selection of displacement measurements could facilitate the quantification of displacement uncertainty on a per region basis for a given field of view in all directions. Also, the displacement fields can only be shown in the imaging coordinate system. An option to allow for the colormap to be presented in the mode I, II, and III coordinate systems would provide a better visual representation of the fracture motion along the crack region in view.

In terms of the crack measurements, several optimizations to the program are possible. For specimens with multiple cracks, only one can be measured at a time in the programs current state. In cases like these, it would be beneficial to allow for multiple cracks to be measured and defined in a single session. Also, automation of the process would allow for a less biased and more expedient process of crack measurement.

There are currently issues with the accuracy of the crack measurements themselves. As previously mentioned, the crack mode measurements assume that the surface is perpendicular to the cameras in the data. But especially for curved surfaces, this is very unlikely to be the case. Incorporating the surface height data from the image correlation software may be able to better incorporate the out-of-plane measurements into the mode I and II calculations. It would also allow the x- and y-displacements to be accounted for in the mode III calculations, allowing for a more accurate 3D crack detail.

Another issue is with the ambiguity of the crack closure in modes II and III. As shown in Figure G-4, it is possible to mistake negative values as crack closure. A crack that starts partially open with an initial offset in the positive direction would experience

closure when moving in the negative direction, as Figure G-4 (a) shows. At reaching absolute closure, like in Figure G-4 (b), the crack width would be zero due to the negative displacement of the crack. However, Figure G-4 (c) shows that continuing past this point would result in crack opening for measurement values that are increasing in the negative direction, thus confounding the observed behavior of the crack. The same is true for a crack starting with a negative offset and displacing in the positive direction. The suggested fix for this issue is to define the starting locations of the crack edges and calculate the crack separation as an absolute measurement of the crack width in addition to the displacement trends. This would allow for the distinction between positive or negative signage and the reduction or growth of a crack.
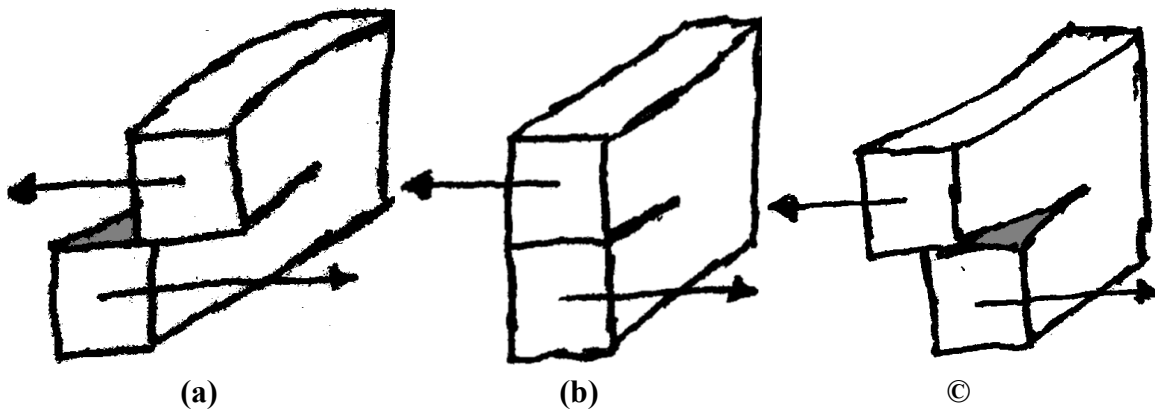

| (a) | (b) | © |

Figure G-4. Ambiguity of crack closure in mode III, showing **(a)** the initial negative displacement representing crack closure at the initial state, **(b)** the continued negative displacement reaching true crack closure, and **(c)** continued negative displacement representing crack widening.

Appendix H: DIC Strain

H.1 Overview

Displayed in Figure H-1 is the MATLAB program developed to analyze strain fields that were extracted from the image correlation results using DaVis 8.4 software. As there are limited licenses for DaVis available at the University of Alberta, this program allows for the image correlation data to be analyzed without occupying one of the licenses thus freeing space for other researchers.
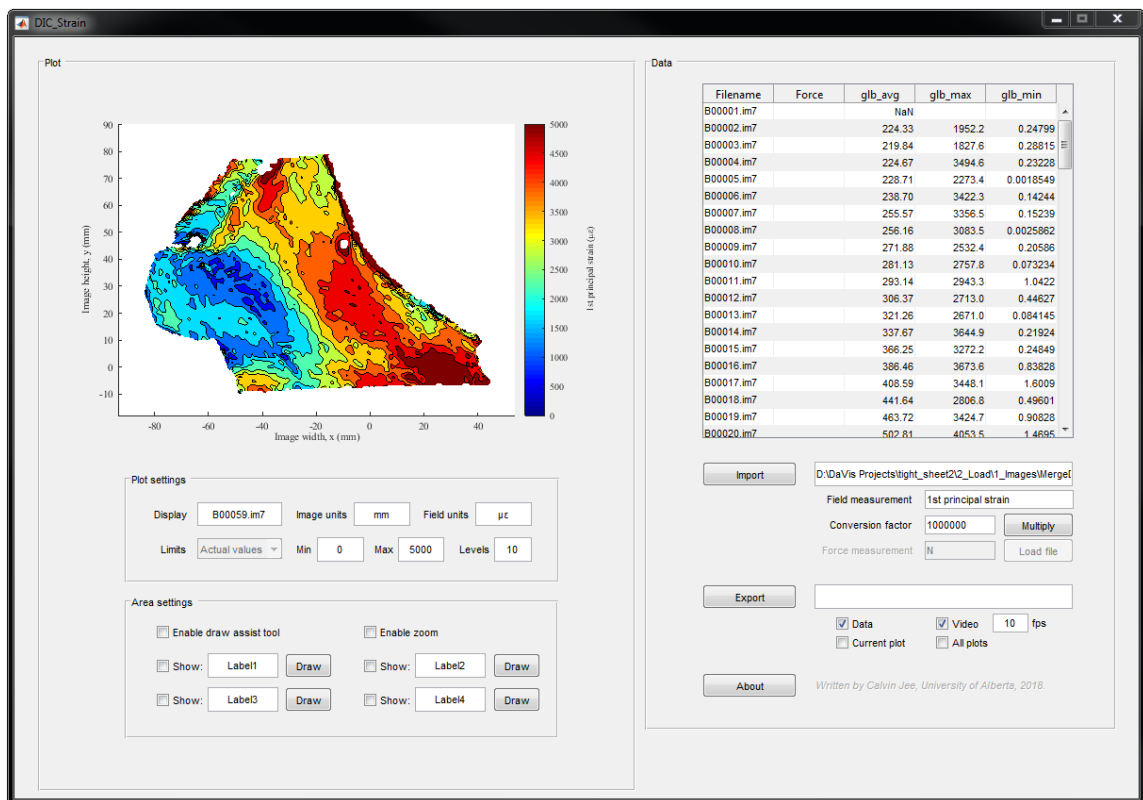

Figure H-1. Interface of MATLAB program developed to analyze extracted strain fields from DaVis imaging software.

H.2   Importing strain data

To analyze a strain field, the data must first be loaded into the program. Press the "import" button and select all files wished to be examined. This program only reads .im7 files, so the desired strain map must first be extracted from the correlation data in DaVis. Use the appropriate function in DaVis to extract the desired strain map (maximum normal 3D strain, maximum normal surface strain, von Mises strain, *etc.*).

Once the files are loaded, they can be converted in bulk to the desired units by specifying the conversion factor and pressing the "multiply" button. The various fields allow for the axes to be labeled appropriately. The colormap limits and resolution can be edited to produce an appropriately distinguishable strain map. To specifically preview a one of the loaded strain maps, click on the appropriate table row.

H.3   Local strains

This program allows areas of the strain map to be isolated and measured independently. Specify the boundaries of the region by pressing any "draw" button. This will prompt for a rectangle to be drawn on the image to define the local area. For small regions, the zoom function provides assistance. Using the "draw assist tool," the local region can be defined numerically through a series of prompts. Once defined, as shown in Figure H-2, the average, maximum, and minimum values within the region of interest will be determined and saved in the data table. The region boundaries for each specified location can be independently labeled, cleared or redrawn, and displayed or hidden.
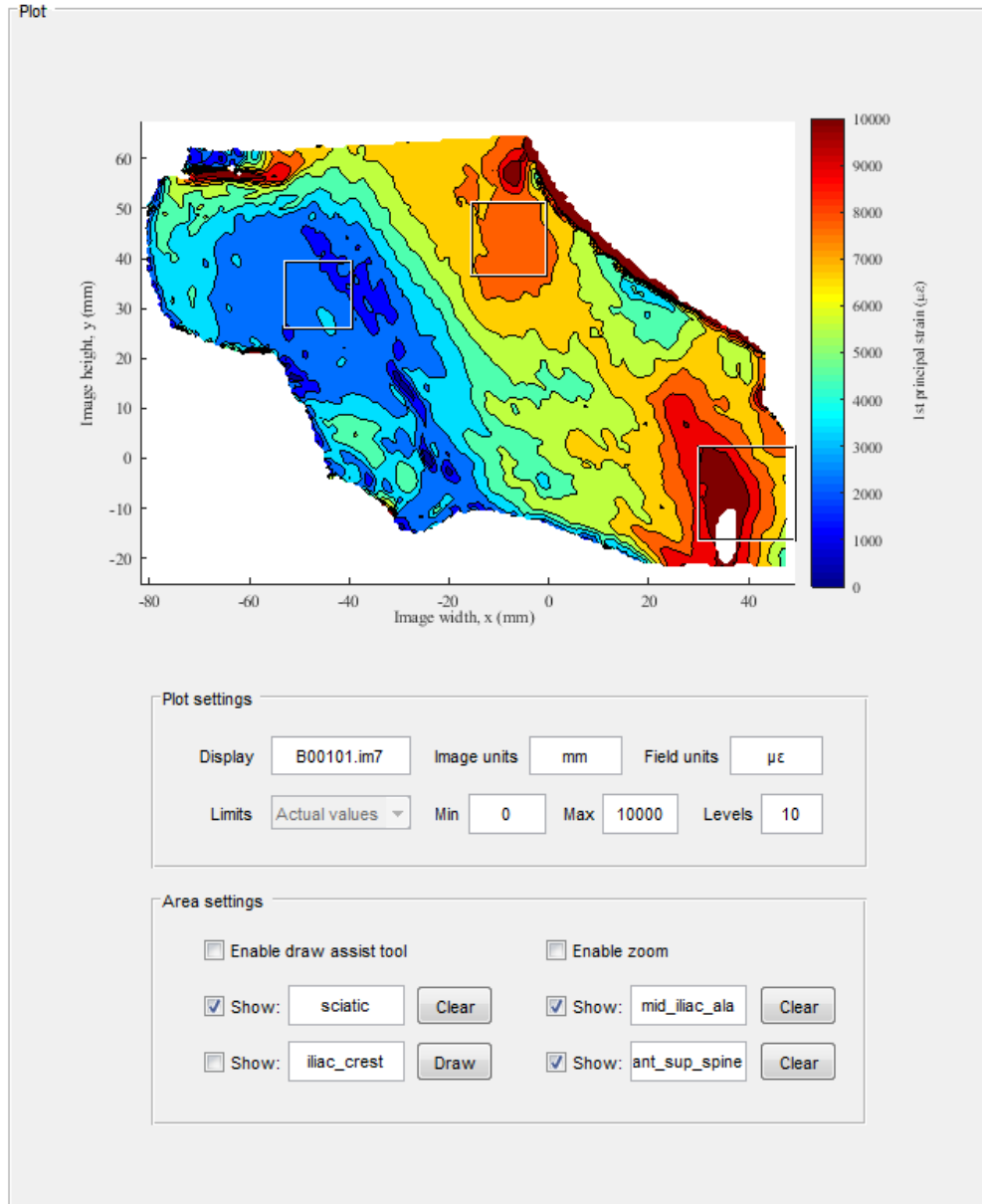
Figure H-2. Defining strain map and local regions of interest.

H.4 Extracting data

After finalizing the plot settings and the local areas, the data can be saved to a user-specified location via the "export" button. Any combination of the four export options can be checked. The "data" option saves the information in the table as a .txt file. The "current plot" option saves the image shown in the plot axes as a .jpg file. The "all plots" option saves the plots of every strain map loaded in the current session as separate .jpg files. And finally, the "video" option writes all strain maps to a .avi file at the specified frame rate.